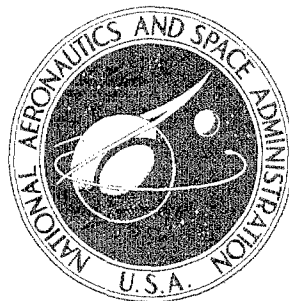


NASA CONTRACTOR
REPORT



Handwritten signature

NASA CR-801

NASA CR-801

AMPTIAC

DISQUALIFICATION AND RESTRICTION
APPLIED FOR PUBLIC RELEASE
DISTRIBUTION UNLIMITED

RESEARCH AND DEVELOPMENT
OF HIGH-PERFORMANCE
AXIAL-FLOW TURBOMACHINERY

Volume 2 - Design of Gas Bearings

by *P. W. Curwen*

20060516250

Prepared by
PRATT & WHITNEY AIRCRAFT
Latham, N. Y.
for Lewis Research Center

~~3072161~~

NASA CR-801

RESEARCH AND DEVELOPMENT OF HIGH-PERFORMANCE
AXIAL-FLOW TURBOMACHINERY

Volume 2 — Design of Gas Bearings

By P. W. Curwen

Distribution of this report is provided in the interest of information exchange. Responsibility for the contents resides in the author or organization that prepared it.

Prepared under Contract No. NAS 3-4179 by
PRATT & WHITNEY AIRCRAFT
Latham, N.Y.

for Lewis Research Center

NATIONAL AERONAUTICS AND SPACE ADMINISTRATION

For sale by the Clearinghouse for Federal Scientific and Technical Information
Springfield, Virginia 22151 — CFSTI price \$3.00

FOREWORD

The work reported herein was performed by Mechanical Technology Incorporated under subcontract from Pratt & Whitney Aircraft (P&WA P. O. 422, 715). Pratt & Whitney Aircraft, in turn, was prime contractor to the NASA-Lewis Research Center (NAS 3-4179). The technical manager was Jack A. Heller, Space Power System Division, NASA-Lewis Research Center, in consultation with Harold E. Rohlik, Calvin L. Ball, William J. Anderson, and George K. Fischer, Fluid System Components Division, NASA-Lewis Research Center.

The MTI Program Manager for this effort was Dr. P. W. Curwen. The Project Engineer for design of the initial turbocompressor bearing system and design of the rotor-bearing system simulator was A. Frost, the Project Engineer for the second and final bearing system designs and for the test evaluation of these designs was J. S. Meacher. The experimental evaluations of various combinations of surface coating materials for the bearings were directed by E. Arwas. The Design Engineer responsible for layout of the rotor-bearing system simulator was W. A. Geiger.

The work under this contract is published in three volumes, as follows:

Volume 1 CR-800 - Design of Turbine-Compressor (Pratt & Whitney Aircraft)

Volume 2 CR-801 - Design of Gas Bearings (Mechanical Technology Incorporated)

Volume 3 CR-802 - Design of Backup Gas Bearings (The Franklin Institute Research Laboratories)

ABSTRACT

The National Aeronautics and Space Administration is conducting an evaluation of candidate Brayton-cycle turbomachinery configurations. As part of this program, Pratt & Whitney Aircraft has designed a turbine-compressor incorporating a single-stage axial-flow turbine driving a six-stage axial-flow compressor supported on gas bearings. The gas bearings were designed and successfully tested in a gas bearing dynamic simulator by Mechanical Technology Incorporated.

TABLE OF CONTENTS

	Page
LIST OF TABLES _____	ix
LIST OF FIGURES _____	xi
SUMMARY _____	1
I. INTRODUCTION _____	4
II. FINAL DESIGN OF TURBOCOMPRESSOR BEARING SYSTEM _____	9
Operating Conditions and Design Specifications _____	9
Selection of Bearing Types _____	11
Performance Characteristics of the Journal Bearings _____	12
Hydrodynamic Thrust Bearing _____	28
Hydrostatic Thrust Bearings _____	36
Rotor-Bearing System Dynamics _____	41
Bearing Cooling Design _____	51
Bearing System Fabrication Materials _____	57 *
Bearing Surfacing Materials _____	59 x
Bearing System Instrumentation _____	60
III. DESIGN OF ROTOR-BEARING SYSTEM SIMULATOR _____	69
Simulator Rotor _____	71
Simulator Bearings _____	74
Control of Bearing Loads _____	74
Simulator Casings _____	75
Simulator Turbine _____	78
Thermal Simulation Capability _____	79
Simulator Instrumentation _____	80
IV. TEST EVALUATION OF THE FINAL BEARING SYSTEM DESIGN _____	81
Description of the Simulator Test Facility _____	82
Evaluation of the Hydrodynamic Thrust Bearing _____	88

	Page
Test Evaluation of the Forward Hydrostatic Thrust Bearing_____	93
Test Evaluation of the Reverse Hydrostatic Thrust Bearing_____	94
Test Evaluation of the No. 1 Journal Bearing_____	96
Test Evaluation of the No. 2 Journal Bearing_____	105
Resonance of the No. 2 Bearing Pad-Flexure Assemblies_____	118
Nature of the Low-Frequency Rotor Whirl Phenomenon_____	124
Whirl Threshold Vs. RPM for the No. 2 Bearing_____	127
Whirl Frequency_____	128
CONCLUSIONS AND RECOMMENDATIONS_____	134
Specific Conclusions_____	134
General Conclusions_____	137
Recommendations_____	139
LIST OF REFERENCES_____	141
NOMENCLATURE_____	142
APPENDICES	
A. Turbocompressor Environmental Specification_____	144
B. Simulator Acceptance Test Specification_____	147
C. Design and Test of Initial Bearing System_____	151
D. Design and Test of Second Bearing System_____	198
E. Final Report - First Bearing Materials Evaluation_____	226
F. Final Report - Second Bearing Materials Evaluation_____	271
G. Test Procedure for Whirl Threshold Tests_____	309

LIST OF TABLES

	Page
TABLE II-1 _____	15
TABLE II-2 _____	30
TABLE II-3 _____	37
TABLE II-4 _____	54
TABLE II-5 _____	63
TABLE C-1 _____	154
TABLE D-1 _____	198
TABLE D-2 _____	204

LIST OF FIGURES

	Page
Fig. II-1 - Calculated Performance In A 12.0 PSIA Argon Environment For The Final Design Of The No. 1 Journal Bearing (Rotor horizontal relative to a 1-g gravitational field) _____	19
Fig. II-2 - Calculated Performance In A 6.0 PSIA Argon Environment For The Final Design Of The No. 1 Journal Bearing (Rotor horizontal relative to a 1-g gravitational field) _____	20
Fig. II-3 - Calculated Performance In A 12.0 PSIA Argon Environment For The Final Design Of The No. 2 Journal Bearing (Rotor horizontal relative to a 1-g gravitational field) _____	21
Fig. II-4 - Calculated Performance In A 6.0 PSIA Argon Environment For The Final Design Of The No. 2 Journal Bearing (Rotor horizontal relative to a 1-g gravitational field) _____	22
Fig. II-5 - View Of The Pivoted-Pads And Pivot-Support Flexures For The No. 1 Journal Bearing _____	23
Fig. II-6 - View Of The No. 1 Bearing Components Assembled In The No. 1 Bearing Housing _____	24
Fig. II-7 - Two Of The Pivoted-Pads For The No. 2 Journal Bearing _____	25
Fig. II-8 - View Of The No. 2 Bearing Components Assembled In The Rotor-Bearing System Simulator _____	26
Fig. II-9 - View Of An Upper Pivot-Support Flexure For The No. 1 Journal Bearing _____	27
Fig. II-10 - View Of An Upper Pivot-Support Flexure For The No. 2 Journal Bearing _____	27
Fig. II-11 - Calculated Performance Of The Forward Hydrodynamic Thrust Bearing At 30,000 RPM And For Ambient Pressures From 6.0 to 12.0 PSIA _____	31
Fig. II-12 - Calculated Performance Of The Forward Hydrodynamic Thrust Bearing At 50,000 PRM And For Ambient Pressures From 6.0 to 12.0 PSIA _____	32
Fig. II-13 - Calculated Performance Of The Forward Hydrodynamic Thrust Bearing At 60,000 RPM And For Ambient Pressures From 6.0 to 12.0 PSIA _____	33

	Page
Fig. II-14 - Thrust Runner and Associated Attachment Parts _____	34
Fig. II-15 - Combination Helical-Grooved Hydrodynamic And Hydrostatic Forward Thrust Bearing Stator And Associated Mounting Parts _____	35
Fig. II-16 - View Of Hydrodynamic And Hydrostatic Forward Thrust Bearing Stator Assembly _____	35
Fig. II-17 - Calculated Performance Of The Forward Hydrostatic Thrust Bearing _____	38
Fig. II-18 - Calculated Performance Of The Reverse Hydrostatic Thrust Bearing _____	39
Fig. II-19 - View Of The Reverse Hydrostatic Thrust Bearing _____	40
Fig. II-20 - Calculated Critical Speeds And Bearing Stiffnesses For The Final Rotor-Bearing System design (Intersections of the No. 1 bearing stiffness curve and the critical speed curves define speeds at which resonance due to rotor unbalance can be expected) _____	46
Fig. II-21 - Calculated Mode Shapes For The Two Rigid-Body Critical Speeds Of The Final Rotor-Bearing System Design _____	47
Fig. II-22 - Calculated Maximum Bearing Loads For The Final Rotor- Bearing System Design Due to 0.002 Ounce-Inches Unbalance In The Turbine Plane _____	48
Fig. II-23 - Maximum Recommended Load Capacity Versus Speed For Continuous-Duty Operation Of The Final No. 1 Journal Bearing Design _____	49
Fig. II-24 - Maximum Recommended Load Capacity Versus Speed For Continuous-Duty Operation Of The Final No. 2 Journal Bearing Design _____	50
Fig. II-25 - View Of Heat Exchanger Located In Bore Of No. 1 Journal Bearing _____	55
Fig. II-26 - View Of Heat Exchanger Located In Bore Of No. 2 Journal Bearing _____	55
Fig. II-27 - Calculated Performance Of Thrust Bearing Cooling System _____	56
Fig. II-28 - Location Of Capacitance Probes In No. 1 Journal Bearing Region _____	65

	Page
Fig. II-29 - Location Of Capacitance Probes In No. 2 Journal Bearing Region _____	66
Fig. II-30 - View Of Various Capacitance Probe Configurations Used For Bearing System Performance Measurement _____	67
Fig. II-31 - Location Of Significant Thermocouples In Journal Bearing Regions _____	68
Fig. III-1 - Cross-Section View Of Rotor-Bearing System Simulator _____	70
Fig. III-2 - View Of Simulator Rotor, Less Thrust Runner _____	73
Fig. III-3 - View Of Complete Simulator Assembly With Rotor Horizontal _____	76
Fig. III-4 - View Of Complete Simulator Assembly With Rotor Vertical — Turbine End Down _____	76
Fig. III-5 - External View Of Bulkhead Instrumentation Pass-Throughs _____	77
Fig. IV-1 - View Of Simulator Mounted On Test Bench (Rotor Vertical, Turbine Down) With Vacuum Casings Removed For In-Place Rotor Balancing On The Gas Bearings _____	85
Fig. IV-2 - View Of Simulator Control Panel And Partial Set-Up Of Bearing System Instrumentation Read-Out Equipment _____	86
Fig. IV-3 - Schematic Diagram Of Simulator Control Panel _____	87
Fig. IV-4 - Measured And Calculated Load Versus Film Thickness Data For The Forward Hydrodynamic Thrust Bearing At 50,400 RPM _____	90
Fig. IV-5 - Measured And Calculated Load Versus Film Thickness Data For The Forward Hydrodynamic Thrust Bearing At 30,100 RPM _____	91
Fig. IV-6 - Thrust Bearing Capacitance Probe Traces Taken At 50,000 RPM _____	92
Fig. IV-7 - Measured Load Versus Film Thickness Data For The Forward Hydrostatic Thrust Bearing _____	95

	Page
Fig. IV-8 - Measured Load Versus Film Thickness Data For The Reverse Hydrostatic Thrust Bearing _____	95
Fig. IV-9 - Comparison Of Measured And Calculated Pad Pivot Film Thickness For The No. 1 Journal Bearing Operating In Air At 12.0 PSIA With The Rotor Horizontal _____	100
Fig. IV-10 - Oscilloscope Time-Base Traces Of Pad-To-Shaft Capacitance Probe Signals For No. 1 Journal Bearing — Taken At 50,500 RPM With Only Residual Rotor Unbalance _____	101
Fig. IV-11 - Oscilloscope Time-Base Traces Of Pad-To-Shaft Capacitance Probe Signals For No. 1 Journal Bearing — Taken At 50,730 RPM With 0.002 Ounce-Inches Of Unbalance Added To Turbine Plane _____	102
Fig. IV-12 - Oscilloscope Traces Of The No. 1 Journal Orbit At An Average Speed Of 50,600 RPM Whowing Effect Of Adding 0.002 Ounce-Inches Of Turbine Unbalance On Journal Response _____	103
Fig. IV-13 - Oscilloscope Traces Of The No. 1 Journal Orbit Showing Effect Of Increasing Speed From 50,000 To 60,000 RPM On Journal Response _____	104
Fig. IV-14 - Comparison Of Measured And Calculated Pad Pivot Film Thickness For The Second No. 2 Journal Bearing Design Operating In Air At 12.0 PSIA With The Rotor Horizontal _____	109
Fig. IV-15 - Comparison Of Measured And Calculated Pivot Film Thickness For The Final No. 2 Journal Bearing Design — Measured Data Taken At Threshold Of Rotor Whirl Condition (50,000 RPM, Rotor Horizontal, 14.7 PSIA Ambient) _____	110
Fig. IV-16 - Comparison Of Measured And Calculated Pivot Film Thickness For The Final No. 2 Journal Bearing Design — Measured Data Taken At Threshold Of Rotor Whirl Condition (50,000 RPM, Rotor Horizontal, 10.0 PSIA Ambient) _____	111
Fig. IV-17 - Comparison Of Measured And Calculated Pivot Film Thickness For The Final No. 2 Journal Bearing Design — Measured Data Taken At Threshold Of Rotor Whirl Condition (50,000 RPM, Rotor Vertical, 14.7 PSIA Ambient) _____	112
Fig. IV-18 - Oscilloscope Time-Base Traces Of Pad-To-Shaft Capacitance Probe Signals For No. 2 Journal Bearing — Taken At 50,120 RPM With Only Residual Rotor Unbalance _____	113

	Page
Fig. IV-19 - Oscilloscope Time-Base Traces Of Pad-to-Shaft Capacitance Probe Signals For The Final No. 2 Journal Bearing Design — Taken At 49,670 RPM With 0.002 Ounce-Inches Of Unbalance Added To Turbine Plane _____	114
Fig. IV-20 - Oscilloscope Time-Base Traces Of Pad-to-Shaft Capacitance Probe Signals For The Second No. 2 Journal Bearing Design — Taken At 50,500 RPM With Only Residual Rotor Unbalance _____	115
Fig. IV-21 - Oscilloscope Traces Of The No. 2 Journal Orbit Showing Effect Of Increasing Speed From 50,000 to 60,000 RPM, With And Without Turbine Unbalance, On Journal Response _____	116
Fig. IV-22 - Oscilloscope Time-Base Traces Of Pad-to-Shaft Capacitance Probe Signals For The Second No. 2 Journal Bearing Design — Taken At 60,000 RPM With 0.002 Ounce-Inches of Unbalance Added To Turbine Plane _____	117
Fig. IV-23 - Oscilloscope Traces Of Pad-to-Shaft Probes Showing Resonant Vibration Amplitudes Of An Upper Pad-Flexure Assembly For The Final No. 2 Journal Bearing Design As A function of Bearing Diametral Clearance (C_D) _____	121
Fig. IV-24 - Measured Resonance Curve For An Upper Pad-Flexure Assembly Of The Second No. 2 Journal Bearing Design _____	122
Fig. IV-25 - Calculated Gas Film Stiffness And Damping Coefficients For One Pad At 50,000 RPM Versus Film Thickness For 1st And 2nd Harmonic Excitation Of The Gas Film (1st and 2nd harmonic excitation is equivalent to synchronous and two-per-rev excitation) _____	123
Fig. IV-26 - Illustration Of Change In No. 2 Journal Orbit And Pad-to-Shaft Probe Traces Due to Low-Frequency Rotor Whirl Phenomenon _____	126
Fig. IV-27 - Effect Of Rotor Orientation On Diametral Bearing Clearance At Threshold Of No. 2 Journal Low-Frequency Whirl _____	130
Fig. IV-28 - Effect Of Ambient Pressure On Diametral Bearing Clearance At Threshold Of No. 2 Journal Low-Frequency Whirl _____	131
Fig. IV-29 - Effect Of Changing Lubricant Gas From Air to Argon On Diametral Bearing Clearance At Threshold Of No. 2 Journal Low-Frequency Whirl _____	132
Fig. IV-30 - Whirl Frequency And Whirl-Frequency Ratio Versus Rotor Speed For The Final No. 2 Journal Bearing Design _____	133

Fig. C-1 - Calculated Performance In A 12.0 PSIA Argon Environment For The Initial Design Of The No. 1 Journal Bearing (Rotor horizontal relative to a 1-g gravitational field) _____	158
Fig. C-2 - Calculated Performance In A 6.0 PSIA Argon Environment For The Initial Design Of The No. 1 Journal Bearing (Rotor horizontal relative to a 1-g gravitational field) _____	159
Fig. C-3 - Calculated Performance In A 12.0 PSIA Argon Environment For The Initial Design Of The No. 2 Journal Bearing (Rotor horizontal relative to a 1-g gravitational field) _____	160
Fig. C-4 - Calculated Performance In A 6.0 PSIA Argon Environment For The Initial Design Of The No. 2 Journal Bearing (Rotor horizontal relative to a 1-g gravitational field) _____	161
Fig. C-5 - View Of No. 1 Bearing Pivot-Support Flexures And Pivoted-Pads For Initial Bearing Design _____	162
Fig. C-6 - Calculated Performance Of The Initial Design Of The Forward Hydrostatic Thrust Bearing With 20 Orifices _____	164
Fig. C-7 - Calculated Critical Speeds And Bearing Stiffness For The Initial Bearing System Design (Bearing stiffness data based on horizontal rotor orientation relative to a 1-g gravitational field and a 12.0 psia argon environment) _____	167
Fig. C-8 - Calculated Maximum Bearing Loads For The Initial Bearing Design Due To 0.002 Ounce-Inches Unbalance In The Turbine Plane _____	168
Fig. C-9 - Maximum Recommended Load Capacity Vs. Speed For Continuous-Duty Operation Of The Initial Design Of The No. 1 Journal Bearing _____	169
Fig. C-10 - Maximum Recommended Load Capacity Vs. Speed For Continuous-Duty Operation Of The Initial Design Of The No. 2 Journal Bearing _____	170
Fig. C-11 - Argon Cooling Gas Flow Diagram For The Initial Design Of The No. 1 Journal Bearing And Thrust Bearing _____	176
Fig. C-12 - Argon Cooling Gas Flow Diagram For The Initial Design Of The No. 2 Journal Bearing _____	177
Fig. C-13 - Heat Exchanger For No. 1 Journal After Brazing Into Rotor _____	178

	Page
Fig. C-14 - Heat Exchanger For No. 2 Journal Prior To Brazing Into Rotor _____	178
Fig. C-15 - Thermal Boundary Conditions And Calculated Isotherms For The Initial Design Of The No. 2 Journal Bearing _____	179
Fig. C-16 - Calculated Performance Of Thrust Bearing Cooling System _____	180
Fig. C-17 - Thermal Boundary Conditions For The Initial Design Of The No. 1 Journal Bearing And Thrust Bearing _____	181
Fig. C-18 - Calculated Isotherms For The Initial Design Of The No. 1 Journal Bearing And Thrust Bearing _____	182
Fig. C-19 - Measured Load Versus Deflection Plot For The Initial Design Of The Pivot-Support Flexures For No. 2 Journal Bearing _____	185
Fig. C-20 - Measured Load Versus Deflection Plot For The Initial Design Of The Pivot-Support Flexures For No. 1 Journal Bearing _____	185
Fig. C-21 - Measured Load Versus Film Thickness For The Initial Design (20 Orifices) Of The Forward Hydrostatic Thrust Bearing _____	186
Fig. C-22 - Measured Stability Map For The Initial Design (20 Orifices) Of The Forward Hydrostatic Thrust Bearing _____	191
Fig. C-23 - Comparison Of Measured Load Versus Film Thickness Data For The Forward Hydrostatic Thrust Bearing Before And After Reduction Of The Number Of Feed Orifices _____	191
Fig. C-24 - Measured Average Pivot Film Thickness For The Loaded Pads, And Corresponding Temperatures, At 31,000 RPM Versus Ambient Pressure (Initial journal bearing designs) _____	192
Fig. C-25 - Measured Average Pivot Film Thickness For The Loaded Pads, And Corresponding Temperatures, At 50,800 RPM Versus Ambient Pressure (Initial Journal bearing designs) _____	193
Fig. C-26 - Oscilloscope Photographs Of The No. 1 Journal Orbit As A Function Of Speed And Rotor Unbalance (Initial bearing system design) _____	194
Fig. C-27 - Oscilloscope Photographs Of The No. 2 Journal Orbit As A Function Of Speed And Rotor Unbalance (Initial bearing system design) _____	195
Fig. C-28 - Oscilloscope Photographs Showing Effect Of Rotor Unbalance At 50,000 RPM On Two Of The No. 1 Journal Bearing Pad-To-Shaft Film Thickness Traces (Initial bearing system design) _____	197

Fig. D-1 - Friction Loss Versus Bearing Diametral Clearance (Preload) For The No. 2 Journal Bearing As A Function of Pad Clearance Ratio (C/R) p	202
Fig. D-2 - Calculated Performance In A 12.0 PSIA Argon Environment For The Second Design Of The No. 1 Journal Bearing (Rotor horizontal relative to a 1-g gravitational field)	205
Fig. D-3 - Calculated Performance In A 6.0 PSIA Argon Environment For The Second Design Of The No. 1 Journal Bearing (Rotor horizontal relative to a 1-g gravitational field)	206
Fig. D-4 - Calculated Performance In A 12.0 PSIA Argon Environment For The Second Design Of The No. 2 Journal Bearing (Rotor horizontal relative to a 1-g gravitational field)	207
Fig. D-5 - Calculated Performance In A 6.0 PSIA Argon Environment For The Second Design Of The No. 2 Journal Bearing (Rotor horizontal relative to a 1-g gravitational field)	208
Fig. D-6 - Calculated Critical Speeds And Bearing Stiffnesses For The Second Bearing System Design (Bearing stiffness data is based on horizontal rotor orientation relative to a 1-g gravitational field and a 12.0 psia argon environment)	210
Fig. D-7 - Calculated Maximum Bearing Loads For The Second Bearing System Design Due To 0.002 Ounce-Inches Unbalance In The Turbine Plane	211
Fig. D-8 - Maximum Recommended Load Capacity Versus Speed For Continuous-Duty Operation Of The Second Design Of The No. 1 Journal Bearing	212
Fig. D-9 - Maximum Recommended Load Capacity Versus Speed For Continuous-Duty Operation Of The Second Design Of The No. 2 Journal Bearing	213
Fig. D-10 - Thermal Boundary Conditions For The Second Design Of The No. 1 Journal Bearing And Thrust Bearing	215
Fig. D-11 - Calculated Isotherms For The Second Design Of The No. 1 Journal Bearing And Thrust Bearing	216
Fig. D-12 - Thermal Boundary Conditions And Calculated Isotherms For The Second Design Of The No. 2 Journal Bearing	217
Fig. D-13 - Measured Load Versus Deflection Plot For The Revised Upper Pivot-Support Flexures For The Second Design Of No. 1 and No. 2 Journal Bearings	220
Fig. D-14 - View Of Revised Upper Pivot-Support Flexures For The Second Design Of The No. 1 and No. 2 Journal Bearings	221

	Page
Fig. D-15 - Views Of One Pad For The Second No. 2 Journal Bearing Design Showing Weights Added To Increase Pad Inertia In Roll Direction _____	222
Fig. D-16 - Comparison Of Measured And Calculated Pad Pivot Film Thickness For The Second No. 1 Journal Bearing Design Operating In Air At 12.0 PSIA With The Rotor Horizontal____	224
Fig. D-17 - Comparison Of Measured And Calculated Pad Pivot Film Thickness For The Second No. 2 Journal Bearing Design Operating In Air At 12.0 PSIA With The Rotor Horizontal_____	225

SUMMARY

Three variations of a basic ^A gas-bearing ^A rotor-support system have been designed, built, and tested by Mechanical Technology Incorporated for the NASA Brayton cycle axial-flow ^A turbocompressor being developed by Pratt and Whitney Aircraft under prime contract from the NASA-Lewis Research Center. (Figure 1 shows a cross-section view of the turbocompressor.) The designs were experimentally evaluated in a full-scale rotor-bearing system test rig which

1. exactly simulated the design of the turbocompressor bearings,
2. very closely simulated the mechanical configuration and physical parameters of the turbocompressor rotor (the actual turbine and compressor components were not, however, used),
3. permitted testing of the rotor-bearing system under operating and environmental conditions similar to those which would exist in the turbocompressor (turbine inlet temperature, however, was not simulated).

All three bearing system designs performed satisfactorily and successfully passed the required P&WA acceptance tests. The final design, described in Sections II and IV of this report, represents a minimum bearing-friction-loss design consistent with whirl-free operation of the rotor.

Following acceptance testing of the first, or initial, gas-bearing rotor-support system, an attempt was made to attain a 61 percent reduction in total journal bearing friction loss by modifying the bearings to operate at larger clearances. Upon test of the modified design, a low-frequency, stable, rotor-whirl phenomenon was observed in the turbine bearing as the clearance was being increased to the larger value. This marks the first observance by MTI of a whirl condition in a gas-lubricated pivoted-pad journal bearing (it also marks the first time that MTI has tested a pivoted-pad bearing designed to operate at "large" clearances). Until the whirl phenomenon is better understood, MTI recommends that the diametral clearances of the journal bearings be maintained less-than-or-equal-to 0.00135 inches as specified in Section V of this report. This will assure whirl-free operation of the rotor. At these clearances, the final design represents a

→ 34.3 percent reduction in total journal bearing friction loss relative to the initial design.

Successful development of a reliable turbocompressor gas-bearing rotor-support system, at least under static environmental conditions, appears to have been achieved. Evaluation and acceptance testing of the three bearing designs was achieved without a single bearing rub or failure. However, extensive testing of the actual turbocompressor, under both static and dynamic environmental conditions, will be required before final substantiation of reliability can be made.

→ p 57

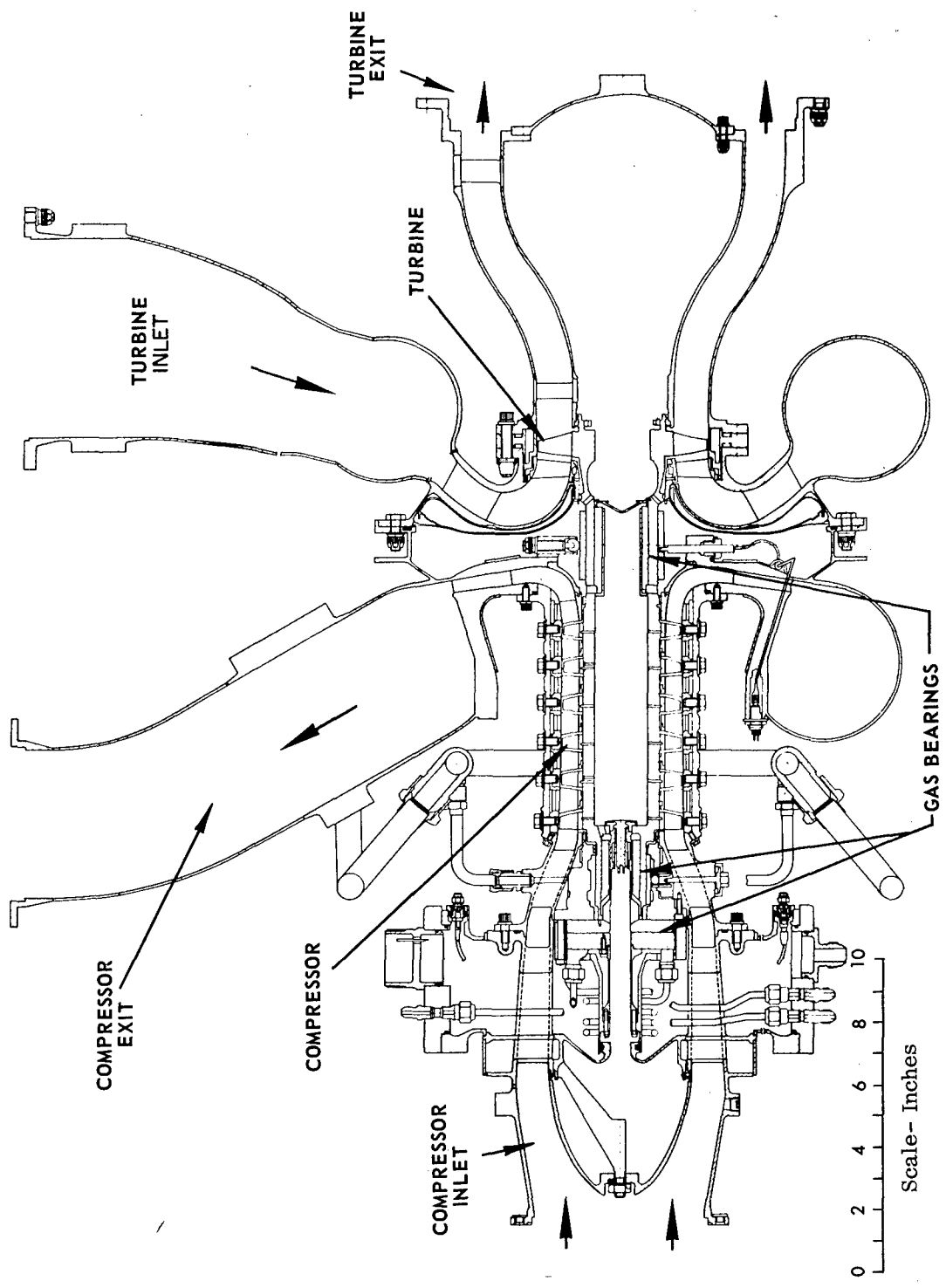


Figure 1 Brayton-Cycle Turbine-Compressor

I. INTRODUCTION

Mechanical Technology Incorporated (MTI), under subcontract from Pratt & Whitney Aircraft (P&WA), has cooperated in the design and development of a gas-lubricated axial flow turbocompressor for the Lewis Research Center of the National Space and Aeronautics Administration (NASA-Lewis). More specifically, MTI's participation in the development has been in the following three areas:

1. Design of a gas-bearing system for the turbocompressor;
2. Test evaluation of several bearing surfacing materials under conditions of (a) start-stop sliding contact, and (b) impact-induced momentary contacts at high rotor speeds;
3. Test evaluation of the complete gas bearing system, using the most promising bearing surfacing material, in a rotor-bearing test machine which closely simulates most of the turbocompressor mechanical parameters and operating conditions.

The development of gas-bearing supported turbomachinery for closed-system Brayton cycle power plants is a significant step in the gas turbine technology. The most noteworthy attribute of gas lubrication for the present turbocompressor application is simplicity. In a conventional gas turbine, the rotating system is supported on oil lubricated bearings (fluid film or rolling element). However, for closed system operation where the same gas is continuously circulated, means must be provided to ensure that the oil cannot contaminate the gas stream. Leakage of oil into this stream would ultimately degrade power plant performance to an unacceptable level due to fouling of critical heat exchanger parts and build up of decomposition products.

To prevent contamination, seal systems must be used to isolate the oil from the cycle gas. Auxiliary equipment in the form of lube pumps, coolers, separators, absorbers, and reservoirs is also required. To obtain long-term non-degrading performance from an oil-lubricated closed-cycle power plant is a problem, particularly if the plant must be capable of repeated start-ups and shut-downs.

In a gas-bearing machine, the rotating system is supported on a film of gas. Recent developments of motor-driven gas-bearing compressors and circulators, which have jointly accumulated over 59,000 hours of field operation, have created an understandable impetus to apply gas-bearings to closed-system gas turbine machinery. By utilizing cycle gas for the bearing system lubricant, the contamination problem and auxiliary equipment requirements for the closed Brayton cycle, as mentioned above, can be eliminated. The potential ability of a well-designed gas-lubricated turbomachine to operate reliably for long periods of time with repeated start-ups and shutdowns should therefore be quite high.

As in all new technologies, problem areas do exist in the design and application of gas bearings. The complete lack of boundary lubrication in the event of an accidental high-speed bearing rub is probably the most critical problem area in the practical application of gas-bearing turbomachinery. Such rubs may occur due to passage of dirt through the bearings, vibration and shock loads, or improper operation of the machine. The solution to this boundary lubrication problem is to obtain bearing surfacing materials which are capable of surviving many dry rubs with negligible wear or performance degradation. A second inherent problem area which is common to self-acting bearings (which are the type of bearings used in the turbocompressor) is that of low load capacity. The load capacity in a self-acting bearing is, for all practical purposes, limited to several psi. Finally, gas bearings have very low damping capability, and hence are prone to rotor dynamic and rotor-bearing stability problems. The limitations of low-load capacity, absence of boundary lubrication, and low damping, imposes several new and stringent requirements on rotor dynamics design. Close attention to these requirements at all times, and particularly during the early conceptual and design phases, is vital to the successful development of gas-lubricated turbomachinery.

*Numbers in brackets refer to references listed on page 207.

The requirements for the turbocompressor bearing system (as described in Section II of this report) necessitated a number of advancements in the technology of gas-bearing design and application. To obtain maximum assurance of a successful development, the following engineering philosophy was used throughout the program.

1. Make maximum use of existing gas-bearing design technology and operational experience with respect to (a) selection of types of bearings to be used and (b) selection of basic design criteria for these bearing types.
2. Conduct component and subsystem test programs in critical areas where existing technology and/or operational experience was either non-existent or inadequate to permit quantitative evaluation of design concepts. Two such test programs were conducted — one to evaluate various bearing surfacing materials in hopes that significantly better sliding capability could be obtained relative to existing materials, and another to evaluate the complete turbocompressor rotor-bearing system design under actual operating conditions.
3. Maintain very close liaison with P&WA during the design phase to ensure that all aerodynamic, thermodynamic, and mechanical interactions and interfaces were properly identified and evaluated. In particular, the areas of aerodynamic thrust and radial loads, rotor design, heat transfer design, casing design, instrumentation provisions, balancing techniques, and assembly procedures, were integrated very closely with the P&WA design effort.

In total, three versions of the basic turbocompressor bearing system were built and tested. The basic system consists of pivoted-pad self-acting journal bearings, a spiral-grooved self-acting unidirectional thrust bearing, and a bi-directional externally pressurized thrust bearing for start-up and shutdown of the machine

(a single thrust bearing runner is used for both the self-acting and pressurized thrust bearings). The first design of the basic bearing system was based upon design criteria which, on the basis of past experience, gave maximum assurance of a successful development. Design and evaluation of this first, or initial, system is described in Appendix C of this report. The system was successfully developed and passed the required P&WA acceptance test.

The second version of the bearing system design involved (1) an increase in the bearing clearance-to-radius ratio to achieve reduced bearing friction losses, (2) a decrease in the stiffness of the journal bearing support flexures to achieve increased tolerance to temperature variations in the journal bearing regions, and (3) an increase in the mass of the journal bearing pads to control their dynamic characteristics at the increased clearance-to-radius ratio. This design modification was only partially successful in the sense of achieving the total hoped-for reduction in bearing friction loss. An unexpected rotor whirl phenomenon was encountered which prevented full achievement of the larger bearing clearance required to realize the total reduction. Nonetheless, a significant reduction of bearing friction was attained, and the modified bearing design successfully passed the required P&WA acceptance tests. This design modification is described in Appendix D.

The final modification of the bearing system involved a readjustment of the mass of the journal bearing pads back to the original design condition. A test program was then conducted to define the stable operating range of the journal bearing system as a function of various operation conditions.

Section II of this report contains a complete description of the third, or final, bearing system design, this being the design which has been recommended by MTI

for incorporation into the turbocompressor. Section III of the report describes the design of the rotor-bearing system simulator which was used to test the various modifications of the bearings. Section IV presents actual test and performance data for the final design of the bearing system. Conclusions and recommendations pertaining to the final design are given in Section V.

II. FINAL DESIGN OF THE TURBOCOMPRESSOR BEARING SYSTEM

As mentioned in the preceeding section of this report, three versions of the basic bearing system for the turbocompressor were built and tested. The initial and second bearing system designs are discussed in Appendices C and D respectively. This section presents design parameters and calculated performance characteristics for the final version of the bearing system.

It should be appreciated that the final design of the turbocompressor system has logically evolved from the initial and second bearing designs, and represents a significant state-of-the-art advance in the application of gas-lubricated bearings. Whereas the initial design was based, wherever possible, upon tried and proven state-of-the-art design criteria, so as to give maximum assurance of successful operation of the first bearing set, the second and final designs represent previously untried extensions of certain design criteria and, in some instances, intentional disregard of previous practice. This was done in an effort to more closely tailor the bearing design to the particular needs of a dynamic space-power system — namely, minimization of machinery parasitic losses and maximum tolerance of rapid and large thermal transients such as may occur during start-up of a space system.

Operating Conditions and Design Specifications

During the first several months of the turbocompressor development program, numerous aerodynamic, rotor-dynamic, bearing sizing, and heat-transfer design studies were made. During this period, frequent design review meetings, jointly attended by P&WA and MTI, were held to evaluate the studies and to be certain that all interactions between the various engineering disciplines were being properly accounted for and properly weighed with respect to obtaining the best overall integrated design of the turbocompressor. As a result of this approach, the following set of bearing system operating conditions were quickly evolved as being reasonable from both the rotor-bearing system and the aerodynamic system standpoints.

Design speed	-	50,000 RPM
Overspeed	-	60,000 RPM
Rotor mass	-	11.35 lb _m .
Bearings lubricant (system fluid)	-	Argon
Bearings ambient pressure (minimum)	-	6.0 psia
Bearings ambient pressure (design point)	-	12.0 psia
Maximum operating thrust load	-	24.0 lb. in the forward direction*
Range of maximum thrust load at start-up	-	100.0 lb. forward to 50.0 lb. in the reverse direction

It is interesting to note that the only change made to the above set of operating conditions during the detailed phase of the turbocompressor development was a slight reduction in rotor weight from 11.35 lb. to approximately 10.5 lb. Since the bearing sizing studies, and the detailed design of the initial bearing system, were done on the basis of 11.35 lb. rotor weight, it was decided, for reasons of direct comparison, to use this same rotor weight for the detailed design of the second and third (i.e., the final) bearing system modifications. Hence, the bearing calculations presented in this section, and in Appendices C and D, are based upon bearing loads which are approximately 0.4 lb. heavier than would actually exist with the turbocompressor horizontal in a 1-g acceleration field.

In addition to the above listed operating conditions, the design of the bearing system was required to also satisfy a set of environmental conditions as designated in NASA Specification No. P0055-1. This specification is enclosed in Appendix A of this report.

*The forward end of the turbocompressor is the compressor-inlet end of the machine. Consequently, a forward thrust load is a force directed from the turbine towards the compressor, and similarly, a reverse thrust load would be a force directed from the compressor towards the turbine.

Selection of Bearing Types

During the early stages of the design phase, careful consideration was given to the type of journal and thrust bearings that should be used in the turbocompressor. The bearing types selected for the initial bearing system design were

1. flexibly supported, pivoted-pad, self-acting journal bearings
2. flexibly supported, helical-grooved (Whipple plate) self-acting thrust bearing
3. inherently compensated, annular, externally-pressurized thrust bearings to support the thrust loads at start-up and shutdown.

No changes in bearing types were made during evolution of the second and third bearing system modifications.

The basic reasons for selection of these bearing types were as follows.

1. Pivoted-pad journal bearings could readily be designed to be stable over the operating range of the machine. The freedom of angular motion of the pivoted-pads also provides good alignment capability. In addition, this freedom of motion, and the deep recesses between pads, have proved to be effective safeguards against damage from foreign particles in the gas stream. Finally, and perhaps most importantly, this type of journal bearing had been successfully used in several previous gas-bearing turbomachinery developments.
2. The load capacity of properly designed helical-grooved thrust bearings is relatively insensitive to the compressibility number $\Lambda = \frac{6\mu\omega R^2}{P_a h^2}$ of the application. This is in sharp contrast to other types of self-acting thrust bearings (e.g., pivoted-pad, tapered land, step type, and others) whose load capacity rapidly approaches an asymptotic value as the compressibility number is increased. In view of the relatively high speeds and low ambient pressures of interest in this application, the preliminary calculations showed the helical-grooved thrust bearing

to have more than twice the load capacity of other self-acting bearing types at the design conditions. The helical-grooved thrust bearing is, however, quite sensitive to the degree of parallelism between the thrust runner and the thrust stator. Accordingly, the thrust stator should be flexibly mounted to permit it to "track" misalignment and wobble of the thrust runner. Once again, this type of bearing had been successfully applied in previous turbomachinery developments.

3. The present application may be subject to high axial loads during start-up and shut down, making it mandatory to externally pressurize the thrust bearing during these intervals. With proper design the inherently-compensated externally-pressurized thrust bearing has a much higher threshold of onset of pneumatic hammer than other externally pressurized bearing types, such as orifice compensated and pocketed bearings.

In the following paragraphs the individual components of the bearing system are reviewed in more detail. Attention is focused on calculated performance data and on practical considerations of the design. Sound theoretical analyses are essential in gas-bearing development, and were used to establish the steady-state and dynamic characteristics of the bearing system. These procedures, however, have been covered extensively in prior research and in general purpose design papers and reports, and hence will not be repeated here. (References 2 through 14 list some of the standard texts and recent publications in these areas.)

Performance Characteristics of the Journal Bearings

As noted previously, the journal bearings selected for the turbocompressor are of the pivoted-pad type. Detailed analyses of this type of bearing are available based on numerical integration of the compressible Reynolds equation. The resulting normalized pad data is assembled as a function of pivot position, pad eccentricity ratio, and compressibility number ($\Lambda = \frac{6\mu\omega}{P} \left(\frac{R}{C}\right)^2$). The static and dynamic characteristics of the bearings are then obtained by vectorial

summation of the characteristics of the individual pads. By storing this bearing data in computer memory, high speed digital computer programs can be utilized for making screening and final design calculations for any specified combination of operating conditions and bearing geometry.

The turbocompressor journal bearings, which are entitled Bearing No. 1 for the bearing at compressor inlet, and Bearing No. 2 for the bearing at the turbine end, have been designed to operate satisfactorily under the following conditions:

1. At any orientation of the turbocompressor in a zero to 0.18-g acceleration field;
2. At any angle between zero and 180 degrees shaft angle (where zero would correspond to a vertically oriented shaft with the compressor-end up and 180 degrees would be vertical with the compressor-end down) in a 1.0-g acceleration field, but limited at the intermediate angular positions to a circumferential orientation in which the journal bearing load vector passes between pivots of the "lower" journal bearing pads*;
3. At any ambient pressure above 6.0 psia;
4. To withstand, while in any of the above orientations, an unbalance of 0.002 ounce-inches in the plane of the turbine wheel.

The pivots for each of the journal bearing pads are mounted on individual support flexures. These flexures serve several purposes.

1. They inherently improve the ability of the bearings to accommodate thermal expansion changes which would tend to change the bearing clearance.
2. They reduce bearing preload changes due to centrifugal growth of the journals.
3. They reduce the rigid-body critical speeds of the system.

*The term "lower" pads in the context of this report refers to the two pads in each journal bearing which are mounted on the "stiff" pivot-support flexures.

Two of the pivot-support flexures in each journal bearing are relatively stiff flexures so as to limit radial displacement of the rotor, relative to the concentric position of the various shaft labyrinth seals, when the turbocompressor is operated in a horizontal position in a 1.0-g acceleration field. These stiff flexures are referred to as the lower (or loaded) flexures for each journal bearing. The remaining two flexures in each bearing, referred to as the upper (or unloaded) flexures, are considerably less stiff than the lower flexures. These softer flexures provide most of the accommodation to changes in the thermal expansion and centrifugal growth of the journals.

A summary of the design parameters and calculated design-point performance characteristics for the two journal bearings is given in Table II-1. It should again be emphasized that the data given in Table II-1 is the result of an evolutionary process starting with design and test of the initial bearing system as described in Appendix C, followed by design and test of a modified (or second) design as described in Appendix D, and concluding with testing of the third modification referred to here as the final design. A more complete presentation of the calculated journal bearing performance is given in Figures II-1 through II-4. These figures show plots of the following performance characteristics as a function of rotor speed:

1. Bearing film thickness at the pivot location of the loaded pads,
2. Bearing friction loss,
3. Bearing radial stiffness,
4. Ratio of pad resonant frequency to rotor synchronous frequency in the roll direction for the upper and lower pads (or equivalently, the unloaded and loaded pads),
5. Ratio of pad resonant frequency to rotor synchronous frequency in the pitch direction for the upper (unloaded) and lower (loaded) pads.

The data of Figures II-1 through II-4 include the effects of flexure deflection and journal centrifugal growth. The temperatures of the bearings were held constant at design-point conditions for all the calculations.

TABLE II-1
 JOURNAL BEARING DESIGN PARAMETERS AND
 CALCULATED PERFORMANCE CHARACTERISTICS

All data given below is based upon the following gas-bearing operating conditions

Rotor speed	-	50,000 RPM
Lubricant gas	-	Argon
Bearing ambient pressure	-	12.0 psia

Configuration	Pivoted-pad (with hydrodynamic lift-off)
Journal Diameter, Inches	
No. 1 (Forward) Bearing	1.500
No. 2 (Turbine End) Bearing	2.125
Bearing Length-to-Diameter Ratio (L/D)	
No. 1 Bearing	1.0
No. 2 Bearing	1.0
Number of Pads Per Bearing	
	4
Pad Orientation (Referenced to horizontal orientation of the rotor)	Rotor weight between pivots
Arc Length (β) of Pad, Degrees	
	80.0
Pivot Location (θ_p / β) from Leading Edge	
	0.65
Pad Clearance Ratio (C_p / R)	
No. 1 Bearing	0.0018
No. 2 Bearing	0.0030
Bearing Preload Ratio (m)	
No. 1 Bearing	0.50
No. 2 Bearing	0.788
Individual Pad Mass, Pounds	
No. 1 Bearing	0.14
No. 2 Bearing	0.21

TABLE II-1 (Cont.)

Pivot Ball Diameter, Inches	
No. 1 Bearing	0.2500
No. 2 Bearing	0.3750
Pivot Socket Diameter, Inches	
No. 1 Bearing	0.2550
No. 2 Bearing	0.3824
Bearing Number (A)	
No. 1 Bearing	2.98
No. 2 Bearing	1.23
Measured Pivot Support Radial Stiffness, lb./in.	
No. 1 Bearing	9,800 (upper pads) 50,000 (lower pads)
No. 2 Bearing	8,400 (upper pads) 70,000 (lower pads)
Bearing Load, Pounds	
Horizontal Orientation (Rotor Weight)	
No. 1 Bearing	3.63
No. 2 Bearing	7.72
Space Operation (Due to 0.002 ounce-inches mass unbalance in turbine plane)	
No. 1 Bearing	0.38
No. 2 Bearing	1.23
Operating Clearance at Pivot, Inches	
Horizontal Orientation (Loaded Pads)	
No. 1 Bearing	0.00057
No. 2 Bearing	0.00058
Space Operation (All Pads)	
No. 1 Bearing	0.00067
No. 2 Bearing	0.00067
Friction Loss Per Journal, Watts	
Horizontal Orientation	
No. 1 Bearing	57.4
No. 2 Bearing	235.8
Space Operation	
No. 1 Bearing	56.5
No. 2 Bearing	232.5
Radial Gas-Film Stiffness, lb./in.	
Horizontal Orientation	
No. 1 Bearing	34,400
No. 2 Bearing	75,000
Space Operation	
No. 1 Bearing	33,100
No. 2 Bearing	72,200

TABLE II-1 (Cont.)

Shaft Material	Waspaloy
Pad Material	M-1 Tool Steel
Pivot Material	M-1 Tool Steel
Journal and Pad Surfacing Material	Chrome Oxide

A photograph of the No. 1 bearing pads, pivots, and pivot-support flexures is shown in Figure II-5 (this is actually a photo of the initial No. 1 bearing components where all flexures had equal stiffness and the pads had a C_p/R ratio of 0.001). Figure II-6 is a view of the No. 1 bearing components assembled in the No. 1 bearing housing. Figures II-7 and II-8 are photographs of (a) two of the No. 2 bearing pads, and (b) the assembly of the No. 2 bearing components in the rotor-bearing system simulator (again, these are pictures of the initial-design No. 2 bearing components where all flexures had equal stiffnesses). Figures II-9 and II-10 are photographs of the final-design upper flexures for the No. 1 and No. 2 bearings respectively.

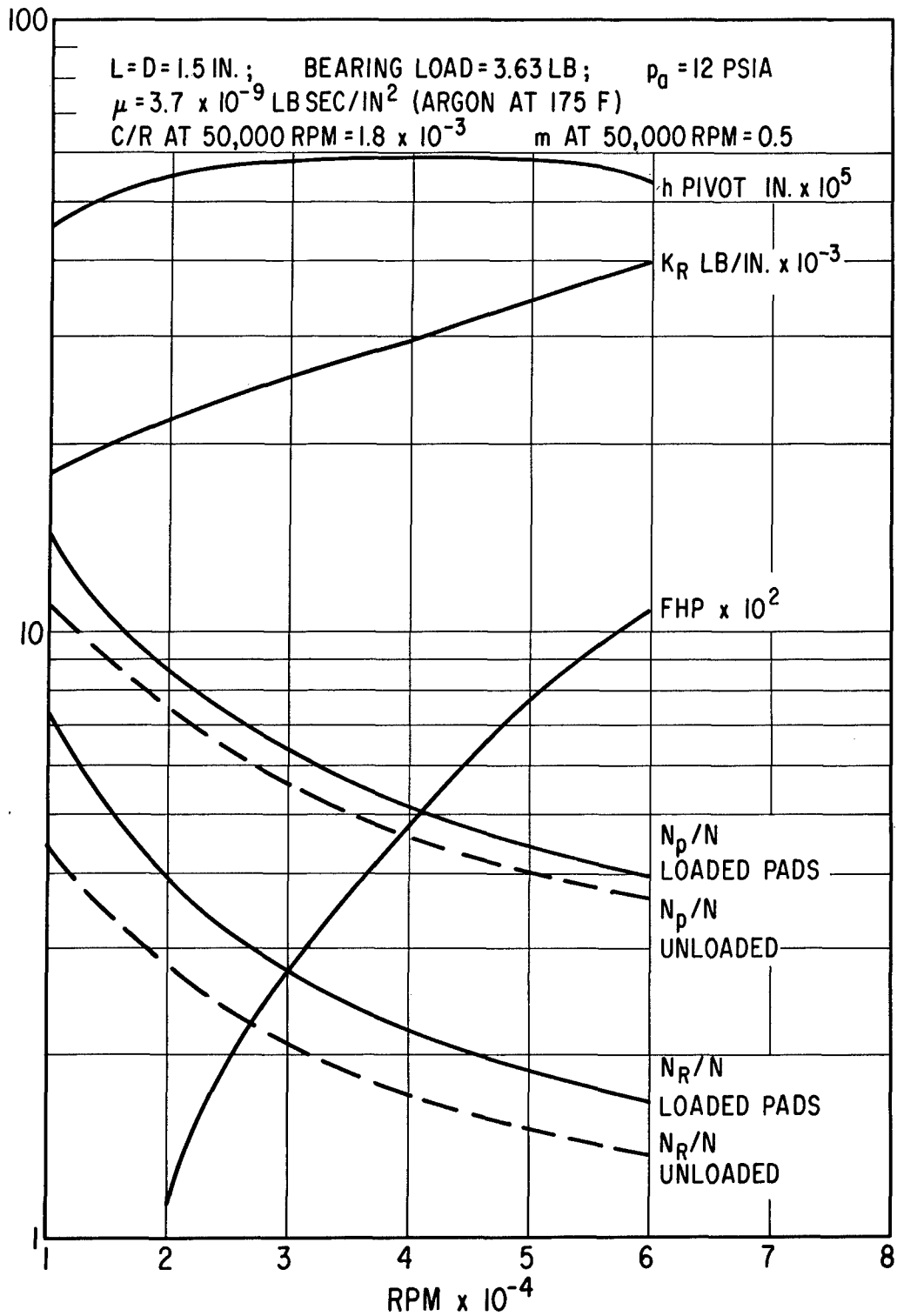


Fig. II-1 - Calculated Performance In A 12.0 PSIA Argon Environment
 For The Final Design Of The No. 1 Journal Bearing (Rotor
 horizontal relative to a 1-g gravitational field)

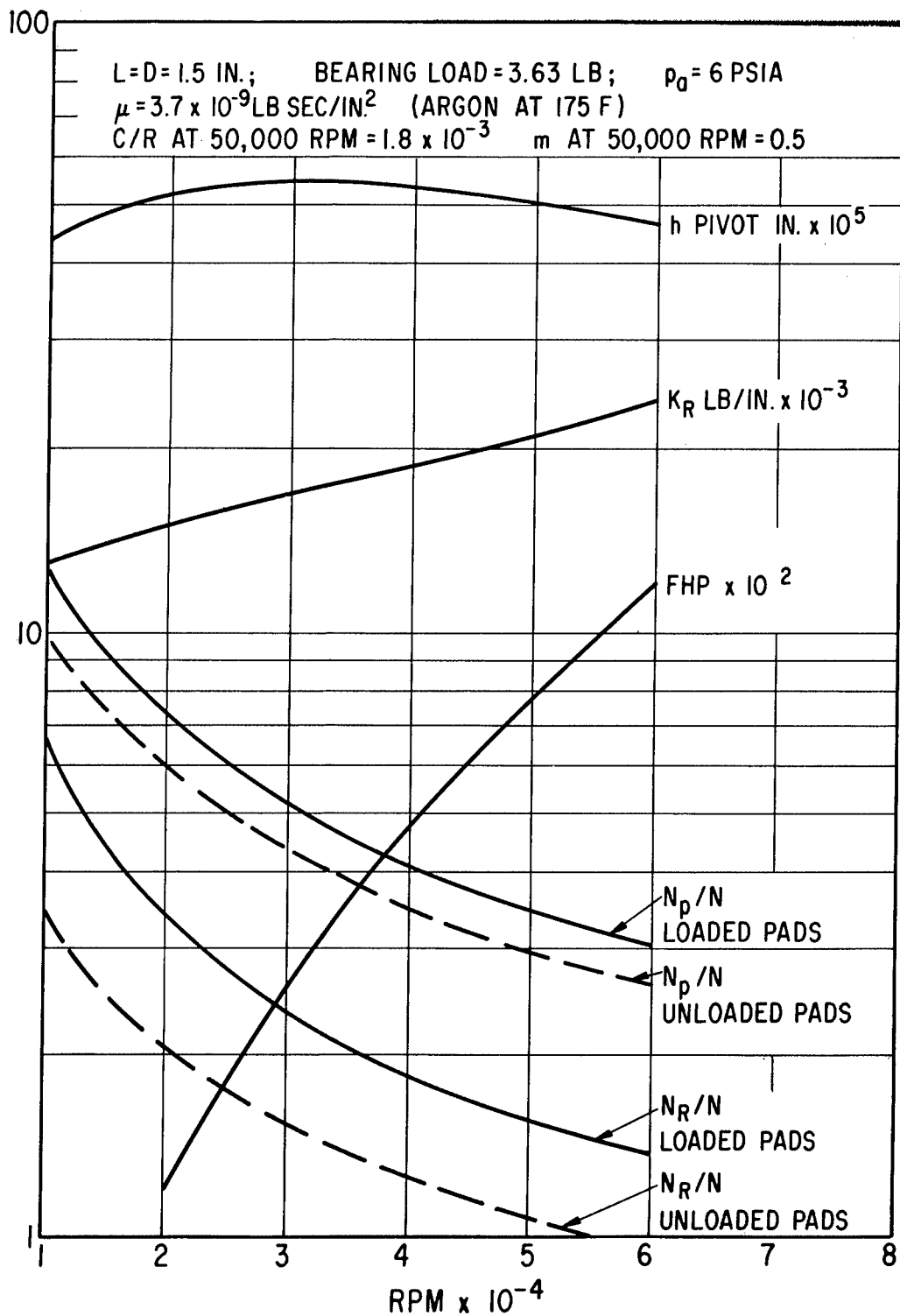


Fig. II-2 - Calculated Performance In A 6.0 PSIA Argon Environment
 For The Final Design Of The No. 1 Journal Bearing (Rotor
 horizontal relative to a 1-g gravitational field)

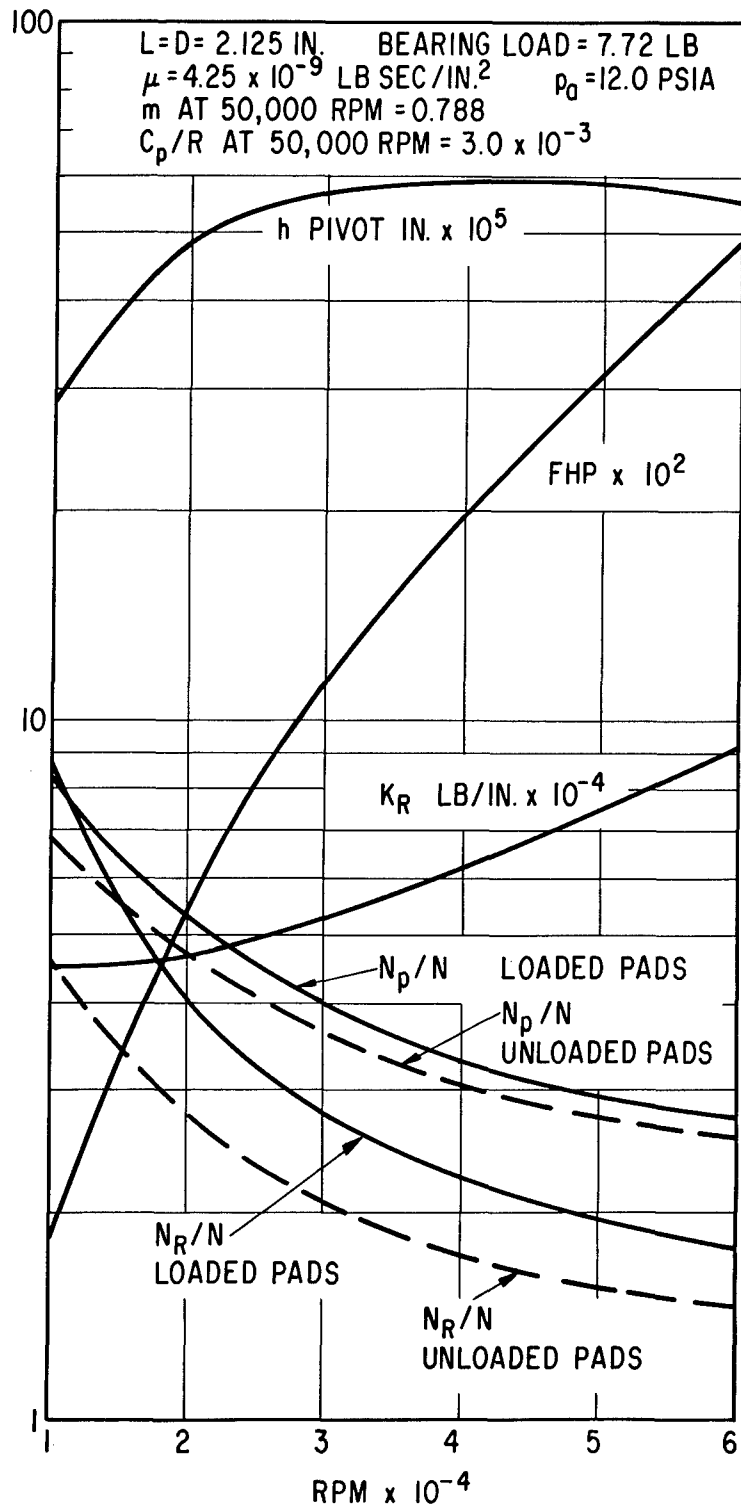


Fig. II-3 - Calculated Performance In A 12.0 PSIA Argon Environment For The Final Design Of The No. 2 Journal Bearing (Rotor horizontal relative to a 1-g gravitational field)

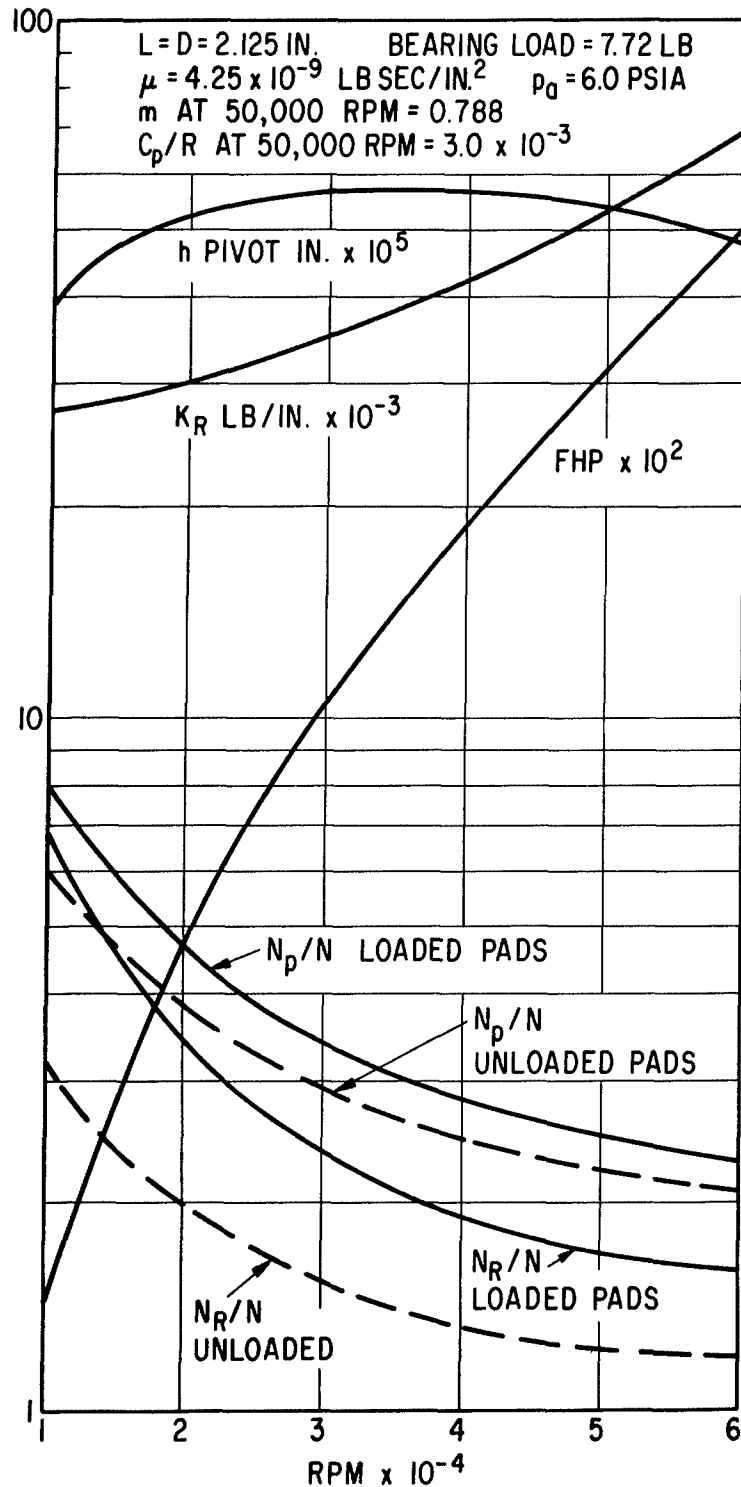


Fig. II-4 - Calculated Performance In A 6.0 PSIA Argon Environment
 For The Final Design Of The No. 2 Journal Bearing (Rotor
 horizontal relative to a 1-g gravitational field)

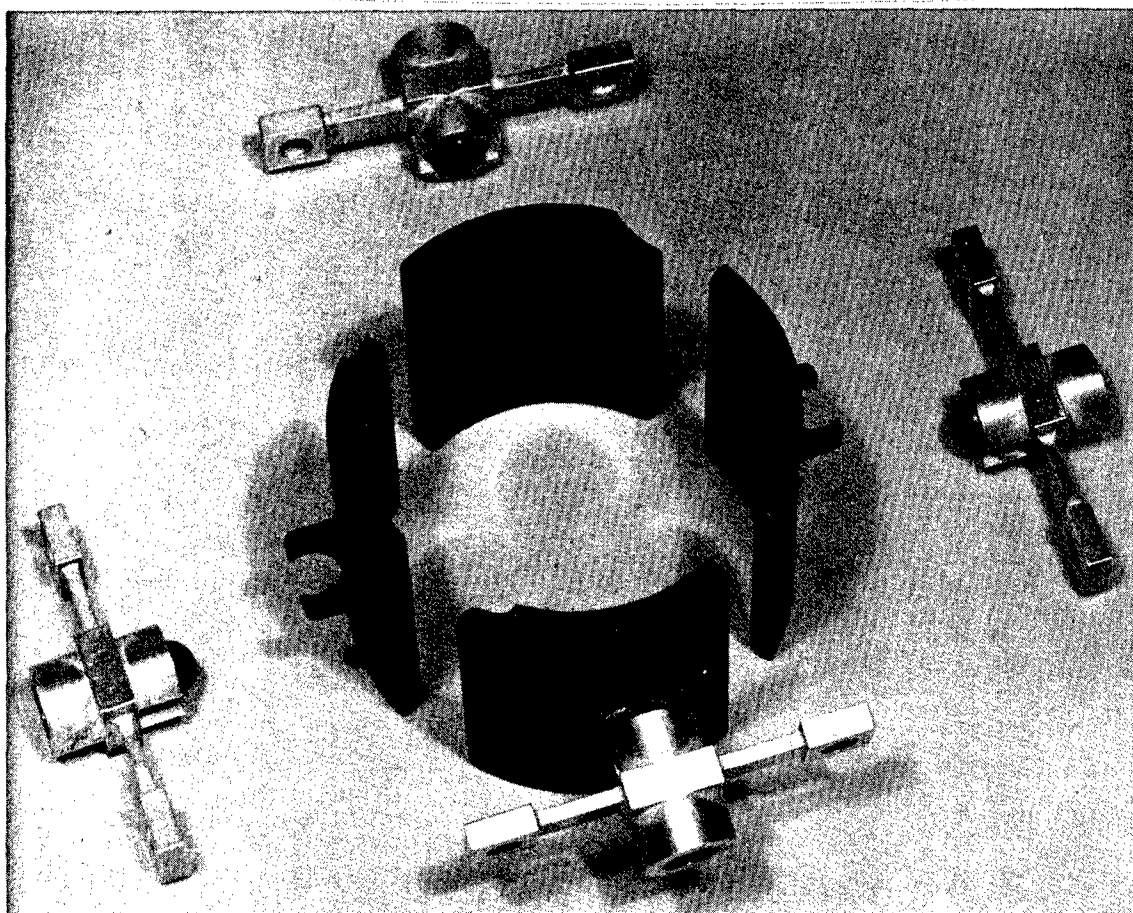


Fig. II-5 - View Of The Pivoted-Pads And Pivot-Support Flexures
For The No. 1 Journal Bearing

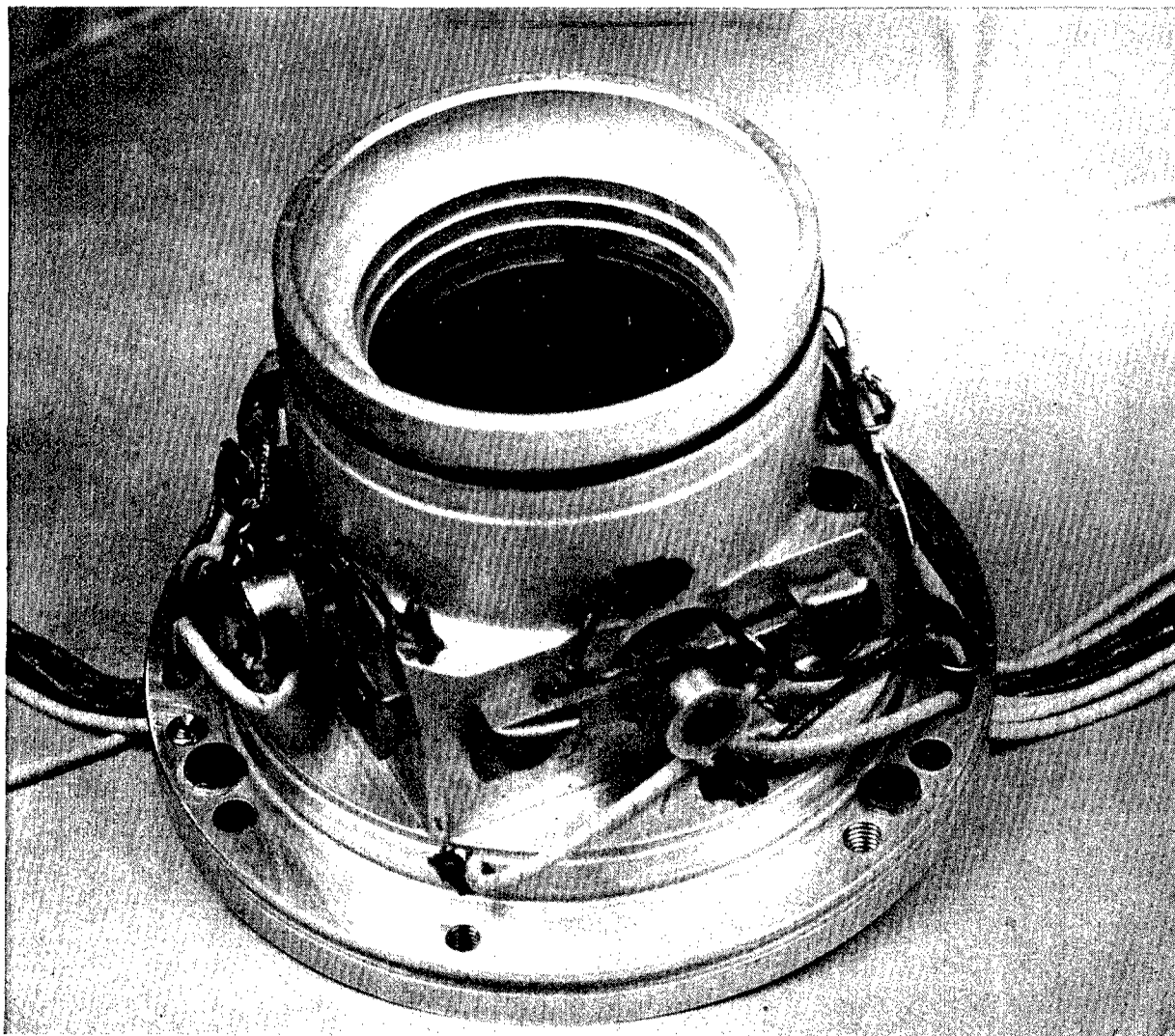


Fig. II-6 - View Of The No. 1 Bearing Components Assembled
In The No. 1 Bearing Housing

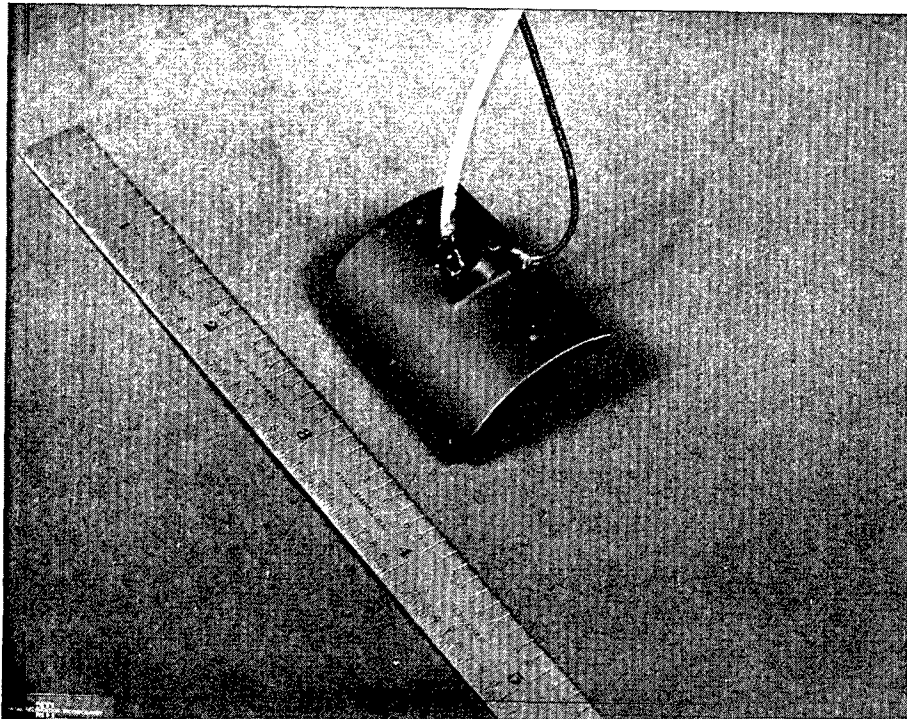
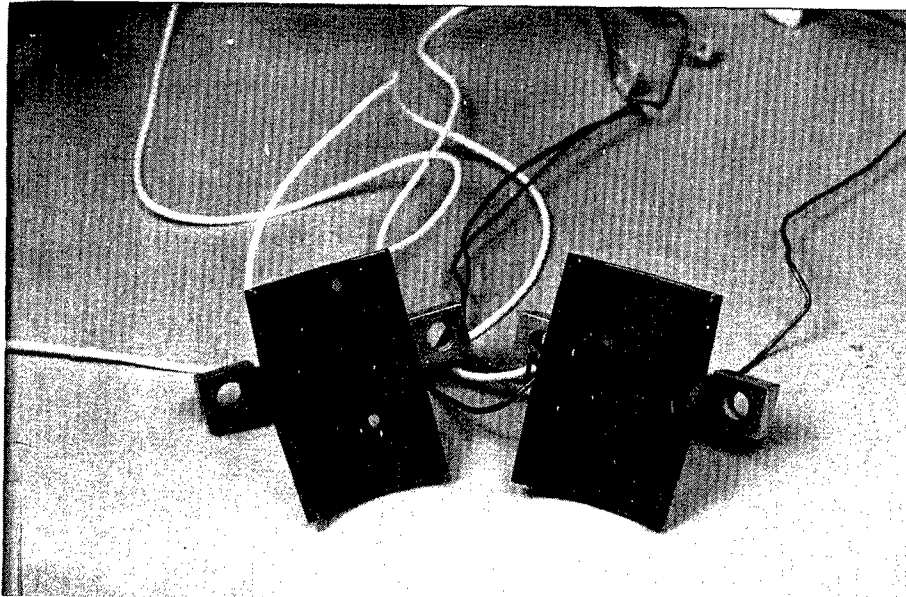


Fig. II-7 - Pivoted-Pads For The No. 2 Journal Bearing

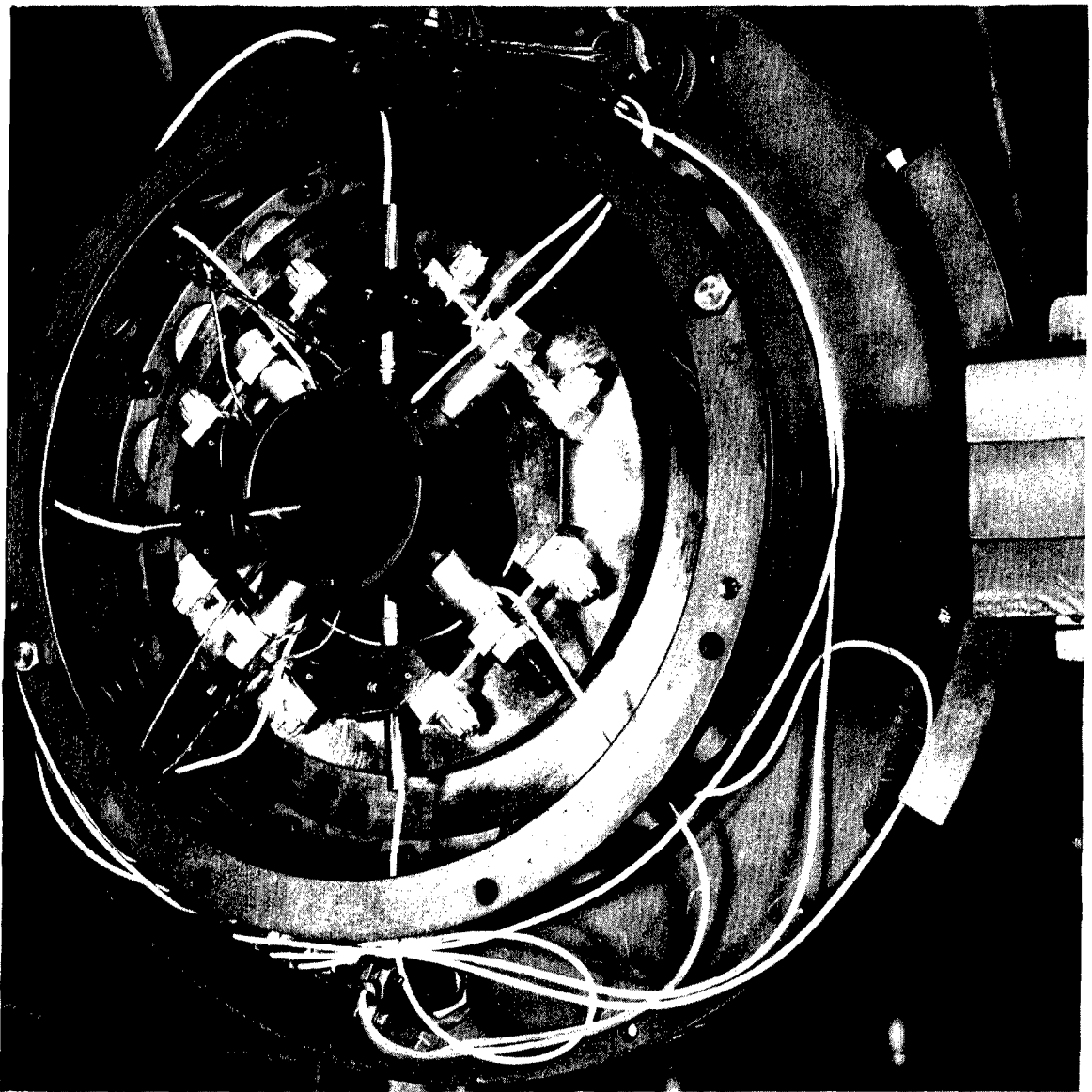


Fig. II-8 - View of the No. 2 Pivoted-Pad Bearing Components
Assembled in the Rotor-Bearing System Simulator

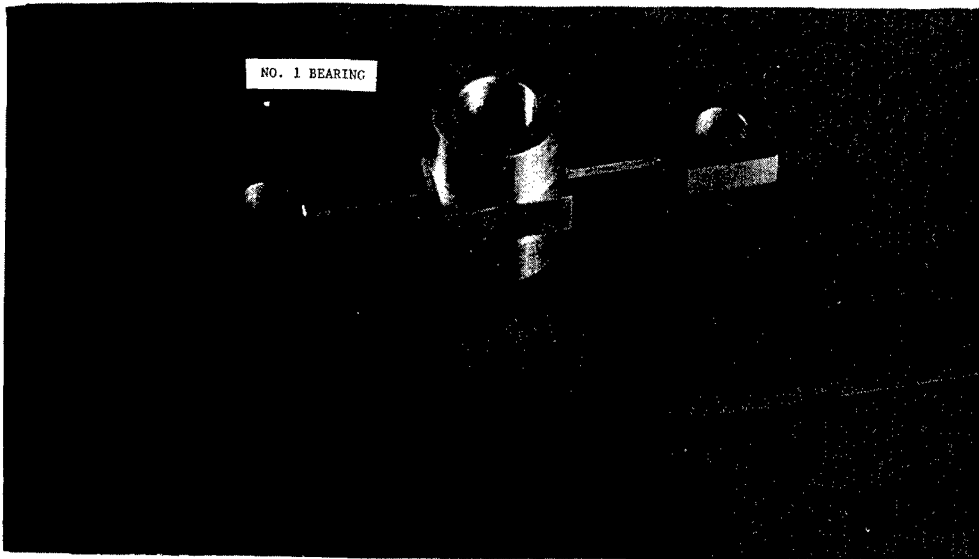


Fig. II-9 - View Of An Upper Pivot-Support Flexure
For The No. 1 Journal Bearing

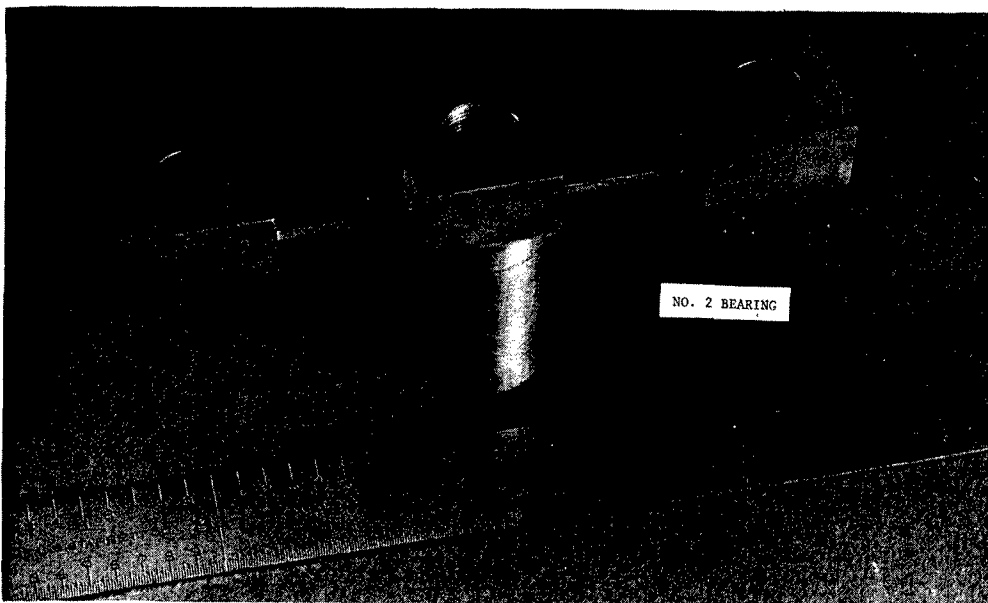


Fig. II-10 - View Of An Upper Pivot-Support Flexure
For The No. 2 Journal Bearing

Hydrodynamic Thrust Bearing

The design of the turbocompressor is such that the thrust load, at design conditions, is in the forward direction, i.e., in the direction from the turbine towards the compressor inlet.

The thrust bearing has been designed to operate satisfactorily under the following conditions:

1. In any orientation of the turbocompressor
2. At any ambient pressure above 6 psia
3. To accommodate small misalignments which may occur during operation.

As previously noted, a helical-grooved (Whipple plate) hydrodynamic bearing with a flexibly mounted stator was selected. This bearing was designed using analytical and computational procedures that were previously developed and programmed by MTI. These take full account of gas compressibility effects, as well as of the important geometrical factors (radius ratio, seal-to-groove ratio, groove width and depth ratios, and helix angle).

To achieve compact, low power-loss design, this bearing is built around the hydrostatic bearing which is used for start-up and shut down. In this design the radius of the row of hydrostatic orifices has been conservatively assumed to be the inner radius of the hydrodynamic bearing.

The 50,000 rpm design load for this bearing is 24 pounds which is achieved at a film thickness of 0.00078 inches. Changes in orientation, however, can reduce this load to 4 pounds, at which time the film thickness will approach 0.0018 inches.

The flexible mount for the thrust stator was designed such that the stator will accurately track dynamic misalignment of the thrust runner in the critical, high-load regions of operation. Such misalignment may result from manufacturing tolerances and from conical shaft motions during operation with mechanical

unbalance. The flexure mount also allows some degree of self-alignment of the stator to the average plane of the thrust runner.

The thrust bearing is maintained at near isothermal temperature, using liquid as the coolant. The calculated performance of the hydrodynamic thrust bearing at 30,000, 50,000 and 60,000 rpm is shown on Figures II-11, II-12 and II-13 respectively. A summary of the design parameters and calculated design-point performance characteristics is given in Table II-2.

Figure II-14 is a photograph of the thrust runner, the combination thrust-runner attachment screw and diaphragm flexure, and the attachment screw locking spline. Figure II-15 shows the hydrodynamic helical-grooved thrust bearing stator components, while Figure II-16 shows the helical-grooved stator assembly.

TABLE II-2
 FORWARD HYDRODYNAMIC THRUST BEARING DESIGN PARAMETERS
 AND CALCULATED PERFORMANCE CHARACTERISTICS

Configuration	Helical grooved, inward pumping
Thrust Runner Diameter, Inches	3.25
Helical-Grooved Bearing O.D., Inches	3.25
Helical-Grooved Bearing I.D., Inches	1.38
Groove Depth, Inches	0.002
Number of Grooves	20
Design Load (Aerodynamic plus rotor weight) for Helical Grooved Bearing, Pounds	24.0
Operating Clearance of Helical-Grooved Bearing, Inches	0.00078
Friction Loss at Design Load, Watts	172.0
Stator Support Stiffness in Axial Direction, lb./in.	670,000
Stator Support Stiffness in Tilt Direction, in.-lb./rad.	34,200
Stator Temperature, °F	175.0
Runner Temperature, °F	216.0
Runner Material	Titanium
Stator Material	AMS-4027 (aluminum)
Stator and Runner Surfacing Material	Chrome Oxide

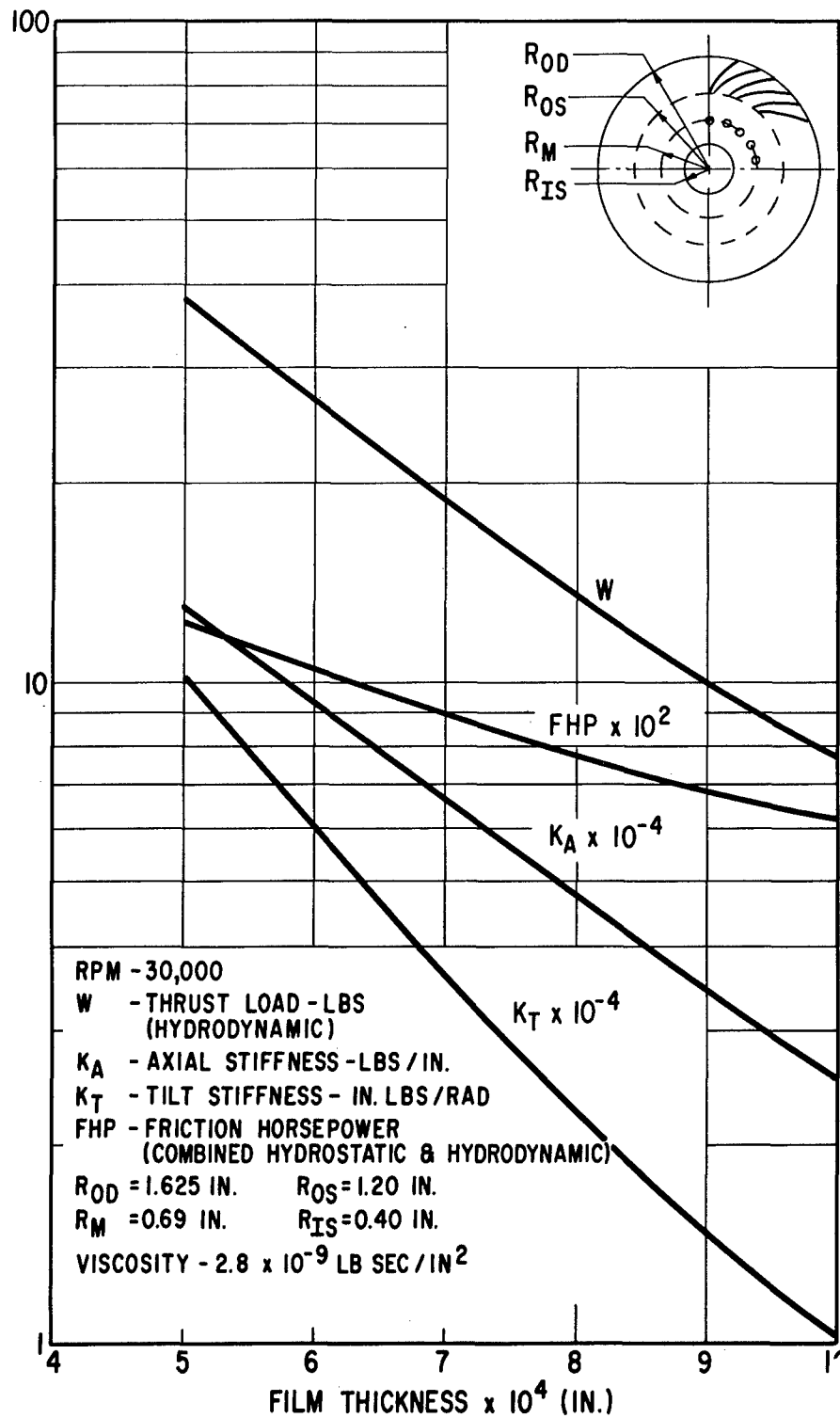


Fig. II-11 - Calculated Performance Of The Forward Hydrodynamic Thrust Bearing At 30,000 RPM And For Ambient Pressures From 6.0 to 12.0 PSIA

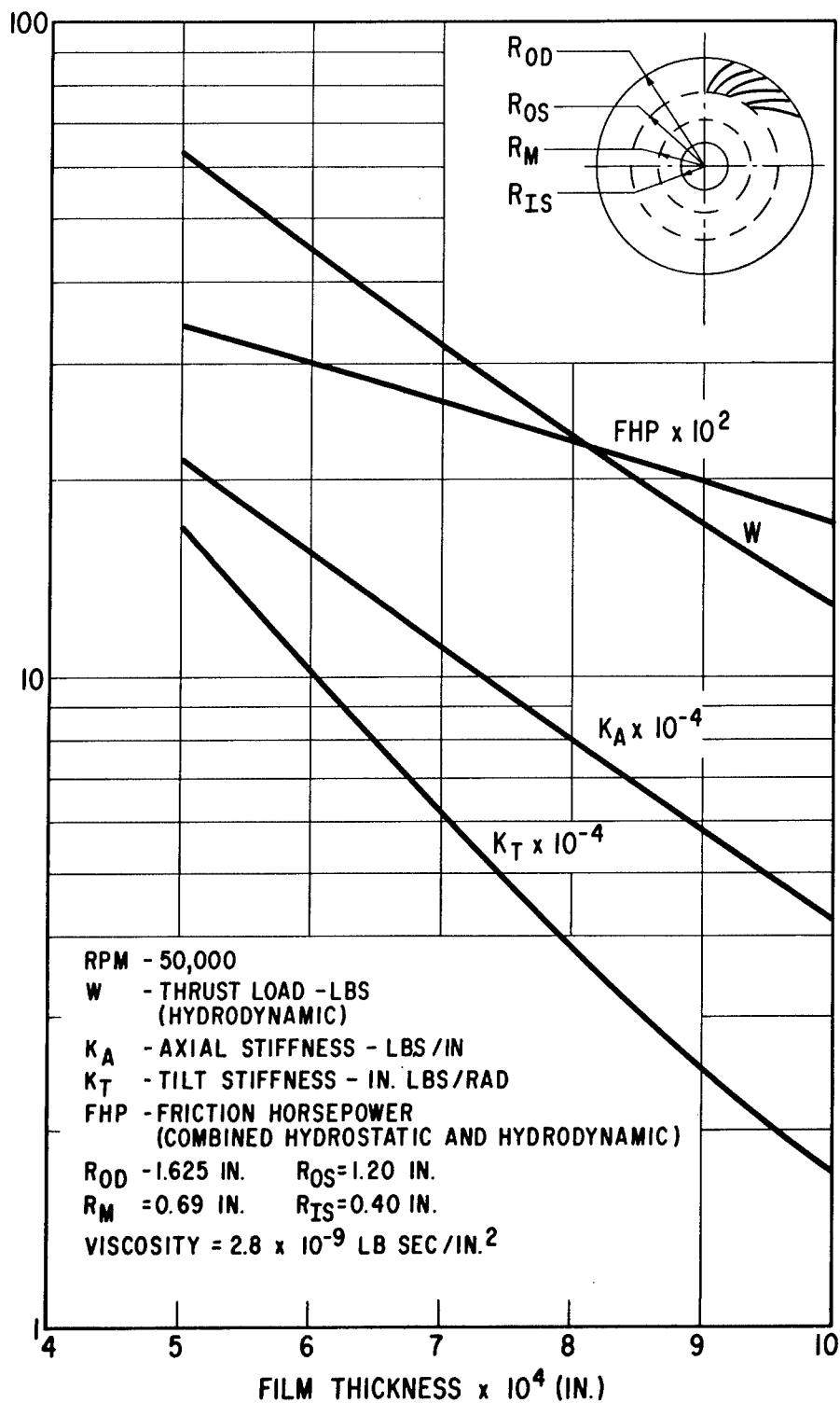


Fig. II-12 - Calculated Performance Of The Forward Hydrodynamic Thrust Bearing At 50,000 RPM And For Ambient Pressures From 6.0 To 12.0 PSIA

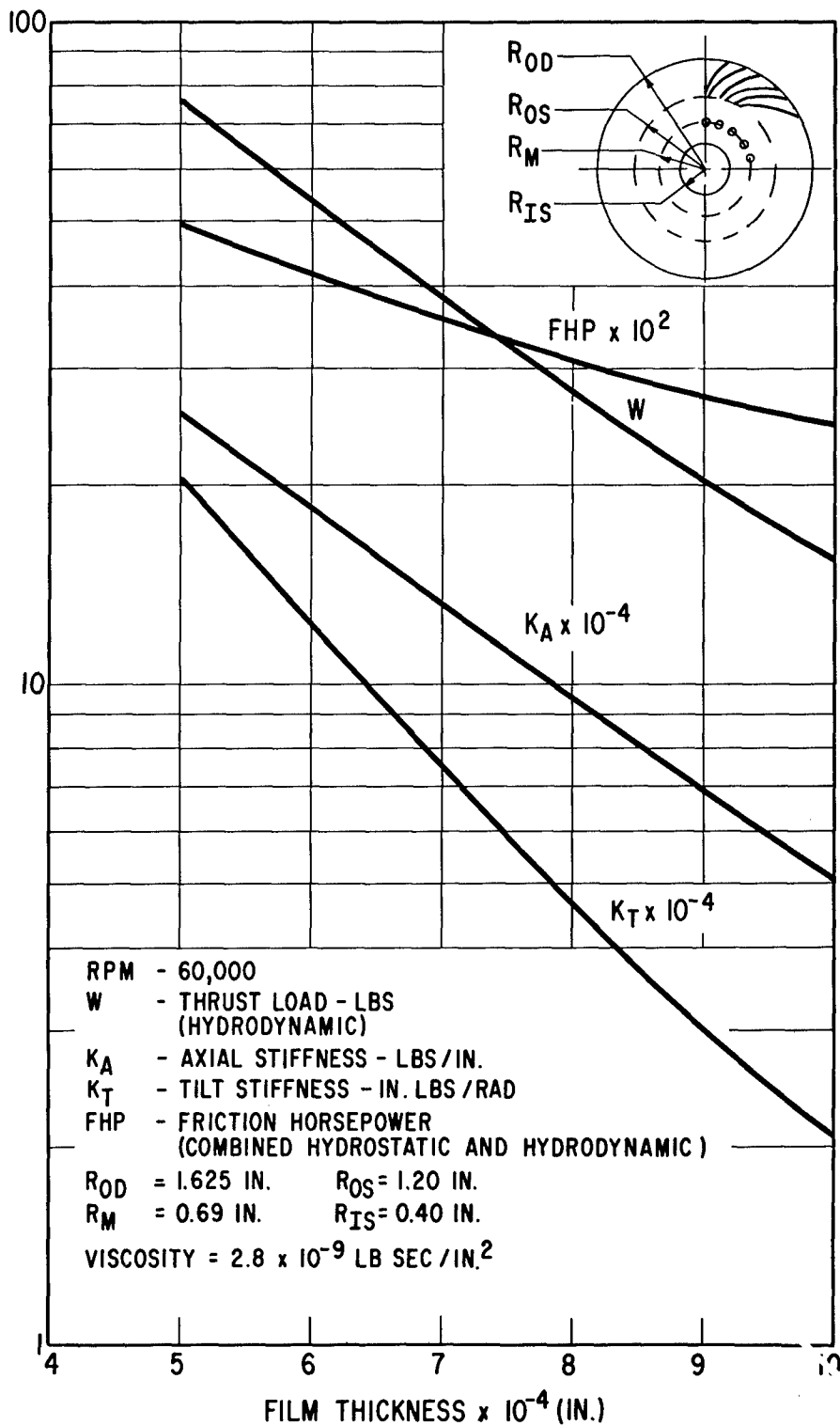


Fig. II-13 - Calculated Performance Of The Forward Hydrodynamic Thrust Bearing At 60,000 RPM And For Ambient Pressures From 6.0 To 12.0 PSIA

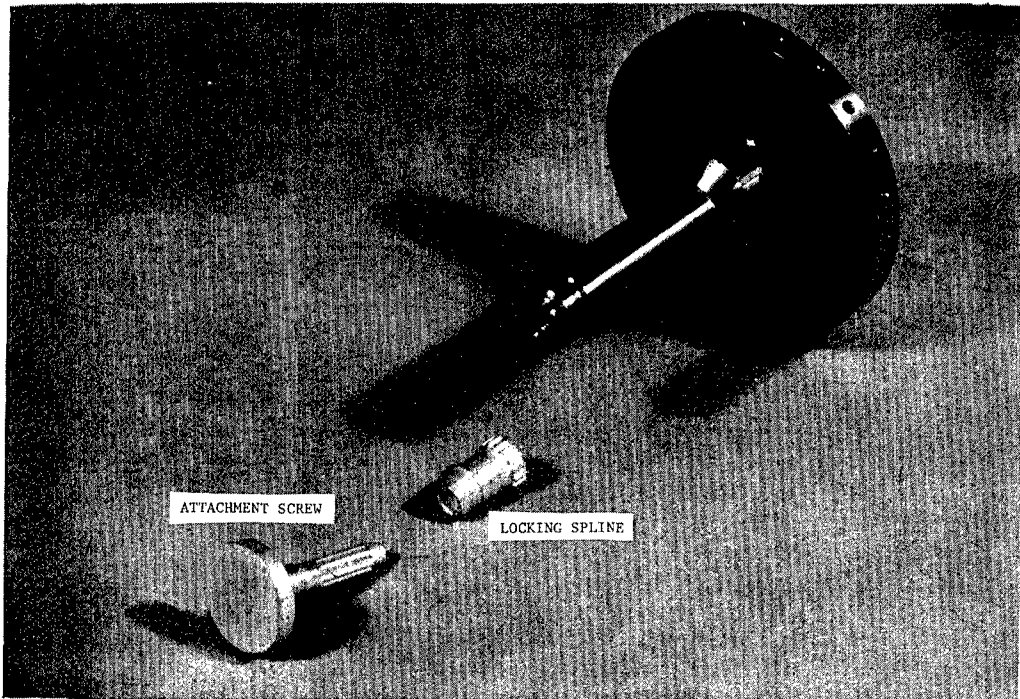
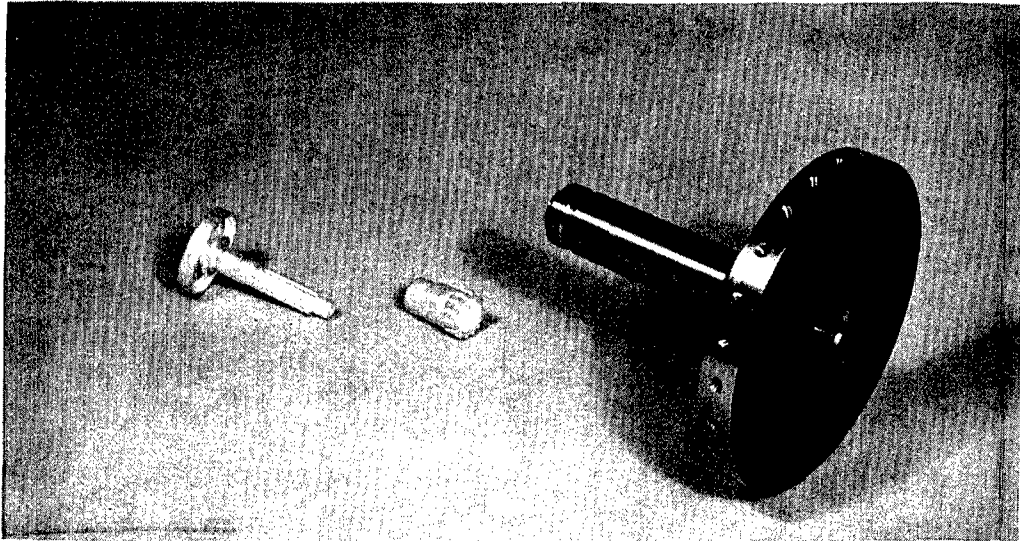


Fig. II-14 - Thrust Runner And Associated Attachment Parts

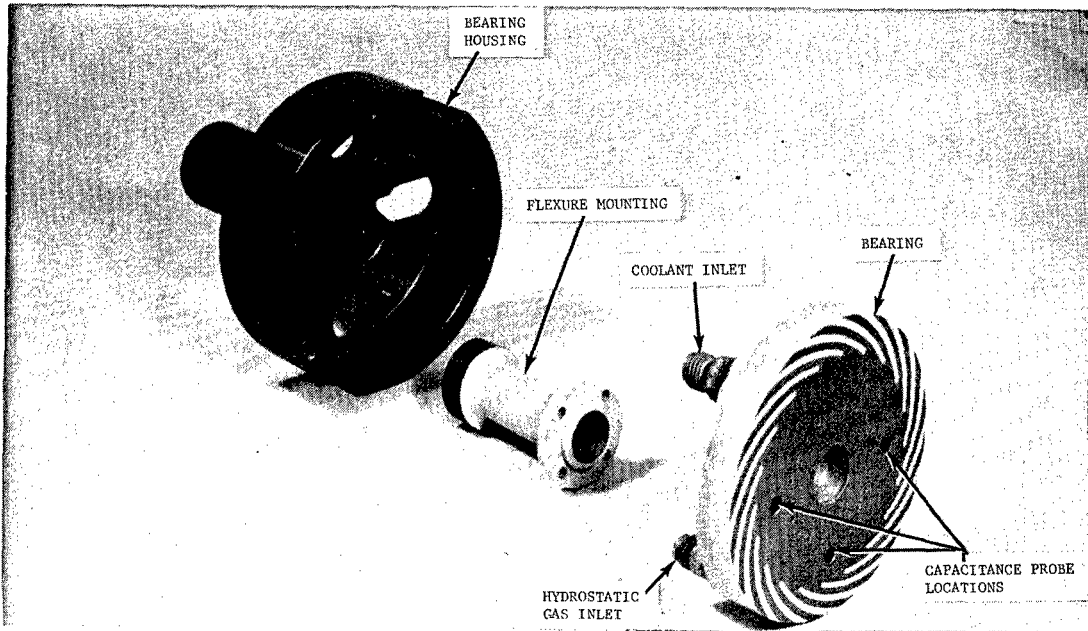


Fig. II-15 - Combination Helical-Grooved Hydrodynamic And Hydrostatic Forward Thrust Bearing Stator And Associated Mounting Parts

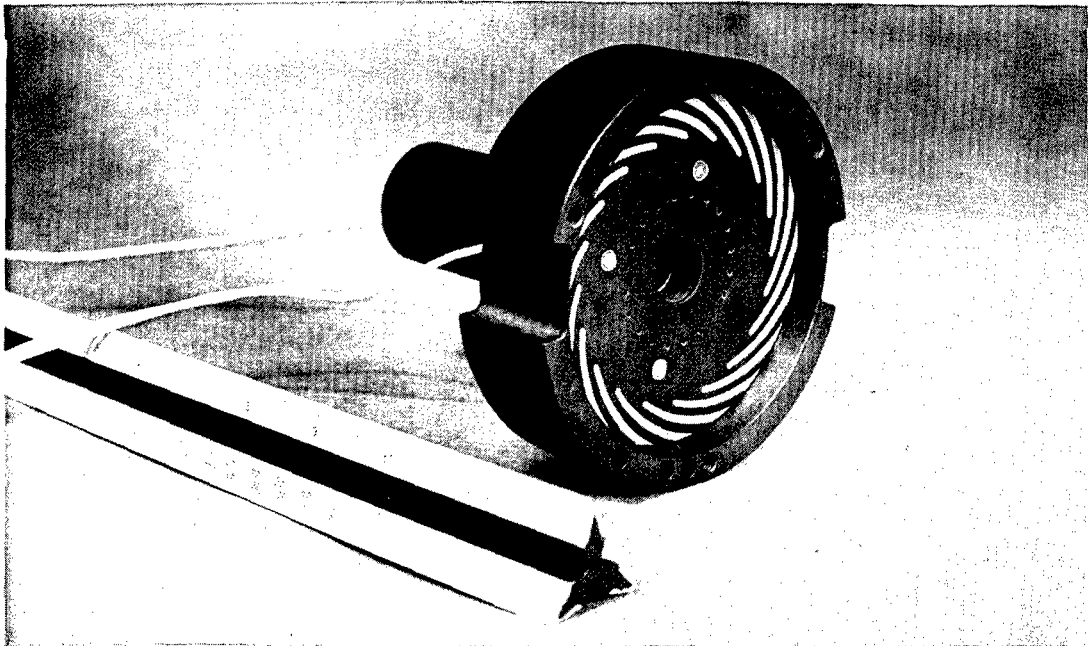


Fig. II-16 - View of the Thrust Bearing Stator Assembly Showing Combined Self-Acting and Externally-Pressurized Bearing Sections

Hydrostatic Thrust Bearings

The method by which the turbocompressor is started may impose large thrust loads at low rotor speeds. Since a hydrodynamic thrust bearing cannot carry large thrust loads at low speeds, two hydrostatic thrust bearings have been provided, one on each side of the thrust runner.

The conditions under which these bearings have been designed to operate are as follows:

	<u>Forward Thrust</u>	<u>Reverse Thrust</u>
Load (lb.)	100	50
Supply pressure (psia)	100	100
Ambient pressure (psia)	6	6

The bearings are of the inherently compensated type in order to minimize the possibility of pneumatic hammer at ambient pressures below 6 psia (this being a possible condition at start-up).

The bearings were designed using existing computer programs which are basically a development of the "line feed" method, but which take account of the discreteness of the individual feeder holes as well as of the circumferential flow between holes. In computing the orifice pressure drops, both the losses in the feeder holes and in the annular "curtain" areas around the rims of the holes are taken into account. Since in this case an inherently compensated design was selected for improved stability, the feeder hole diameters are large enough that the dominant restriction occurs in the annular "curtain" areas instead of inside the feeder holes.

The calculated performance of the forward and reverse hydrostatic bearings is shown on Figures II-17 and II-18 respectively. A summary of the design parameters and calculated design-point performance characteristics is given in Table II-3. The orifices of the initial design configuration for the forward hydrostatic bearing can be seen in Figure II-16 (in the final design

configuration only 5, rather than 20, of these orifices are used). Figure II-19 is a photograph of the reverse hydrostatic thrust bearing (this bearing is an integral part of the No. 1 bearing housing).

TABLE II-3

HYDROSTATIC THRUST BEARING DESIGN PARAMETERS AND CALCULATED PERFORMANCE CHARACTERISTICS

Forward Hydrostatic Bearing

Bearing OD, Inches	2.4
Bearing ID, Inches	0.6
Number of Orifices	5
Diameter of Orifices, Inches	0.040
Hydrostatic Gas Supply Pressure	
At Start-Up, PSIA	100.0
Ambient Pressure, PSIA	6.0
Bearing Load At Start-Up, Pounds	100.0
Bearing Film Thickness At	
Start-Up, Inches	0.0008
Stator Material	AMS-4027 (aluminum)
Stator Surfacing Material	Chrome Oxide

Reverse Hydrostatic Bearing

Bearing OD, Inches	1.53
Bearing ID, Inches	0.91
Number of Orifices	15
Diameter of Orifices, Inches	0.040
Hydrostatic Gas Supply Pressure	
At Start-Up, PSIA	100.0
Ambient Pressure, PSIA	6.0
Bearing Load At Start-Up, Pounds	50.0
Bearing Film Thickness At Start-Up,	
Inches	0.0013
Stator Material	AMS-6415 (steel)
Stator Surfacing Material	Chrome Oxide

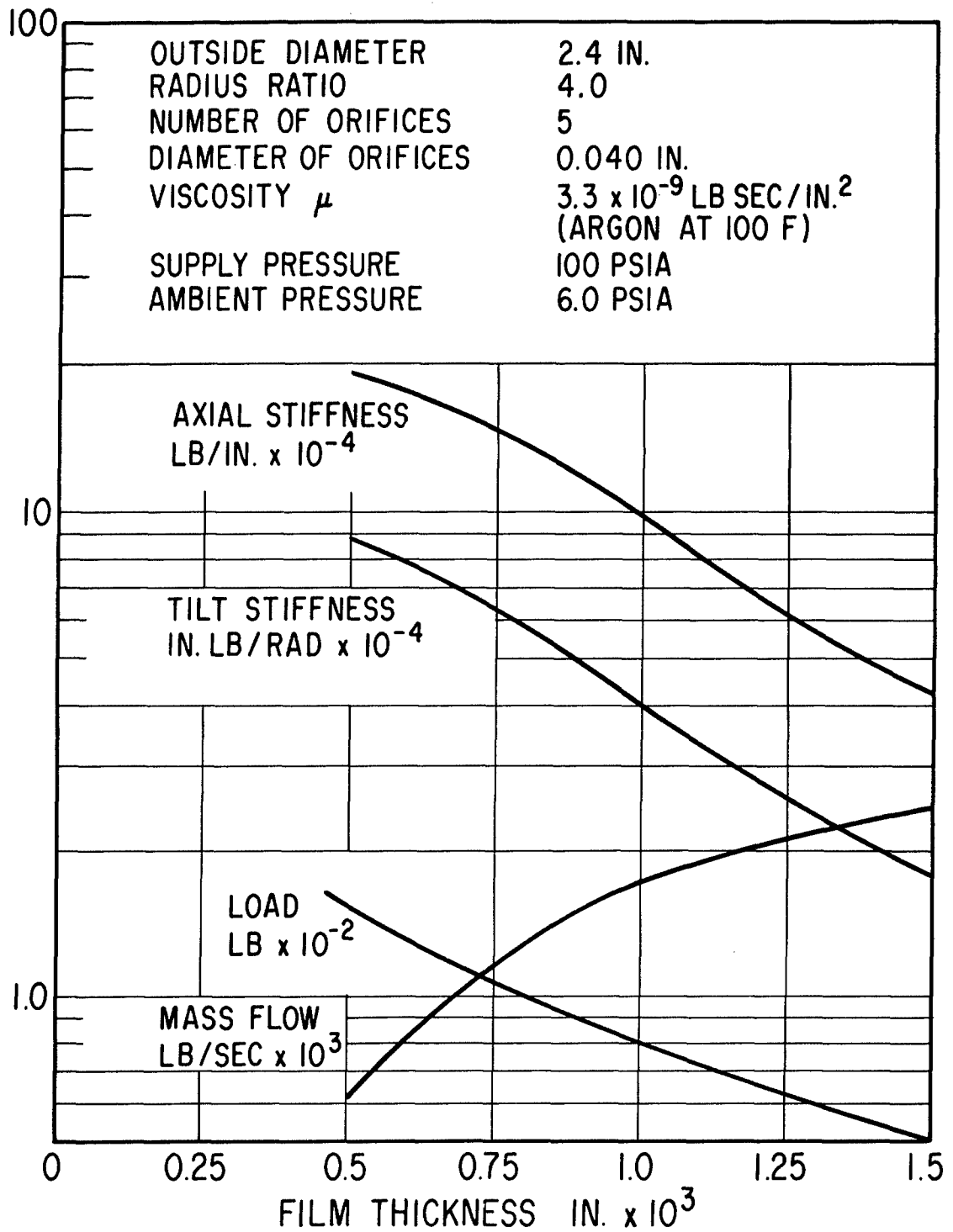


Fig. II-17 - Calculated Performance Of The Forward Hydrostatic Thrust Bearing

OUTSIDE DIAMETER	1.53 IN.
RADIUS RATIO R_o/R_i	1.675
NO. OF ORIFICES	15
DIAMETER OF ORIFICES	0.040 IN.
VISCOSITY	3.3×10^{-9} LB SEC/IN. ²
SUPPLY PRESSURE	100 PSIA
AMBIENT PRESSURE	6 PSIA

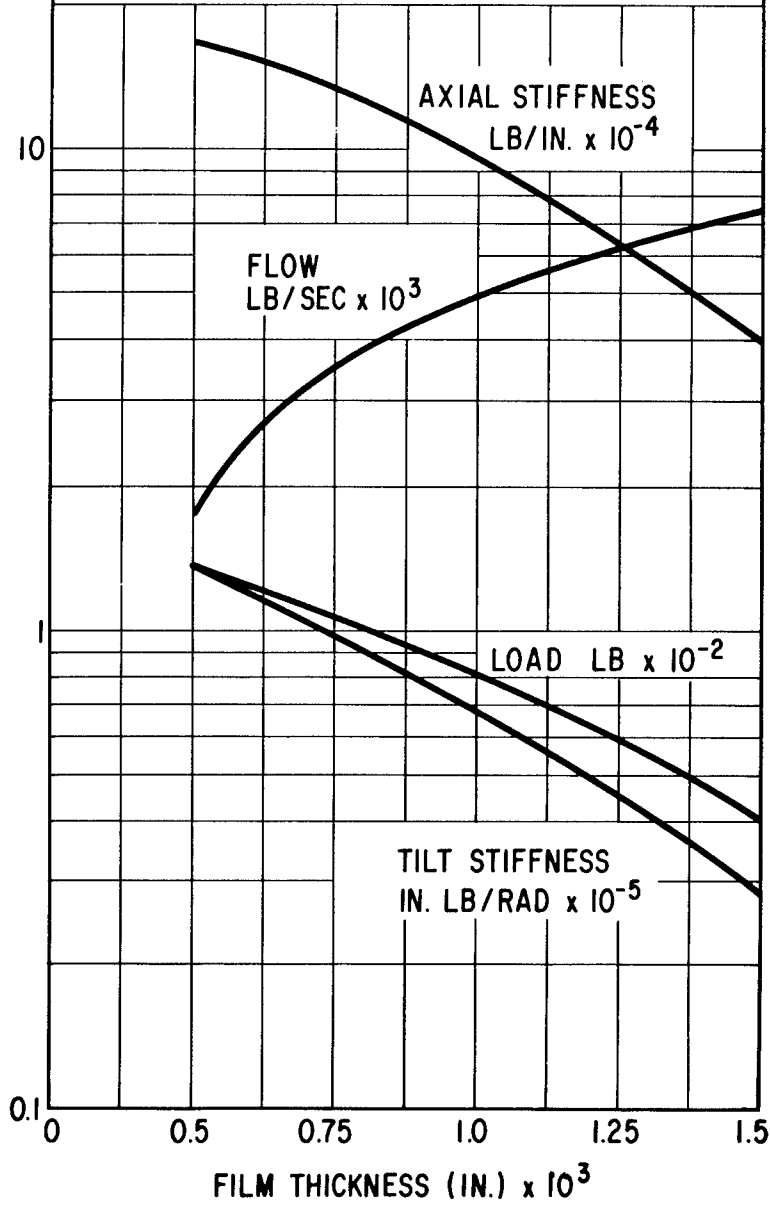


Fig. II-18 - Calculated Performance Of The Reverse Hydrostatic Thrust Bearing

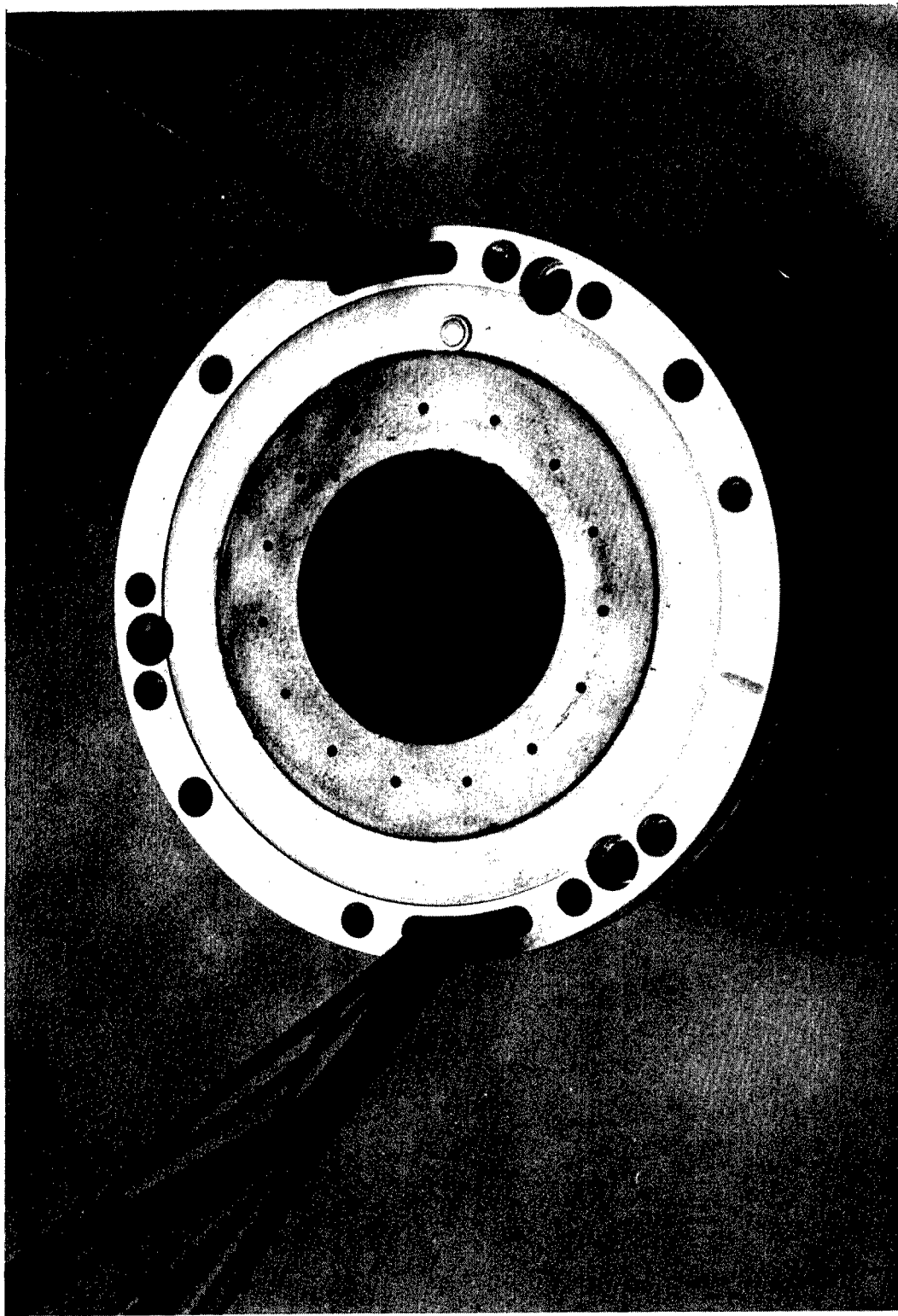


Fig. II-19 - View Of The Reverse Hydrostatic Thrust Bearing

Rotor-Bearing System Dynamics

It is particularly important in the design of gas-bearing machinery to be sure that the rotor-bearing system will not develop excessive amplitudes of either stable or unstable vibration over the desired range of operating speeds. The simplest and most common form of vibration is synchronous rotor whirl resulting from excitation of transverse resonant frequencies of the rotor in its rigid or flexible beam modes. The excitation most commonly derives from mechanical unbalance of the rotor, although other forms of excitation are possible. The speeds at which transverse resonant beam modes of rotor whirl can occur are called the transverse critical speeds of the rotor.

Because of the limited amount of damping in a gas bearing, it is difficult to design a gas-bearing machine for safe operation through a "bent shaft" critical speed unless some auxiliary means of damping is provided. Accordingly, in keeping with the design philosophy used on all previous gas-lubricated machinery developments, a criterion of the turbocompressor design was that the "bent shaft" critical should be well above the 60,000 rpm turbocompressor overspeed condition.

A critical speed analysis for the turbocompressor was carried out using a Holzer type calculation programmed for digital computer solution. The calculation provides both the critical speeds and the associated rotor displacement mode shapes, and includes the effects of rotor mass, rotor stiffness, bearing mass, bearing stiffness, bearing support stiffness, and rotor gyroscopic effects.

The critical speeds for the final design of the rotor-bearing system are plotted in Figure II-20 as a function of journal bearing stiffness. Superimposed on this plot are the calculated stiffnesses at 12.0 psia ambient pressure of the No. 1 and No. 2 journal bearings as a function of speed (obtained from Figures II-1 and II-3). The intersections of the critical speed curves and the No. 1 journal bearing stiffness curve identify the speeds at which rotor resonances could be expected to occur in the presence of sufficient rotor unbalance. The two lowest critical speeds are essentially rigid-body resonances of the rotor due to the stiffnesses of the

gas film and the pivot-support flexures. It is seen from Figure II-20 that the two rigid-body resonances should occur at approximately 11,100 and 11,600 rpm, which are sufficiently low to be of little concern to turbocompressor operation. The third critical speed, which is slightly above 93,000 rpm, is the first free-free "bent shaft" critical of the rotor and is virtually unaffected by bearing stiffness. Although a slight influence of this critical speed would be expected at the 50,000 and 60,000 rpm design and overspeed conditions, it is sufficiently above these speeds to be considered a minimal development problem and well within the state-of-the-art of present balancing techniques.

The rigid-body critical speed mode shapes for the rotor are plotted in Figure II-21. It is seen that for pure modal excitation, only the No. 2 journal would experience resonant amplitudes at the lowest rigid-body critical, while only the No. 1 journal would resonate at the second rigid-body critical. In other words, the nodal point for the lowest rigid-body critical is located approximately at the No. 1 bearing, while the nodal point for the second critical speed is located at the No. 2 bearing.

The calculated steady-state plus dynamic bearing loads for a horizontal rotor orientation in a 1-g field and 0.002 ounce-inches of unbalance in the turbine plane (the rotor being otherwise perfectly balanced) are plotted in Figure II-22 as a function of speed. The value of 0.002 ounce-inches of unbalance was assumed to occur over a period of 10,000 hours due to unsymmetrical mass shift (creep) in the turbine. It is seen from Figure II-22 that the unbalance causes both journals to resonate simultaneously between 10,000 and 13,000 rpm. There is no distinction between the first and second rigid-body criticals because of the closeness of these two criticals.

It should be pointed out that the bearing damping values used in the calculation of the dynamic bearing loads of Figure II-22 are, rigorously speaking, valid only at 50,000 rpm. Hence, the absolute values of bearing forces in the vicinity of the rigid body criticals are approximate. Over the range of 40,000 to 60,000 rpm (where the calculated loads should be quite valid), it is seen that the 0.002 ounce-inches of unbalance adds approximately 0.38 pounds of rotating load to the steady-state loading of the No. 1 journal, and approximately 1.25 pounds of rotating load to the No. 2 journal.

Maximum recommended bearing loads as a function of speed and ambient pressure for the two journal bearings are plotted in Figures II-23 and Figures II-24. It is

seen that the bearings can "safely" support the combined rotating unbalance and steady-state 1-g horizontal loads at speeds above 20,000 rpm and ambient pressures above 6.0 psia for both the No. 1 and No. 2 bearings. The maximum load criterion used in calculating the plots of Figures II-23 and II-24 was $\epsilon_b \cos \phi = 0.4$ at 50,000 rpm. This criterion is based upon engineering judgement and field experience with previously developed gas-bearing machinery, and results in film thicknesses always greater than or equal to 0.40 mils for both the No. 1 and No. 2 bearings from 20,000 to 50,000 rpm. However, it is seen from Figures II-2 and II-4 that the bearings should actually be able to carry the maximum anticipated loads down to very low rotor speeds before the gas film would actually be ruptured.

In a rigorous sense, the turbocompressor rotor-bearing system has a great many degrees of freedom. Since the pivoted-pads are flexibly mounted, each pad has at least three significant degrees of freedom — namely, roll and pitch rotations, and radial translation. Since there are a total of eight pads, it takes 24 degrees of freedom to define the position of the pads at any instant of time. The pads, in turn, are coupled via the gas films to the rotor which, in itself, is an elastic system having an infinite number of degrees of freedom. Fortunately, the rotor can be represented, for practical purposes, as a finite number of masses with each mass having several degrees of freedom. However, at best, a rigorous mathematical model of the turbocompressor rotor-bearing system would still be a coupled system having over 30 degrees of freedom, and with the stiffness and damping properties of the gas film being nonlinear functions of speed and bearing eccentricity. Clearly, the dynamic analysis of such a system, for either stable or unstable modes of vibration, would be a major undertaking and one which could be justified on a hardware development program only if the necessary analytical understanding, computer programs, and experimental verifications were readily available and in a form suitable for efficient application to design analysis. Such was not the case at the time of the turbocompressor design, and only recently have the first steps been taken to provide tools for analytical investigation of the more rigorous rotor-dynamic problem.

In lieu of a rigorous analytical approach, it has been common practice to analyze each of the pivoted-pads as a completely uncoupled linear vibration system.

The resonant frequency of each possible mode of pad vibration is calculated based on a simple one-degree-of-freedom model. A more-or-less intuitive design criterion has been to design the pads such that the resonant frequency of each vibration mode is at least 30 percent higher than the maximum operating speed of the machine. This implies that the pads should be able to track motions of the rotor with little phase lag. Hence, the dynamics of the pads should have little effect on rotor dynamics.

The pad frequencies which were computed are the roll and pitch resonant frequencies of the pad against the gas-film stiffness, and the radial resonant frequency of the pad, pivot-screw, and flexure assembly against the gas-film and flexure stiffnesses. Figures II-1 through II-4 show calculated ratios of roll and pitch resonant frequencies to rotor speed for both the loaded and unloaded pads (assuming horizontal rotor orientation in a 1-g acceleration field). It is seen that the pitch resonant frequencies of all the No. 1 and No. 2 bearing pads are always greater than twice rotor speed for ambient pressures down to 6.0 psia. Similarly, the roll resonant frequencies of all the No. 1 and No. 2 pads are always 36 percent, or more, higher than rotor speed at design ambient pressure of 12.0 psia. However, at 6.0 psia ambient pressure, Figure II-2 indicates that the calculated roll resonant frequency of the unloaded No. 1 bearing pads will coincide with rotor speed at approximately 55,000 rpm. The resonant frequencies of the loaded No. 1 pads and all No. 2 pads are at least 20 percent higher than rotor speed at 6.0 psia. Consequently, the 6.0 psia ambient pressure condition does not fully satisfy the design criterion. However, since operation at 6.0 psia was not a primary design requirement, it was decided to accept the possibility of a roll resonant condition at low ambient pressures and to find out by test whether this condition would present an operational problem.

The calculated radial resonant frequencies of the No. 1 and No. 2 bearing pads were all found to be well above rotor speed throughout the 60,000 rpm speed range.

In concluding this section on rotor dynamics, it should again be emphasized that the criteria and procedures used for assessing possible pad or rotor dynamic problems leave much to be desired from the standpoint of demonstrated validity,

particularly since the rotor-bearing system is a highly coupled system and since the bearing stiffness and damping parameters are (1) frequency dependent and (2) nonlinear over large eccentricity excursions. In particular, the procedures used to calculate pivoted-pad gas-film stiffnesses in the roll, pitch, and radial directions, have yet to be verified by controlled experiment.

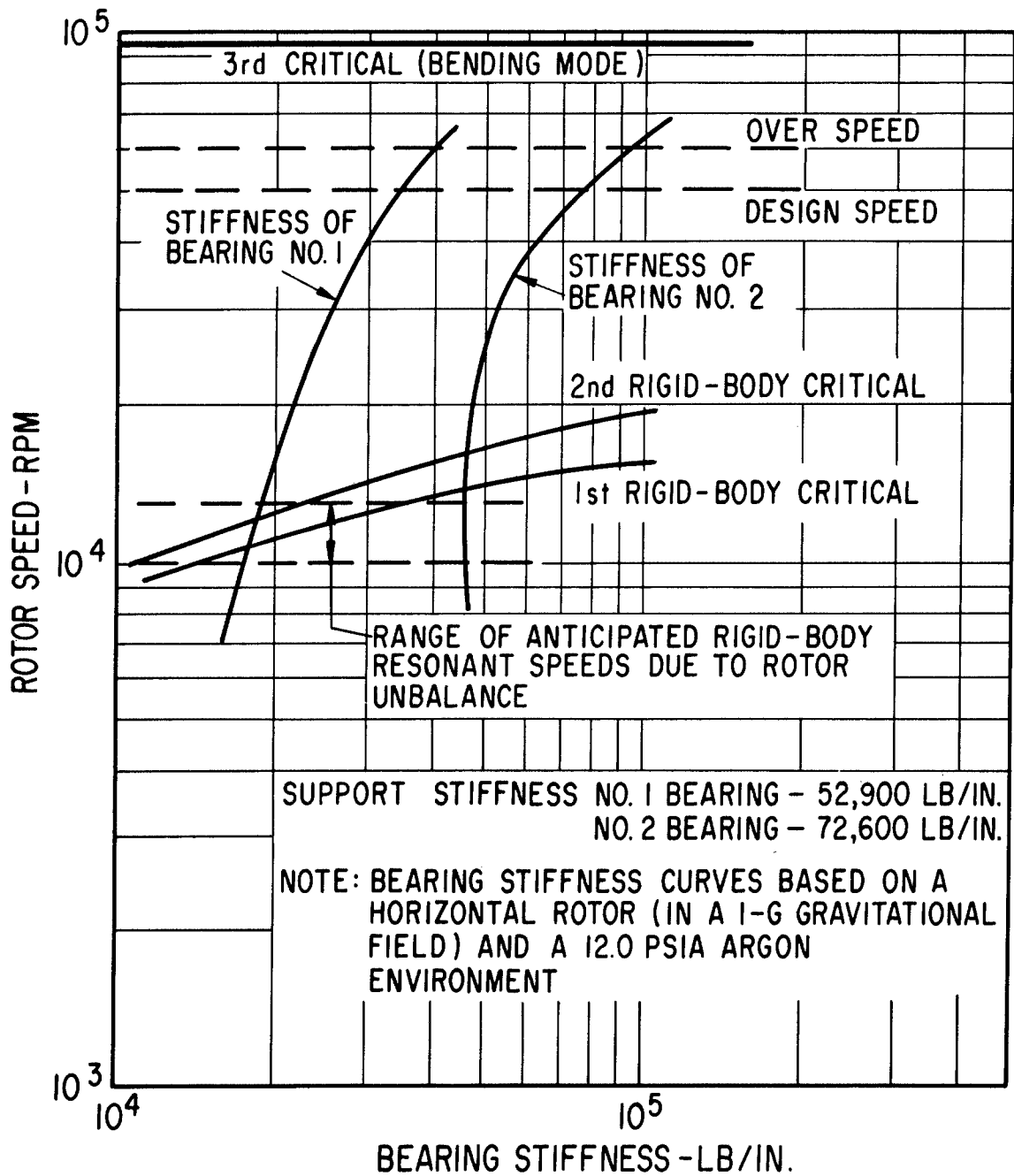
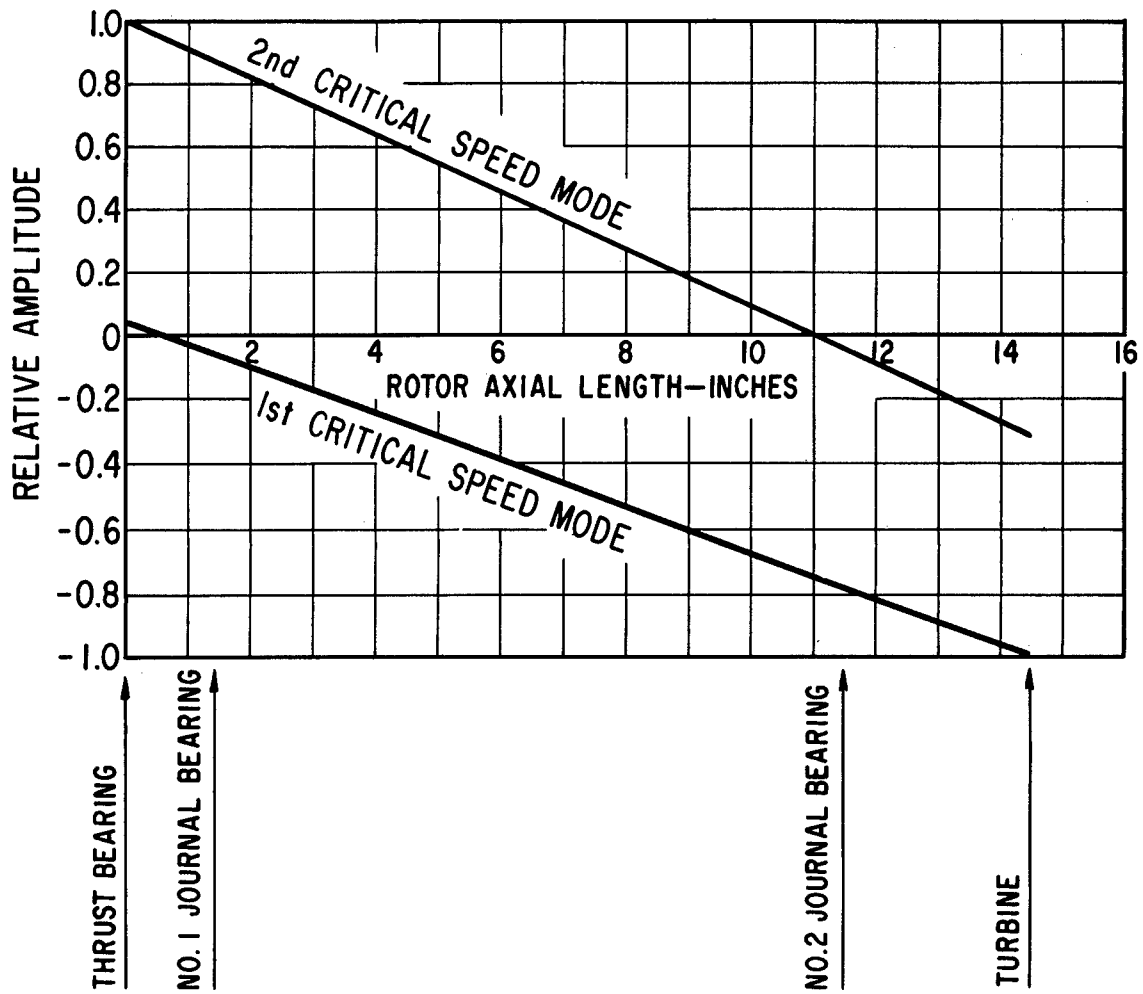


Fig. II-20 - Calculated Critical Speeds And Bearing Stiffnesses For The Final Rotor-Bearing System Design (Intersections of the No. 1 bearing stiffness curve and the critical speed curves define speeds at which resonance due to rotor unbalance can be expected)



<u>JOURNAL BEARING</u>	<u>NO. 1</u>	<u>NO. 2</u>
GAS FILM STIFFNESS (LB/IN.)	17,500	46,000
SUPPORT STIFFNESS (LB/IN.)	52,900	72,000

Fig. II-21 - Calculated Mode Shapes For The Two Rigid-Body Critical Speeds Of The Final Rotor-Bearing System Design

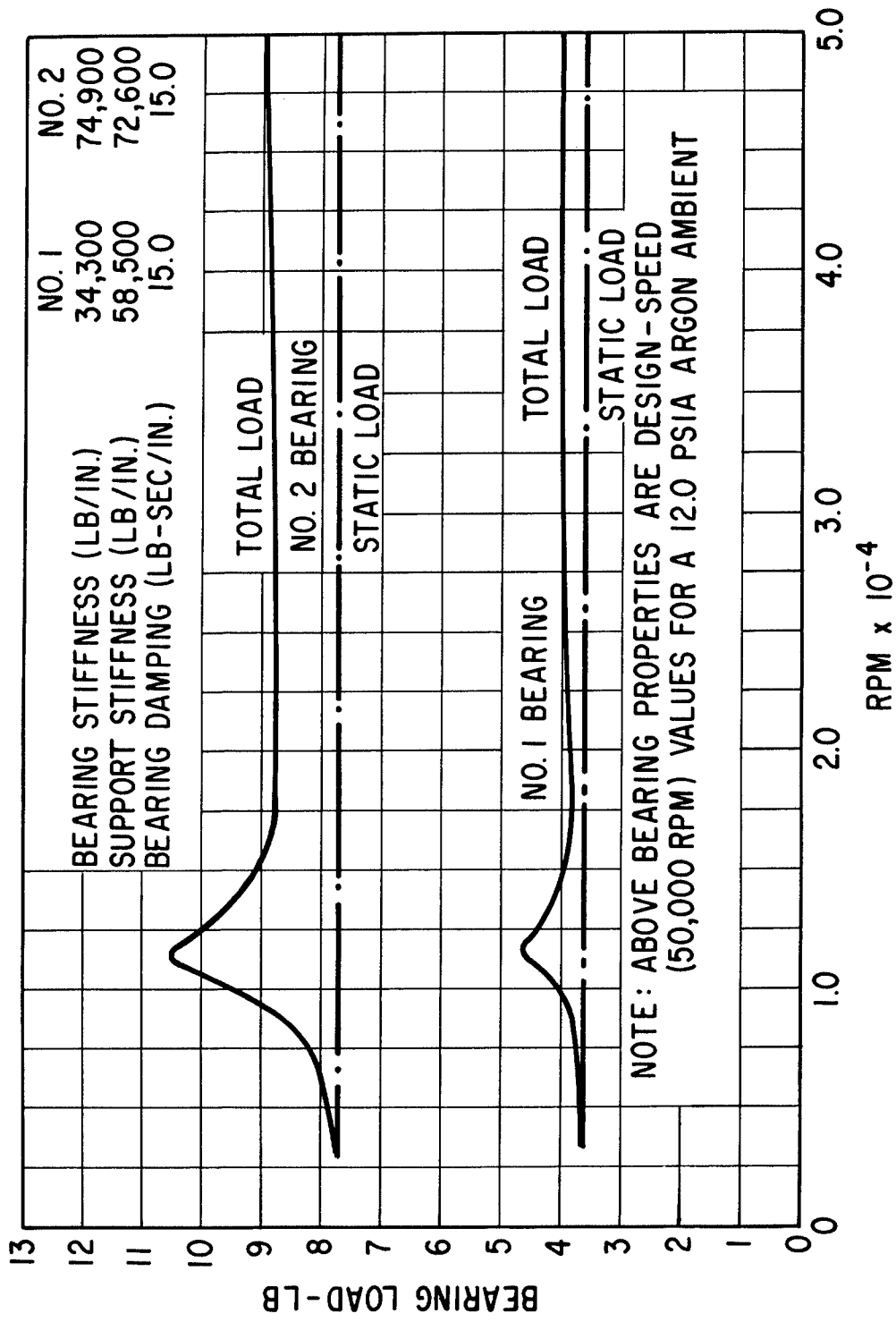


Fig. II-22 - Calculated Maximum Bearing Loads For The Final Rotor-Bearing System Design Due to 0.002 Ounce-Inches Unbalance In The Turbine Plane

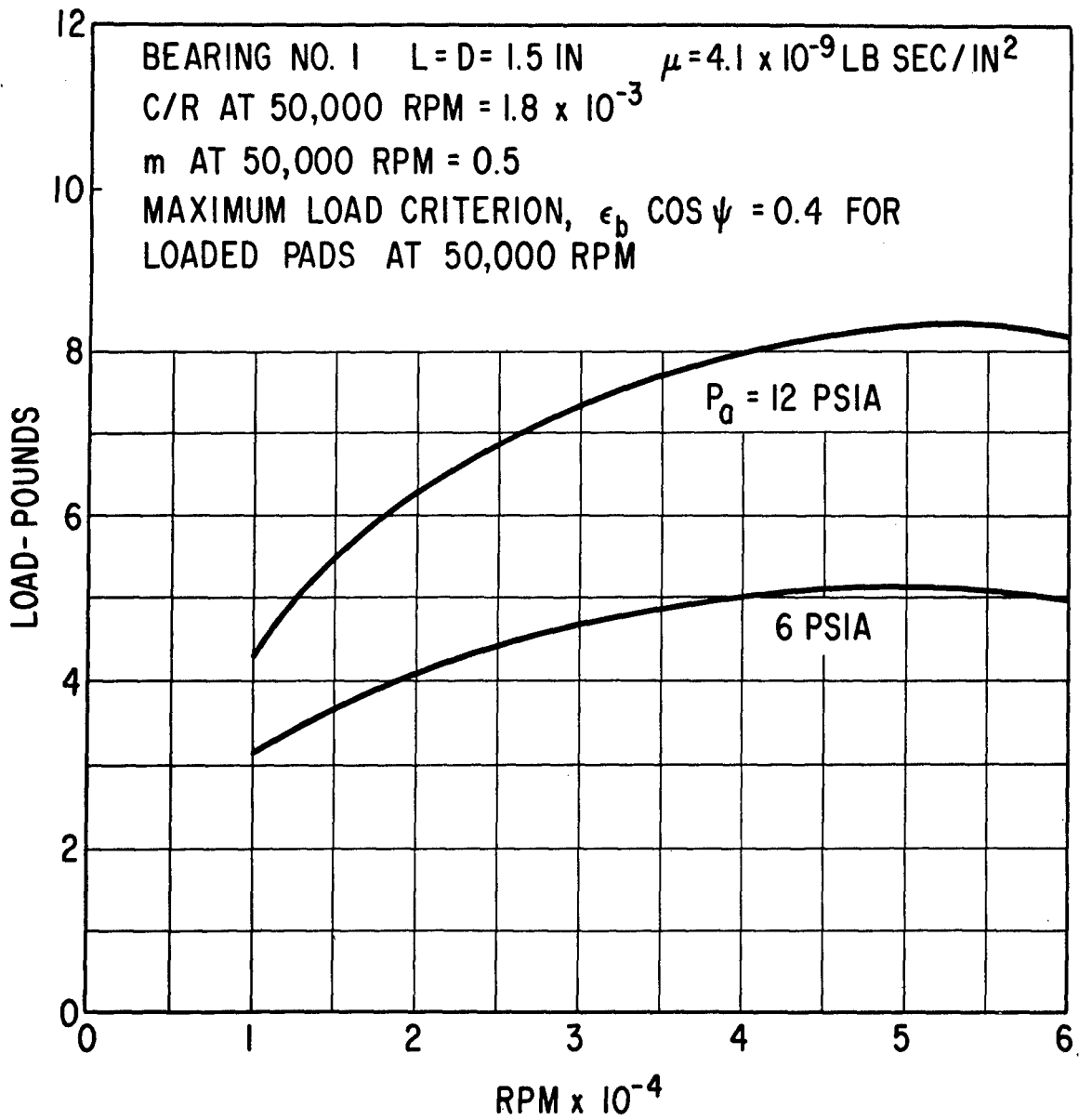


Fig. II-23 - Maximum Recommended Load Capacity Versus Speed For Continuous-Duty Operation Of The Final No. 1 Journal Bearing Design

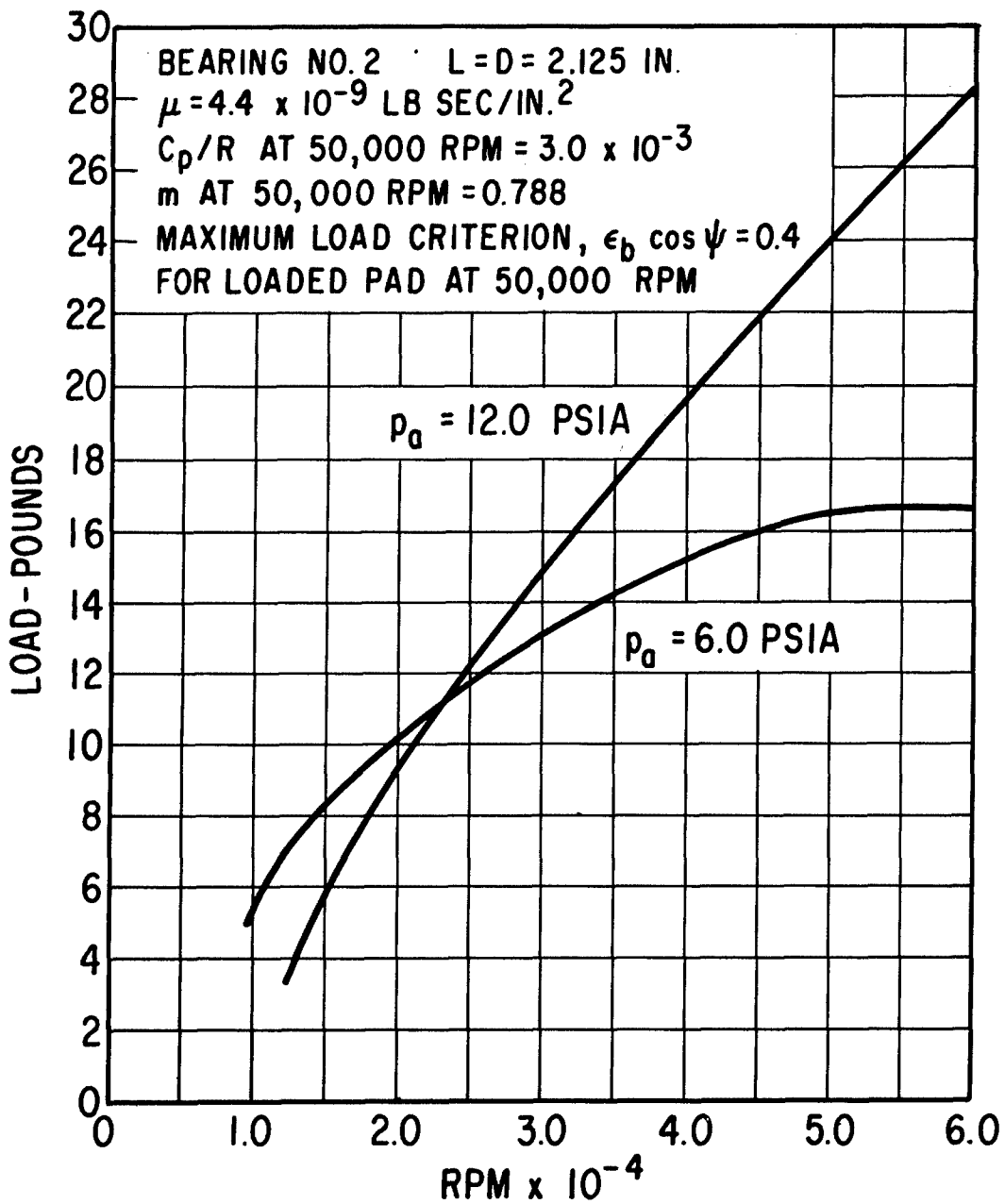


Fig. II-24 - Maximum Recommended Load Capacity Versus Speed For Continuous-Duty Operation Of The Final No. 2 Journal Bearing Design

Bearing Cooling Design

The design of a satisfactory cooling mechanism for the turbocompressor bearing system was a difficult task and one that illustrates the importance of careful consideration of all the various interrelated aspects of turbomachinery design. The problem was defined as one of maintaining safe gas-bearing clearances while removing bearing friction losses with (1) a minimum of temperature rise in the bearing regions, (2) a minimum of thermal distortion of the bearing parts, and (3) a minimum of system power loss for auxiliary bearing coolant flows (in the form of either turbocompressor bleed-gas flows or externally circulated liquid flows).

Maximum allowable bearing region temperature was fixed at 400 F by the insulation of the lead wire for the bearing system capacitance probes (the bearing materials themselves had been successfully tested for short periods of time at temperatures up to 500 F as described in Appendix F.

Three different approaches to cooling the bearings were considered.

1. Transfer of friction losses by conduction to a naturally occurring heat sink within the turbocompressor (i.e., compressor discharge gas).
2. Transfer of losses by conduction and convection to a flow of argon passing through the journal bearing regions.
3. Transfer of losses by convection and/or conduction to a flow of secondary liquid coolant fluid.

All of these techniques were examined for the turbocompressor application in conjunction with design of the initial bearing system. The results of the various studies are described in Appendix C, together with a description of the heat transfer technique finally selected. In brief, the two journal bearings are cooled by conducting the bearing friction losses radially through the rotating journals into axially-finned TD nickel heat exchangers brazed into the ID of each of the journals. A small bleed flow of argon is taken from compressor

discharge, cooled to about 100 F, and then ducted into the rotor bore via a hole through the center of the thrust bearing. Once inside the rotor bore, the argon coolant flows first through the No. 1 bearing heat exchanger and then through the No. 2 exchanger, and picks up the bearing friction losses by convective heat transfer. Figures II-25 and II-26 are photographs of the heat exchangers located in the bores of the No. 1 and No. 2 journals (photographs of the heat exchangers prior to brazing into the bores are shown in Figures C-13 and C-14 of Appendix C). It is seen that the heat exchanger fins are considerably canted, rather than being purely radial. This was done to (1) minimize fin stresses due to differences in centrifugal growth of the bearing journal and the hub of the heat exchanger, and (2) to minimize restraint of the journal which could result in either waviness of the journal surface or unsymmetrical growth of the journal with attendant mass unbalance. The detailed design of the gas-cooling system and the heat exchangers was performed by Pratt & Whitney Aircraft. Initial verification of the heat exchanger fabricability was likewise performed by Pratt & Whitney Aircraft.

All attempts to gas cool the forward (hydrodynamic) thrust bearing were found to be unsatisfactory in that excessively high thrust bearing temperatures resulted and/or significant temperature gradients existed which would produce excessive thermal distortion of the thrust plate. Consequently, the concept of a liquid-cooled thrust stator was adopted wherein the coolant (Versilube, glycol, or a similar fluid) is circulated through annular passages within the aluminum thrust plate. Figure II-27 shows the calculated performance of the thrust bearing liquid cooling system as a function of coolant flow rate. It is seen that a flow rate between 100 and 200 lb./hr., at an inlet temperature of 150 F, will result in reasonable thrust bearing temperatures and temperature gradients, as well as low values of coolant pressure drop.

Comprehensive thermal calculations were made for the initial and second bearing system designs. The coolant flow paths, thermal boundary conditions, and computed temperature maps for the No. 1 and No. 2 bearing regions are presented in Figures C-11 through C-18 (Appendix C) for the initial bearing design, and in Figures D-10 through D-12 (Appendix D) for the second bearing design. Comparable thermal calculations were not made for the final bearing system design. However, to realize practical zero-speed room temperature set-up clearances for the No. 1 and No. 2 journal bearings, it has been determined that the steady-state design-point bearing

region temperatures will have to be approximately as given in Table II-4. Achievement of these temperatures will require a reduction in argon flow through the No. 2 heat exchanger. If the No. 2 journal bearing temperature at design-point conditions cannot be raised to the value given in Table II-4, it would be necessary to increase, somewhat, the stiffness of the upper pivot-support flexures in order to obtain a reasonable zero-speed room temperature set-up clearance.

TABLE II-4

RECOMMENDED DESIGN POINT BEARING TEMPERATURES AND ALLOWABLE TEMPERATURE DEVIATIONS

Rotor In A zero-G Gravitational Field

	<u>No. 1 Bearing</u>	<u>No. 2 Bearing</u>
Flexure Stiffness, lb./in.		
Upper	10,000	10,000
Lower	50,000	70,000
Maximum Film Thickness Criterion	$\epsilon_p \cos\phi = 0.40$	$\epsilon_p \cos\phi = 0.77$
Minimum Film Thickness Criterion	$\epsilon_p \cos\phi = 0.80$	$\epsilon_p \cos\phi = 0.90$
Design-point temperature differentials, °F		
$T_s - T_o$	95	330
$T_s - T_p$	-11	-25
$T_h - T_s$	69	-60
Maximum $T_h - T_s$ for maximum film thickness criterion, °F	105	-45.9
Maximum pivot film thickness for $(T_h - T_s)_{\text{max.}}$, mils	0.80	0.73
Minimum $T_h - T_s$ for min. film thickness criterion, °F	-94	-226
Minimum pivot Film thickness for $(T_h - T_s)_{\text{min.}}$, mils	0.27	0.30

Temperature Designations

T_o - Journal reference temperature (taken as 70 F throughout this report)

T_s - Journal temperature

T_h - Bearing housing temperature

T_p - Pad temperature

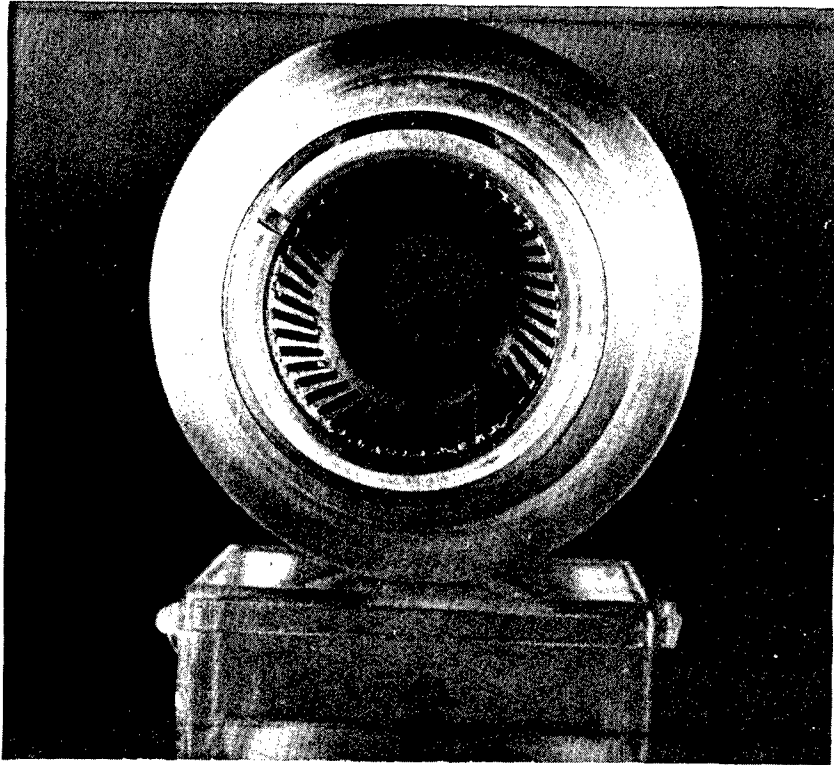


Fig. II-25 - View Of Heat Exchanger Located In Bore Of No. 1 Journal Bearing

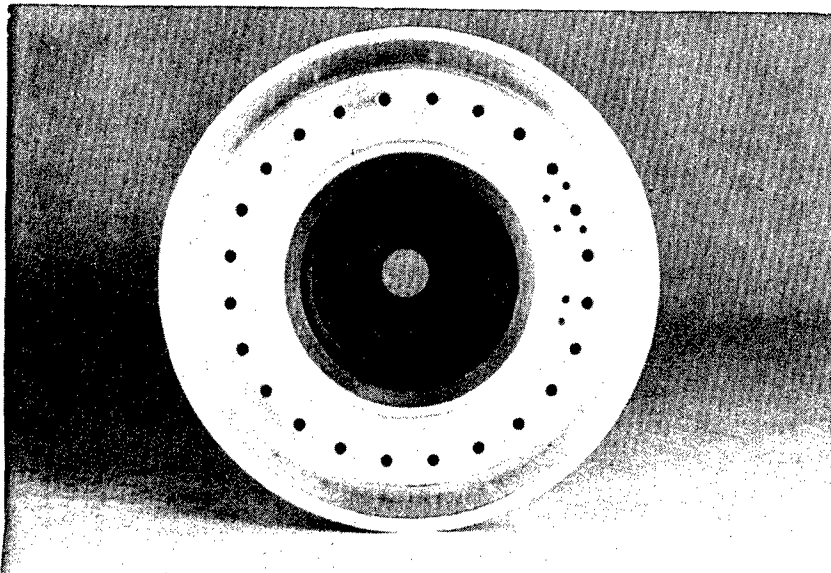


Fig. II-26 - View Of Heat Exchanger Located In Bore Of No. 2 Journal Bearing

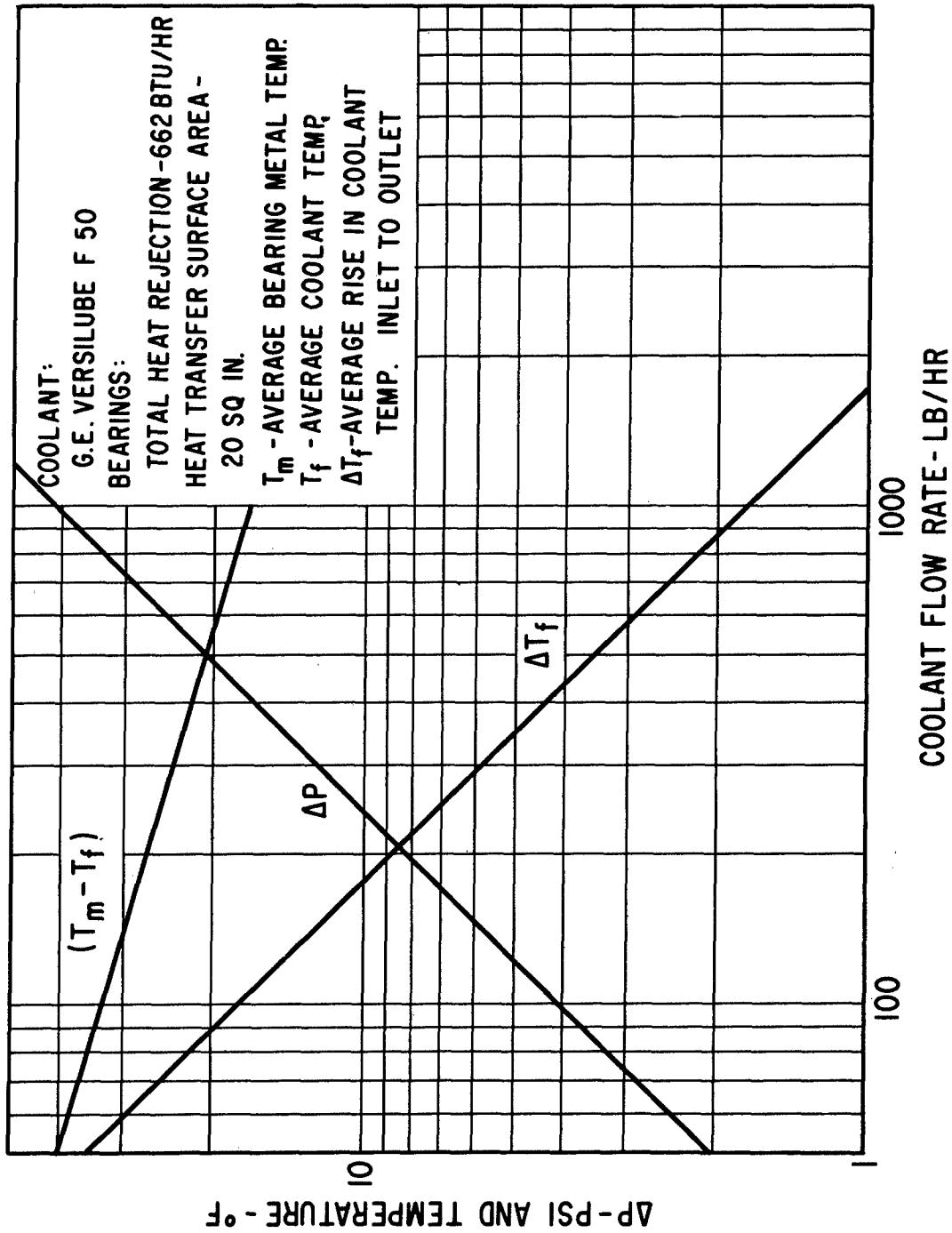


Fig. II-27 - Calculated Performance Of Thrust Bearing Cooling System

Bearing System Fabrication Materials

The materials selected for the basic bearing parts are listed below.

Rotor Journals [shaft]	NiB <u>Waspaloy</u>
Pivot-support flexures	No. 1 br'g. - AISI ^{ES} 4130 No. 2 br'g. - <u>Discaloy SS</u>
Pivoted-pads	^{ES} <u>M-1 tool steel</u>
Pivots	M-1 tool steel
Forward thrust stator	^{al} <u>AMS-4027</u> aluminum
Forward thrust stator flexure	^{al} <u>7075-T6</u> aluminum
Thrust runner	Titanium
Reverse thrust stator	^{ES} <u>AMS-6415</u> low-alloy carbon steel

→ p59

The basis for selection of the above materials is as follows.

1. Rotor Journals

The turbine is an integral part of the turbocompressor rotor, hence, the turbine material requirements dictated the rotor journal material.

2. Pivoted-Pads

The use of M-1 tool steel hardened to $R_c 58$ has proved successful in previous designs employing pivoted-pad journal bearings. The predominant reason for this selection is to obtain a material which is suitable for stress levels of approximately 100,000 psi in the pivot contact zone. Dimensional stability is a second important consideration for the pivoted-pad material.

3. Pivots

Previous experience has demonstrated the suitability of using M-1 tool steel pivots against M-1 tool steel pads. The use of an electrofilm coating on one or both of these components has proved helpful in inhibiting corrosion and fretting damage of the pivot contact zone.

4. Forward Thrust Stator

The material properties required for this item are those of low density for dynamic tracking reasons, high thermal conductivity for heat transfer reasons, and high dimensional stability for bearing performance reasons. These requirements were satisfied by the use of aluminum alloy AMS-4027.

5. Thrust Runner

The selection of material for this component was based on low density in order to keep the "bent shaft" critical speed of the rotor as high as possible, and low coefficient of expansion to limit distortion of the thrust bearing surface. The properties of Titanium met these requirements.

6. Reverse Thrust Stator

The selection of AMS-6415 low-alloy carbon steel for this component was based on a requirement that the coefficient of expansion should be essentially equal to that of the rotor and bearings. This simplifies control of the bearing clearances over the operating temperature range of the No. 1 journal bearing. To prevent corrosion of the low-alloy carbon steel, various types of platings are used.

7. Pivot-Support Flexures

AISI 4130 steel hardened to R_c 36-40 was selected for the flexure material of the No. 1 bearing because of its high fatigue strength and good dimensional stability. AMS 5733 (Discaloy) steel hardened to R_c 25-35 was used for the No. 2 flexures to control thermal expansion effects in the No. 2 bearing clearance. Silver plating is used for corrosion protection on both flexures.

Bearing Surfacing Materials

Gas-lubricated bearings have no boundary lubrication safeguards. It is therefore extremely important that the bearing surfaces be of highly compatible materials, so that incidental high-speed contacts due to shock, vibration, passage of dirt through the bearings, or improper operation of the machine, will not result in serious damage to the rotor-bearing system. Also, where it is desired to omit the complexity of hydrostatic jacking of the bearings (which was the case with respect to the turbocompressor journal bearings), the bearing surfaces must be capable of surviving sliding contact over an appreciable number of starts and stops without damage or significant wear. Since MTI had only limited prior experience with self-acting start-up of pivoted-pad bearings, and known experience with self-acting start-up of full-circular bearings was not good, an experimental program was undertaken to evaluate promising surfacing materials under conditions of start-stop and high-speed contact operation.

It was known that the compatibility of the bearing fabrication materials, as defined in the preceding subsection, would not be acceptable for the sliding and high-speed contact conditions. The test program thus centered on the evaluation of various combinations of coatings applied to the substrate fabrication materials. In particular, the following coatings were evaluated.

Shaft [Waspaloy]

^{NiB}
Al₂O₃ flame-spray

^{NiB, Mo}
Mo arc-spray

^{NiB, SS}
Hardened (R 40) 416 stainless steel

^{NiB}
Chrome oxide flame-spray

^{NiB}
WC flame-spray

Pad [M-1 Tool Steel]

^{ES}
WC flame-spray

^{ES}
DU

^{ES}
Electrofilm 4396

^{ES}
Chrome oxide flame-spray

^{ES}
Hardened (R 60) M-50 tool

steel

└ end

For good assurance of duplicating the conditions of the journal bearings, the tests were conducted with a single pad of a 1.5 inch diameter pivoted-pad bearing. Both start-stop tests at bearing unit loads up to 4 psi and high-speed rubs due to impact loading at 60,000 rpm were made. Tests were conducted at 350 and 500 F in argon.

The test results clearly showed chrome oxide versus chrome oxide to be the best coating combination on the basis of both its performance under start-stop conditions and its tolerance of high-speed rubs. It survived 1000 starts and stops without surface damage and with negligible wear. Under repeated shock-load contacts at 60,000 rpm there was an increase in the contact area of the pad, but both the pad and shaft surfaces were smooth and polished, without any evidence of surface damage.

On the basis of these tests, as well as the past history of its successful application in gyroscope gas bearings, the combination of chrome oxide versus chrome oxide was selected for all the bearings in the present application. A complete description of the evaluation programs at 350 and 500 F are given in Appendices E and F of this report.

Bearing System Instrumentation

Successful and rapid development of advanced high-speed gas-bearing turbomachinery requires that the static and dynamic behavior of the rotor-bearing system be monitored with extreme precision during the test and evaluation phases. In particular, the rotor-bearing system instrumentation must

1. provide data for quantitative evaluation of overall performance,
2. provide data for detailed evaluation of component performance and for refinement of component design, and
3. indicate whether or not the equipment is in a safe mode of operation.

To measure static and dynamic bearing film thicknesses in the prototype turbo-compressor, displacement measuring instrumentation was selected based on measuring electrical capacitance of the gas film between the tip of a capacitance probe and

the moving surface of the journal and thrust bearings. Specifically, a capacitance system based on the Wayne-Kerr Model DM 100 Distance Meter was selected for the following reasons:

1. calibration of the combined transducer and readout system is extremely stable with time and temperature,
2. the calibration factor is essentially constant over a wide range of probe clearance gap (i.e., output is linear over a wide displacement range) and hence, recalibration is not required each time the transducer probes are reset,
3. the calibration factor is essentially constant over a wide range of temperature (i.e., from 75 to 700 F) — only slight changes in calibration occur up to 1200 F,
4. high sensitivities are possible, ranging from 0.2 volts per mil to 0.1 volts per mil for the capacitance probes selected for the turbo-compressor,
5. frequency response, though not outstanding, was adequate for the application — being flat to approximately 6,000 hertz,
6. the capacitance probe is unaffected by magnetic fields, and
7. the capacitance probes could be made very small, light, and rugged.

In order to adequately measure bearing system performance, a total of 21 capacitance probes were incorporated into the bearing system design to measure (1) thrust bearing film thickness, (2) orbital motion of the two journals, and (3) actual film thickness between the eight pivoted-pads and the journals at a point close to the pivot location. In addition, several probes were incorporated to measure dynamic motions of several of the pads and of the forward thrust stator relative to the "fixed" bearing housings.

Locations of the various capacitance probes are listed in Table II-5. Figures II-28 and II-29 show location of the probes in the No. 1 and No. 2 journal bearings in more detail. Figure II-30 is a photograph showing the various sizes of capacitance probes used. Views of the probes installed in the thrust bearings

and pivoted-pads can be seen in the photographs of Figures II-6, II-7, II-8, II-16 and II-19.

In addition to the capacitance probe instrumentation, a total of 33 chromel-alumel thermocouples were incorporated to measure temperatures of the bearing housings, thrust plates, and pivoted-pads. Figure II-31 shows typical thermocouple location patterns on the pivoted-pads.

TABLE II-5

LOCATION OF BEARING SYSTEM CAPACITANCE PROBES

Thrust Bearing And No. 1 Journal Bearing

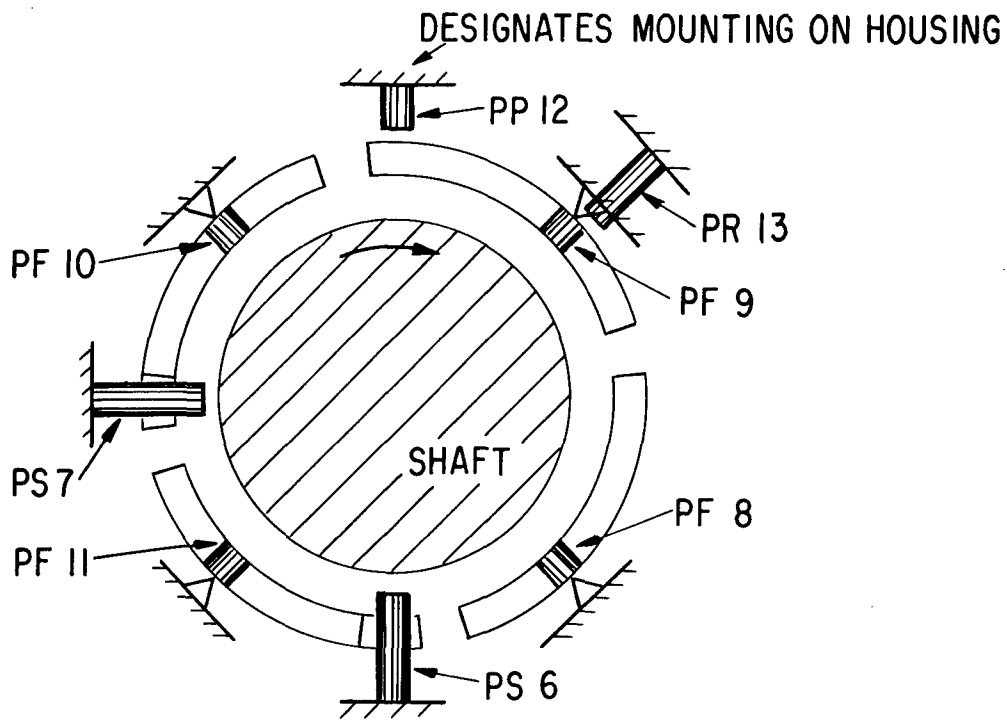
<u>Location</u>	<u>Measurement</u>	<u>Number of Probes</u>	<u>Probe Designation</u>
Forward thrust bearing housing (Ground to forward thrust stator)*	Dynamic movement of forward thrust stator	1	PT 1
Forward thrust bearing stator (Forward stator to runner)	Forward thrust bearing film thickness	3	PT 2, PT 3, PT 4
Reverse thrust bearing stator (Ground to runner)	Reverse thrust bearing film thickness	1**	PT 5
No. 1 housing (Ground to shaft)	Dynamic orbit of No. 1 journal	2 at 90°	PS 6, PS 7
Pivoted-pads (Pad to shaft)	Film thickness between each pad and No. 1 journal	4 at 90°	PF 8, PF 9, PF 10, PF 11
Pad flutter (Ground to back of pad)	Pad flutter in pitch direction (unloaded pad)	1	PP 12
Pad flutter (Ground to back of pad)	Pad flutter in roll direction (unloaded pad)	1	PR 13
<u>No. 2 Journal Bearing</u>			
Pivoted-pads (Pad to shaft)	Film thickness between each pad and No. 2 journal	4 at 90°	PF 20, PF 21, PF 22, PF 23
Pad flutter (Pad to shaft)	Dynamic movement between pad and journal in the roll direction (unloaded pad)	1	PR 24

TABLE II-5 (Cont.)

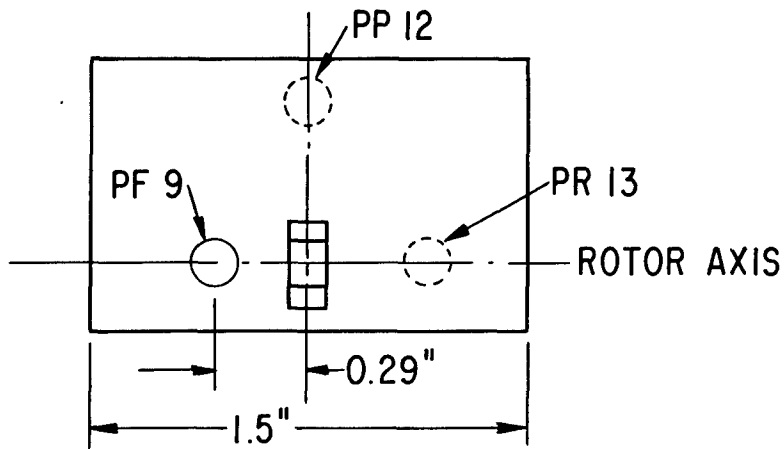
<u>Location</u>	<u>Measurement</u>	<u>Number of Probes</u>	<u>Probe Designation</u>
No. 2 housing (Ground to shaft)	Dynamic orbit of No. 2 journal	2 at 90°	PS 26, PS 27
Pad flutter (Ground to back of pad)	Pad flutter in the pitch direction (unloaded pad)	1	PP 25

*the word 'Ground' refers to any static structure to which a probe is rigidly attached

**This probe can also be used as a speed pick-up by sensing a small recess in the rearward face of the thrust runner.



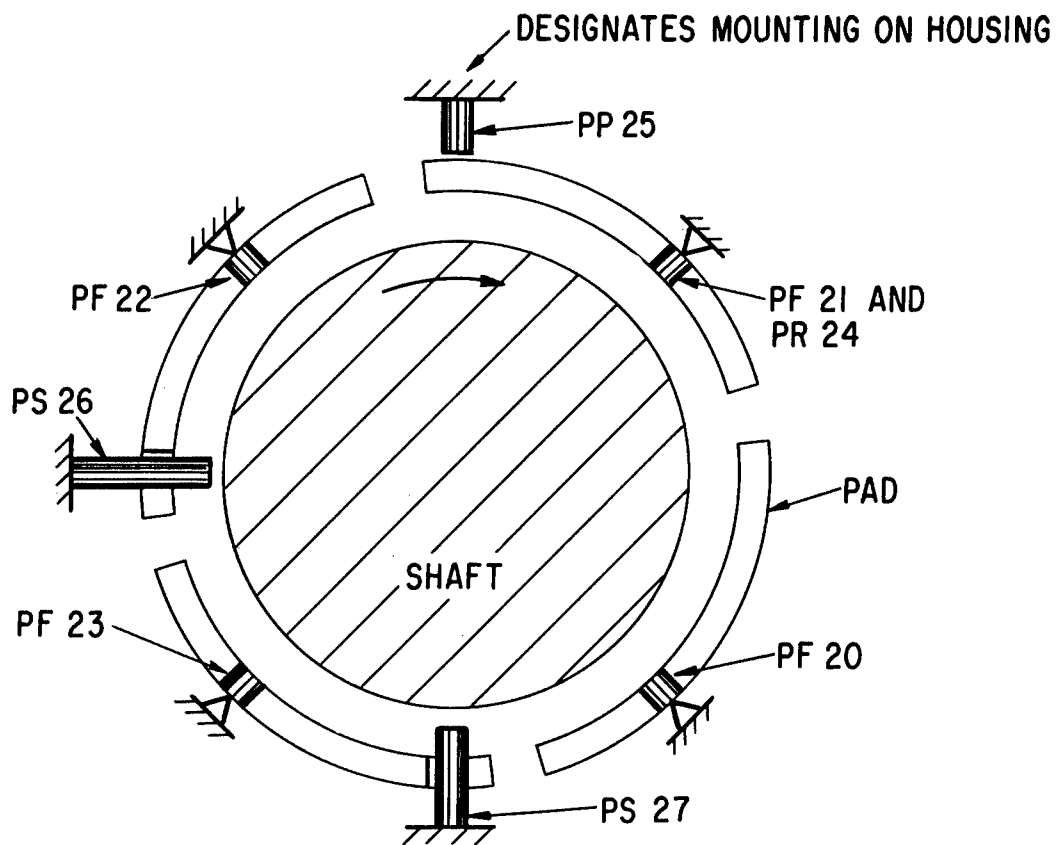
SECTION THRU BEARING CENTER
LOOKING TOWARD THRUST BEARING



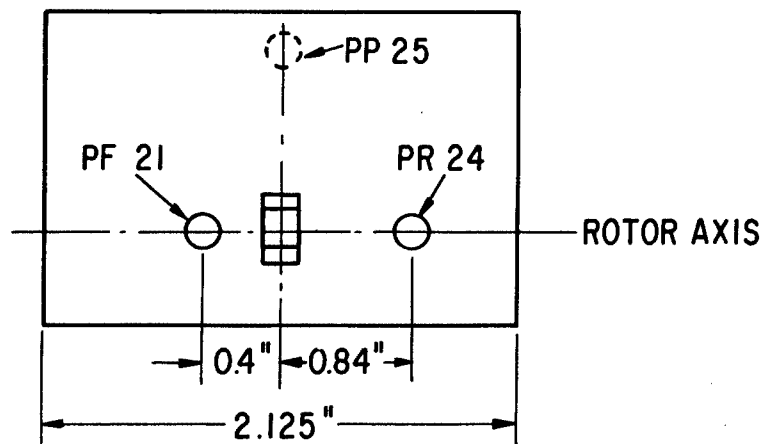
VIEW OF BACK FACE OF UPPER PAD

PF - PAD PIVOT-FILM THICKNESS PP - PAD PITCH PROBE
PS - HOUSING-TO-SHAFT PROBES PR - PAD ROLL PROBE

Fig. II-28 - Location Of Capacitance Probes In No. 1 Journal Bearing Region



SECTION THRU BEARING CENTER
LOOKING TOWARD THRUST BEARING END



VIEW OF BACK FACE OF UPPER PAD

PF - PAD PIVOT - FILM THICKNESS
PS - HOUSING - TO - SHAFT PROBES

PP - PAD PITCH PROBE
PR - PAD ROLL PROBE

Fig. II-29 - Location Of Capacitance Probes In No. 2 Journal Bearing Region

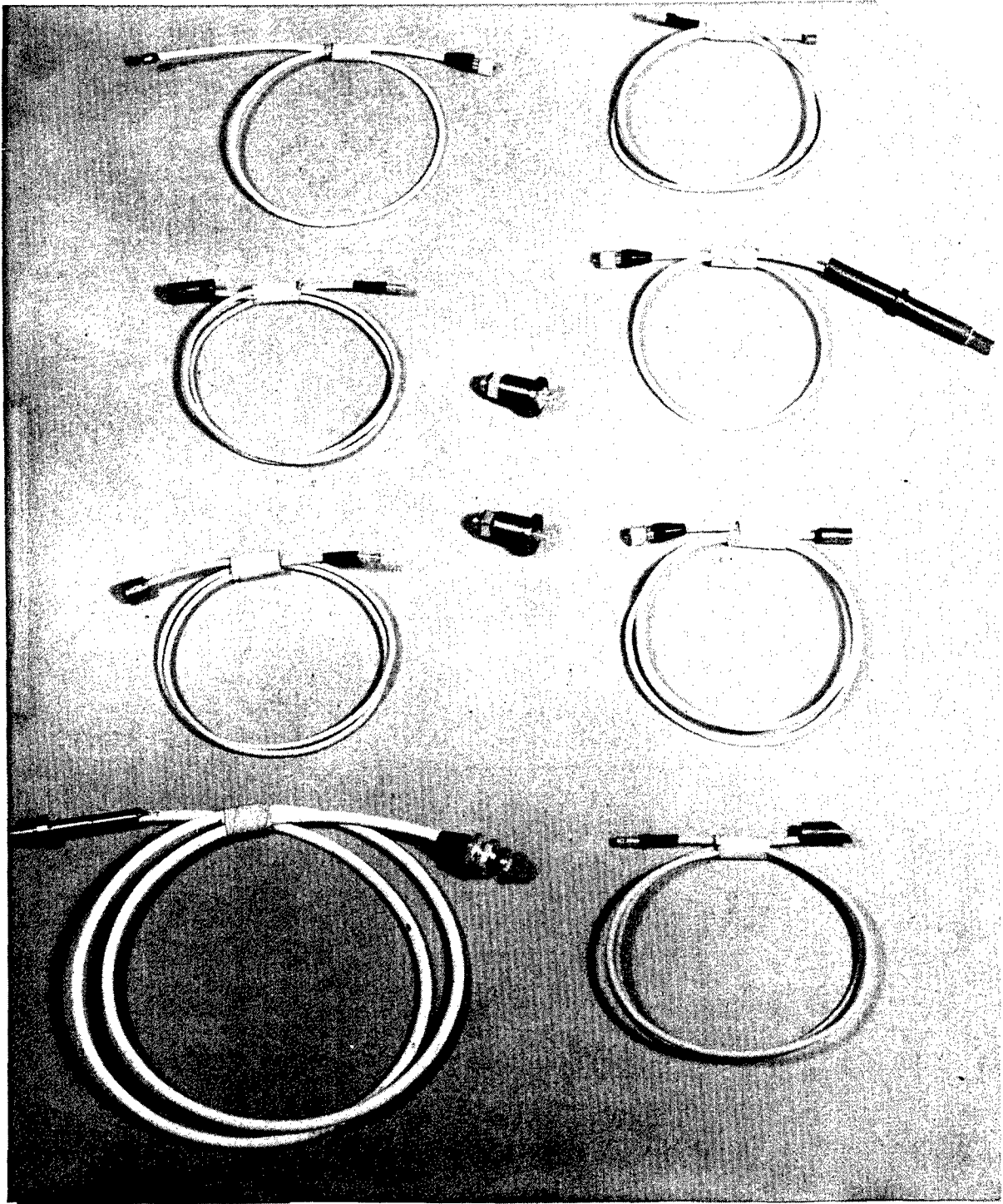
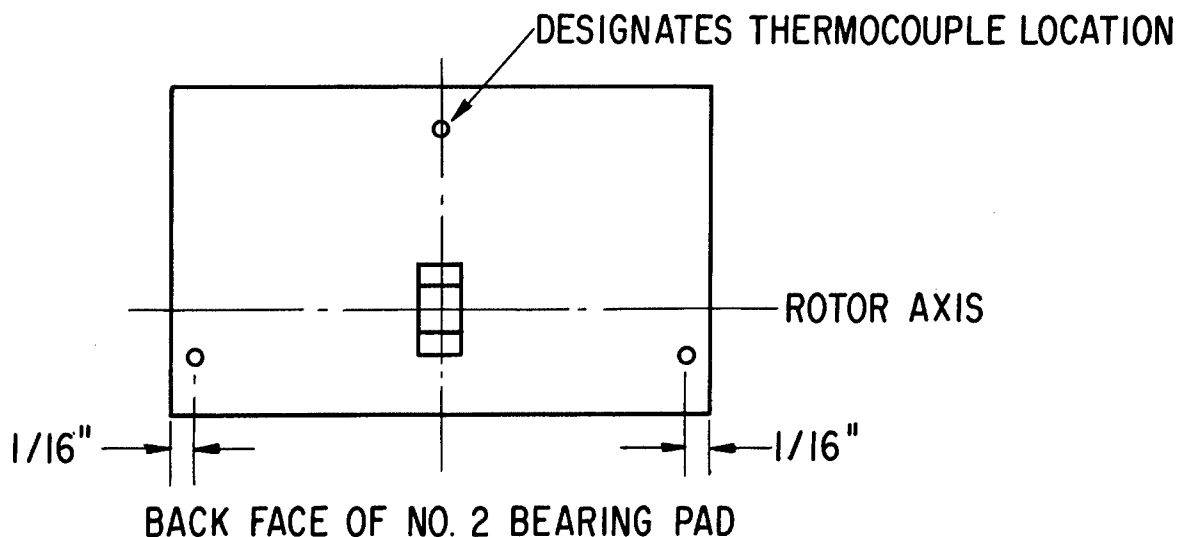
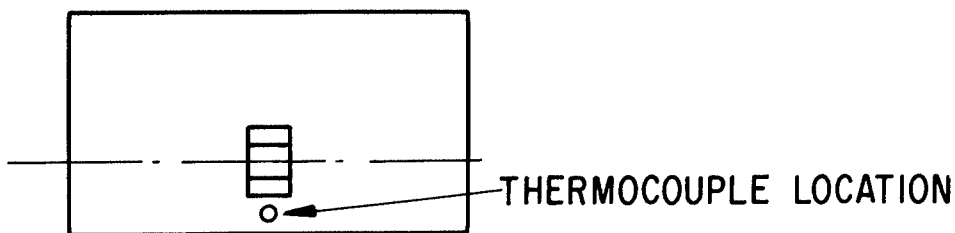


Fig. II-30 - View Of Various Capacitance Probe Configurations Used For Bearing System Performance Measurement



TYPICAL FOR ONE LOADED PAD AND ONE UNLOADED PAD
 (Thermocouples spot welded to back surface of pads; after welding, the installation was covered with epoxy.)

Three thermocouples were installed on the No. 2 bearing housing at a radius of 2.44", 90° apart.



TYPICAL FOR ONE LOADED PAD AND ONE UNLOADED PAD
 (Installation method same as that for no. 2 bearing pad thermocouples.)

A total of 10 thermocouples were installed on the no. 1 bearing housing.

Fig. II-31 - Location Of Significant Thermocouples In Journal Bearing Regions

III. DESIGN OF ROTOR-BEARING SYSTEM SIMULATOR

In any major development program where relatively new techniques are being extended to the limits of known experience, and where the cost and complexity of the prototype machinery demands the utmost assurance of sound design, it becomes exceedingly important to be able to isolate, evaluate and remedy possible problem areas by means of component or subsystem test programs. With respect to the NASA axial flow turbocompressor, it was recommended that the design of the gas-lubricated rotor-bearing system, as described in Section II and Appendices C and D of this report, be experimentally evaluated and optimized in a specially constructed rotor-bearing system simulator. This would permit development and acceptance testing of the rotor-bearing system independent of, and yet parallel to, the turbocompressor aerodynamic components.

The recommendation for a rotor-bearing system simulator was approved by NASA, and design of the simulator was begun in October, 1964. The design was carried out such that the simulator could readily be used to

1. define rotor balancing requirements and procedures
2. evaluate bearing system performance under both balanced and unbalanced rotor conditions
3. evaluate bearing system performance at design-point and off design conditions (such as at maximum overspeed, at reduced ambient pressure, and at higher-than-expected thrust loads)
4. evaluate bearing system performance at steady-state bearing temperatures representative of those anticipated in the turbocompressor
5. assess the adequacy of the bearing cooling techniques
6. experimentally optimize the bearing system design parameters to minimize bearing friction losses
7. identify unknown problem areas.

A cross-section view of the rotor-bearing system simulator is shown in Figure III-1. Significant features of the simulator are described in the following subsections.

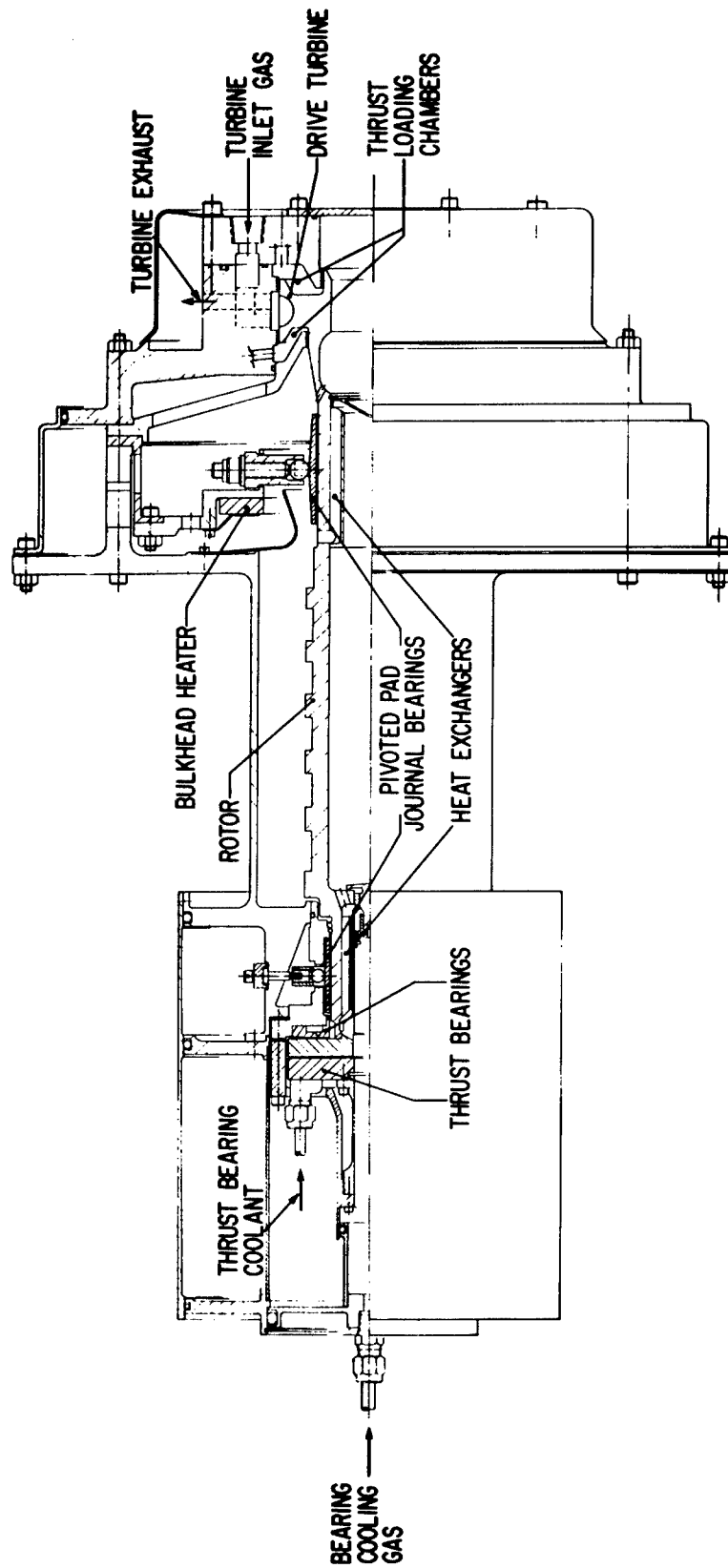


Fig. III-1 Cross-Section View Of Rotor-Bearing System Simulator

Simulator Rotor

A photograph of the simulator rotor (less thrust runner) is shown in Figure III-2. The rotor possesses the same principle dimensions, total mass, mass distribution, and stiffness characteristics as will be exhibited by the turbocompressor rotor. The total calculated weight, and polar and transverse (about the c.g.) mass moments of inertia of the complete rotor assembly (including thrust runner) were 10.62 pounds, 0.033 in.-lb.-sec.², and 0.63 in.-lb.-sec.² respectively. The calculated location of the c.g. for the complete assembly was 8.75 inches from the forward-most face of the thrust runner. Actual measured weight and c.g. location for the complete rotor assembly was 10.5 pounds and 8.531, ± 0.031 inches respectively.

Heat exchanger elements were brazed into the rotor on the ID of each of the journals. These exchangers, which transfer bearing friction losses to a flow of coolant gas, are identical in design to those which will be used in the turbocompressor. They were included in the simulator for the following reasons. First, the mechanical integrity of the brazed construction under high-speed strains due to centrifugal growth and possible effects of this growth on rotor balance, needed to be evaluated. Secondly, inclusion of the heat exchangers made it possible to verify the intended heat transfer function of these components. Photographs of the heat exchangers, before and after brazing into the rotor, are shown in Figures C-13, C-14, II-25 and II-26.

The material from which the turbocompressor rotor will be manufactured is Waspaloy. The simulator rotor, however, is not subjected to the same high turbine inlet temperatures and, consequently, high-temperature material properties were not required. Selection of the simulator rotor material was based on the following requirements:

1. Good stability to meet dimensional and tolerance requirements
2. A yield stress of 100,000 psi to meet the turbine wheel bore stress requirements

3. An NDT point well below turbine wheel temperature with a high Charpy V-notch energy value at 0 F.
4. Good machinability and freedom from distortion as a consequence of heat treatment and brazing.

These requirements were met by the use of correctly heat treated AMS 6415 F (AISI 4343). The essential feature of the heat treatment is the transformation to a micro-structure which is 100 percent martensite, after which further heat treatment or brazing is undertaken at a temperature below the transformation point. The properties of the material after heat treating and brazing are as follows:

yield strength	-	1.4×10^5 PSI
Hardness	-	25 - 30 Rc
Charpy V notch	-	50 ft.-lb. in the temperature range -100 to +100 F.

The journal bearing portions of the simulator rotor are, like the turbocompressor rotor, coated with flame-sprayed chrome oxide. The basis of selection for the chrome oxide surfacing material is described in Section II, and Appendices E and F, of this report.



Fig. III-2 - View of Simulator Rotor, Less Thrust Runner

Simulator Bearings

The simulator was designed to use precisely the same bearing system as designed for the turbocompressor. Photographs of the journal bearing parts are shown in Figures II-5 through II-10, and of the thrust bearing parts in Figures II-14 through II-19. For the No. 1 journal and thrust bearing region (which is located at the compressor inlet end of the turbocompressor), the bearing components include pivoted-pads, pivots, flexures, thrust stator, journal and thrust bearing support housings, and bearing system instrumentation transducers (capacitance probes and thermocouples). These components form a complete assembly which has the same interface for both the simulator and the turbocompressor. In the No. 2, or turbine, journal bearing region, the bearing components include pivoted-pads, pivots, flexures, and instrumentation transducers. Again, the interface for the bearing components is identical in both the simulator and the turbocompressor.

Control of Bearing Loads

Variation in journal bearing loads, from zero to full rotor weight reaction, is possible by rotation of the complete simulator on its mounting trunnions from a vertical to a horizontal rotor orientation. Figures III-3 and III-4 are photographs of the complete simulator assembly in a horizontal and vertical orientation respectively.

For control of thrust load, at any orientation of the rotor, the simulator casings fore and aft of the turbine wheel have been extended radially inwards, and labyrinth seals provided between these extensions and the rotor (see Figure III-1). This permits the turbine wheel to be used as a double-acting piston. Variable magnitude and direction of thrust load can thus be obtained by control of pressure in the cavities on each side of the turbine wheel. These cavities are connected by suitable pressure control valves to a gas supply manifold (as shown in Figure IV-3). Leakage past the labyrinths passes into the main simulator casing from where it is vented to atmosphere (via a vacuum pump when the simulator is being operated at sub-atmospheric ambient pressures).

Simulator Casings

The primary functions of the simulator casings are to provide an enclosure and support structure for the bearing system and turbine drive. As the ambient conditions for simulator operation involve sub-atmospheric pressures in the bearing areas and considerably elevated pressures in the turbine supply system, the casings have been designed with suitable labyrinth seals to separate the high and low pressure regions within the enclosure, while at the same time permitting correct distribution of heating and cooling gas flows as required for control and simulation of bearing region temperatures.

Two spinnings are provided to form exhaust ducts at the turbine end of the simulator. The first of these is connected to a vacuum pump by means of suitable piping and control valves. This permits the control of ambient pressure in the simulator and exhausts the various bearing system gas flows, and also the labyrinth leakage flow in the thrust loading system, to atmosphere. The second spinning is used to collect turbine discharge gas. This gas is then ducted to atmosphere. This duct also depresses turbine noise to a more tolerable level than would be the case with an open exhaust.

The casings were also designed to roughly approximate the mass and stiffness characteristics of the turbocompressor casings. Mounting of the simulator is accomplished in approximately the same plane as the turbocompressor mounting. This was done so that any potential structural resonance problems could be identified during the test program.

An item of considerable importance in the design of the simulator casings is the accommodation and accessibility of leak tight instrumentation and supply connections to the bearings. The design as shown in Figure III-1 utilizes permanently installed pass-throughs in the fore and aft bulkheads at No. 1 bearing, and the forward bulkhead in the No. 2 bearing area. This permits the easy coupling of all connections on the inboard side prior to completing the enclosure by means of the O-ring sealed outer sleeve at No. 1 bearing and the exhaust duct O-ring and gasket-sealed spinning at No. 2 bearing. Figure III-5 shows some of the bulkhead instrument connections for the assembled simulator.

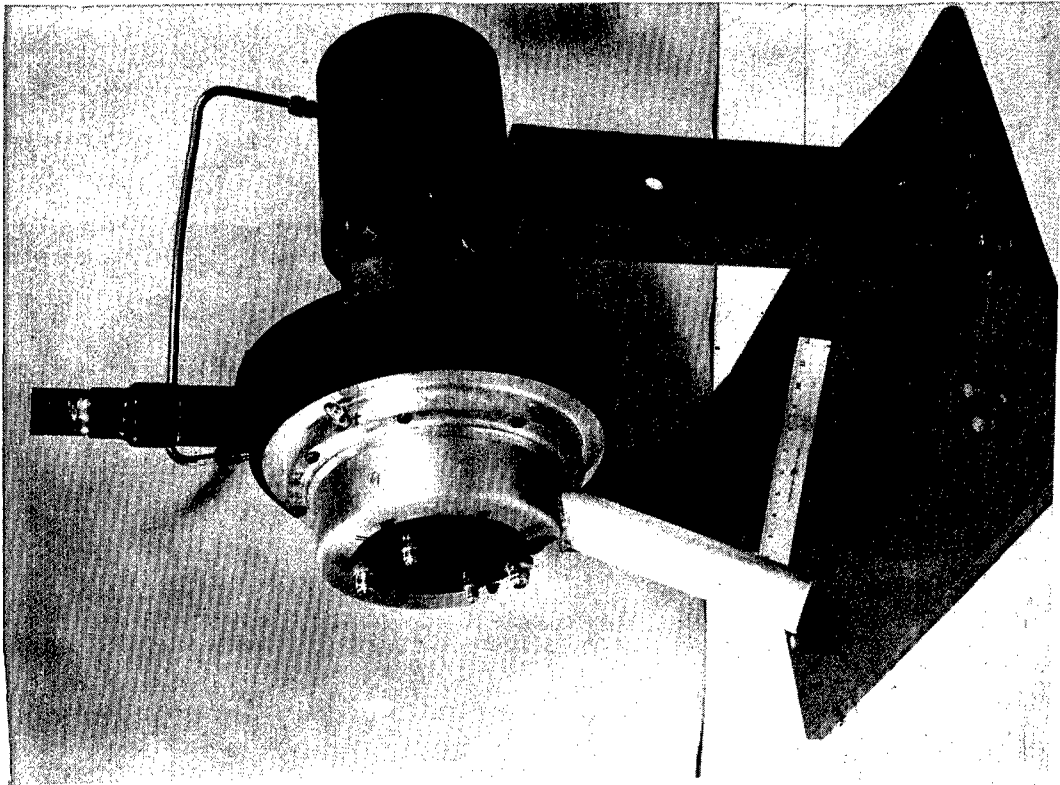


Fig. III-3 - View of Complete Simulator Assembly
With Rotor Horizontal

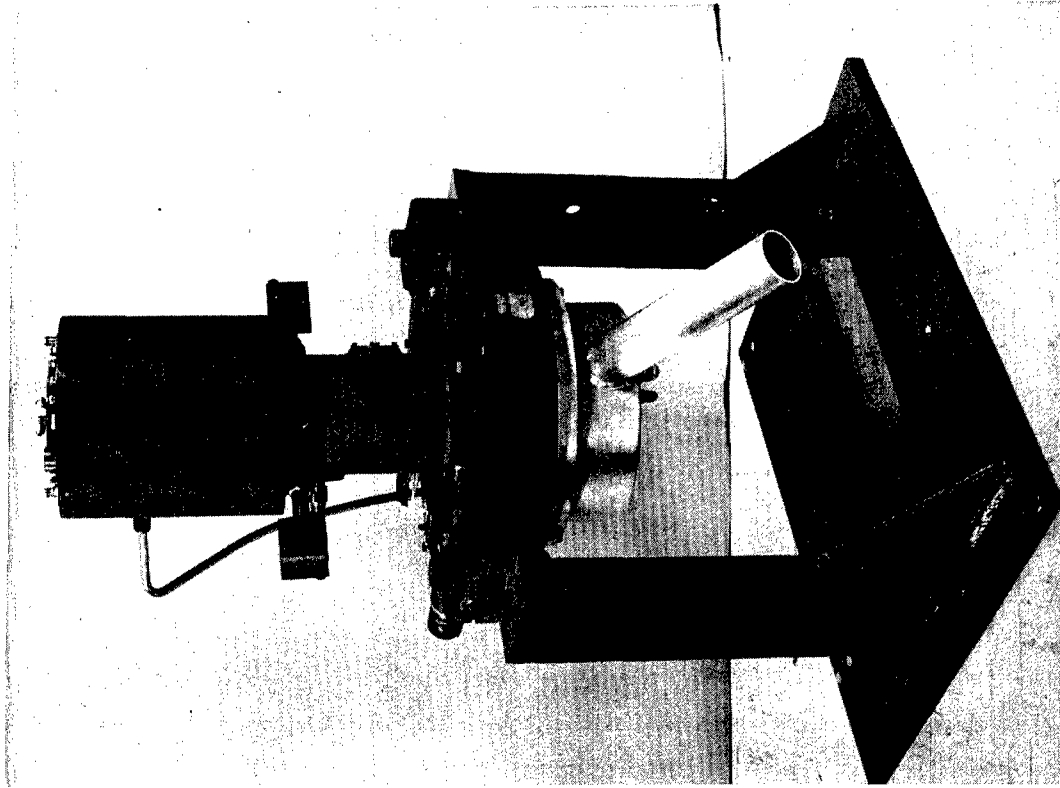


Fig. III-4 - View of Complete Simulator Assembly
With Rotor Vertical --- Turbine End Down

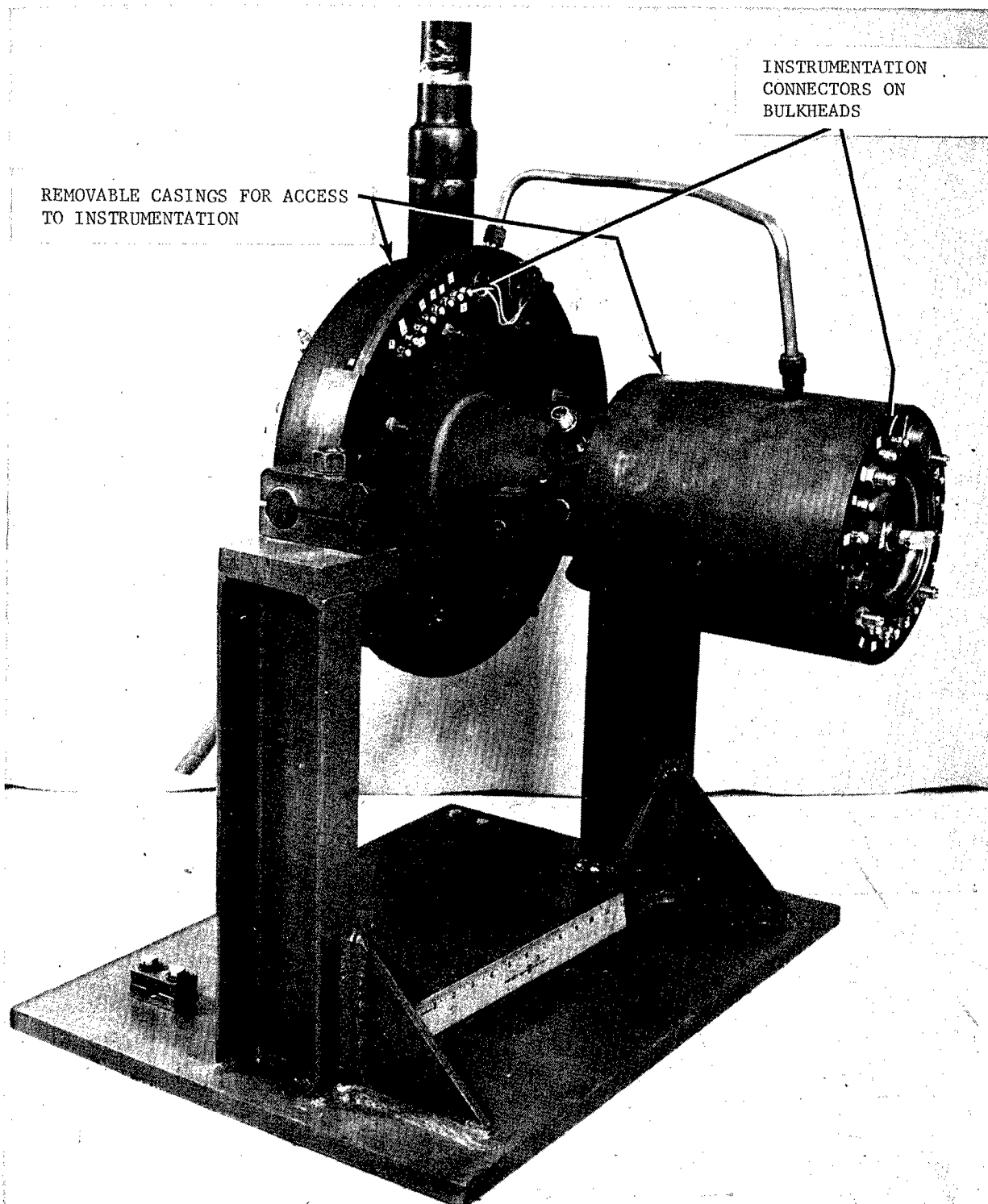


Fig. III-5 - External View Of Bulkhead Instrumentation Pass-Throughs

Simulator Turbine

In selecting the type of drive for the rotor-bearing dynamic simulator, a number of requirements were taken into consideration. These are listed as follows.

1. The speed range requirement was zero to 60,000 rpm with variable speed control.
2. The maximum power requirement would be approximately 2.5 HP at 60,000 rpm. This power requirement was based on bearing friction and rotor windage losses at the minimum anticipated bearing clearances and maximum ambient pressures and temperatures.
3. The selected drive should not interact with rotor-bearing dynamic performance or introduce characteristics which would prove difficult to correctly interpret.
4. The selected drive should not introduce indeterminate axial forces which would interfere with the thrust loading system.
5. Speed control should be sufficiently precise to permit in-place balancing of the rotor.

To meet these requirements an impulse turbine was selected. The design of this turbine, however, was strongly influenced by the primary requirement for correctly simulating the size, inertia, and elastic characteristics of the turbocompressor rotor. The resulting turbine wheel, although not possessing optimum specific diameter or specific speed for the available shop air line pressures, was capable of producing sufficient power for 50,000 rpm design speed operation. To reach the overspeed condition of 60,000 rpm, it was necessary to increase the nozzle inlet pressure to 215 psia, a pressure which was available from a large-volume nitrogen storage system. During operation of the turbine under the above conditions, the efficiency was very low (approximately 25 percent). The duration of testing, however, was relatively short and the low efficiency value was of no concern.

The nominal dimensions of the turbine are as follows:

wheel diameter	-	3.742 inches
number of buckets	-	21
number of nozzles	-	4
diameter of nozzles	-	0.124 inches
radius of buckets	-	0.300 inches.

The turbine buckets are formed on the outside diameter of the wheel by end milling, using a 0.60 inch diameter cutter. The four convergent-divergent nozzles are manufactured as separate components which are then inserted into the simulator casing. The flow to the nozzles is supplied via drillings from an annulus located within the simulator casing.

Exhaust from the turbine is by four radial slots cut into the simulator casing, each of which is 0.25 inches wide and extends over a 45 degree circumferential arc.

Thermal Simulation Capability

The simulator is equipped with the same bearing system thermal control capability as is provided by the design for the prototype turbocompressor. This includes the following features.

1. Provision for introducing bearing cooling gas into the bore of the rotor via the center hole in the thrust bearing. (Provision for preheating the cooling gas was also provided as described in Section IV of this report.)
2. Provision for introducing heated gas around the No. 1 bearing housing.
3. Provision for controlling temperature of the No. 2 bearing housing via a 500 watt Chromalox annular electrical bulkhead heating element, located as shown in Figure III-1.
4. Provision for introducing coolant liquid into the forward thrust bearing stator. (Provision for preheating the coolant was likewise provided in the simulator control system.)

All parts of the simulator are designed to operate at the maximum anticipated steady-state temperatures which could occur in the turbocompressor bearing regions.

Simulator Instrumentation

As mentioned in Section II of this report, successful and timely development of a prototype gas-bearing machine requires extensive rotor-bearing system instrumentation for quantitative measurement of performance and for minimum risk operation. Accordingly, the simulator rotor-bearing system was equipped with exactly the same capacitance probe and thermocouple transducers as was recommended for the prototype turbocompressor design (see pages 87 through 91).

In addition to the bearing system instrumentation, numerous additional thermocouples were installed to monitor simulator casing temperatures, as well as temperatures of the various coolant fluids. A Model 3040 Electro Products Laboratories magnetic speed pickup was used to measure rotor speed. The pickup sensed six notches cut in the OD of the rotor ring used to simulate the mass of the second-stage compressor blades. The speed pick-up can be seen projecting from the small-diameter center section of the simulator casing in Figure III-5. Finally, the simulator was equipped with numerous pressure taps for measurement of turbine, thrust loading, and bearing ambient pressures.

A description of the simulator instrumentation readout equipment, and the simulator control system is given in the next section of this report. A schematic of the control system is shown in Figure IV-3.

IV. TEST EVALUATION OF THE FINAL BEARING SYSTEM DESIGN

Three series of tests were performed with the rotor-bearing system simulator described in Section III of this report. The first test series, begun on July 17, 1965, was an evaluation of the initial bearing system design. The results of this evaluation are documented in Appendix C of this report. Testing of the initial design was concluded on October 20, 1965 with a successful acceptance test in accordance with P&WA Specification 6355-A (this specification is enclosed in Appendix A of this report).

The second series of tests, begun on December 30, 1965, was an evaluation of the second bearing system design. The results of this evaluation are documented in Appendix D. Testing of the second design was concluded on January 14, 1966, again with a successful acceptance test in accordance with P&WA Specification 6355-A.

It was during the second series of simulator tests that a low-frequency rotor whirl phenomenon was first identified. As discussed in Appendix D, onset of the whirl phenomenon occurred as the diametral clearance of the No. 2 journal bearing was being increased to the nominal design-point value, this value being considerably greater than the design clearance of the initial bearing system design. Full attainment of the hoped-for increase in clearance would have resulted in a 66 percent reduction in friction loss for the No. 2 journal bearing, this being the primary objective of the second bearing system design. As a result of the whirl condition, the acceptance test for the second bearing design had to be performed at considerably less than the design-point clearance value. Nonetheless, a significant increase in diametral clearance, with its attendant decrease in bearing friction loss, was obtained relative to the design-point conditions of the initial design.

The third series of simulator tests was begun on March 9, 1966, and was concluded on March 17, 1966 with a successful acceptance test. The purpose of the third test series was to evaluate the performance of the final bearing system design (which was

identically the same as the second bearing design, except that the mass properties of the No. 2 journal bearing pads were restored to those of the initial bearing design) and to determine the maximum bearing diametral clearance (i.e., the minimum bearing friction loss condition) at which whirl-free operation of the turbocompressor would be assured under various operating conditions. More specifically, the effect on the boundaries of the whirl-free clearance envelope were determined for the following operational variables:

1. Bearing ambient pressure - 10.0 to 14.7 psia
2. Bearing lubricant gas - air and argon
3. Orientation of rotor axis - horizontal and vertical
4. Rotor balance condition - residual unbalance and residual plus 0.0034 ounce-inches unbalance.

The following subsections describe (1) the simulator test facility in which the various bearing system evaluation tests were performed and (2) the specific test results pertaining to performance of the final bearing system design as documented in Section II of this report.

Description of the Simulator Test Facility

The simulator test facility consisted of the following items:

1. the rotor-bearing system simulator (described in Section III),
2. the simulator control panel,
3. instrumentation read-out equipment.

Figure IV-1 is a photograph of the rotor-bearing system simulator mounted on a test bench behind the control panel. In this photograph the simulator is vertical with the turbine-end down. The vacuum casings around the No. 1 and No. 2 bearing regions are removed and the machine is set up for in-place rotor balancing on the gas bearings.

Figure IV-2 is a photograph of the simulator control panel and a partial set-up of the instrumentation read-out equipment. A Hewlett Packard 521A electronic counter, seen mounted above the left-hand end of the control panel, was used to continuously monitor rotor speed. A 24-point temperature recorder, located on the right-hand table, was used to monitor bearing system temperatures. Microdyne consoles (located at the immediate right and left of the control panel), together with Wayne-Kerr DM-100 distance meters and Tektronic 502-A oscilloscopes, were used to monitor bearing system capacitance probe signals.

Figure IV-3 is a schematic diagram of the simulator control system. All controls, except for heater exit temperatures and air-manifold supply pressure, were manually operated. It is seen from Figure IV-3 that individual control valves were supplied for

1. fine and coarse control of turbine nozzle pressure (V-4 and V-5),
2. control of forward thrust loading pressure (V-6),
3. control of reverse thrust loading pressure (V-7),
4. control of forward hydrostatic thrust bearing supply pressure (V-10),
5. control of reverse hydrostatic thrust bearing supply pressure (V-8),
6. control of water coolant supply pressure to the forward thrust bearing stator (V-12),
7. control of cooling gas flow into the rotor bore (V-9),
8. control of heating gas flow into the No. 1 bearing housing cavity (V-11),
9. control of simulator bearing region ambient pressure (V-14, V-15 and V-16).

All pertinent pressures and flows for the above listed control functions were measured via bourdon tube pressure gages and rotometer flowmeters mounted on the control panel, as seen in Figure IV-2. Control of the No. 2 bearing housing bulk-head heater was obtained via a manually controlled variac (auto transformer) also mounted on the control panel.

Shop air at 120 psig was used to drive the simulator turbine at speeds up to about 51,000 rpm. To achieve the 60,000 rpm overspeed condition, a nozzle pressure of approximately 200 psig was required. Since this pressure was not available from the shop air supply, nitrogen from a high-pressure tank truck was used for 60,000 rpm overspeed operation.

As seen from Figure IV-3, the manifold used to supply gas flows for all other simulator requirements (excluding turbine drive gas) could be connected either to the shop air supply, the nitrogen tank truck supply, or to a completely separate argon supply. When it was desired to operate the simulator in an argon environment, the supply manifold was isolated from the turbine air (or nitrogen) supply line via valves V-18 and V-3. Valve V-20 was then opened to admit argon from high-pressure bottles into the supply manifold.

Control of journal bearing temperatures was achieved by regulating flow rate and inlet temperature of (1) the rotor-cooling gas flow, and (2) the No. 1 bearing housing heating flow, and by adjustment of the supply voltage to the No. 2 bearing housing bulkhead heater. Control of thrust bearing temperature was obtained by regulating flow and inlet temperature of the thrust bearing coolant water.

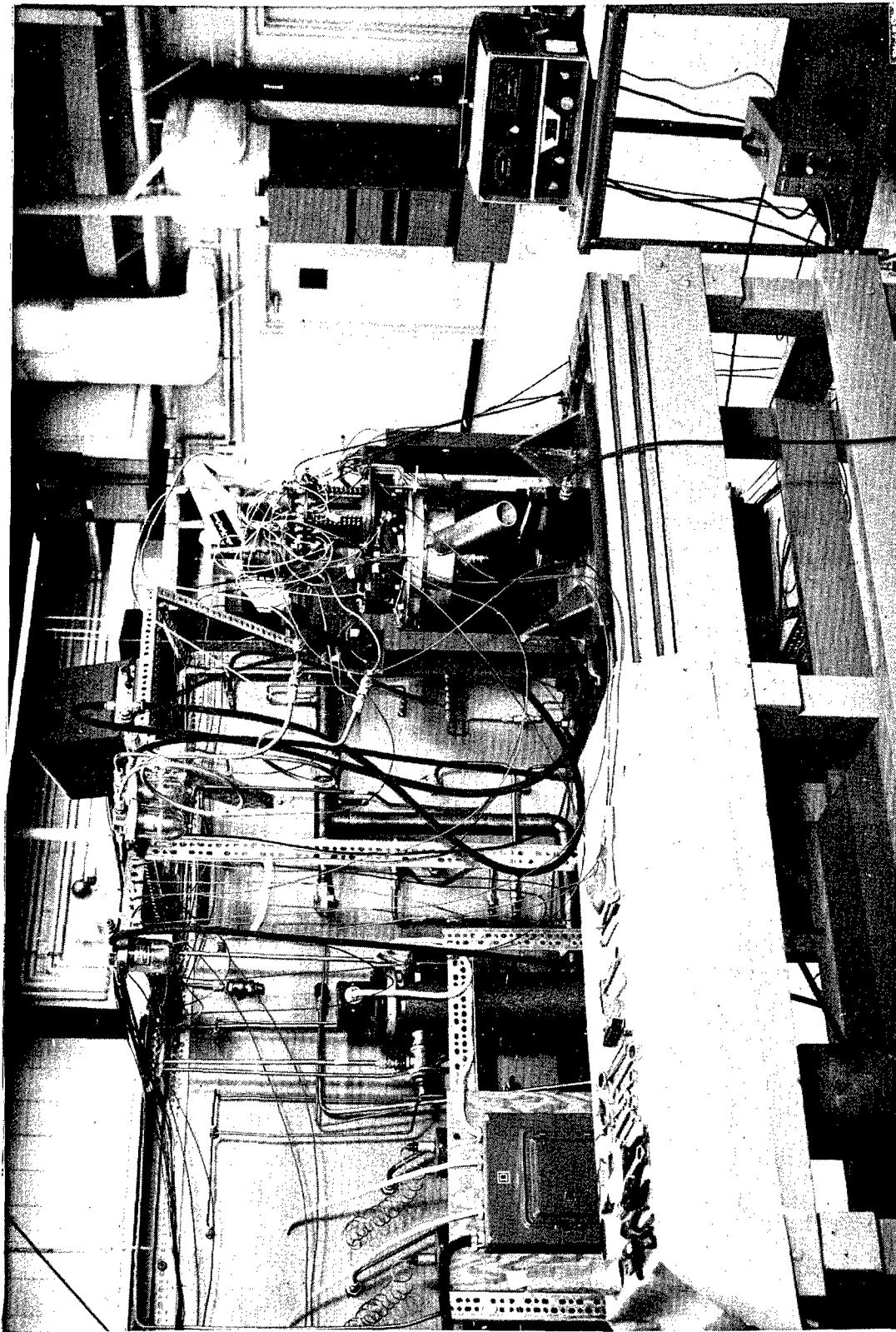


Fig. IV-1 - View Of Simulator Mounted On Test Bench (Rotor Vertical, Turbine Down) With Vacuum Casings Removed For In-Place Rotor Balancing On The Gas Bearings

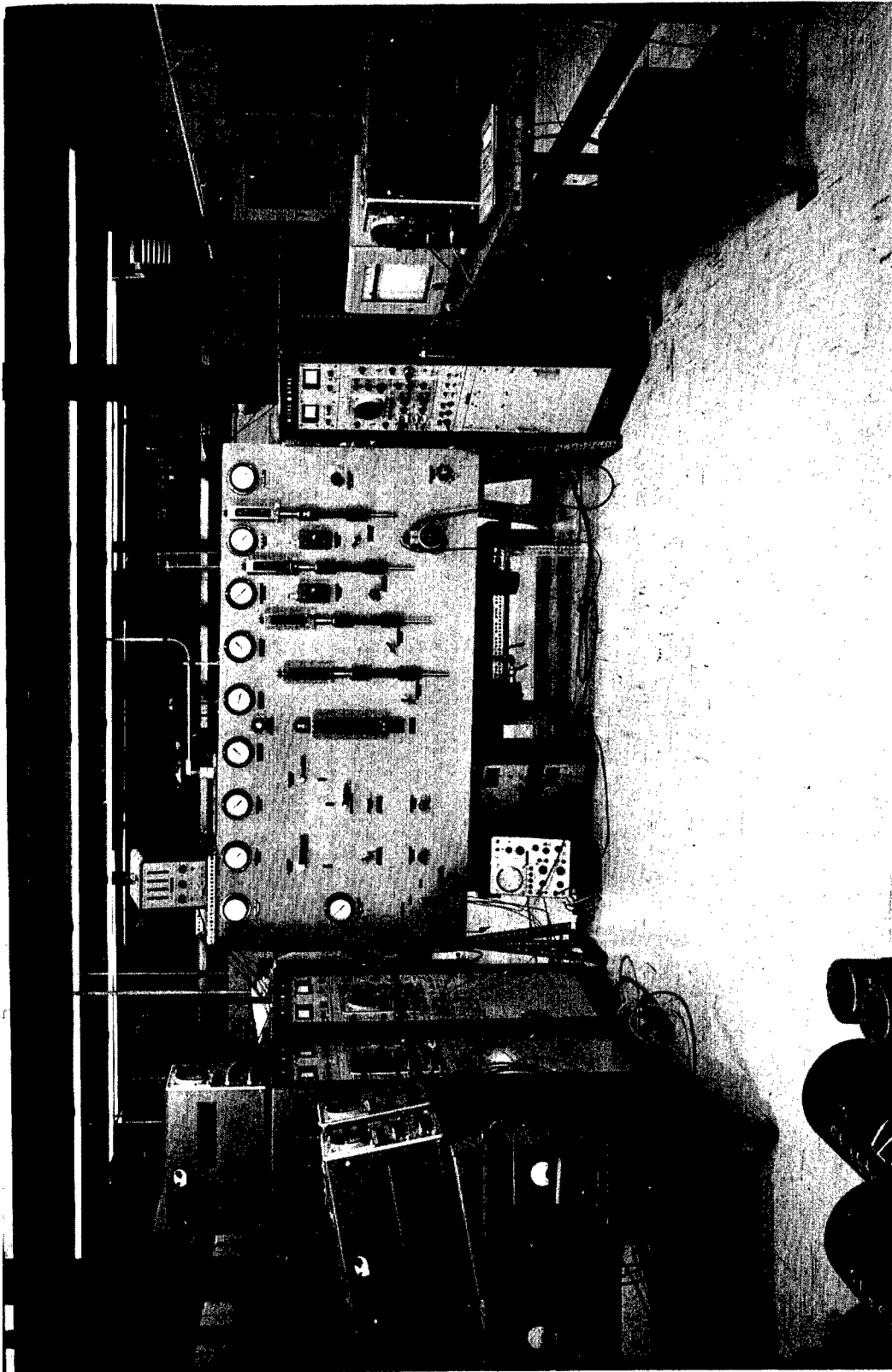


Fig. IV-2 - View Of Simulator Control Panel And Partial Set-Up
Of Bearing System Instrumentation Read-Out Equipment

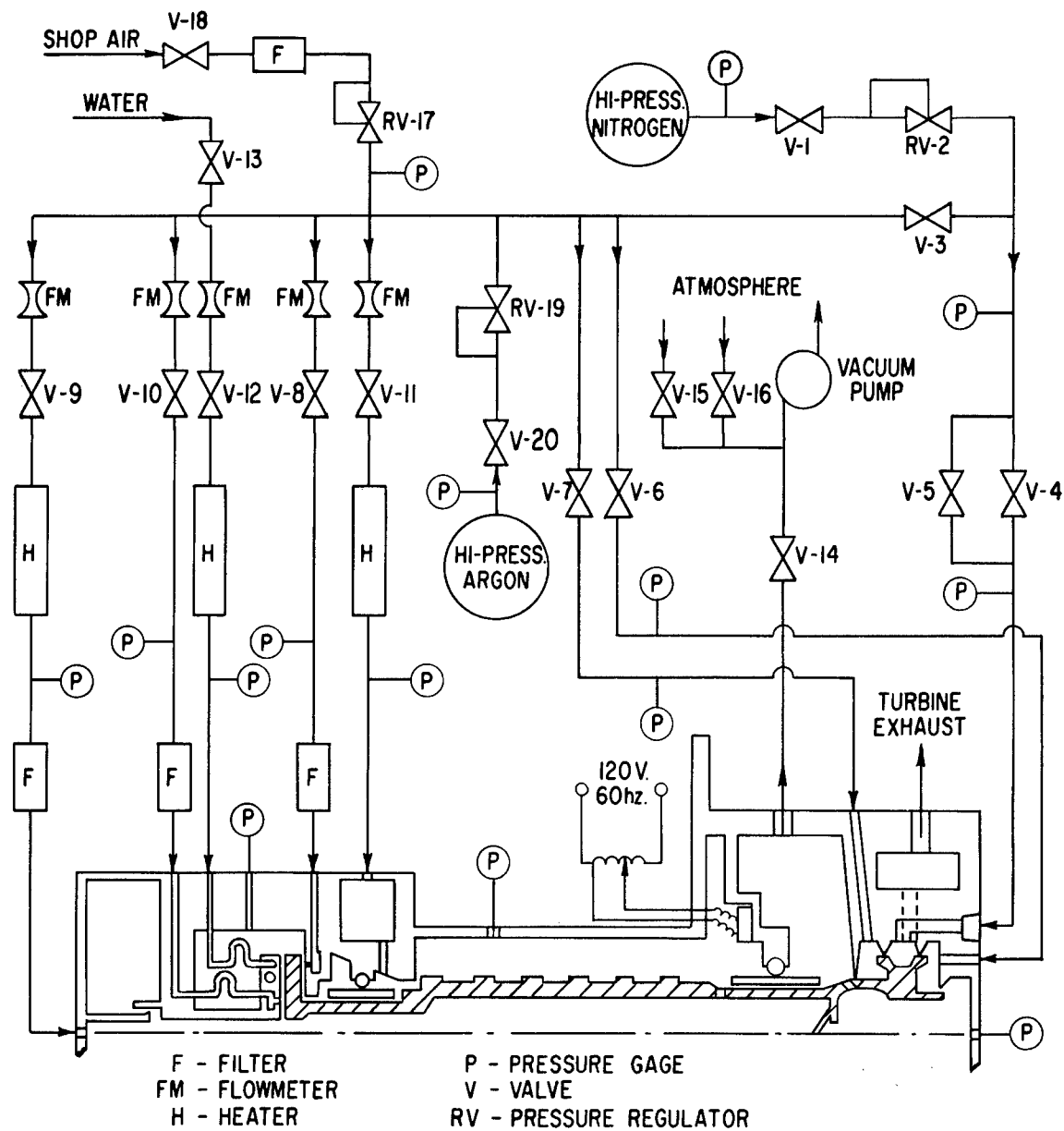


Fig. IV-3 - Schematic Diagram Of Simulator Control System

Evaluation of the Hydrodynamic Thrust Bearing

The same hydrodynamic thrust bearing was used throughout the simulator test program — no modifications to its design were required. During all tests, film thickness of the hydrodynamic thrust bearing was measured with three capacitance probes circumferentially spaced 90 degrees apart on a 1.834 inch base circle. As can be seen from the photograph of Figure II-16, the probes were located in the "seal" region of the hydrodynamic bearing.

Figure IV-4 is a plot of measured and calculated film thickness versus thrust load for the hydrodynamic thrust bearing at 50,000 rpm. The test data were obtained with the axis of the simulator rotor inclined 7.5 degrees from the horizontal and at bearing ambient pressures of 7.5 and 12.2 psia. The film thickness data is based upon an average of the three probe readings. However, individual probe readings clearly indicated that the forward thrust stator was misaligned from the thrust runner by about 0.00035 radians at low loads and by about 0.00015 radians at the highest loads. This decrease in misalignment with increasing load is a demonstration of the self-aligning capability of the forward thrust stator due to the flexure mounting arrangement which was provided for this bearing.

The thrust load data shown on Figure IV-4 was calculated using measurements of pressure acting on the forward and reverse thrust-loading faces of the drive turbine (see Figure III-1) and subtracting out the component of rotor weight due to the 7.5 degree inclination of the rotor. All other internal differential areas of the simulator were vented to bearing ambient pressure and, hence, contributed no thrust forces.

It is seen from Figure IV-4 that there is quite good agreement between the calculated and measured plots of load versus film thickness, particularly at the design load of 24 pounds where the agreement is essentially exact. The test data show, as predicted by theory, that the load capacity of the bearing is not significantly effected by ambient pressure from 7.5 to 12.2 psia.

The hydrodynamic thrust bearing was evaluated at speeds from 30,000 to 60,000 rpm. Performance over this range of speeds was excellent. Figure IV-5 is a comparison of measured and calculated thrust bearing film thickness versus load at 30,000 rpm for ambient pressures of 9.9 and 11.75 psia. Like the data at 50,000 rpm, it is seen that good agreement exists between calculated and measured performance.

Throughout the simulator test program, dynamic once-per-rev runout of the thrust runner, as measured with the capacitance probes, was approximately 0.07 mils with residual rotor unbalance and 0.09 mils with 0.002 ounce-inches additional unbalance in the turbine plane. This can be seen from Figure IV-6 which shows oscilloscope photographs of the three thrust bearing capacitance probe traces taken at 50,000 rpm during the second simulator acceptance test. (The photos for test run No. 252 correspond to residual rotor unbalance, while the photos for test run No. 236 correspond to 0.002 ounce-inches additional unbalance in the turbine plane.) Since the ratio of thrust bearing OD to capacitance probe base circle diameter was 1.77, the actual runout of the thrust runner at its OD was about 0.124 mils with residual unbalance and 0.159 mils with the additional unbalance. Based on rotor inspection records of squareness of the thrust runner mounting face to the centerline of the journals, the TIR at the OD of the thrust runner should have measured 0.104 mils. Hence, there is quite good agreement in thrust bearing runout based on static inspection room measurements and dynamic (50,000 rpm) capacitance probe measurements.

It is clearly seen from Figure IV-6 that the thrust bearing runout displacements, as measured by probes No. 2 and 4, are 180 degrees out of phase. This is a further confirmation that the oscilloscope traces are showing thrust bearing runout, rather than axial displacement of the whole rotor, since probes 2 and 4 were 180 degrees circumferentially displaced from each other as illustrated in Figure II-16.

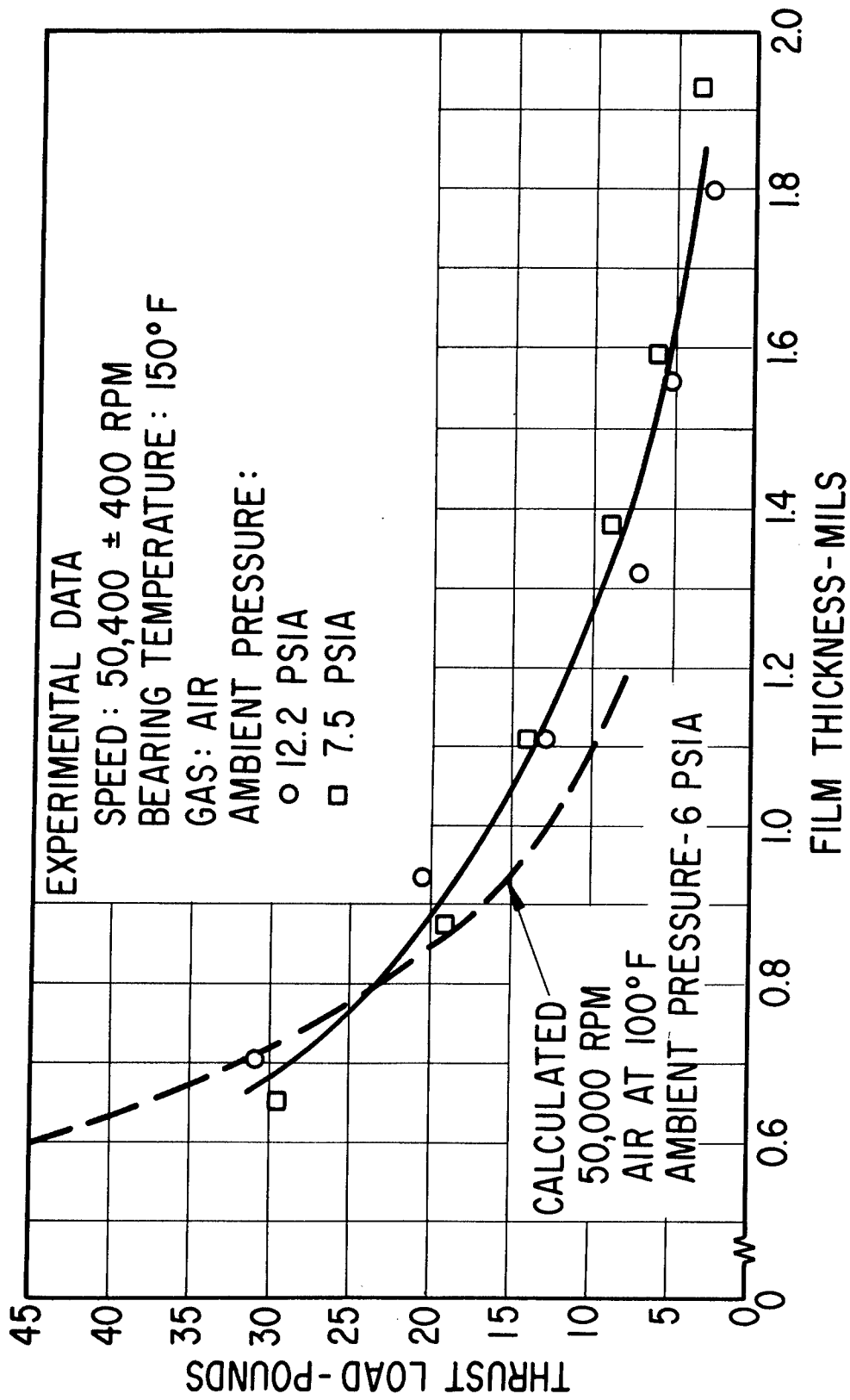


Fig. IV-4 - Measured and Calculated Load Versus Film Thickness Data For The Forward Hydrodynamic Thrust Bearing At 50,400 RPM

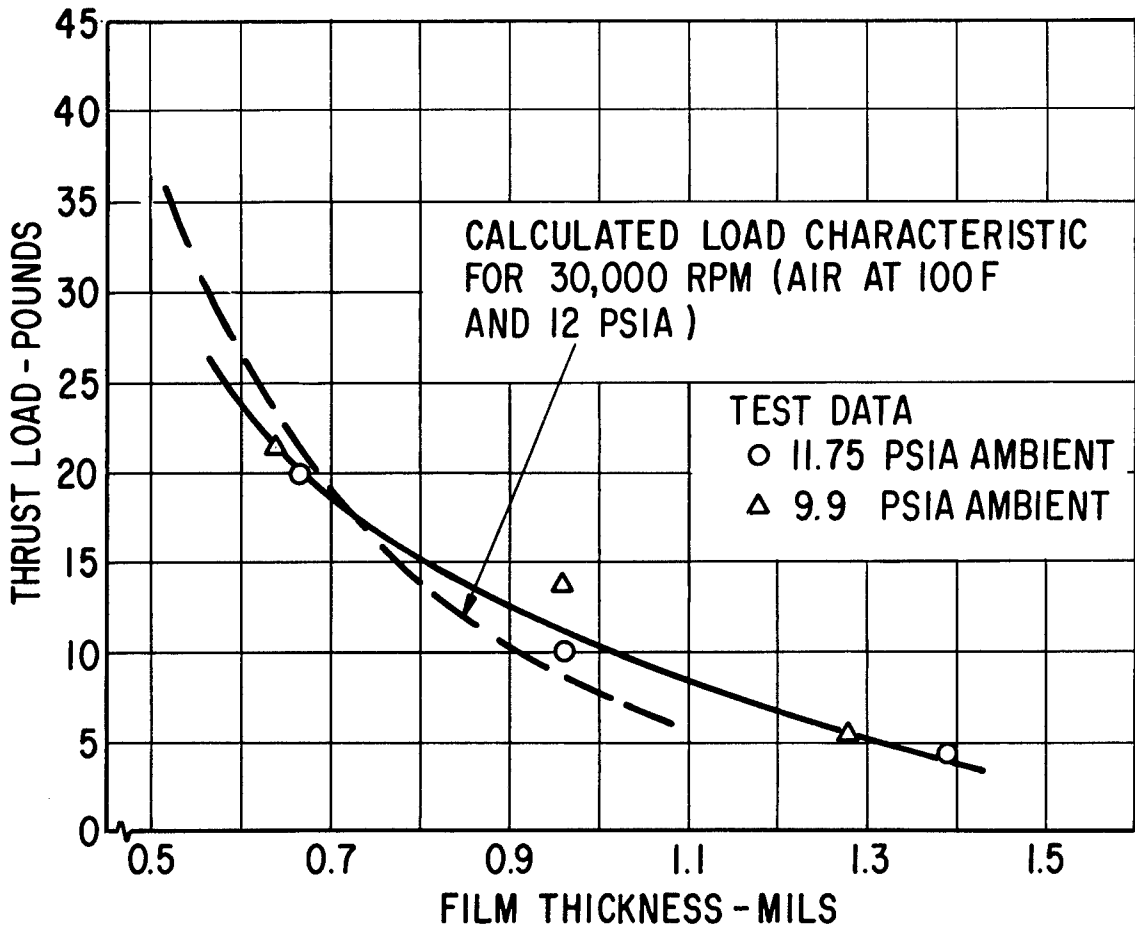
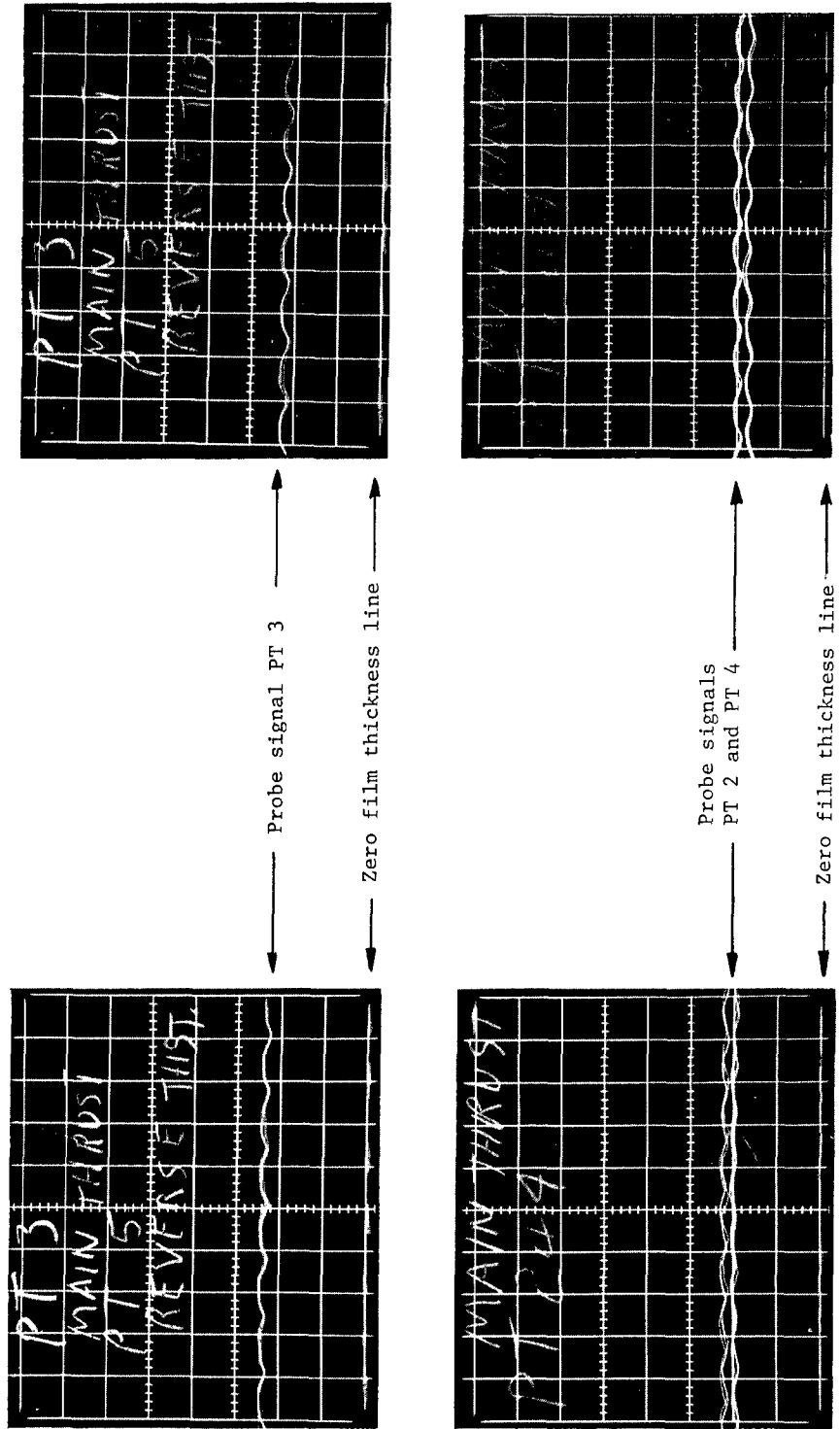


Fig. IV-5 - Measured And Calculated Load Versus Film Thickness
 Data For The Forward Hydrodynamic Thrust Bearing At
 30,100 RPM



Test Run 236
Residual Plus 0.002 oz.-in.
Unbalance In Turbine Plane

Test Run 252
Residual Rotor Unbalance

Oscilloscope Calibration

Vertical - 0.5 mil per major grid division
Horizontal - 1.0 millisecond per major grid division

Fig. IV-6 - Thrust Bearing Capacitance Probe Traces Taken At 50,000 RPM

Test Evaluation of the Forward Hydrostatic Thrust Bearing

Test data for the forward hydrostatic thrust bearing is presented in Figure IV-7. The plotted curve was obtained from a "bench" test in which the thrust runner was disassembled from the rotor and allowed to freely float on the thrust stator. Weights of 50, 75 and 100 pounds were then suspended from the hole through the ID of the bearing to obtain the desired calibration loads. This, of course, was the optimum set-up condition for the bearing, since the runner was completely free to seek its position of minimum misalignment and, hence, maximum load capacity.

Also plotted on Figure IV-7 are two test points taken during the initial acceptance test of the forward hydrostatic thrust bearing (with 5 supply orifices). These points, obtained at rotor speeds of 40,000 and 50,000 rpm, confirm the zero speed calibration data taken during the bench tests.

The calculated design-point condition for the forward hydrostatic thrust bearing is also plotted on Figure IV-7. It is seen that all of the test data exceed the calculated design-point clearance. This is probably due to a conservative assumption used for the calculated point — namely, the OD of the hydrostatic bearing was assumed to be the same as the root diameter of the spiral grooves for the hydrodynamic bearing. The higher values of measured load capacity indicate that hydrostatic pressurization probably did exist, to some extent, across the spiral-grooved section of the hydrodynamic bearing.

At no time during any of the three acceptance tests performed on the rotor-bearing simulator was pneumatic hammer of the forward hydrostatic thrust bearing observed. (Pneumatic hammer was, however, observed with the initial design of the forward hydrostatic thrust bearing which had 20 hydrostatic supply orifices. This instability is discussed in Appendix C of this report. The instability was eliminated by reducing the number of supply orifices from 20 to 5.)

Test Evaluation of the Reverse Hydrostatic Thrust Bearing

Figure IV-8 shows test data obtained for the reverse hydrostatic thrust bearing. This data was obtained with the thrust runner assembled to the rotor and the simulator oriented vertically with the turbine-end down. Thrust loads were applied by pressurizing the reverse thrust-loading face of the drive turbine.

Also shown on Figure IV-8 is one of the test points taken during the initial acceptance tests of the reverse hydrostatic thrust bearing. It is seen that the load capacity of the reverse bearing under the acceptance test conditions is less than the static calibrations obtained at non-rotating conditions and 14.7 psia ambient pressure. The reason for this measured difference in film thickness at approximately 50 pounds thrust load is not apparent from the test data. Nonetheless, the measured film clearance of approximately 1.0 mil at the acceptance test condition is quite adequate for safe continuous operation of the machine at 50 pounds reverse thrust load.

The calculated design-point condition for the reverse hydrostatic thrust bearing is also plotted on Figure IV-8. It is seen that the non-rotating calibration data fall slightly short of the calculated design-point clearance. Again, the reason for this slight discrepancy in film thickness is not immediately apparent from the test data.

Throughout the simulator test program, no evidence of pneumatic hammer of the reverse thrust bearing was detected.

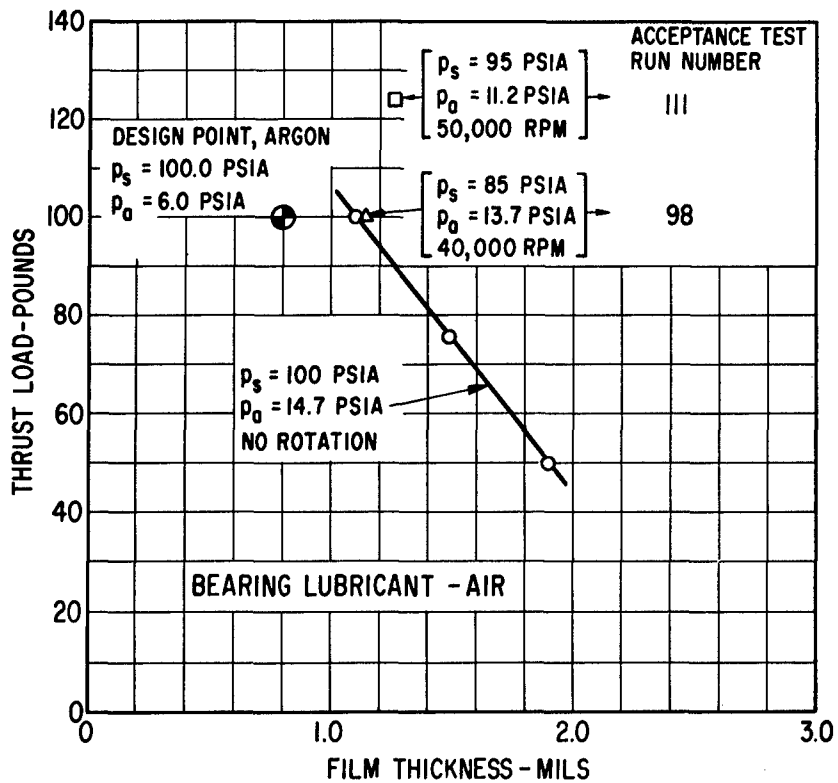


Fig. IV-7 - Measured Load Versus Film Thickness Data For The Forward Hydrostatic Thrust Bearing

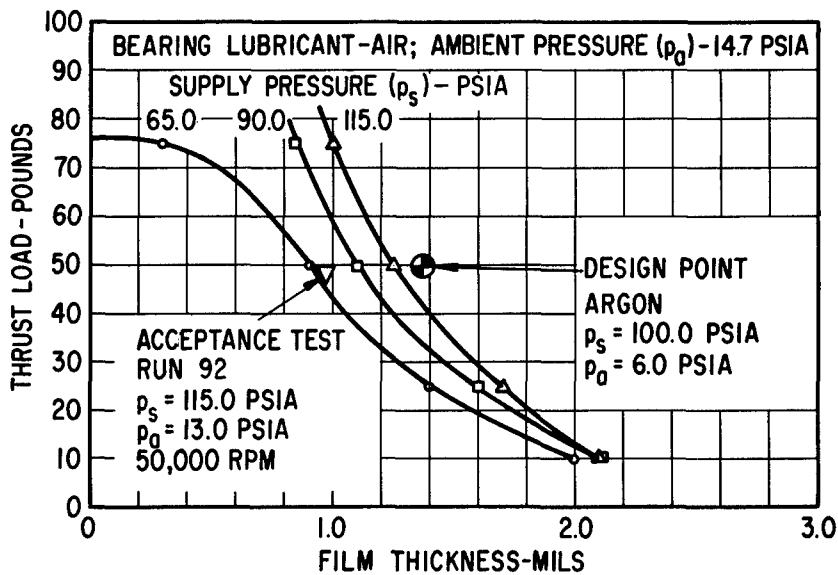


Fig. IV-8 - Measured Load Versus Film Thickness Data For The Reverse Hydrostatic Thrust Bearing

Test Evaluation of the No. 1 Journal Bearing

The design values of stiffness for the "upper" and "lower" pivot-support flexures for the No. 1 journal bearing were 10,000 and 63,000 lb./in. respectively. Experimental load-deflection data, plotted in Figures C-20 and D-13, show that the actual values of stiffness for the upper and lower flexures were 9,800 and 50,000 lb./in. respectively. The discrepancy between design and measured values of flexure stiffness is believed to be due to "non-ideal" boundary conditions which exist at the ends of the flexure sections. For the purposes of design, a zero-slope boundary condition was assumed at the ends of the two beam sections of which each flexure is comprised. In actual fact, this assumption was probably somewhat in error due to (1) some deflection of the thicker central portion of the flexure (which carries the pivot screw), and (2) some deflection within the clamping zone at the two ends of the flexure.

For the second simulator acceptance test, the No. 1 journal bearing was set up with a zero-speed room temperature diametral clearance between 0.79 to 0.85 mils. Neither this set-up clearance, nor any other facet of the No. 1 bearing design, was changed between the acceptance tests for the second and final bearing system designs.

Figure IV-9 shows a comparison of measured pivot film thickness for the No. 1 bearing at 50,000 and 60,000 rpm with calculated values of film thickness. The measured data were obtained during the second simulator acceptance test (test runs No. 243 and 244). The test condition was horizontal operation in air at an ambient pressure of 12.0 psia. Measured temperatures of the No. 1 bearing pads and bearing housing were 170 and 165 F respectively.

The calculated film thickness curves drawn on Figure IV-9 are based on the measured values of upper and lower flexure stiffness, the actual zero-speed set-up clearance of the bearing, the measured values of pad and housing temperature, and include the effects of journal centrifugal growth (which is 0.35 and 0.50 mils radially at 50,000 and 60,000 rpm respectively). The other design parameters for the bearing are the same as given in Table II-1 (Section II of this report).

It is seen from Figure IV-9 that the measured and calculated values of pivot film thickness are in fairly close agreement, with the measured films being somewhat larger than the calculated films.

Figures IV-10 and IV-11 are oscilloscope time-base traces of the pad-to-shaft capacitance probe signals for the No. 1 journal bearing taken during test runs 258 and 239, respectively, of the second simulator acceptance test. (See Figure II-27 for location of the various No. 1 bearing capacitance probes.) The test conditions for these runs were as follows:

	Test No. 239 (Fig. IV-11)	Test No. 258 (Fig. IV-10)
Gas	Air	Air
Ambient pressure - psia	10.5	10.9
Rotor Orientation	Horizontal	Horizontal
Speed - rpm	50,730	50,500
Rotor Unbalance Condition	Residual plus 0.002 ounce-inches unbalance added to turbine plane	Residual

The significant difference between test runs 239 and 258 was the condition of rotor unbalance. Whereas there is virtually no once-per-rev relative pad-to-shaft motion indicated on the traces of Figure IV-10, the addition of unbalance in the turbine plane produced definite once-per-rev relative motions (particularly for the upper or unloaded pads) as shown in Figure IV-11. The fact that the relative motion traces for the upper pads show a larger dynamic amplitude than do those for the lower pads may be due to a slight resonance of the upper pad-flexure assemblies due to the unbalance excitation. The resonant frequency of the upper pad assemblies, while considerably above 50,000 rpm, is significantly lower than that of the lower pad assemblies due to the lower stiffness value of the upper flexures. Hence the upper assemblies would be more responsive to a 50,000 rpm excitation than would the lower assemblies. From the standpoint of adequate film thickness, the effect of the additional unbalance is of no concern whatsoever.

Figure IV-12 shows oscilloscope photographs of the No. 1 journal orbit during test runs 258 and 239 as measured by "X and Y" capacitance probes mounted on the No. 1 bearing housing. The fuzziness of the bearing orbits is due to the fact that only half the detection area of the X and Y displacement capacitance probes was actually exposed to the No. 1 journal surface. The other half of the probe faces were exposed to an irregular chrome oxide radius which caused a high-frequency low-amplitude noise signal to be superimposed on the primary signal. The fuzziness is a result of this high-frequency hash. It is seen that there appears to be only a slight, if any, increase in the orbit for run 239 relative to run 258. This would seem to confirm that the upper pad-to-shaft traces of Figure IV-11 show primarily vibration of the pad-flexure assemblies rather than journal motion. However, the orbit traces of Figure IV-12 are too fuzzy to analytically confirm this conclusion.

Figure IV-13 shows three oscilloscope photographs of the No. 1 journal orbit as follows:

<u>Test Run</u>	<u>Speed - rpm</u>	<u>Rotor Balance Condition</u>
264	49,800	Residual unbalance only
265	59,800	Residual unbalance only
242	60,100	Residual plus 0.002 ounce-inches unbalance added to the turbine plane

It is seen from Figure IV-13 that, regardless of the condition of rotor unbalance, the orbit diameter of the No. 1 journal almost doubles from 50,000 to 60,000 rpm. This is due to the influence of the 93,000 rpm third critical speed resonance mode which is the fundamental free-free (i.e., rotor bending) mode. It is quite probable that the residual unbalance orbits could have been considerably reduced from those shown in Figure IV-13 by utilizing a three-plane rotor balancing technique rather than the simpler two-plane technique which was actually used.

Throughout the simulator test program, performance of the No. 1 bearing was excellent. At no time was any tendency or evidence of either rotor or pad

instability detected. The correlation between measured and calculated film clearances shown in Figure IV-9 gives assurance that operation in argon will be essentially as predicted in Figures II-1 and II-2.

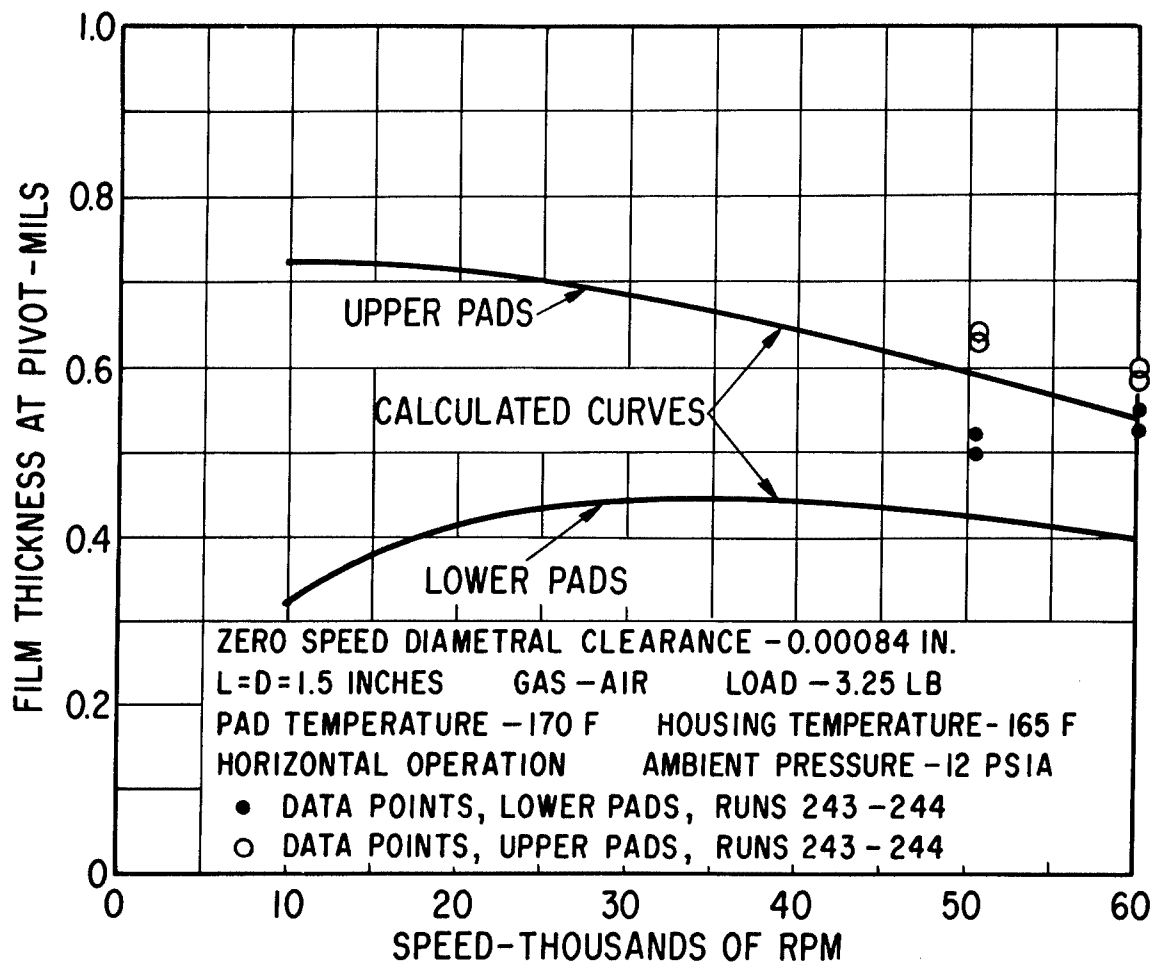
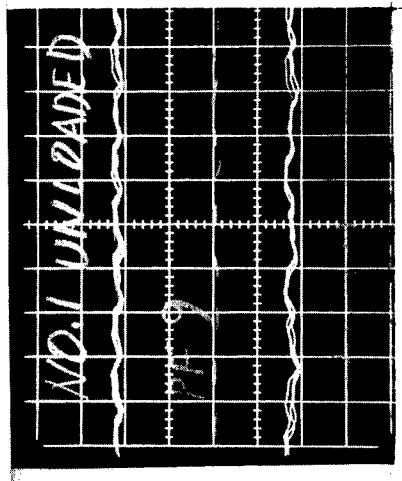
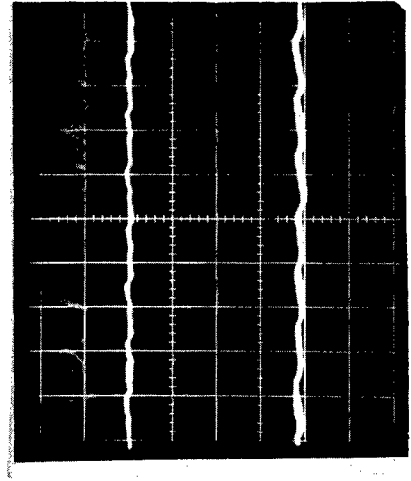


Fig. IV-9 - Comparison Of Measured And Calculated Pad Pivot Film Thickness For The No. 1 Journal Bearing Operating In Air At 12.0 PSIA With The Rotor Horizontal



Unloaded Pads



Loaded Pads

Probe Signal PF-9

Zero film for PF-9

Probe signal PF-10

Zero film for PF-10

Test Run 258

Rotor horizontal
Ambient - air at 10.9 psia

Oscilloscope Calibration

Vertical - 0.25 mil per major grid division
Horizontal - 1.0 millisecond per major grid division

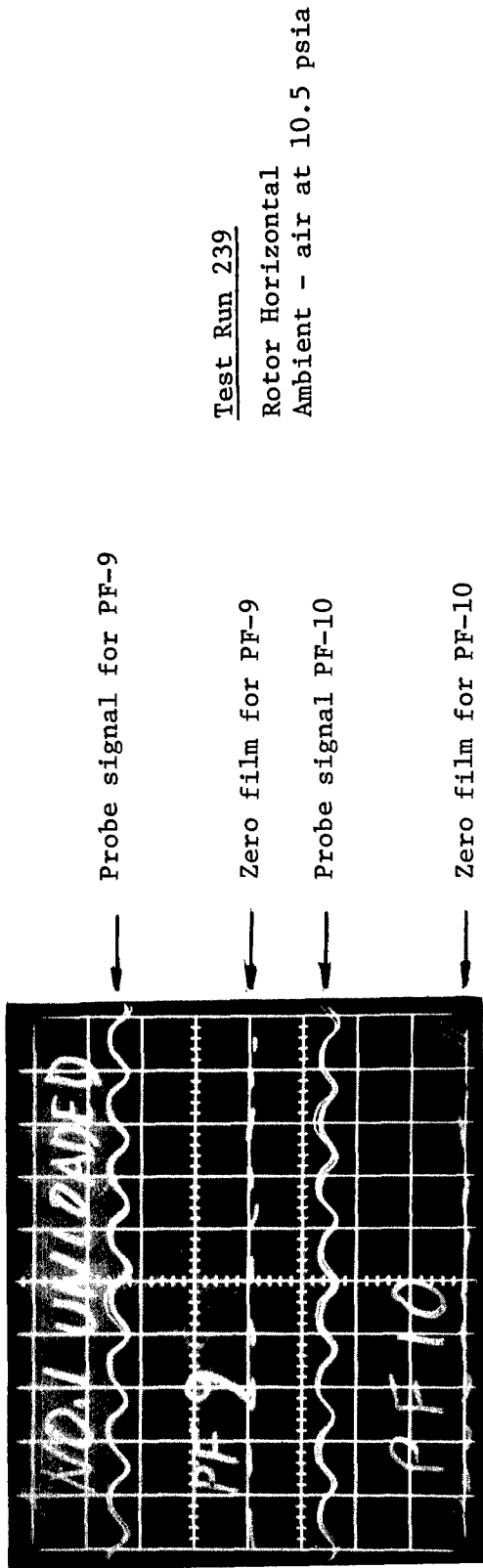
Probe signal PF-8

Zero film for PF-8

Probe signal PF-11

Zero film for PF-11

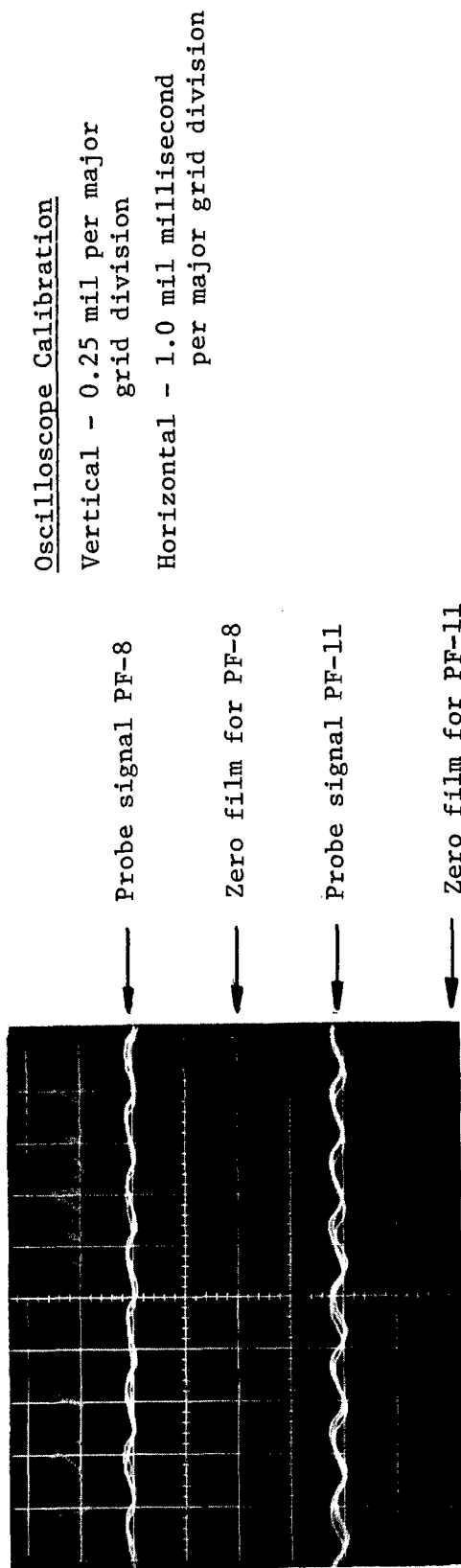
Fig. IV-10 - Oscilloscope Time-Base Traces Of Pad-To-Shaft Capacitance Probe Signals For No. 1 Journal Bearing — Taken At 50,500 RPM With Only Residual Rotor Unbalance



Test Run 239

Rotor Horizontal
Ambient - air at 10.5 psia

Unloaded Pads



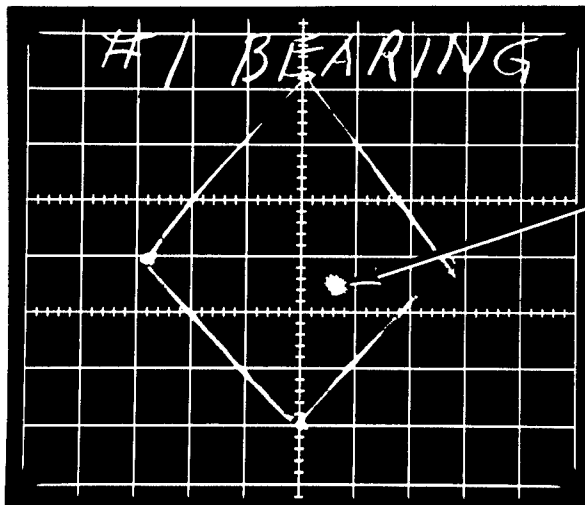
Oscilloscope Calibration

Vertical - 0.25 mil per major grid division

Horizontal - 1.0 mil millisecond per major grid division

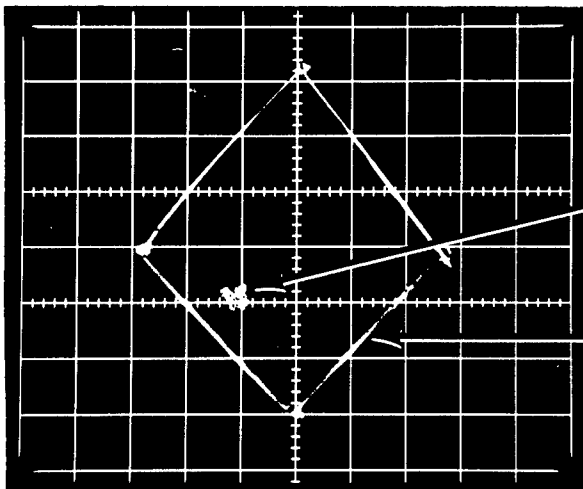
Loaded Pads

Fig. IV-11 - Oscilloscope Time-Base Traces Of Pad-To-Shaft Capacitance Probe Signals For No. 1 Journal Bearing — Taken At 50,730 RPM With 0.002 Ounce-Inches Of Unbalance Added To Turbine Plane



Test Run 258
Residual Rotor Unbalance

Note: There is no relationship between location of the orbits and the zero-speed clearance squares.

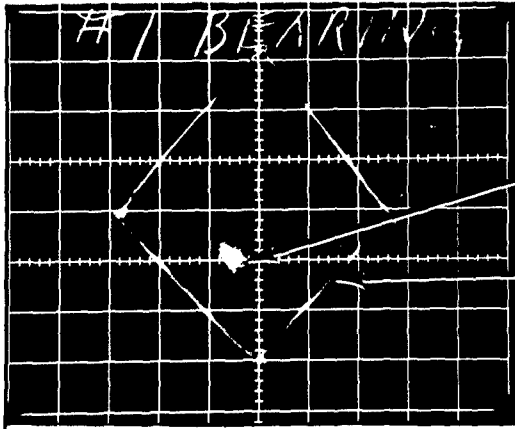


Test Run 239
Residual Plus 0.002 oz.-in.
Unbalance In Turbine Plane

Oscilloscope Calibration

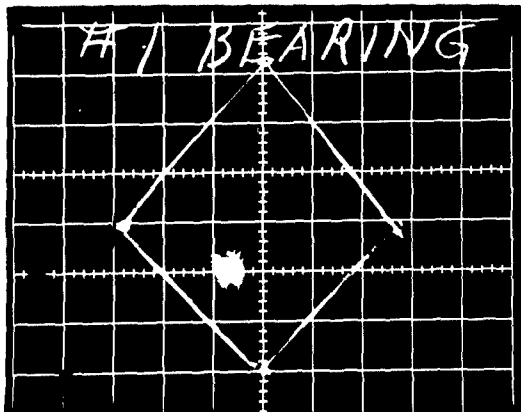
Vertical and Horizontal - 0.5
mils per major grid division

Fig. IV-12 - Oscilloscope Traces Of The No. 1 Journal Orbit At An Average Speed Of 50,600 RPM Showing Effect Of Adding 0.002 Ounce-Inches Of Turbine Unbalance On Journal Response



Test Run 264
49,800 RPM, Residual Unbalance

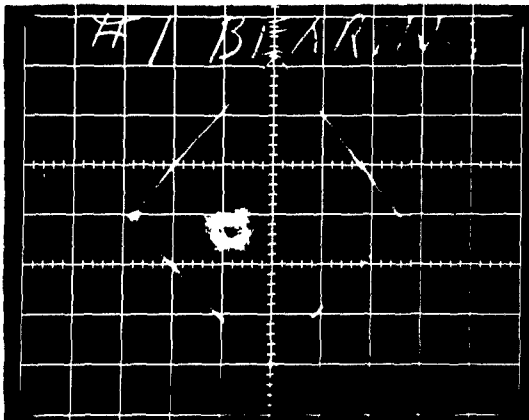
Note: There is no relationship between location of the orbits and the zero-speed clearance squares.



Test Run 265
59,800 RPM, Residual Unbalance

Oscilloscope Calibration

Vertical and Horizontal -
0.5 mils per major grid
division



Test Run 242
60,100 RPM, Residual Plus
0.002 oz.-in. Unbalance In
Turbine Plane

Fig. IV-13 - Oscilloscope Traces Of The No. 1 Journal Orbit
Showing Effect Of Increasing Speed From 50,000
To 60,000 RPM On Journal Response

Test Evaluation of the No. 2 Journal Bearing

The design values of stiffness for the "upper" and "lower" pivot-support flexures for the No. 2 journal bearing were 10,000 and 100,000 lb./in. respectively. Experimental load-deflection data, plotted in Figures C-19 and D-13, show that the actual values of stiffness for the upper and lower flexures were 8,400 and 70,000 lb./in. respectively. The probable reasons for the discrepancy between design and measured values are the same as mentioned in the preceding subsection with respect to the No. 1 flexures.

For the third, or final, simulator acceptance test and rotor-whirl investigation, the No. 2 journal bearing was set up with a zero-speed room temperature diametral clearance between 1.1 and 1.2 mils. This, incidentally, was the same clearance used for the second simulator acceptance test. In fact, the only change made to the No. 2 bearing between the second and final acceptance tests was a reduction in the mass and roll inertia of each of the No. 2 pivoted-pads as documented in Table D-1 (Appendix D).

Figure IV-14 shows a comparison of measured pivot film thickness for the No. 2 bearing at 50,000 and 60,000 rpm with calculated values of film thickness. The measured data were obtained during the second simulator acceptance test (test runs No. 243 and 244). The test condition was horizontal operation in air at an ambient pressure of 12.0 psia. Measured temperatures of the No. 2 bearing pads and bearing housing were 207 and 165 F respectively.

The calculated film thickness curves of Figure IV-14 are based on the measured values of upper and lower flexure stiffness, the actual zero-speed set-up clearance, the measured values of pad and housing temperature, and include the effects of journal centrifugal growth (which is 0.44 and 0.62 mils radially at 50,000 and 60,000 rpm respectively). It is seen from Figure IV-14 that the measured and calculated values of pivot film thickness are in fairly close agreement, with the measured films being, for the most part, slightly larger than the calculated films.

Figures IV-15 through IV-17 are plots of measured and calculated pivot film thickness for the final design of the No. 2 bearing (i.e., with the mass of the No. 2 pads reduced relative to the conditions of Figure IV-14). The measured data points on Figures IV-15 through IV-17 were all obtained just prior to the onset of a low-frequency rotor whirl condition which is discussed in a following subsection. The test conditions are fully noted on the figures. Again it is seen that fairly good agreement exists between the measured and calculated data. However, it is interesting to note that for the whirl onset condition, the measured films are all slightly smaller than the calculated films, which is the opposite of the data shown in Figures IV-9 and IV-14. It is not clear at this time whether there is any particular significance to this observation.

Figures IV-18 and IV-19 are oscilloscope time-base traces of the pad-to-shaft capacitance probe signals for the No. 2 journal bearing taken during test runs 302 and 306, respectively, of the final simulator acceptance test. The test conditions for these runs were as follows:

	Test No. 302 (Fig. IV-18)	Test No. 306 (Fig. IV-19)
Gas	Air	Air
Ambient pressure, psia	12.6	12.6
Rotor orientation	Vertical	Vertical
Speed - rpm	50,120	49,670
Rotor unbalance condition	Residual	Residual plus 0.002 ounce-inches unbalance added to the turbine plane

The principle difference between test runs 302 and 306 was the condition of rotor unbalance. It is seen from Figures IV-18 and IV-19 that there is a small increase in the amplitudes of the dynamic relative motions between the pads and the No. 2 journal due to the addition of turbine unbalance in test run 306. Of more significance, however, is the presence of a strong two-per-rev vibration in the relative motion signals of the two "upper" or "unloaded" pad-to-shaft probes. This

vibration was found to be due to the upper pad-flexure assemblies having a resonant frequency in the vicinity of 100,000 rpm. This resonance is discussed in more detail in the next subsection.

Figure IV-20 shows three oscilloscope photographs of the No. 2 pad-to-shaft capacitance probe signals taken during test run 258 of the second simulator acceptance test. The test conditions were simulator horizontal, 50,500 rpm, residual unbalance only, and ambient air pressure of 10.9 psia. In addition to the four pad-to-shaft probes located near the pivot point (probes PF-20, PF-21, PR-22, and PF-23), traces from a fifth pad-to-shaft probe (PR-24) and a housing-to-pad probe (PP-25) are also shown. (Location of these various capacitance probes within the No. 2 bearing is shown in Figure II-29.) Again, pivot probes PF-21 and 22 in the two upper pads show evidence of the pad-flexure resonant vibration frequency. It is interesting to note that the trace from probe PR-24, which is mounted in the same pad as PF-21, contains considerably more once-per-rev content (in addition to an obvious content of two-per-rev vibration) than does the PF-21 trace. Since PR-24 was located slightly more than twice the distance from the pivot as was PF-21 (see Figure II-28), this would indicate that a slight once-per-rev roll vibration of the pad may have also been occurring.

Figure IV-21 shows four oscilloscope photographs of the No. 2 journal orbit as measured by "X and Y" probes PS-26 and 27 mounted on the No. 2 bearing housing. The following conditions are represented in Figure IV-21:

<u>Test Run</u>	<u>Speed -rpm</u>	<u>Rotor Balance Condition</u>
252	49,700	Residual unbalance only
239	50,730	Residual plus 0.002 ounce-inches unbalance added to the turbine plane
263	60,800	Residual unbalance only
240	60,600	Residual plus 0.002 ounce-inches unbalance added to the turbine plane

It is seen from Figure IV-21 that the No. 2 journal orbit is definitely increased by the addition of turbine unbalance at both 50,000 and 60,000 rpm. It is also

seen that regardless of the condition of rotor unbalance, the journal orbit almost doubles from 50,000 to 60,000 rpm. This is due to the influence of the 93,000 rpm. third critical speed resonance mode which is the fundamental free-free (i.e., rotor bending) mode. It is quite probable that the residual unbalance orbits could have been considerably reduced from those shown in Figure IV-21 by utilizing a three-plane rotor balancing technique rather than the simpler two-plane technique which was actually used.

Figure IV-22 shows three oscilloscope photographs of the No. 2 pad-to-shaft capacitance probe traces taken at 60,000 rpm during test runs 265 and 267 of the second simulator acceptance test. The test conditions were simulator vertical and 0.002 ounce-inches unbalance added to the turbine plane. (Refer to Figure II-29 and the previous discussion of Figure IV-20 for definition of the capacitance probe locations.) Relative to operation at 50,000 rpm (Figure IV-20) it is seen that the dynamic component of relative motion between the "lower" pads and the rotor is greater than between the "upper" pads and the rotor. There is also definite indication of two-per-rev vibration of the lower pad-flexure assemblies, probably due to excitation of the resonant frequency of the lower pad-flexure assemblies.

In spite of the various effects of rotor unbalance and pad-flexure assembly vibrations illustrated by Figures IV-18 through IV-22, operation of the No. 2 journal bearing was, at all times, satisfactory from the standpoint of film thickness at the pivot point. The correlation between measured and calculated film clearances shown in Figures IV-14 through IV-17 gives assurance that operation in argon will be essentially as predicted in Figures II-3 and II-4.

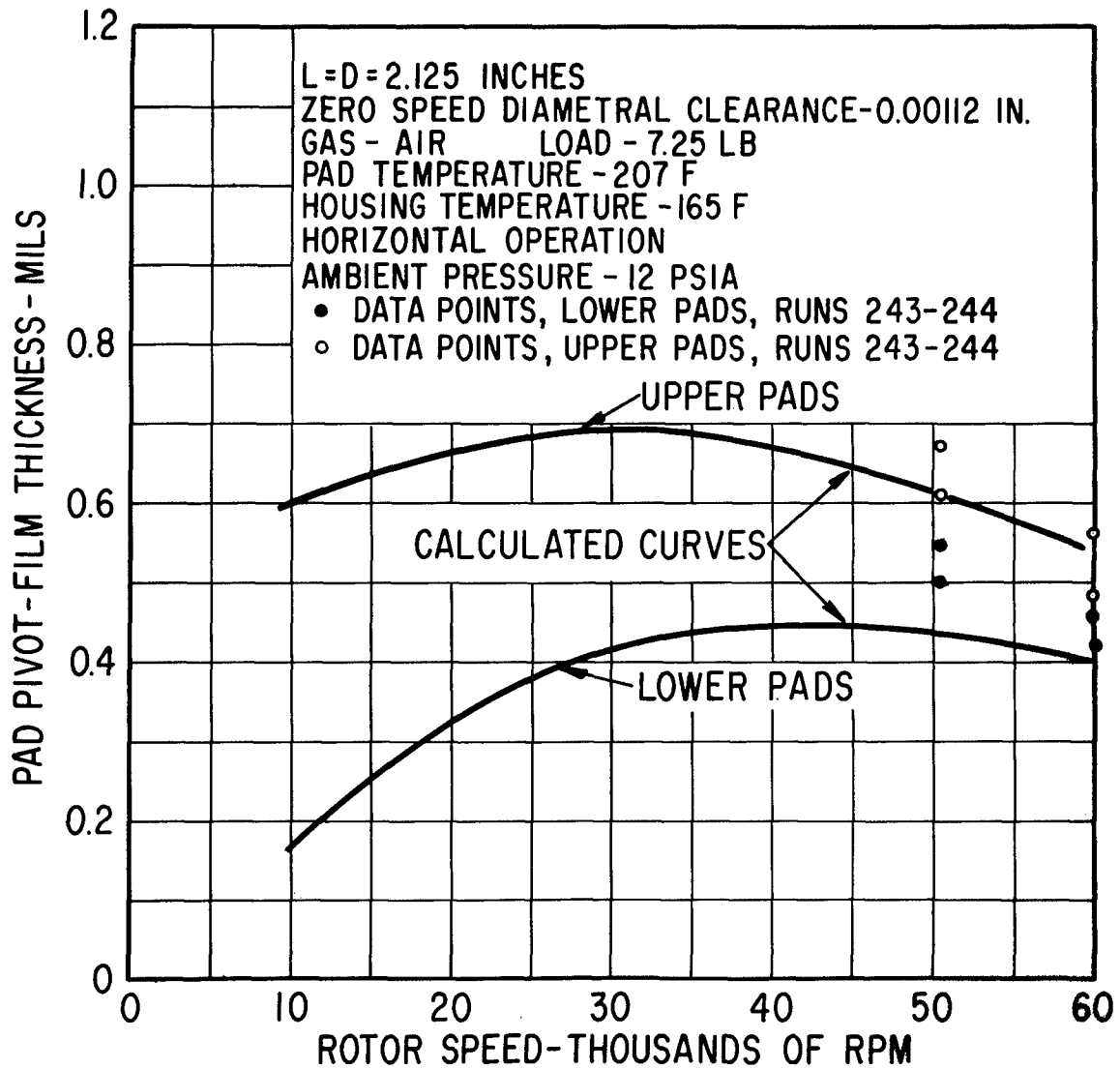


Fig. IV-14 - Comparison Of Measured And Calculated Pad Pivot Film Thickness For The Second No. 2 Journal Bearing Design Operating In Air At 12.0 PSIA With The Rotor Horizontal

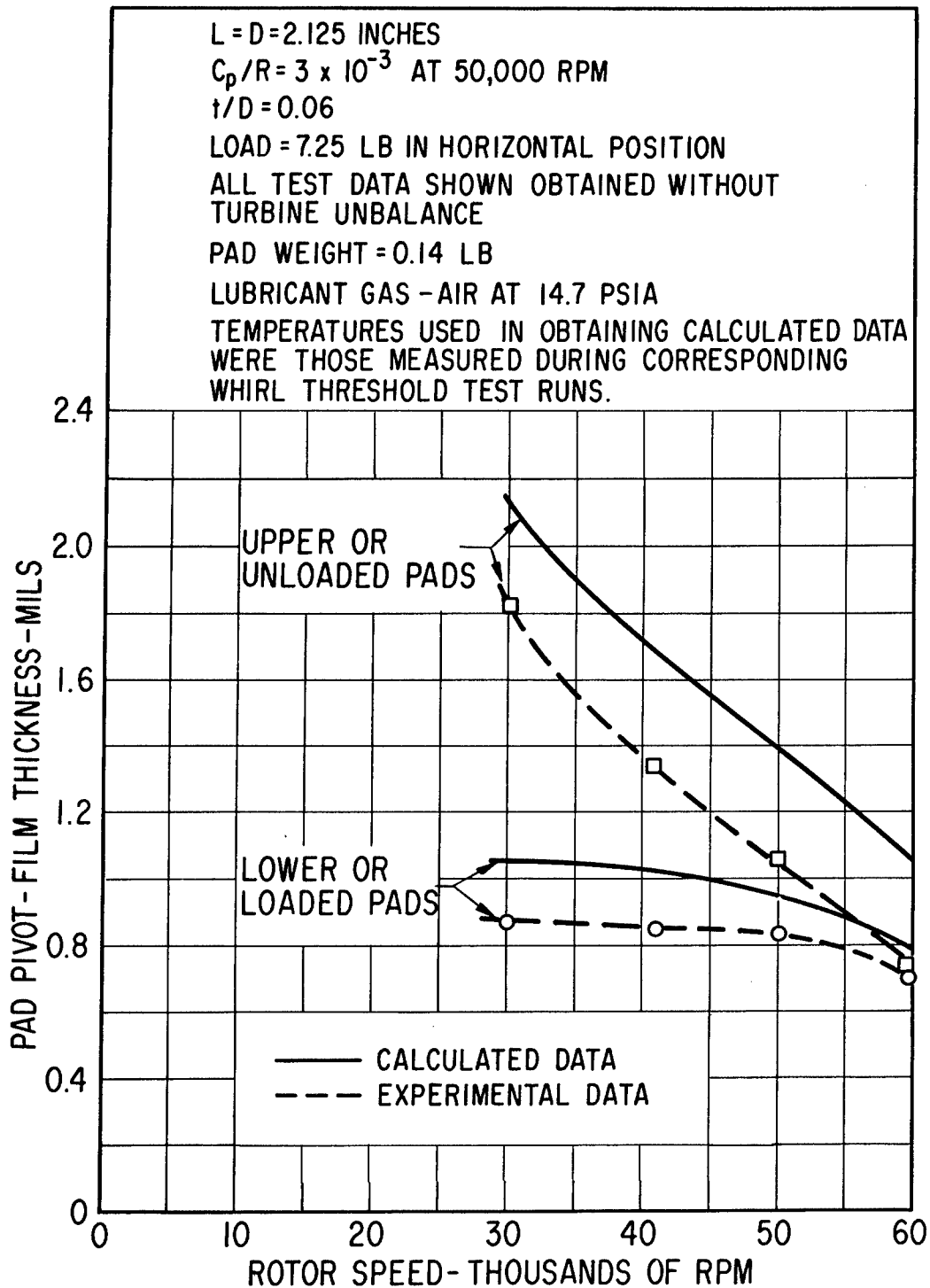


Fig. IV-15 - Comparison Of Measured And Calculated Pivot Film Thickness For The Final No. 2 Journal Bearing Design — Measured Data Taken At Threshold Of Rotor Whirl Condition (50,000 RPM, Rotor Horizontal, 14.7 PSIA Ambient)

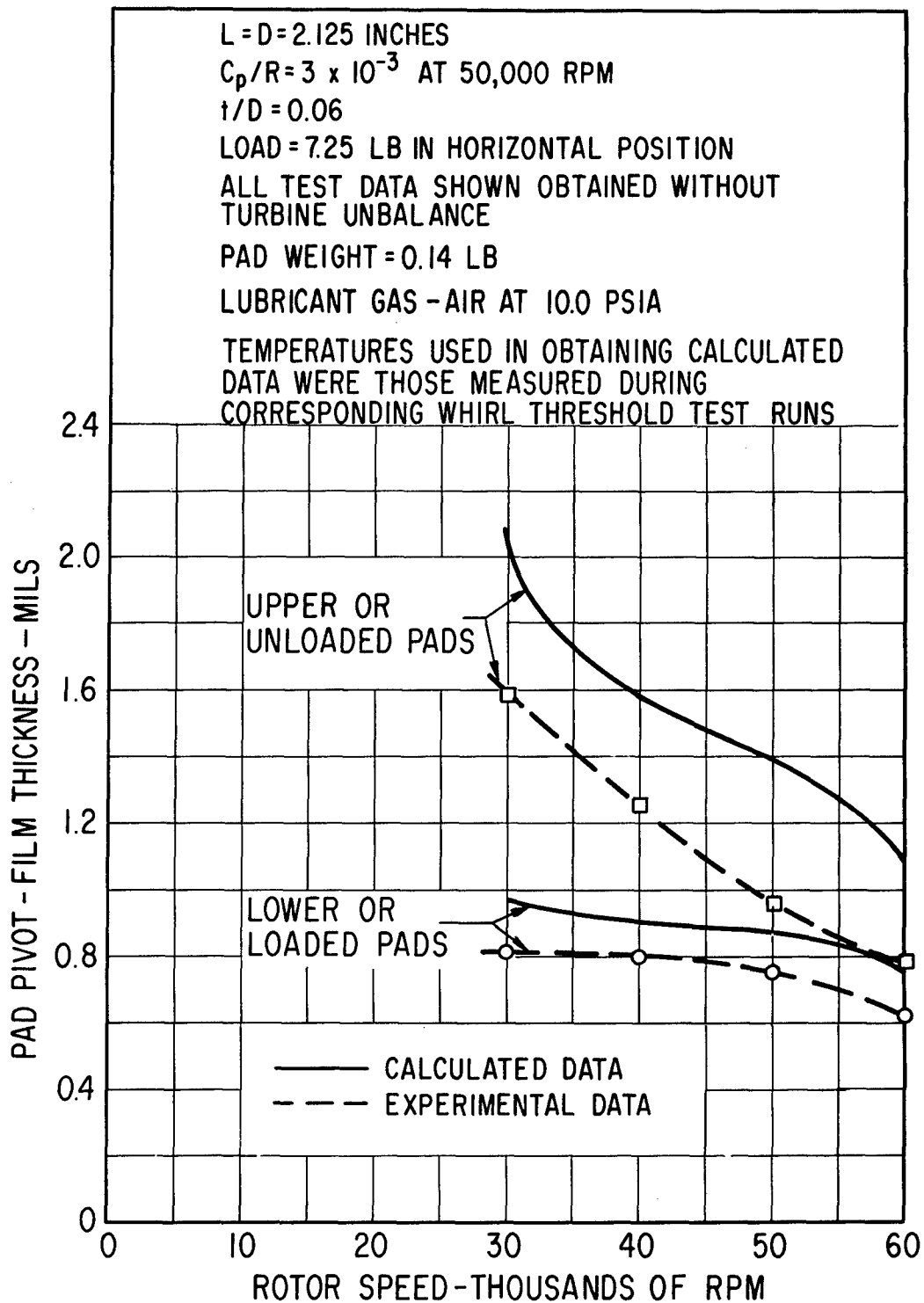


Fig. IV-16 - Comparison Of Measured And Calculated Pivot Film Thickness For The Final No. 2 Journal Bearing Design — Measured Data Taken At Threshold Of Rotor Whirl Condition (50,000 RPM, Rotor Horizontal, 10.0 PSIA Ambient)

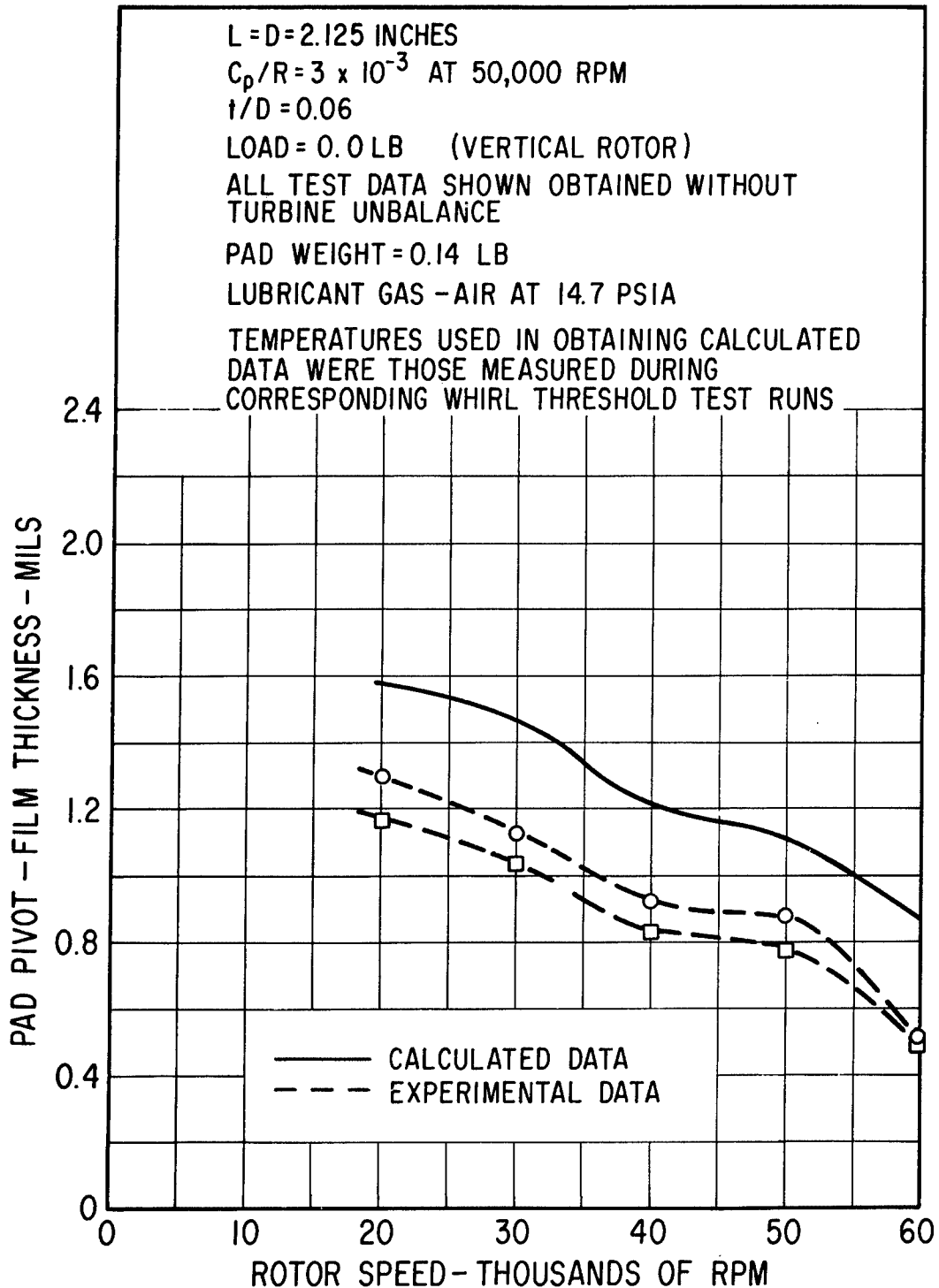
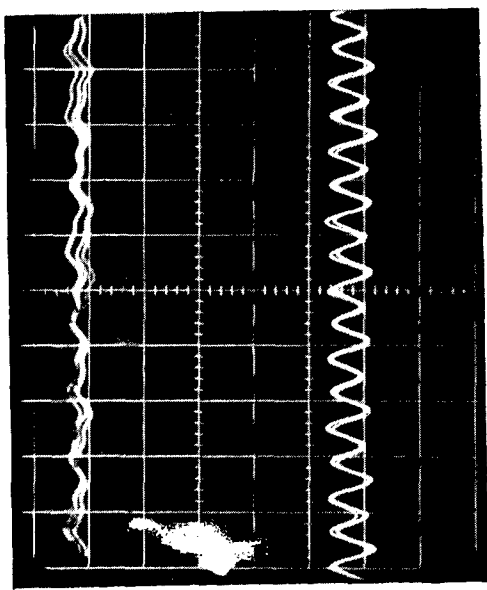
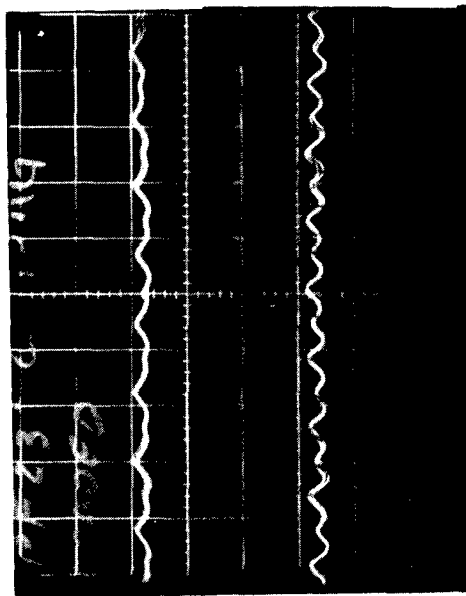


Fig. IV-17 - Comparison Of Measured And Calculated Pivot Film Thickness For The Final No. 2 Journal Bearing Design — Measured Data Taken At Threshold Of Rotor Whirl Condition (50,000 RPM, Rotor Vertical, 14.7 PSIA Ambient)



Test Run 302
Rotor Vertical, Air at 12.6 psia



→ Probe signal PF-23 (Lower Pad)

→ Zero film for PF-23

→ Probe signal PF-21 (Upper Pad)

→ Zero film for PF-21

Oscilloscope Calibrations

Vertical - 0.25 mils per major grid division

Horizontal - 1.0 millisecond per major grid division

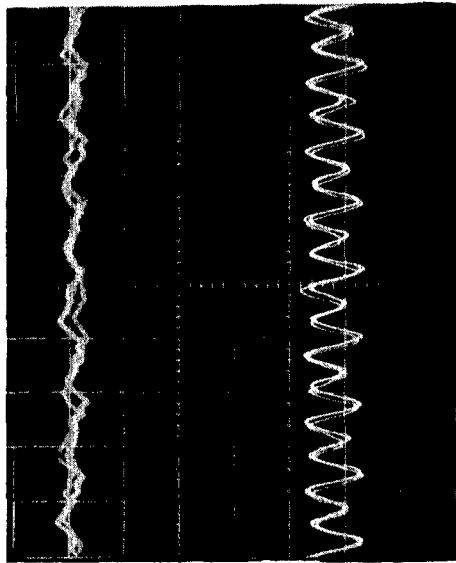
→ Probe signal for PF-20 (Lower Pad)

→ Zero film for PF-20

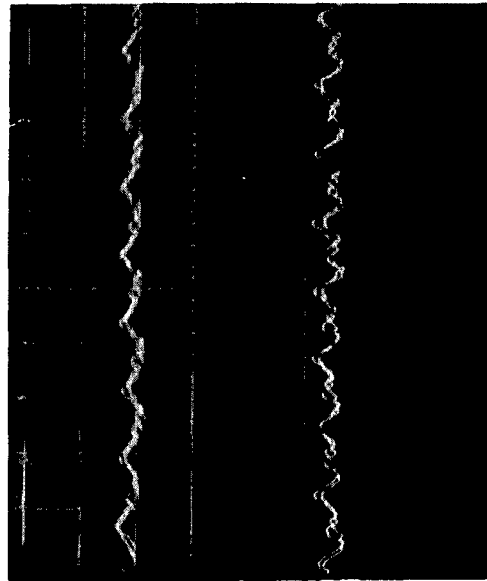
→ Probe signal for PF-22 (Upper Pad)

→ Zero film for PR-22

Fig. IV-18 - Oscilloscope Time-Base Traces Of Pad-To-Shaft Capacitance Probe Signals For No. 2 Journal Bearing --- Taken At 50,120 RPM With Only Residual Rotor Unbalance



Test Run 306
Rotor Vertical, Air at 12.6 psia



← Probe signal for PF-20 (Lower Pad)

← Zero film for PF-20

← Probe signal for PF-22 (Upper Pad)

← Zero film for PF-22

Oscilloscope Calibrations

Vertical - 0.25 mills per major grid division

Horizontal - 1.0 millisecond per major grid division

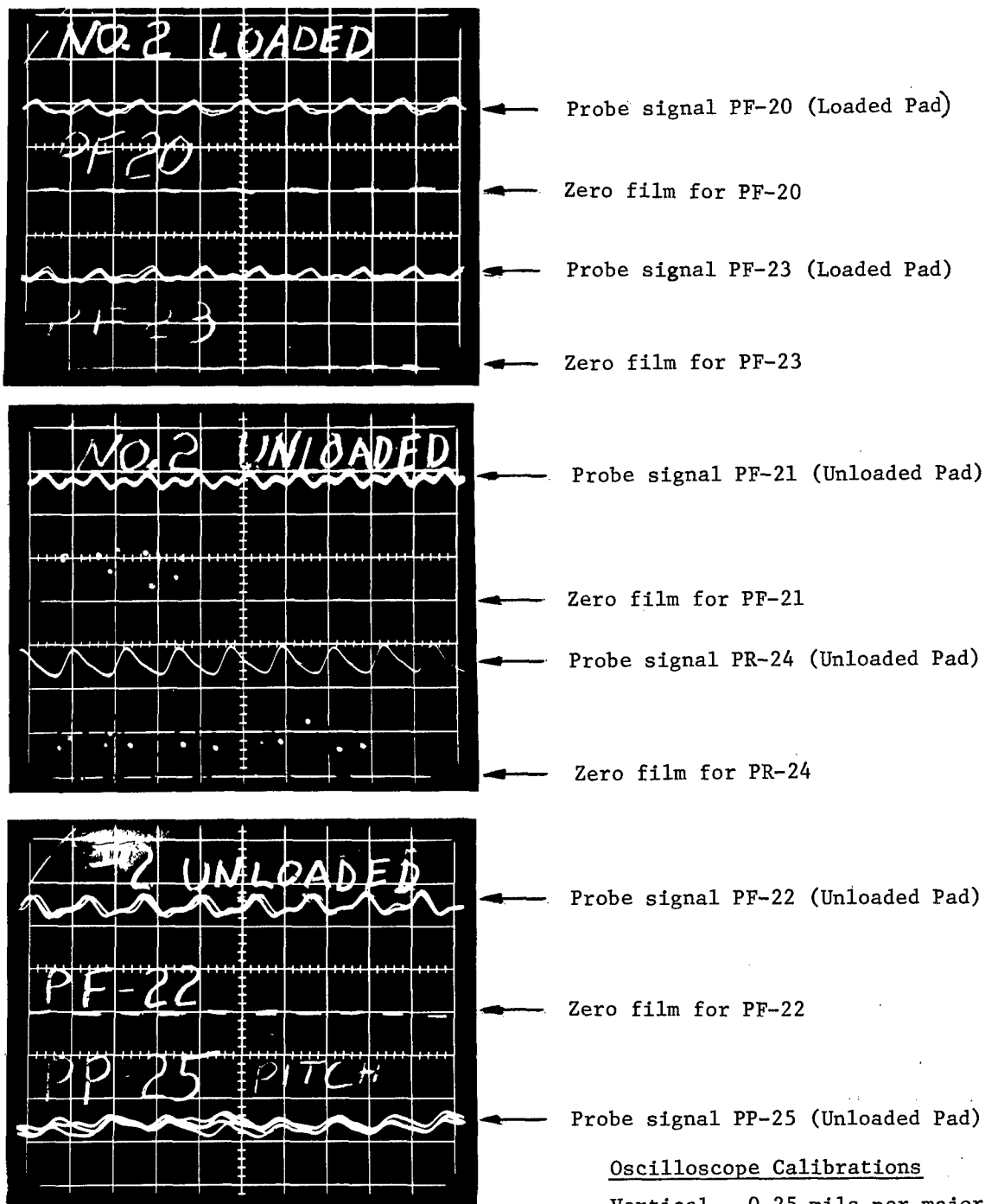
← Probe signal for PF-23 (Lower Pad)

← Zero film for PF-23

← Probe signal for PF-21 (Upper Pad)

← Zero film for PF-21

Fig. IV-19 - Oscilloscope Time-Base Traces Of Pad-to-Shaft Capacitance Probe Signals For The Final No. 2 Journal Bearing Design Taken At 49,670 RPM With 0.002 Ounce-Inches Of Unbalance Added To Turbine Plane



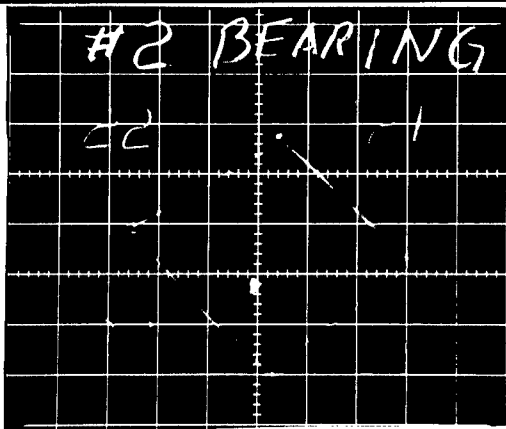
Test Run 258
 Rotor Horizontal
 Ambient - air at 10.9 psia

Oscilloscope Calibrations

Vertical - 0.25 mils per major grid division, except PP-25 which is 0.5 mils per major division

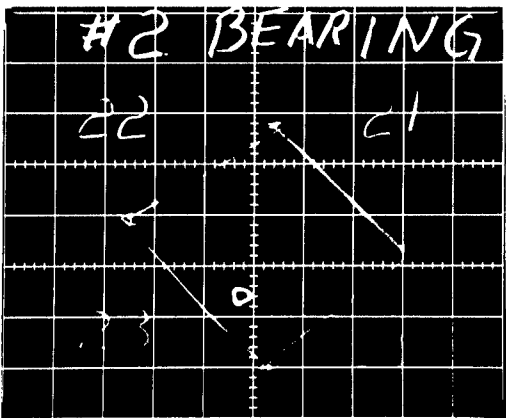
Horizontal - 1.0 millisecond per major grid division

Fig. IV-20 - Oscilloscope Time-Base Traces Of Pad-to-Shaft Capacitance Probe Signals For The Second No. 2 Journal Bearing Design Taken At 50,500 RPM With Only Residual Rotor Unbalance

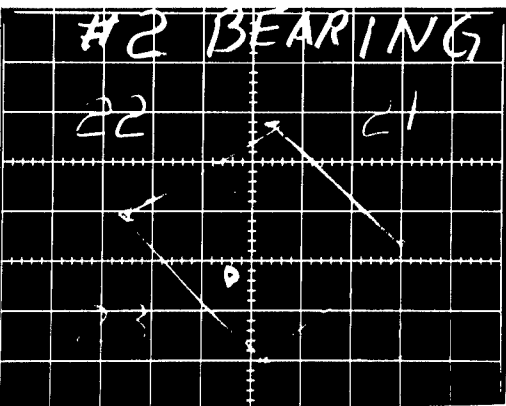


Test Run 252
 49,700 RPM
 Residual Unbalance

Note: There is no relationship between location of the orbits and the zero-speed clearance squares

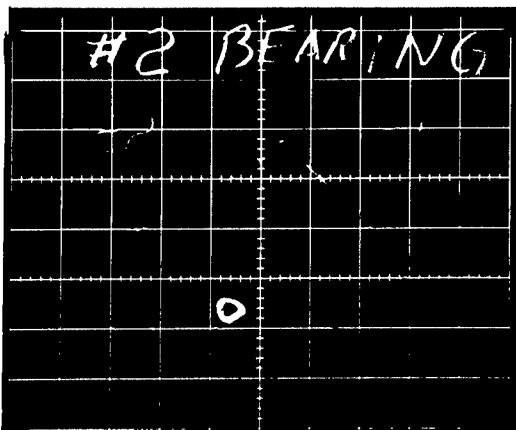


Test Run 239
 50,730 RPM
 Residual plus 0.002 oz.-in.
 unbalance in turbine plane



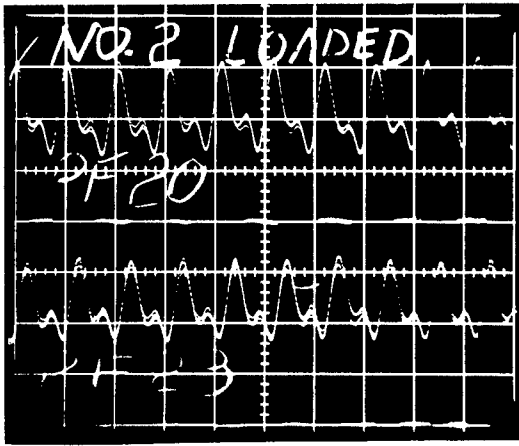
Test Run 263
 60,800 RPM
 Residual unbalance

Oscilloscope Calibrations
 Vertical and Horizontal -
 0.5 mils per major grid
 division



Test Run 240
 60,600 RPM
 Residual plus 0.002 oz.-in.
 unbalance in turbine plane

Fig. IV-21 - Oscilloscope Traces Of The No. 2 Journal Orbit Showing Effect Of Increasing Speed From 50,000 To 60,000 RPM, With and Without Turbine Unbalance, On Journal Response



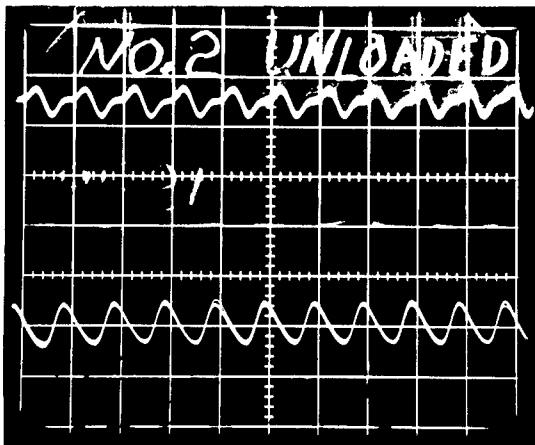
Probe signal PF-20 (Lower Pad)

Zero film for PF-20

Probe signal PF-23 (Lower Pad)

Zero film for PF-23

Test Run 265
59,800 RPM



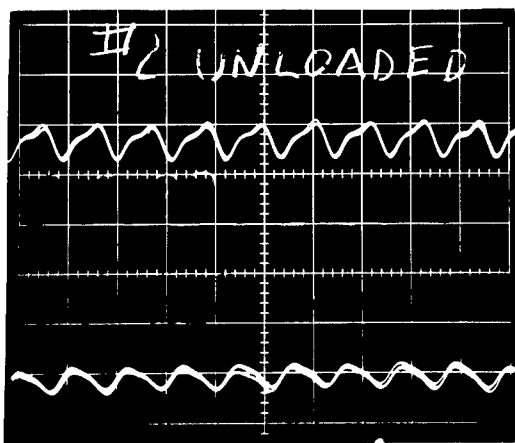
Probe signal PF-21 (Upper Pad)

Zero film for PF-21

Probe signal PR-24 (Upper Pad)

Zero film for PR-24

Test Run 267
60,200 RPM



Probe signal PF-22 (Upper Pad)

Zero film for PF-22

Probe signal PP-25 (Upper Pad)

Oscilloscope Calibrations

Vertical - 0.25 mils per major grid
division except PP-25
which is 0.5 mils per
major division

Horizontal - 1.0 millisecond per major
grid division

Rotor Vertical
Residual plus 0.002 oz.-in.
unbalance in Turbine plane

Test Run 267
60,200 RPM

Fig. IV-22 - Oscilloscope Time-Base Traces Of Pad-to-Shaft Capacitance
Probe Signals For The Second No. 2 Journal Bearing Design —
Taken At 60,000 RPM With 0.002 Ounce-Inches Of Unbalance Added
To Turbine Plane

Resonance of the No. 2 Bearing Pad-Flexure Assemblies

As noted in the preceding discussion and illustrated in Figures IV-18 and IV-19, the upper pad-flexure assemblies of the final No. 2 journal bearing design exhibited a definite vibration resonance at rotor speeds between 45,000 and 55,000 rpm. Within this speed range, the actual speed at which peak amplitude occurred was dependent on the diametral clearance, ambient pressure and lubricant gas. The resonant condition was quite sensitive to diametral clearance. This is illustrated in Figure IV-23 which shows oscilloscope traces of the pivot film clearance for the resonating pad-flexure assembly and the diametrically opposite assembly. These data were taken during vertical operation in argon at 12 psia. The rotor speed was held approximately constant at 50,000 rpm while the diametral clearance was slowly increased. Note that the amplitude of the lower trace increased to about 0.2 mil at a diametral clearance of 1.16 mil and then decreased as the diametral clearance was increased still further. The vibration frequency seen in the resonant pad was twice rotational frequency.

A slight resonance of one of the upper pads was also noticed during the second simulator acceptance as illustrated in Figure IV-20. Figure IV-24 shows a measured resonance curve which was obtained at that time. The data for this curve was obtained from a harmonic analysis investigation of the capacitance probe signals. For the particular conditions of Figure IV-24, the resonant frequency is about 1,350 cps (81,000 rpm).

The pad resonance has been identified as a simple resonance of the pad-flexure system in the radial direction. The resonant frequency can be reasonably predicted from the following equation:

$$f_n = \frac{1}{2\pi} \sqrt{\frac{(K_{flex} + K_{film}) 386}{W}}$$

- where
- K_{flex} = spring rate of the upper flexure, lb/in.
 - K_{film} = spring rate of the gas film, lb/in.
 - W = total weight of the pad-flexure assembly, lb.
 - f_n = natural frequency, cps.

Use of this equation can be illustrated with respect to the data of Figure IV-23 as follows.

The measured spring rate for the upper flexures was 8,400 lb./in. Figure IV-25 shows calculated gas-film stiffness and damping data corresponding to vertical operation at 50,000 rpm in argon at 12 psia, this being close to the test conditions of Figure IV-23. Average film thickness under the pads at the resonant condition of Figure IV-23 (based on one-half the total diametral clearance) was about 0.6 mils. The resonant pad frequency (measured) was 1,640 cps (98,400 rpm) and shaft speed was 50,050 rpm. Thus, the pad resonance is clearly excited by a second harmonic of rotor displacement. Using the following values of

$$K_{\text{flex}} = 8,400 \text{ lb./in.}$$

$$K_{\text{film}} = 77,000 \text{ lb./in. (from Figure IV-25 for a pivot film thickness of 0.6)}$$

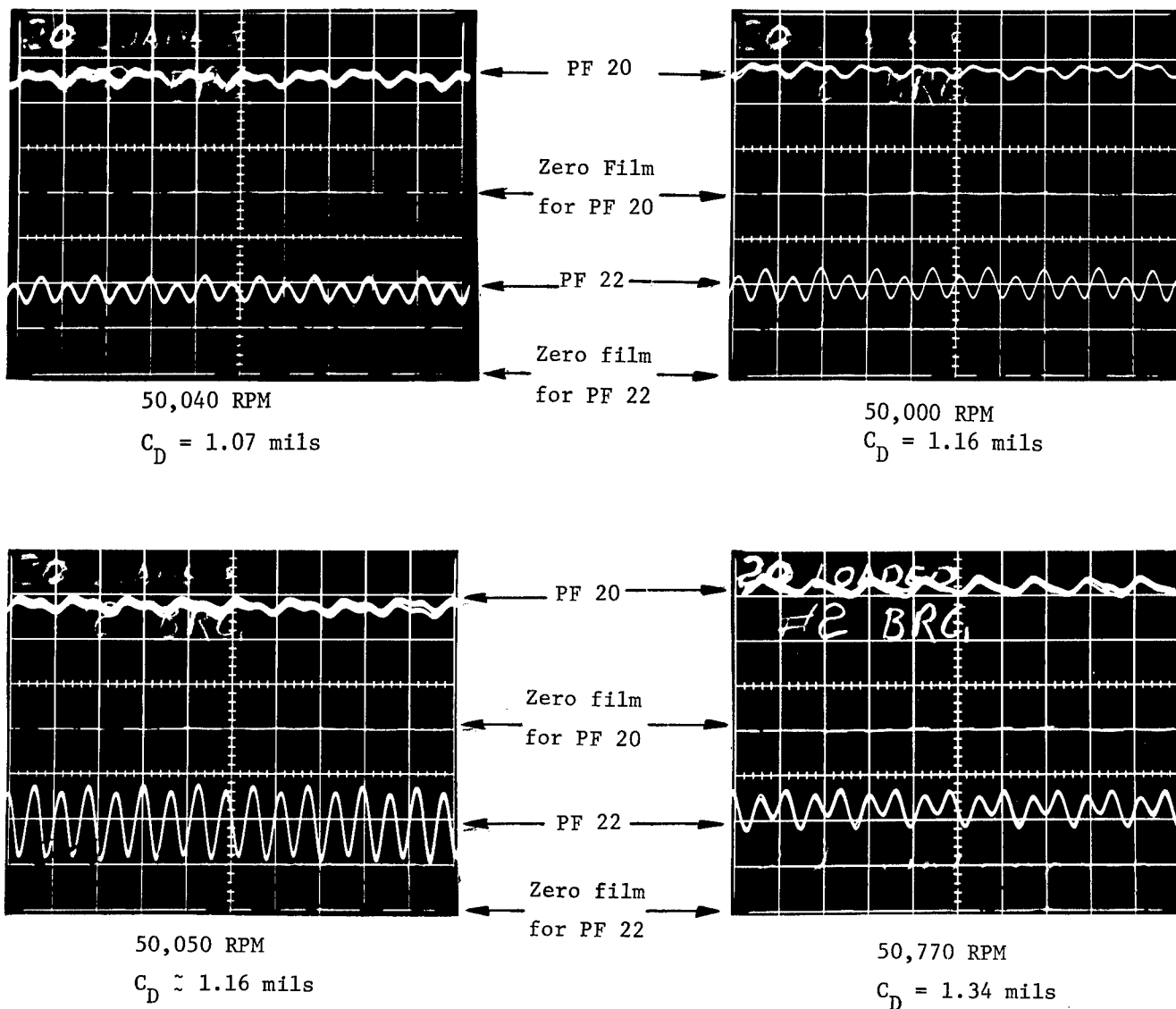
$$W = 0.225 \text{ lb. (includes weight of pad, pivot screw and a portion in the flexure)}$$

gives a calculated pad-flexure resonant frequency (f_n) of 1,926 cps. Although the measured frequency from the test data is 15 percent below the calculated frequency, it is felt that this degree of accuracy, together with the response curve of Figure IV-24, confirms that the resonant condition is due to excitation of the resonant frequency of the pad-flexure system in the radial direction. The fact that the measured resonant frequency of Figure IV-24 is even less than the above frequencies is due to the fact that W was 0.295 lb. during the second simulator acceptance test (i.e., additional weights were added to the No. 2 pads during these tests).

It is seen from Figure IV-25 that the damping capability of the gas film is of the order of 1.0 lb.-sec./in. at the second harmonic (i.e., at the two-per-rev) excitation frequency. This corresponds to a damping ratio of 0.07 which represents a highly underdamped condition. Consequently, the pad assembly would be quite responsive to any rotor excitation in the vicinity of 100,000 rpm. Since some two-per-rev excitation due to out-of-roundness of the journal should be anticipated, it would be desirable to move the resonant frequency safely above any possible

two-per-rev excitation frequency of the machine. Two possible methods for accomplishing this are described in Section V of this report (page 204). The only other solution would be to introduce damping into the pad-flexure system. However, this would require some development and considerable test evaluation.

Pad resonance in the pitch and roll mode was not detected at any time during the simulator test program.



Operation In Argon At 12.0 PSIA With Rotor Vertical

Oscilloscope calibration

Vertical - 0.25 mils per major grid division

Horizontal - 1.0 millisecond per major grid division

Fig. IV-23 - Oscilloscope Traces Of Pad-to-Shaft Probes Showing Resonant Vibration Amplitudes Of An Upper Pad-Flexure Assembly For The Final No. 2 Journal Bearing Design As A Function Of Bearing Diametral Clearance (C_D)

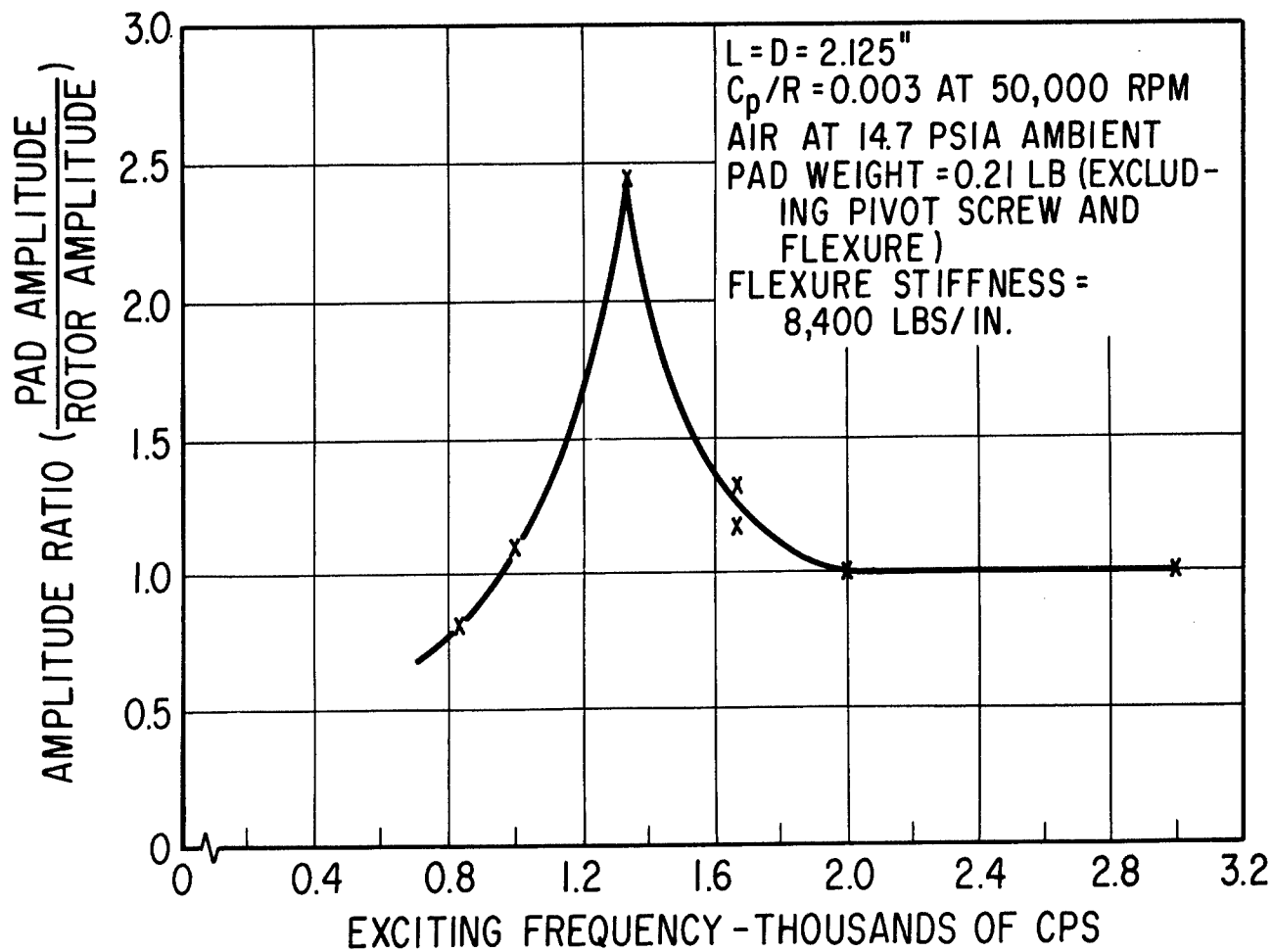


Fig. IV-24 - Measured Resonance Curve For An Upper Pad-Flexure Assembly Of The Second No. 2 Journal Bearing Design

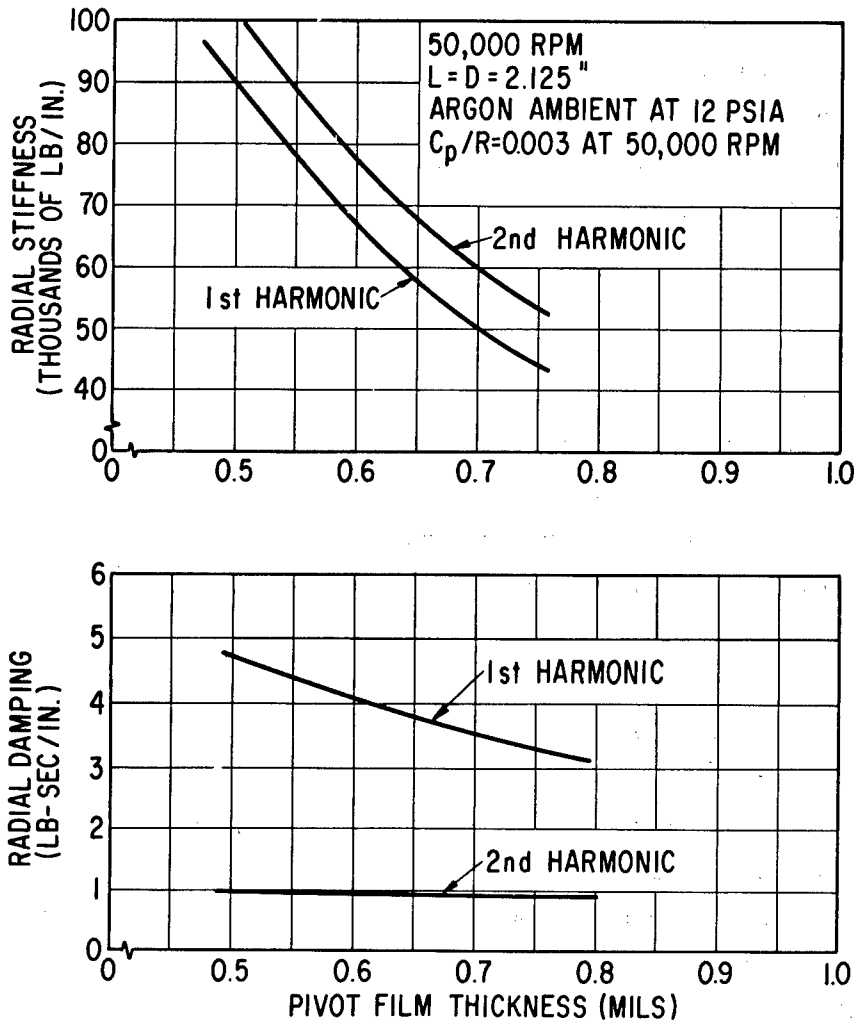


Fig. IV-25 - Calculated Gas Film Stiffness And Damping Coefficients For One Pad At 50,000 RPM Versus Film Thickness For 1st And 2nd Harmonic Excitation Of The Gas Film (1st and 2nd harmonic excitation is equivalent to synchronous and two-per-rev excitation)

Nature of the Low-Frequency Rotor Whirl Phenomenon

Since one of the prime objectives of the third (final) simulator test series was to determine the "boundaries" of whirl-free operation, a description of the whirl phenomenon is in order. As a preface, let it be stated that during the entire course of simulator testing, the phenomenon was observed only in the No. 2 bearing. Attempts made to induce whirl in the No. 1 bearing were unsuccessful. However, significant increases in the diametral clearance of No. 1 bearing (beyond design-point clearance) could not be achieved due to the lack of a bulkhead heater.

The whirl phenomenon was observed as an increase in the mean diameter of the No. 2 journal orbit, and as a sub-rotational frequency variation of the pad-to-shaft clearance at all four pads of the No. 2 bearing. Taken in concert, these two observations imply that the journal was whirling in a roughly circular orbit, within the clearance bounded by the bearing pads, at a fraction of rotational frequency.

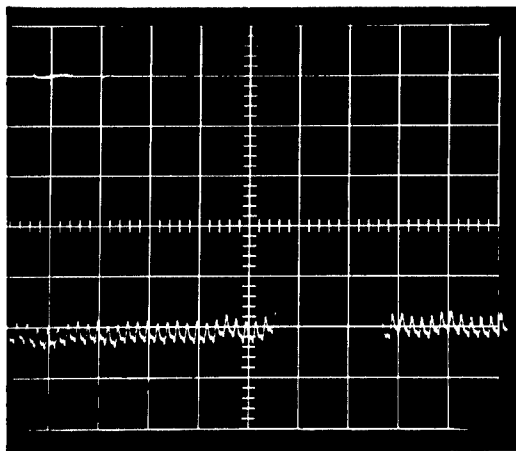
The transition from stable operation to the whirl condition was not well defined. During simulator threshold tests, the transition was made at a condition of constant rotor speed by slowly increasing the diametral clearance of the No. 2 bearing (clearance was varied by controlling the temperature of the No. 2 bearing housing via the bulkhead heater). At the threshold of whirl, the journal orbit exhibited momentary increases in size which occurred at apparently random intervals. While observing the oscilloscope display of pad-to-shaft clearance during this transition, one would note the transitory appearance of a low-frequency sine wave upon which would be superimposed the once-per-rev rotor displacements caused by residual rotor unbalance. These appearances were simultaneous with the momentary increases in journal orbit diameter.

As the diametral clearance was further increased, the most significant change observed was that the diameter of the journal orbit tended to remain more consistently at the larger value which it had assumed only momentarily at lesser clearance. There did not appear to be an immediate tendency to a further increase in orbit size. After the whirl orbit was permanently established, additional increases in

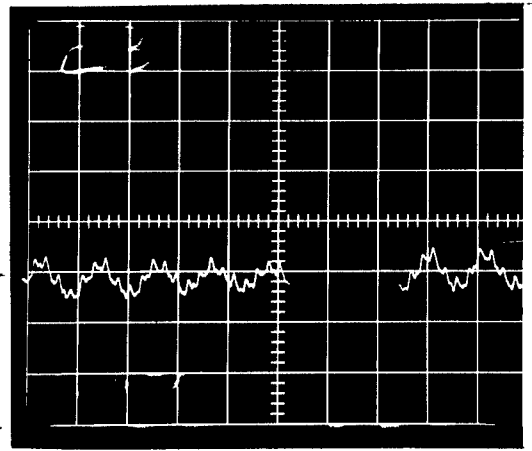
diametral clearance did produce increases in the orbit diameter.

For the purposes of the whirl threshold test series, the inception or threshold of the whirl phenomenon was defined as that condition when the No. 2 bearing orbit evidenced clearly visible fluctuations in diameter of 0.0001 inch. The nature of the transition from stable to whirl operation allowed considerable leeway in the pronouncement of just where the threshold occurred. Consequently, the "threshold" data presented herein reflects, to some extent, the judgement of the test engineer. However, the data are consistent in that respect, as all tests were conducted by the same personnel.

Due to the random occurrence and short duration of the whirl orbit at the "threshold" condition, it was practically impossible to photograph the oscilloscope trace of the whirl orbit at the "threshold" conditions. It was only by chance that the camera shutter opening would coincide with the occurrence of a "whirl orbit." Consequently, most of the photographs of the whirl traces were obtained at conditions well within the whirl region. The change in orbit and pad-to-shaft clearance traces during the whirl condition is illustrated in Figure IV-26.



Stable Operation At 59,800 RPM



Low Frequency Whirl At 50,000 RPM

PF 23

Zero Film

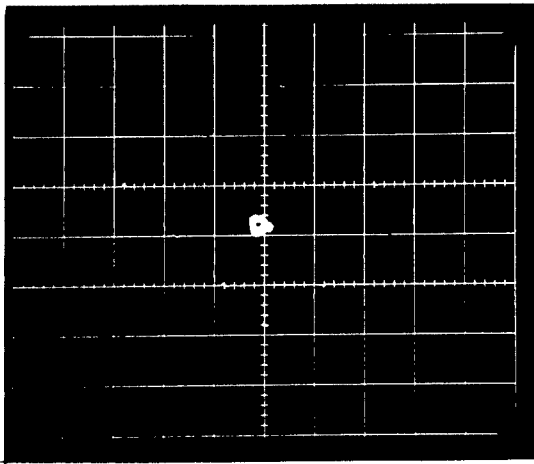
for PF 23

PAD PIVOT-FILM TRACES

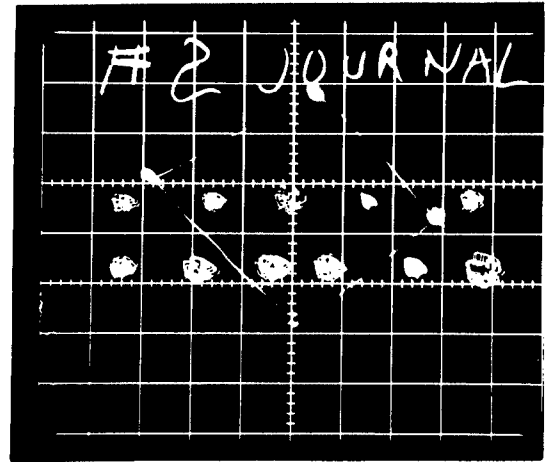
Oscilloscope Calibration

Vertical - 0.25 mils per major grid division

Horizontal - 5.0 milliseconds per major grid division



Stable Operation At 59,400 RPM



Multiple Exposure During Low-Frequency Whirl At 50,000 RPM

JOURNAL ORBIT TRACES

Oscilloscope Calibration

Vertical and Horizontal - 0.5 mils per major grid division

Fig. IV-26 - Illustration Of Change In No. 2 Journal Orbit And Pad-to-Shaft Probe Traces Due To Low-Frequency Rotor Whirl Phenomenon

Whirl Threshold Vs. RPM for the No. 2 Bearing

The procedures and test conditions used to obtain the whirl threshold data for the No. 2 journal bearing are described and documented in Appendix G. Following is a presentation and discussion of the test results.

The average diametral clearance at the threshold of low-frequency whirl is plotted versus rotor speed in Figure IV-27 for both horizontal and vertical operation in air at 14.7 psia. The "average diametral clearance" is defined as one half the sum of the pivot film thickness of all four pads. The mean variation between the two diametral clearances (90 degrees apart) measured at each threshold point was 0.06 mil. It is apparent from Figure IV-27 that imposing a load on the bearing (which is the consequence of running with a horizontal rotor) causes the threshold of low-frequency whirl to occur at a larger diametral clearance. The magnitude of this shift is approximately 0.4 mil at the 50,000 rpm design speed.

The effect on threshold diametral clearance of reducing the bearing ambient pressure from 14.7 psia to 10.0 psia is shown in Figure IV-28. The upper portion of the figure illustrates the effect for operation with the rotor horizontal. The reduction in ambient pressure caused a reduction in threshold diametral clearance of about 0.1 mils at 50,000 rpm. The lower portion of Figure IV-28 shows the effect of reduced ambient pressure for operation with the rotor vertical. In this case, the reduction in ambient pressure caused a more pronounced reduction in threshold diametral clearance. At 50,000 rpm this reduction was 0.28 mils.

The effect of changing the lubricant gas from air to argon is illustrated in Figure IV-29. The data are for operation at 10 psia with the rotor vertical. The change from air to argon produced an increase in the threshold diametral clearance. This increase was about 0.22 mils at 50,000 rpm. This is qualitatively consistent with the differences between bearing stiffness and load capacity in air as compared with those in argon. These differences are due to the higher viscosity of argon (3.9×10^{-9} lb.-sec./in.² for argon at 225 F as opposed to 3.2×10^{-9} lb.-sec./in.² for air at 225 F).

The primary objective of the second bearing system design (as described in Appendix D) was to minimize the turbocompressor bearing power losses by increasing the clearance. Encountering the low-frequency whirl phenomenon modified this objective to the achievement of minimum bearing power losses (maximum bearing clearance) consistent with the avoidance of whirl throughout the operational regime of the turbocompressor

It is apparent from Figure IV-27 that the recommended clearance for the achievement of the above objective must be established on the basis of data for vertical orientation of the simulator rotor. This running condition for the simulator is equivalent to zero-g operation of the turbocompressor in space so far as the journal bearings are concerned. The data of Figures IV-28 and IV-29 also indicate that ambient pressure, ambient gas, and rotor speed have appreciable effects on the threshold clearance. Consequently, an all-inclusive maximum permissible bearing clearance can be defined only after all possible combinations of rotor speed, ambient pressure and ambient gas are specified. The specific case of turbocompressor design-point conditions (i.e., 50,000 rpm in argon at 12 psia) was selected for the determination of a "recommended" maximum clearance for whirl-free operation. This clearance was chosen from the data of Figure IV-29 as 1.35 mils. This clearance offers some margin of safety at the turbocompressor design condition as it is the threshold clearance at the lower ambient pressure of 10 psia.

Acceptance tests in air were conducted with a No. 2 bearing diametral clearance of approximately 1.15 mils, as the data of Figure IV-29 indicate that this value in air is equivalent to the recommended value in argon.

Whirl Frequency

The whirl phenomenon reported herein has been referred to as "low-frequency whirl" because the whirling of the rotor axis within the bearing clearance occurs at considerably less than rotational frequency. Unlike the "half-speed" whirl observed in 360 degree hydrodynamic bearings, the whirl frequency observed during these tests ranged from one-quarter to one-fifth the rotational frequency.

Referring to Figure IV-26, the oscilloscope trace of pad pivot-film thickness during low-frequency whirl at 50,000 rpm plainly shows the whirl frequency

corresponding to approximately one major grid division. Measurement of the average "wave length" and application of the oscilloscope horizontal axis calibration factor indicates a whirl frequency of about 180 cps, equivalent to 10,800 rpm. Similar determinations of whirl frequency were made for those cases where the whirl was detectable in the recorded oscilloscope traces.

The whirl frequency and whirl ratio (whirl frequency/rotational frequency) are plotted against rotor speed in Figure IV-30. These data points are not all at threshold conditions; about half the data were taken at conditions beyond the threshold. Those data taken with the rotor horizontal appear to have a consistent trend, whereas the vertical rotor data do not. No trend is apparent based on variation in ambient pressure. In general, the whirl frequency increases slightly as rotor speed increases.

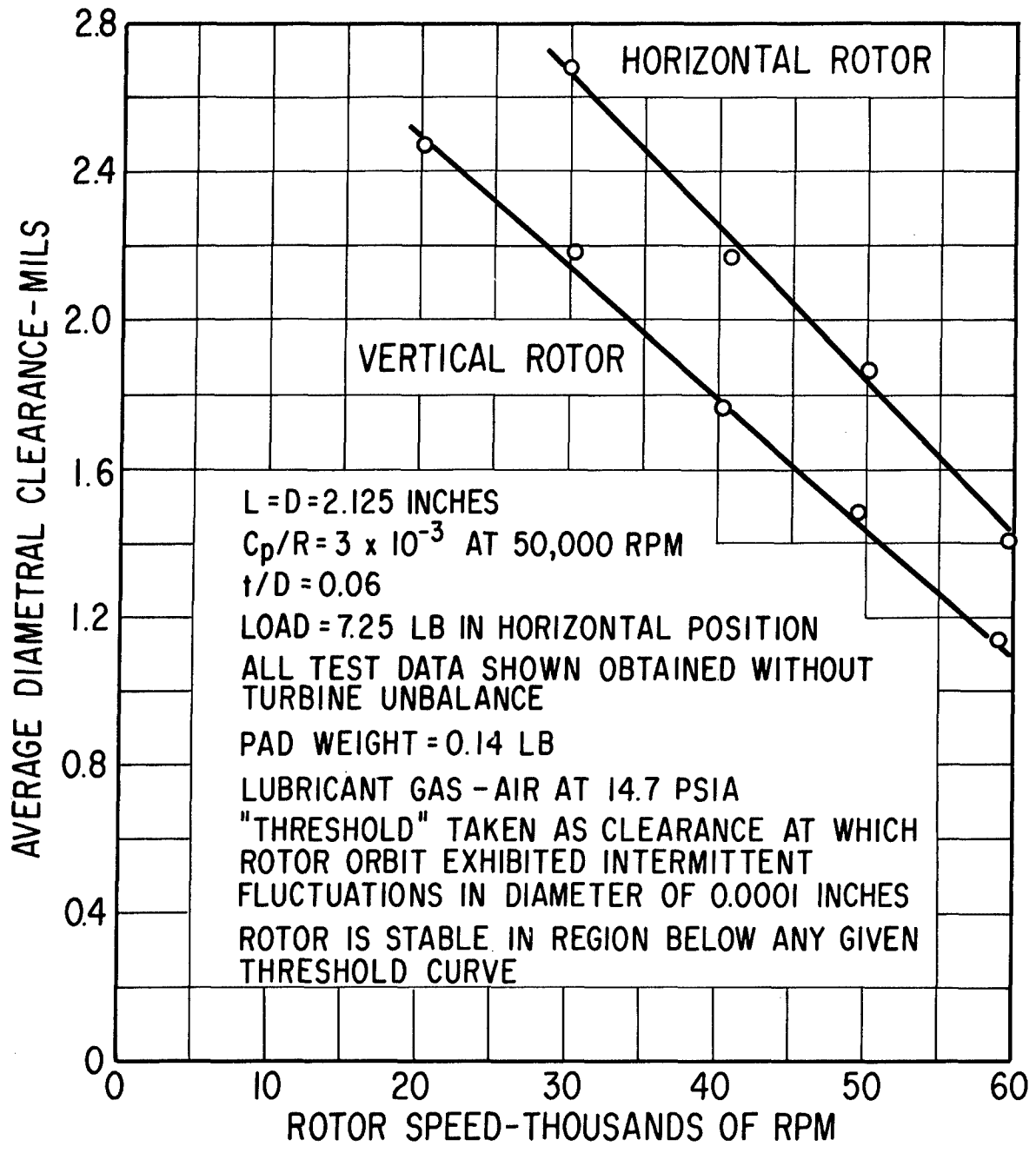


Fig. IV-27 - Effect Of Rotor Orientation On Diametral Bearing Clearance At Threshold Of No. 2 Journal Low-Frequency Whirl

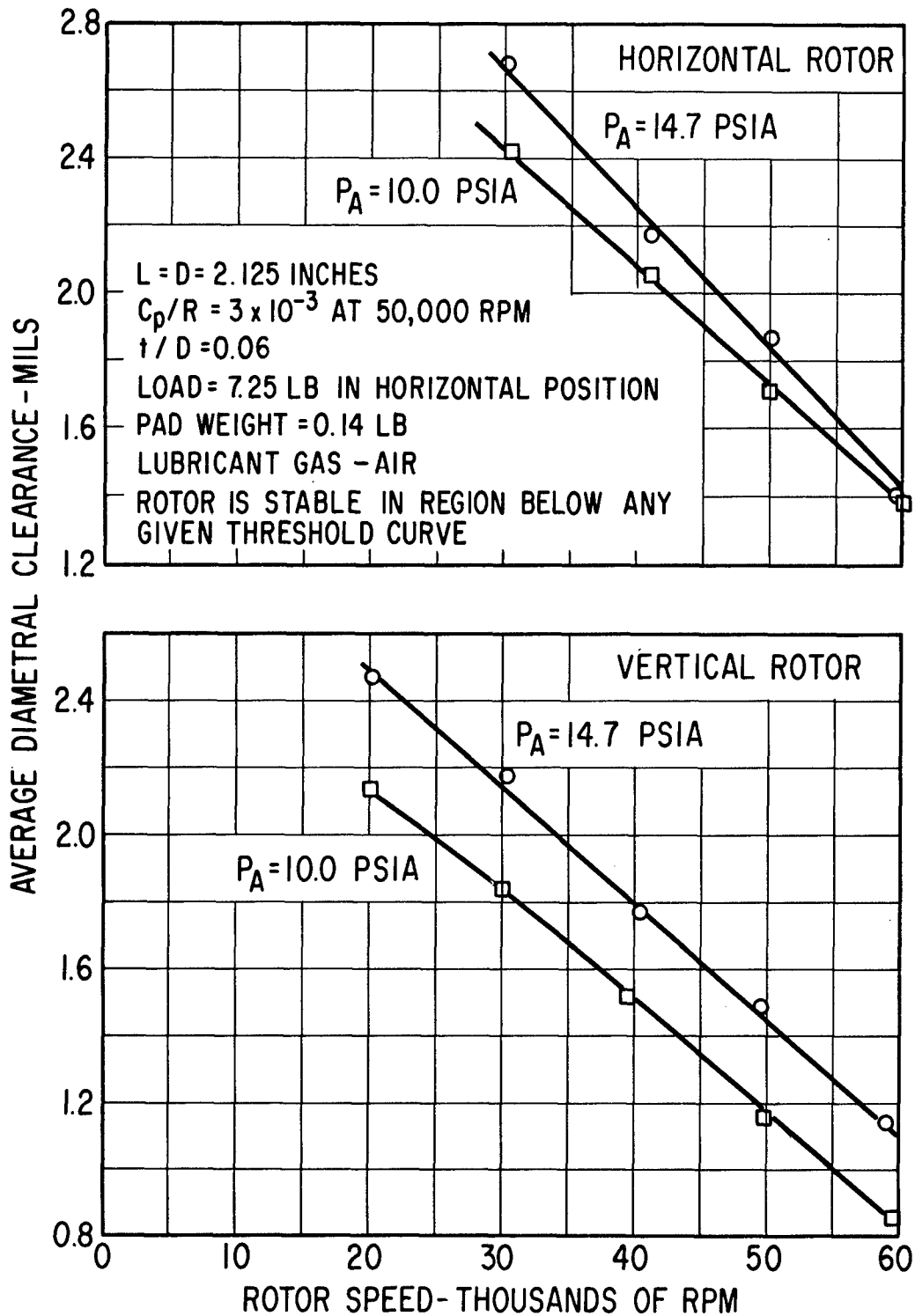


Fig. IV-28 - Effect Of Ambient Pressure On Diametral Bearing Clearance At Threshold Of No. 2 Journal Low-Frequency Whirl

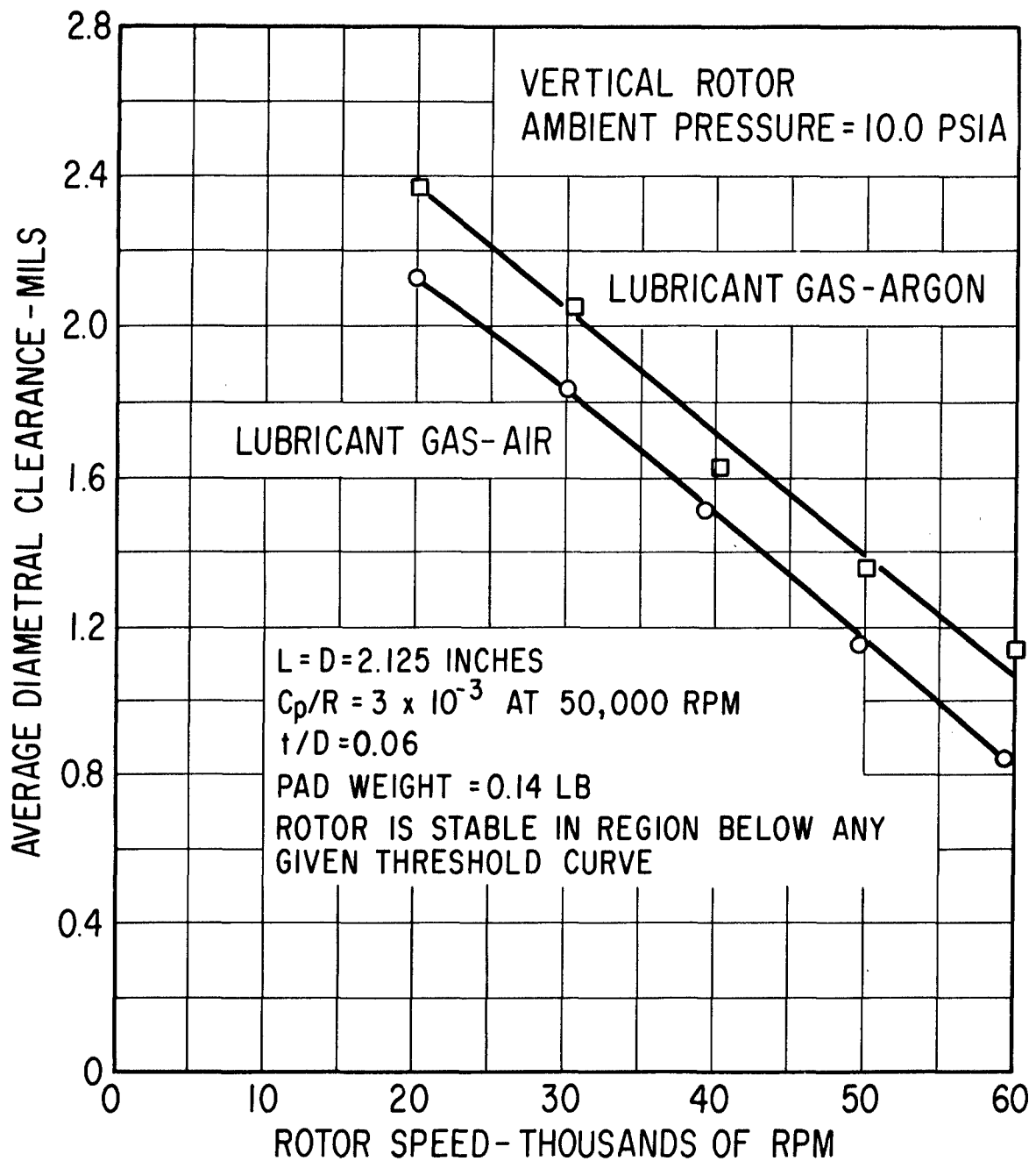


Fig. IV-29 - Effect Of Changing Lubricant Gas From Air to Argon On Diametral Bearing Clearance At Threshold Of No. 2 Journal Low-Frequency Whirl

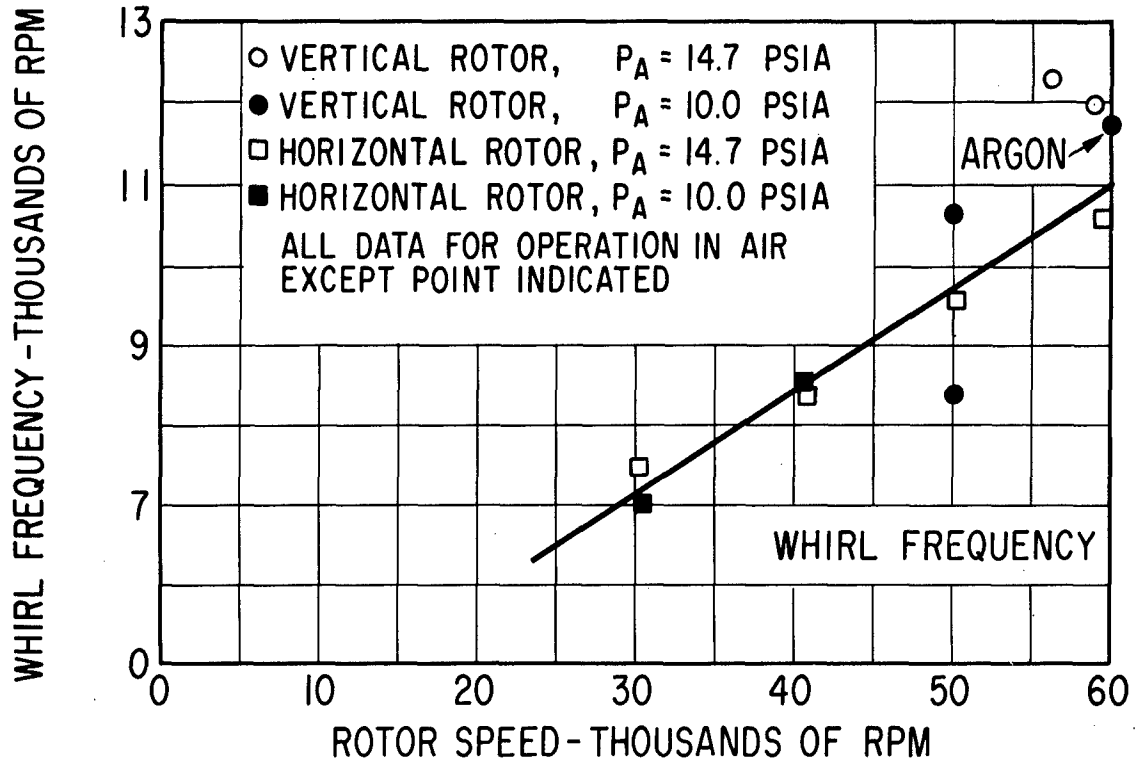
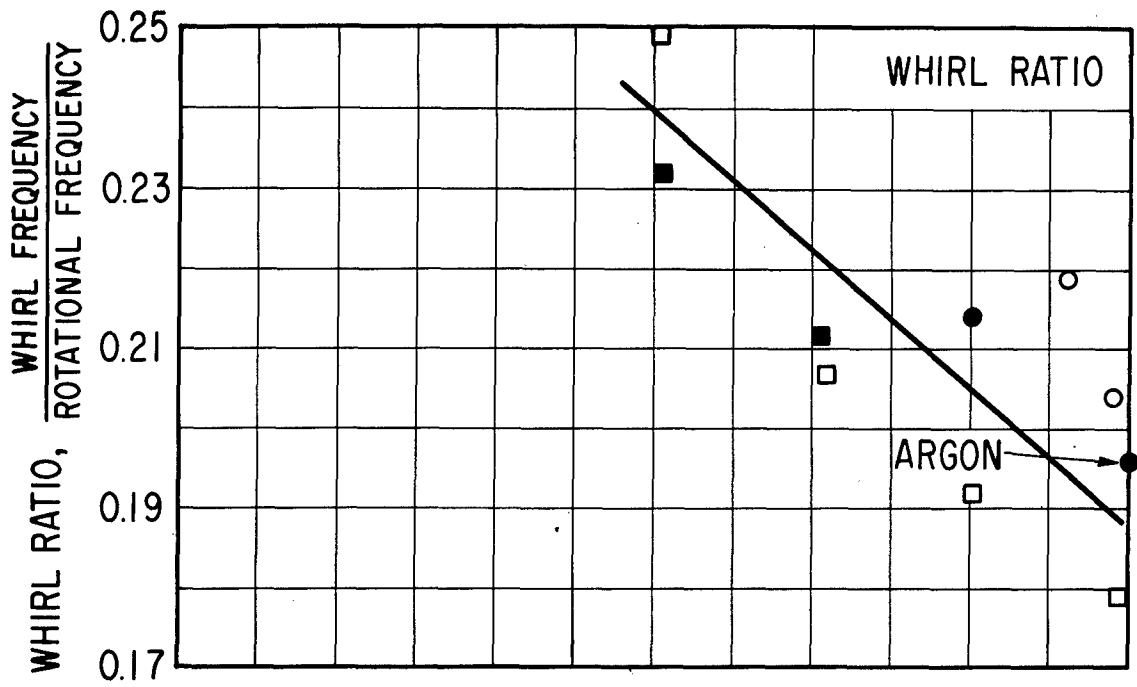


Fig. IV-30 - Whirl Frequency And Whirl-Frequency Ratio Versus Rotor Speed For The Final No. 2 Journal Bearing Design

V. CONCLUSIONS AND RECOMMENDATIONS

Three variations of a basic gas-bearing rotor-support system have been designed, built, and tested by MTI for the NASA Brayton cycle axial-flow turbocompressor being developed by P&WA under prime contract from the NASA-Lewis Research Center. The designs were experimentally evaluated in a full-scale rotor-bearing system test rig which

1. exactly simulated the design of the turbocompressor bearings,
2. very closely simulated the mechanical configuration and physical parameters of the turbocompressor rotor (the actual turbine and compressor components were not, however, used),
3. permitted testing of the rotor-bearing system under operating and environmental conditions similar to those which would exist in the turbocompressor (turbine inlet temperature, however, was not simulated).

All three bearing system designs performed satisfactorily and successfully passed the required P&WA acceptance tests. The final design described in Sections II and IV of this report represents a minimum bearing friction loss design consistent with whirl-free operation of the rotor. Until a solution to the whirl phenomenon is found which will permit operation of the No. 2 journal bearing at still larger clearances, no further significant reduction in friction loss can be made.

Specific Conclusions

Following is a list of specific conclusions relating to the final design of the turbocompressor bearing system as documented in Section II of this report. These conclusions are, of course, substantiated by the test results for the final design, as well as by the test results for the initial and second designs documented in Appendices C and D.

1. Forward Hydrodynamic Thrust Bearing

Performance of this bearing agrees very well with calculated performance,

and as far as can be ascertained at this time meets all the design requirements. A slight resonance of the thrust-plate-flexure assembly can be excited under certain circumstances between 28,000 and 30,000 rpm. However, operation in this resonant region was thoroughly investigated and under no condition were the vibration amplitudes large enough to be of concern. Under most operating conditions, the resonance did not even occur.

Performance of the thrust bearing liquid cooling mechanism was excellent, even at coolant flow rates less than 100 pounds per hour. Dimensional stability of the aluminum thrust plate over the 8-month test period was, from all indications, excellent (at no time during the test period, however, was flatness of the plate ever rechecked).

2. Forward and Reverse Hydrostatic Thrust Bearings

Performance of the forward hydrostatic thrust bearing is slightly better than calculated, while performance of the reverse bearing falls slightly short of design values. Nonetheless, film thickness of the reverse thrust bearing at the required start-up load condition is more than adequate for safe, reliable operation.

A pneumatic hammer problem in the initial design of the forward hydrostatic thrust bearing was corrected prior to acceptance testing of the initial design (see Appendix C). No pneumatic hammer or other instability was ever observed in either of the hydrostatic thrust bearings subsequent to this correction.

3. No. 1 Journal Bearing

Performance of the No. 1 pivoted-pad journal bearing was excellent throughout the test program and in good agreement with predicted performance. Operation of the pivot-support flexures was likewise excellent. At no time was any instability of the No. 1 journal or pivoted-pads, or simple resonance of the pads or flexures, detected. Neither was the bearing performance unduly affected by the prescribed amounts of turbine unbalance.

Hydrodynamic starting and stopping of the No. 1 bearing was accomplished without difficulty, and with no apparent damage or appreciable wear of the chrome oxide surface coatings. The cooling system for the No. 1 bearing likewise performed quite adequately.

4. No. 2 Journal Bearing

Performance of the No. 2 pivoted-pad journal bearing was in good agreement with calculated performance during operation below the threshold of low-frequency journal whirl. The whirl region, to the limited extent that it was penetrated during the test program, was found to be a stable region which did not adversely effect bearing operation. However once the threshold is crossed and the journal develops its whirling motion, further increases in bearing clearance appear to be accompanied by a corresponding increase in whirl orbit.

Based on the whirl threshold tests discussed in Section IV, the following specific conclusions with respect to the whirl condition can be drawn.

- a) A diametral clearance less than or equal to 1.35 mils will assure whirl-free operation of the No. 2 bearing at the design point conditions of 50,000 rpm in a 12 psia argon ambient a zero-g or vertical-rotor load conditions, and also in a 1-g orientation.
- b) The diametral clearance corresponding to threshold of whirl is a minimum when the bearing is unloaded (vertical rotor zero-g operation in space). Imposing a load on the bearing (e.g., operation with the rotor horizontal) causes the threshold to occur at a larger diametral clearance.
- c) For ambient pressures between 10 and 14.7 psia (this being range of pressures covered by the test program), the threshold diametral clearance decreases as the ambient pressure is decreased.
- d) The threshold diametral clearance is affected by the composition of the ambient gas. The threshold clearance is greater in

argon than in air. This effect correlates approximately with gas viscosity.

For the final design of the No. 2 bearing, each upper pivot-support flexure and its associated pad, together with the pad gas film, form a dynamic vibration system which has a resonant frequency in the radial direction of approximately 100,000 rpm. The second harmonic of rotor speed thus coincides with this resonance when operating in the vicinity of the 50,000 rpm design speed. Pad resonance was noted in the speed range from 45,000 to 55,000 rpm, at diametral clearances in the vicinity of 1.1 to 1.2 mils. The vibration amplitude peaked sharply with small changes of diametral clearance within this range; peak-to-peak amplitudes up to 0.4 mils were observed. Although the condition was not considered hazardous during laboratory testing of the simulator, it would not seem desirable to have such a resonance so near to the design speed in the actual turbocompressor.

Aside from the pad-flexure resonance condition, the pivot-support flexures for the No. 2 bearing did an excellent job of accommodating journal centrifugal and thermal growths.

Addition of the prescribed amounts of turbine unbalance did not unduly affect bearing performance.

Hydrodynamic starting and stopping of the No. 2 bearing was accomplished without difficulty and without any apparent damage or significant wear of the chrome oxide surface coatings. The bearing cooling mechanism worked quite satisfactorily. Maximum pad temperatures attained during simulator testing (during an argon acceptance test run) were 311 to 322 F — fairly close to the 390 F average pad temperature predicted for the initial No. 2 bearing design.

General Conclusions

Successful development of a reliable turbocompressor gas-bearing rotor-support system, at least for static environmental conditions, appears to have been achieved. However,

extensive testing of the actual turbocompressor, under both static and dynamic environmental conditions, will be required before final substantiation of reliability can be made.

In terms of technological advancements directly related to gas-bearing turbomachinery design, these can best be illustrated by the following list of "MTI firsts" associated with the turbocompressor bearing system design:

1. First use of pivot flexures in a pivoted-pad self-acting journal bearing.
2. First use of chrome oxide as the surfacing material for the bearing parts (the material evaluation tests performed during the program were a highly significant contribution).
3. First machine to utilize self-acting start-up of the journal bearings (previous designs have utilized auxiliary hydrostatic bearings to lift the rotor during start-up and shutdown).
4. First self-acting bearing system designed for operation to 60,000 rpm (previous maximum speed for a self-acting system was 24,000 rpm).
5. First design where start-up thrust loads are supported by a hydrostatic bearing built into the self-acting helical-grooved thrust bearing.
6. First use of internally brazed, axially finned, TD nickel heat exchangers to remove journal bearing friction losses (detail design of these exchangers was done by P&WA).
7. First use of a liquid-cooled, aluminum thrust stator.
8. First use of a titanium thrust runner.
9. First use of miniaturized capacitance probes embedded near the pivot point of the journal bearing pivoted pads.

Initial start-up of the simulator took place on July 17, 1965. The third acceptance test was completed almost eight months later. The eight month test program was accomplished without a single bearing rub or failure.

Recommendations

The following recommendations are made based on the results of the work reported herein.

1. Until a better understanding of the low-frequency rotor whirl phenomenon is obtained, a diametral clearance of 1.35 mils should be adopted as the maximum clearance value for both the No. 1 and No. 2 turbocompressor journal bearings. This recommendation will assure whirl-free operation of the rotor.
2. Additional work of both an analytical and experimental nature should be performed to conclusively identify the cause of the low-frequency whirl phenomenon encountered in high-speed pivoted-pad gas-lubricated journal bearings operating at large clearances. Reliable analytical prediction of the maximum allowable clearance for whirl-free operation would facilitate the design of such bearings for minimum friction losses. Once the whirl phenomenon is understood and the factors which produce it are known, it may be found that certain elements of the bearing design can be changed to allow whirl-free operation at the large diametral clearances necessary to achieve minimum possible friction losses.
3. The design of the No. 2 journal bearing should be modified to move the resonant frequency of the upper pad-flexure assemblies above any possible two-per-rev excitation frequency of the turbocompressor. Two methods are readily available to increase the natural frequency of the pad-flexure system:
 - a) reduce the pad mass by using titanium for the pad material (which would require incorporation of a hardened insert at the pivot point);
 - b) increase the upper flexure stiffness from 10,000 lb./in. to about 45,000 lb./in. and reduce the lower flexure stiffness from 70,000 lb./in. to 45,000 lb./in. This second method is simpler, but reduces somewhat the ability of the bearing to absorb thermal and centrifugal growth of the rotor relative to the bearing housing.

Additional analysis of these two alternates for raising the resonant frequency should be made to determine the better of the two. The better alternative should then be evaluated in the rotor-bearing system simulator.

4. The final design of the turbocompressor bearing system should be experimentally evaluated under the various operating and non-operating vibration and shock conditions designated in NASA Specification P0055-1 (see Appendix A). Here again, the rotor-bearing system simulator would be an excellent vehicle with which to make the necessary evaluations.

REFERENCES

1. Curwen, P. W., "Operational Experience With Gas-Bearing Turbomachinery", presented at a panel discussion on Gas Bearing Applications held on November 30, 1966 at the ASME 1966 Winter Annual Meeting, New York, New York.
2. Pinkus, O. and B. Sternlicht, "Theory of Hydrodynamic Lubrication", McGraw Hill Book Co., 1960.
3. Gross, W. A., "Gas Film Lubrication", John Wiley & Sons, 1962.
4. "First International Symposium on Gas Lubricated Bearings" (1959), edited by D. D. Fuller, ACR-49, Office of Naval Research, Department of the Navy, Washington, D. C.
5. Grassam, N. S. and J. W. Powell, "Gas Lubricated Bearings", Butterworth & Co., (London) 1964.
6. Wernick, R. J. and C.H.T. Pan, "Static and Dynamic Characteristics of Self Acting, Partial-Arc, Gas Journal Bearing", ASME Paper 63-Lub-5.
7. Malanoski, S. B. and C.H.T. Pan, "The Static and Dynamic Characteristics of the Spiral Grooved Thrust Bearing", ASME Paper 64-Lub-9.
8. Lund, J. W., "A Theoretical Analysis of Whirl Instability and Pneumatic Hammer for a Rigid Rotor in Pressurized Gas Journal Bearings", (submitted for Publication in ASME).
9. Pan, C.H.T., "Spectral Analysis of Gas Bearing Systems for Stability Studies", MTI Report 64TR58.
10. Gunter, E. J., Jr., J. G. Hinkle and D. D. Fuller, "The Effects of Speed, Load and Film Thickness on the Performance of Gas Lubricated, Tilting Pad, Journal Bearings", Trans. ASLE, Vol. 7, No. 4, October 1964.
11. Muijderman, E. A., "Spiral Grooved Bearings", Phillips Research Laboratories (Netherlands), 1964.
12. Sternlicht, B. and E. B. Arwas, "State-of-the-Art of Gas-Lubricated Turbomachinery", MTI Report 65TR5-I.
13. Cheng, G., C. Y. Chow and S. F. Murray, "The Hydrodynamic Gas Journal Bearing and the Hydrodynamic Gas Thrust Bearing", MTI Report 65TR5-II, Vol. 1.
14. Lund, J. W., "The Hydrostatic Gas Journal Bearing and the Hydrostatic Gas Thrust Bearing", MTI Report 65TR5-II, Vol. 2

NOMENCLATURE

C, C_P	Pad clearance (radius of curvature of pad minus radius of curvature of journal) - inches
D	Diameter of journal or thrust bearing - inches
FHP	Friction horsepower
h	Heat transfer film coefficient - $\frac{\text{BTU}}{\text{hr.}\cdot\text{ft.}^2\cdot\text{F}}$
h	Bearing film thickness - inches
h_{pivot}	Pivoted-pad film thickness at pivot location - inches
k	Thermal conductivity - $\frac{\text{BTU}}{\text{hr.}\cdot\text{ft.}\cdot\text{F}}$
K_A	Axial stiffness of thrust bearing gas film - lb./in.
K_{flex}	Stiffness of pivot-support flexure - lb./in.
K_R, K_{film}	Radial stiffness of journal bearing gas film - lb./in.
K_T	Angular stiffness of thrust bearing gas film - lb./in.
L	Length of journal bearing - inches
m	Journal bearing preload coefficient
N	Rotor speed - revolutions per second
N_P	Resonant frequency of a journal bearing pivoted-pad in the pitch direction - revolutions per second
N_R	Resonant frequency of a journal bearing pivoted-pad in the roll direction - revolutions per second
P_a	Bearing ambient pressure - psia
P_s	Hydrostatic bearing supply pressure - psia
Q	Bearing heat generation rate - $\frac{\text{BTU}}{\text{hr.}}$
R	Radius of journal or thrust bearing - inches
t	Thickness of journal bearing pivoted-pad - inches

T_h	Temperature of bearing housing - °F
T_o	Reference temperature of bearing system (taken as 70 F in this report) - °F
T_p	Average temperature of pivoted-pad - °F
T_s	Average temperature of journal - °F
W	Bearing load - pounds
β	Total angular arc of one pivoted-pad - degrees
ϵ_b	Bearing eccentricity ratio
ϵ_p	Pad eccentricity ratio
θ_p	Angular distance from the leading edge of a pad to its pivot point - degree
Λ	Compressibility number
μ	Viscosity - lb.-sec./in. ²
ϕ	Pad attitude angle - degrees
ψ	Pivot-to-bearing-load angle - degrees
ω	Angular velocity - radians/second

APPENDIX A

SPECIFICATION NO. P0055-1 (NASA)

July 15, 1963

SOLAR BRAYTON CYCLE SPACE POWER SYSTEM
ENVIRONMENTAL SPECIFICATION

1.0 SCOPE

1.1 This specification covers the anticipated environmental conditions listed below to which the Solar Brayton Cycle Space Power System and components shall be designed to withstand without malfunction or performance degradation.

This specification does not cover development and/or acceptance tests.

1.2 Environments

Environmental conditions specified are applicable to each of the components and the complete solar space power system through manufacture, storage, transportation, lift-off, boost, orbit, and orbital transfer.

2.0 Environmental Conditions

2.1 Storage and Transportation

The components and their associated equipment shall be capable of withstanding without performance impairment the following loads applied along each of three mutually perpendicular axes of its container.

2.1.1 Shock - 4 G shock within one of the following times and wave shape:

2.1.1.1 Triangular pulse of 10 milliseconds.

2.1.1.2 Half-sine pulse of 8 milliseconds.

2.1.1.3 Rectangular pulse of 5 milliseconds.

2.1.2 Vibration:

2.1.2.1 2 - 10 cps 0.40 inches double amplitude

2.1.2.2 10 - 500 cps 2.0 G peak

2.2 Launch, Lift-Off, Boost

The non-operating system and components shall be capable of withstanding without performance impairment the following simultaneous launch loads applied at the system mounting points and in the directions and magnitudes specified:

2.2.1 Shock

35 G shock along each of three mutually perpendicular axes within one of the wave shape and pulse times in 2.1.1. above.

2.2.2 Vibration

Sinusoidal input applied at the system mounting points along each of three mutually perpendicular axes

16 - 100 cps	@ 6 G peak
100 - 180 cps	@ 0.0118" double amplitude
180 - 2000 cps	@ 19 G peak

2.2.3 Acceleration

The non-operating system and its accessory components shall be capable of withstanding the following launch accelerations for five (5) minutes duration:

- 2.2.3.1 7 G - along boost vehicle lift-off axis.
3 G - along boost vehicle lift-off axis in opposite direction.
4.5 G - all directions in plane normal to lift-off axis.

2.2.4 Acoustic Noise

The non-operating system and its components shall be capable of withstanding the induced vibrations while subjected to an acoustic noise field with an integrated level of 148 d.b., Re 0.0002 micro-bar.

2.3 Orbital Operation

The equipment shall be designed to be capable of start-up and continuous operation at rated power in earth orbits of from 300 to 20,000 nautical miles without malfunction for 10,000 hours time.

2.3.1 Shock

Prior to system startup and deployment, the components shall sustain up to 7 G shock (course correction) along the lift-off or flight axis with one of the wave forms and time durations indicated in paragraph 2.1.1.

2.3.2 Vibration

The system and components will sustain vibrations in orbit while in operation of 0.25 G peak over a frequency range of 5 to 2000 cps for a time period of five minutes for each occurrence.

2.3.3 Acceleration

2.3.3.1 Undeployed

The undeployed system and components will sustain accelerations of 3-1/2 G in one direction along the lift-off axis, and plus or minus 1 G in all directions in the plane normal to the lift-off axis. These accelerations will be sustained individually for a period of five minutes maximum for each occurrence.

2.3.3.2 Deployed

The deployed operating system will also be required to be capable of sustaining a continuous, unidirectional acceleration arising from a 4 RPM spin rate of the spacecraft. The G loading on the system components will be a function of their radial location with respect to the spin axis. For the purposes of this application, the centerline axis of the collector and system is located at a radius of 33 feet from the spin axis and experiences an 0.18 G acceleration.

APPENDIX B

PRATT & WHITNEY AIRCRAFT
SPECIFICATION FOR ACCEPTANCE
TESTING A TURBINE-COMPRESSOR
ROTOR DYNAMIC SIMULATOR

1. SCOPE - This specification covers the acceptance test for a turbine-compressor rotor dynamic simulator incorporating hydrodynamic gas bearings.

2. REQUIREMENTS

2.1 General - The test specified below is intended to demonstrate satisfactory operation of the dynamic simulator incorporating hydrodynamic gas bearings.

2.2 Data - The following data, within the accuracy shown, shall be continuously monitored and any condition which indicates that the limits of paragraph 3 have been exceeded shall be recorded.

- a. Time of day -----
- b. Rotational speed ----- ± 500 rpm
- c. Position of shaft relative to bearing ----- ± 0.00005 inch
- d. Dynamic displacement of at least one bearing pad in each bearing ----- ± 0.00005 inch
- e. Journal bearing housings and pad and thrust bearing stator temperatures -- ± 2 Farenheit degrees
- f. Ambient gas pressure at each bearing ---- ± 0.3 psi
- g. Vibration at each bearing support ----- ± 0.0005 inch

2.3 Acceptance Test - The acceptance test shall consist of runs a through g of Table I. The test runs need not be conducted in the order listed. The applicable test cycles are defined in paragraph 2.3.1.

TABLE I
ACCEPTANCE TEST

Test Run	Position of Rotor Axis	Rotor Unbalance	Location of Rotor Unbalance	Applicable Test Cycle	Number of Test Cycles Applied
a.	horizontal	Less than 0.001 oz-in	Not specified	I	3
b.	horizontal	0.002 oz-in	3.3 inches overhung beyond rear bearing	I	3
c.	vertical	Less than 0.001 oz-in	Not specified	I	3
d.	vertical	0.002 oz-in	3.3 inches overhung beyond rear bearing	I	3
e.	horizontal	Less than 0.001 oz-in	Not specified	II	1
f.	vertical	0.002 oz-in	3.3 inches overhung beyond rear bearing	II	1
g.	horizontal	0.002 oz-in	3.3 inches overhung beyond rear bearing	III	1

2.3.1 Test Cycles - During each of the test cycles the bearing lubricant shall be dry, oil free air or inert gas. Ambient pressure at the bearings shall be equal to or less than 12.5 pounds per square inch absolute. Gas at pressure above ambient may be supplied to the bearings during acceleration, deceleration or as specified herein. The following three test cycles shall apply as specified herein:

2.3.1.1 Test Cycle I - Lubricant shall be oil free air.

- a. Accelerate rotor to 50,000 RPM and maintain $50,000 \pm 500$ RPM for a period of 10 minutes.
- b. Accelerate rotor to 60,000 RPM and maintain $60,000 \pm 1000$ RPM for a period of 1 minute.
- c. Decelerate rotor to a complete stop.

2.3.1.2 Test Cycle II - Lubricant shall be oil free air.

- a. Accelerate the rotor to 50,000 RPM and maintain $50,000 \pm 1,000$ RPM for a period of at least 10 minutes. While the rotor is maintained at $50,000 \pm 1000$ RPM and while gas at pressure above ambient is applied to the thrust bearing, apply the following thrust loads: 100 ± 10 pounds forward, 0 ± 5 pounds and 50 ± 5 pounds rearward or reversed.

While the rotor is maintained at $50,000 \pm 1000$ RPM and while no gas at pressure above 12.5 psia is applied directly to the bearings, apply the following thrust loads in the forward direction, 15 ± 5 , 10 ± 5 and 5 ± 5 pounds.

- b. Decelerate rotor to a complete stop.

2.3.1.3 Test Cycle III - Lubricant shall be commercially pure argon.

- a. Accelerate rotor to 50,000 RPM and apply 15 ± 5 pounds thrust. Maintain $50,000 \pm 500$ RPM for a period of 10 minutes or until thermal equilibrium of the bearing components and bearing supports is established, whichever results in a longer period.
- b. Decelerate rotor to a complete stop.

3. ACCEPTANCE

The test shall be satisfactorily completed when the entire acceptance test has been completed without changes to the configuration, except as authorized by the Pratt & Whitney Aircraft program manager, and the following conditions have been met.

- a. There shall be no indication of bearing seizure or contact between the rotor shaft and bearing at 50,000 RPM or above with no gas at pressure above ambient supplied. With gas supplied at a pressure above ambient there is no indication of bearing seizure or contact above 2500 RPM.
- b. Vibration at the bearing mounts does not exceed 0.002 inches double amplitude.
- c. Maximum rotor excursion does not exceed 0.005 inch axially or 0.001 inch radially
- d. Bearing pad motion does not exceed 0.0005 inch double amplitude at the free end furthest removed from the pivot.
- e. The thrust bearing axial vibratory motion at the outer rim shall not exceed 0.0006 inch double amplitude.

APPENDIX C - DESIGN AND TEST OF THE INITIAL BEARING SYSTEM

As mentioned in the introduction to this report, three variations of the basic bearing system for the turbocompressor were designed and tested. This appendix documents the bearing and rotor-dynamics design and test data for the first, or initial, bearing system.

As implied above, final design of the gas-bearing system for the turbocompressor (as described in Section II of this report) is identically the same as the initial design with regard to types of bearings used, bearing sizes, bearing locations, and bearing heat transfer mechanisms. Since the data given in Section II pertaining to (1) basic turbocompressor operating conditions, and (2) overall bearing system requirements, did not change between the initial and final bearing system designs, this data will not be repeated here. Furthermore, since the discussions given in Section II pertaining to selection of bearing types, bearing sizes, bearing materials, and bearing instrumentation, were, in fact, originally formulated with regard to the initial bearing system design, there is likewise no need to repeat these discussions here.

Differences Between Initial and Final Bearing System Designs

The only differences between the initial and final designs of the journal bearings are

1. the values of the pad clearance-to-radius ratio (C_p/R) for each bearing,
2. the selection of operating clearances for each bearing, and
3. the stiffness values of the support flexures for the "upper" pads in each bearing.

The significant advantages of the final journal bearing designs (relative to the initial designs) resulting from these changes are

1. lower friction losses, and

2. improved ability to accommodate temperature changes and temperature differentials within the bearing regions without exceeding safe bearing clearances.

A comparison of the design parameters and calculated performance characteristics for the initial and final journal bearing designs is given in Table C-1. It is seen that the pad clearance ratio (C_p/R) of both bearings is smaller for the initial design, while the bearing preload ratio (m) is the same or larger. The net result is that the operating clearances of the initial design are smaller than those of the final design, resulting in considerably higher friction losses in the initial design.

The choice of values for the C_p/R and m parameters of the initial bearing designs were not arbitrary, but rather reflected the state of operational experience from other successful gas-bearing machinery developments. The criterion which led to the specific selection of 0.001 and 0.5 as values for C_p/R and m , respectively, was that the roll and pitch resonant frequencies of the individual bearing pads should always be significantly above shaft speed throughout the turbocompressor operating range. This would insure that all pads would track shaft precessions accurately and without sizeable phase lag, thus insuring stable operation. It is seen from Figures C-1 through C-4 that the calculated roll and pitch frequency ratios (N_p/N and N_R/N) for the initial bearing designs are always larger than 1.5 at the design value of ambient pressure (12 psia). Even at the reduced value of ambient pressure (6 psia) the calculated ratios are never less than 1.2. These results were representative of state-of-the-art design practice and hence constituted the most logical point at which to begin development of the bearings.

The obvious disadvantage of the initial design was the rather high bearing friction losses relative to losses which would be expected at larger values of the C_p/R parameter (assuming constant preload ratio). However, at larger C_p/R values, the pad resonant frequency criterion would not have been satisfied. Since the consequences of not satisfying this criterion were not known, the prudent decision was to accept the higher friction losses in return for maximum assurance of a successful first design. It was felt that attempts to optimize the bearing design, from

the standpoint of minimizing friction losses, should most properly follow successful demonstration of an initial design which best reflected state-of-the-art design practice.

With respect to the turbocompressor thrust bearings, the only change between the initial and final designs was a reduction (from 20 to 5) in the number of supply orifices in the forward hydrostatic thrust bearing. This change was necessitated by pneumatic instability in the initial design. The reduction in number of orifices eliminated this instability without detrimental loss in bearing load capacity, as is discussed in a later section of this appendix.

TABLE C-1
 JOURNAL BEARING DESIGN PARAMETERS AND
 CALCULATED PERFORMANCE CHARACTERISTICS

All data given below is based upon the following gas-bearing operating conditions

Rotor speed	- 50,000 RPM
Lubricant gas	- Argon
Bearing ambient pressure	- 12.0 psia

	<u>Initial Design</u>	<u>Final Design</u>
Configuration	Pivoted-pad (with hydrodynamic lift-off)	Pivoted-pad (with hydrodynamic lift-off)
Journal Diameter, Inches		
No. 1 (Forward) Bearing	1.500	1.500
No. 2 (Turbine End) Bearing	2.125	2.125
Bearing Length-to-Diameter Ratio (L/D)		
No. 1 Bearing	1.0	1.0
No. 2 Bearing	1.0	1.0
Number of Pads Per Bearing	4	4
Pad Orientation (Referenced to horizontal orientation of the rotor)	Rotor weight between pivots	Rotor weight between pivots
Arc Length (β) of Pad, Degrees	80.0	80.0
Pivot Location (θ_p/β) from Leading Edge	0.65	0.65
Pad Clearance Ratio (C_p/R)		
No. 1 Bearing	0.0010	0.0018
No. 2 Bearing	0.0010	0.0030
Bearing Preload Ratio (m)		
No. 1 Bearing	0.50	0.50
No. 2 Bearing	0.50	0.788

TABLE C-1 (cont.)

	<u>Initial Design</u>	<u>Final Design</u>
Individual Pad Mass, Pounds		
No. 1 Bearing	0.14	0.14
No. 2 Bearing	0.21	0.21
Pivot Ball Diameter, Inches		
No. 1 Bearing	0.2500	0.2500
No. 2 Bearing	0.3750	0.3750
Pivot Socket Diameter, Inches		
No. 1 Bearing	0.2550	0.2550
No. 2 Bearing	0.3824	0.3824
Bearing Number (Λ)		
No. 1 Bearing	10.7	2.98
No. 2 Bearing	11.5	1.23
Measured Pivot-Support Radial Stiffness, lb./in.		
No. 1 Bearing	50,000 (all pads)	9,800 (upper pads) 50,000 (lower pads)
No. 2 Bearing	70,000 (all pads)	8,400 (upper pads) 70,000 (lower pads)
Bearing Load, Pounds		
Horizontal Orientation (Rotor Weight)		
No. 1 Bearing	3.63	3.63
No. 2 Bearing	7.72	7.72
Space Operation (Due to 0.002 ounce- inches mass unbalance in turbine plane)		
No. 1 Bearing	1.01	0.38
No. 2 Bearing	1.67	1.23
Operating Clearance at Pivot, Inches		
Horizontal Orientation (Loaded Pads)		
No. 1 Bearing	0.00033	0.00057
No. 2 Bearing	0.00046	0.00058
Space Operation (All Pads)		
No. 1 Bearing	0.00037	0.00067
No. 2 Bearing	0.00053	0.00067
Friction Loss Per Journal, Watts		
Horizontal Orientation		
No. 1 Bearing	110.5	57.4
No. 2 Bearing	336.0	235.8
Space Operation		
No. 1 Bearing	109.0	56.5
No. 2 Bearing	331.0	232.5

TABLE C-1 (cont.)

	<u>Initial Design</u>	<u>Final Design</u>
Radial Gas-Film Stiffness, lb./in.		
Horizontal Orientation		
No. 1 Bearing	73,000	34,400
No. 2 Bearing	104,100	75,000
Space Operation		
No. 1 Bearing	70,940	33,100
No. 2 Bearing	100,900	72,200
Gas Film Temperature, °F		
No. 1 Bearing	213	
No. 2 Bearing	376	
Shaft Temperature, °F		
No. 1 Bearing	206	
No. 2 Bearing	330	
Pad Temperature, °F		
No. 1 Bearing	230	
No. 2 Bearing	390	
Shaft Material	Waspaloy	Waspaloy
Pad Material	M-1 Tool Steel	M-1 Tool Steel
Pivot Material	M-1 Tool Steel	M-1 Tool Steel
Journal and Pad Surfacing Material	Chrome Oxide	Chrome Oxide

Initial Design of the Journal Bearings

The procedure used for calculating performance of the journal bearings is described in Section II of this report. The calculated performance in argon for the initial design of the No. 1 and No. 2 bearings at 6.0 and 12.0 psia ambient pressure is shown in Figures C-1 through C-4. The calculations include the effects of centrifugal growth of the journals and deflection of the pivot flexures due to the individual pad loads. The measured values of flexure stiffness were used for these calculations.

For the initial journal bearing designs, the four pivot-support flexures for each bearing were designed to have the same stiffness, this stiffness being approximately equal to the stiffness of the gas film. The design stiffness of the individual flexures was 100,000 lb./in. for the No. 2 (turbine) bearing and 63,000 lb./in. for the No. 1 (compressor) bearing. Actual measured stiffness of the flexures was 70,000 and 50,000 lb./in. for the No. 2 and No. 1 bearings, respectively. The discrepancy between design and measured values of flexure stiffness is believed to be due to "non-ideal" boundary conditions which exist at the ends of the flexure sections. For the purposes of design, a zero-slope boundary condition was assumed at the ends of the two beam sections of which each flexure is comprised (see Figure C-5). In actual fact, this assumption was probably somewhat in error due to (1) some deflection of the thicker central portion of the flexure (which carries the pivot screw), and (2) some deflection within the clamping zone at the two ends of the flexure.

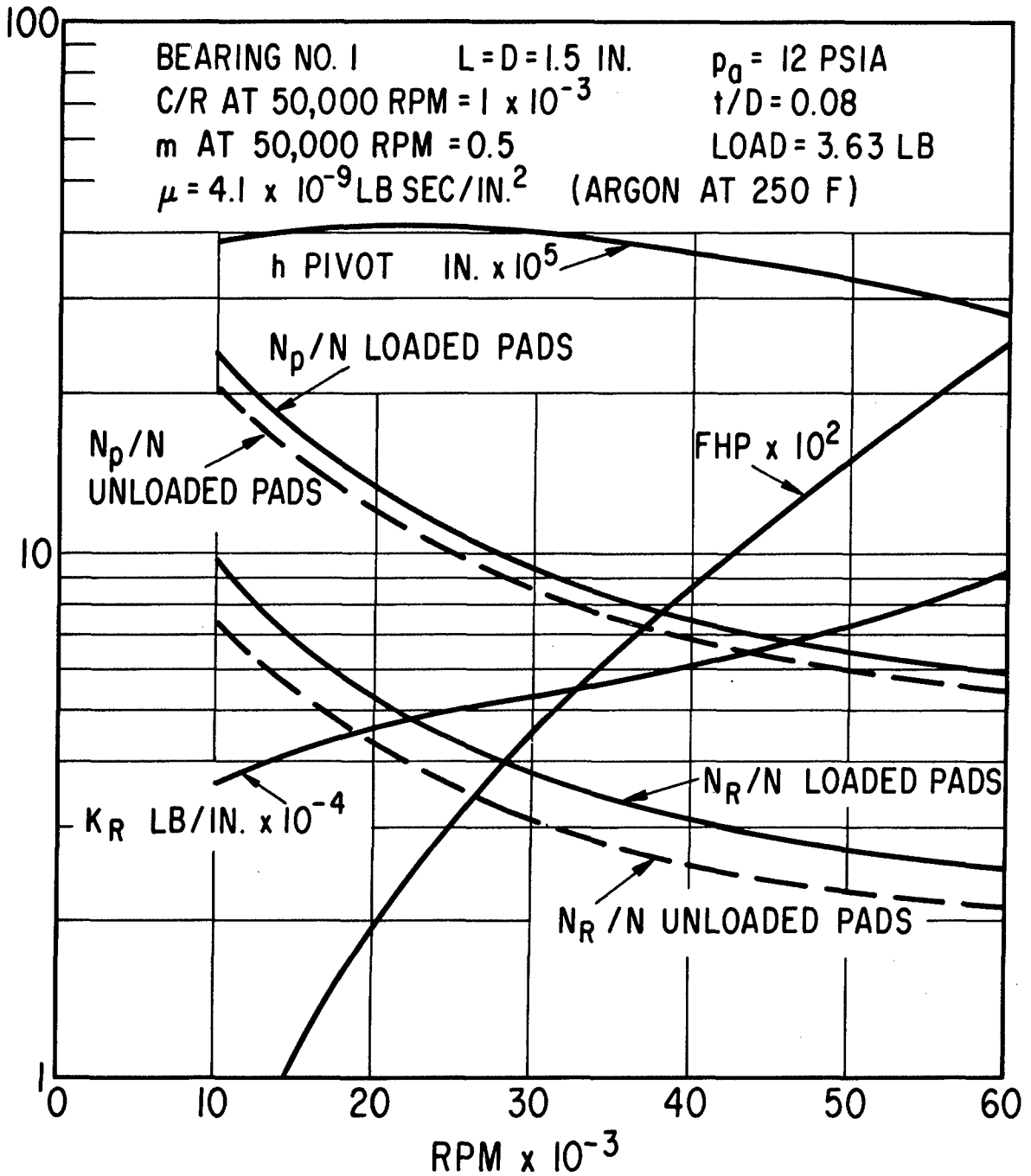


Fig. C-1 - Calculated Performance In A 12.0 PSIA Argon Environment For The Initial Design Of The No. 1 Journal Bearing (Rotor horizontal relative to a 1-g gravitational field)

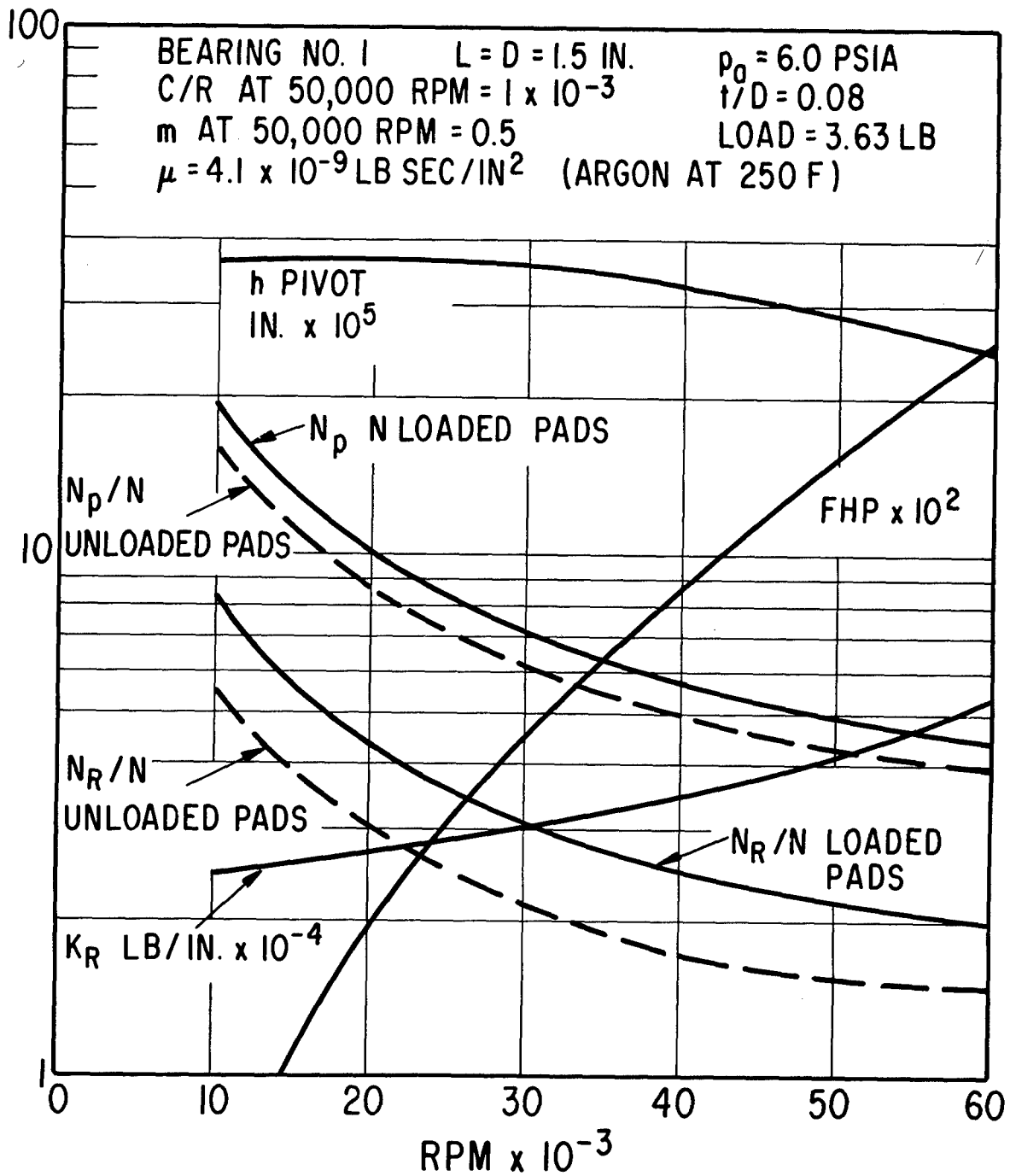


Fig. C-2 - Calculated Performance In A 6.0 PSIA Argon Environment For The Initial Design Of The No. 1 Journal Bearing (Rotor horizontal relative to a 1-g gravitational field)

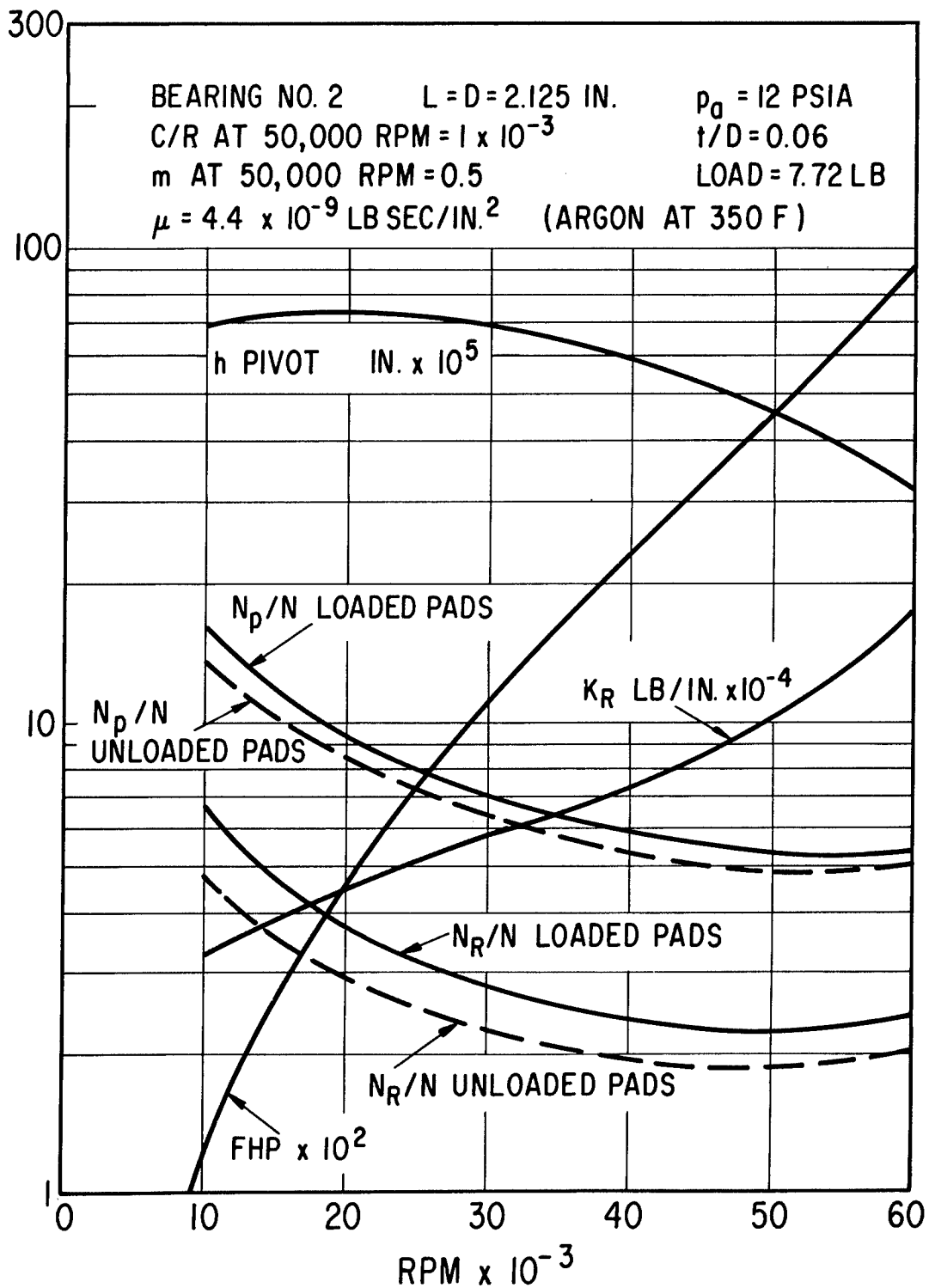


Fig. C-3 - Calculated Performance In A 12.0 PSIA Argon Environment For The Initial Design Of The No. 2 Journal Bearing (Rotor horizontal relative to a 1-g gravitational field)

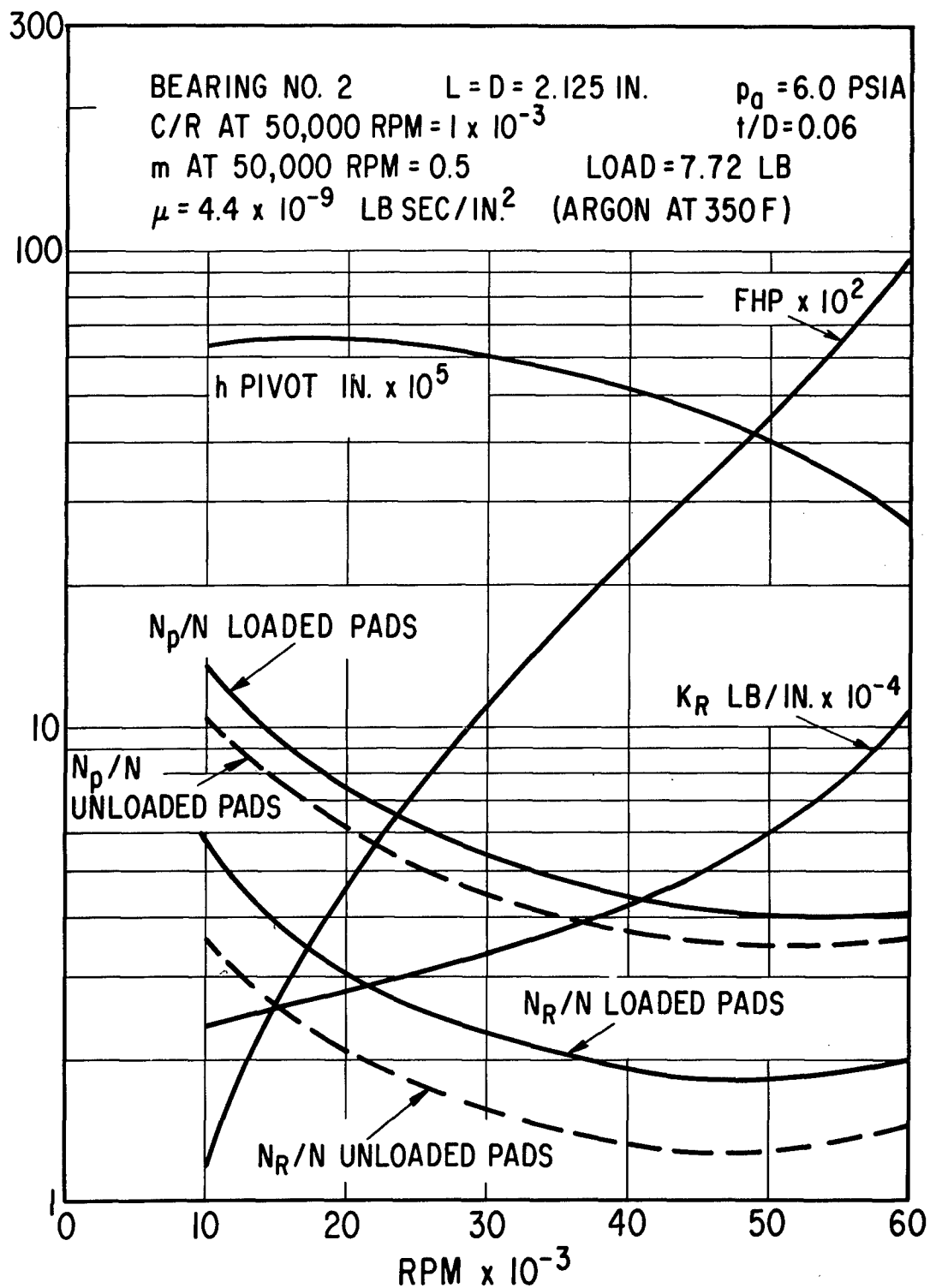


Fig. C-4 - Calculated Performance In A 6.0 PSIA Argon Environment For The Initial Design Of The No. 2 Journal Bearing (Rotor horizontal relative to a 1-g gravitational field)

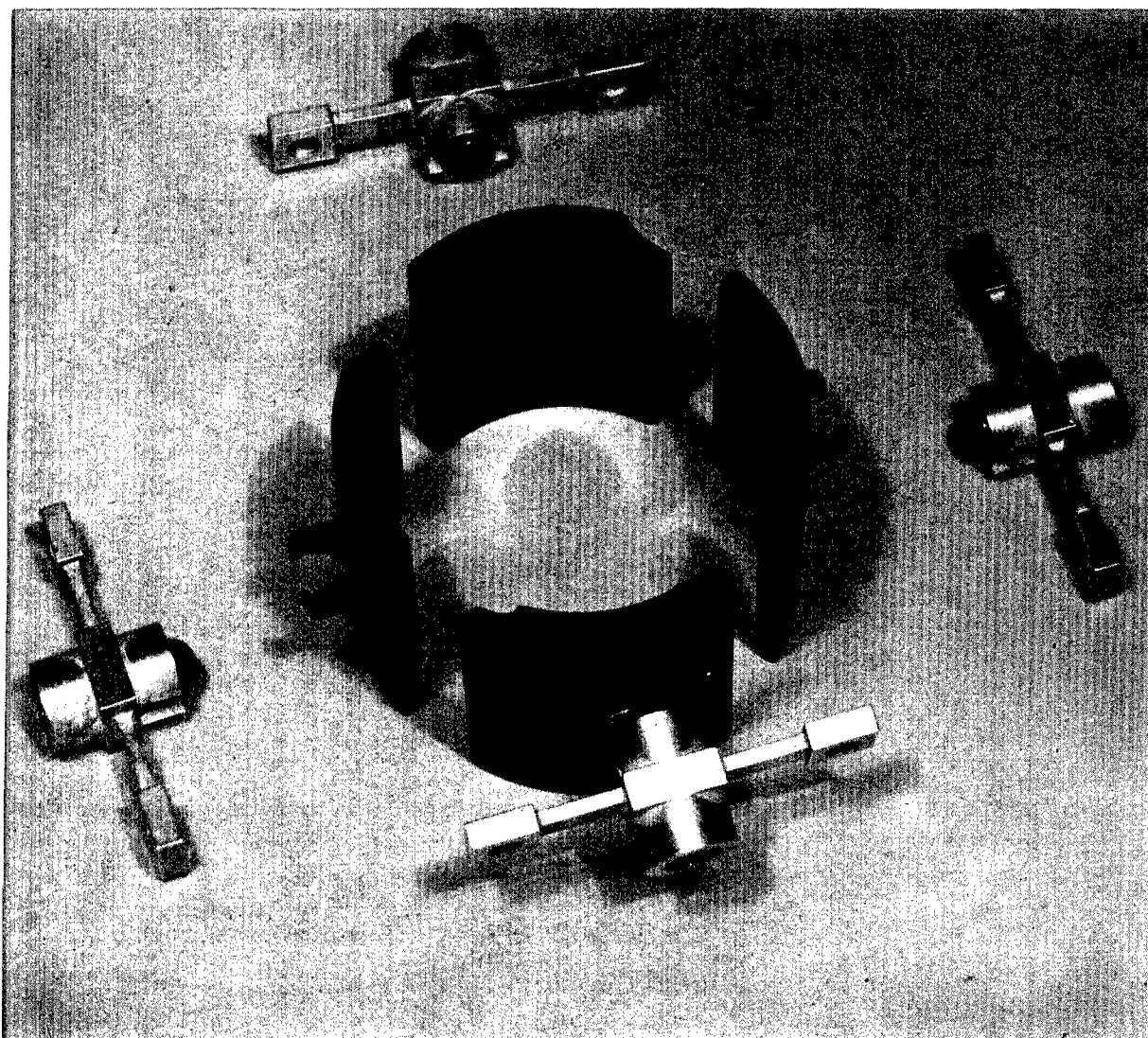


Fig. C-5 - View of No. 1 Bearing Pivot-Support Flexures And Pivoted-Pads For Initial Bearing Design

Initial Design of the Thrust Bearings

The operating conditions and requirements for the hydrodynamic and hydrostatic thrust bearings are described in Section II of this report. As mentioned previously, the only difference between the initial and final design of the thrust bearings is in the number of orifices in the forward hydrostatic thrust bearing. Due to a pneumatic instability in the initial design (which will be discussed shortly) the number of orifices was reduced from 20 to 5.

The calculated performance characteristics of the reverse hydrostatic and forward hydrodynamic thrust bearings are given in Section II and are not repeated here since there is no difference between the initial and final configurations of these bearings. The calculated performance characteristics of the initial forward hydrostatic thrust bearing with 20 orifices is shown in Figure C-6.

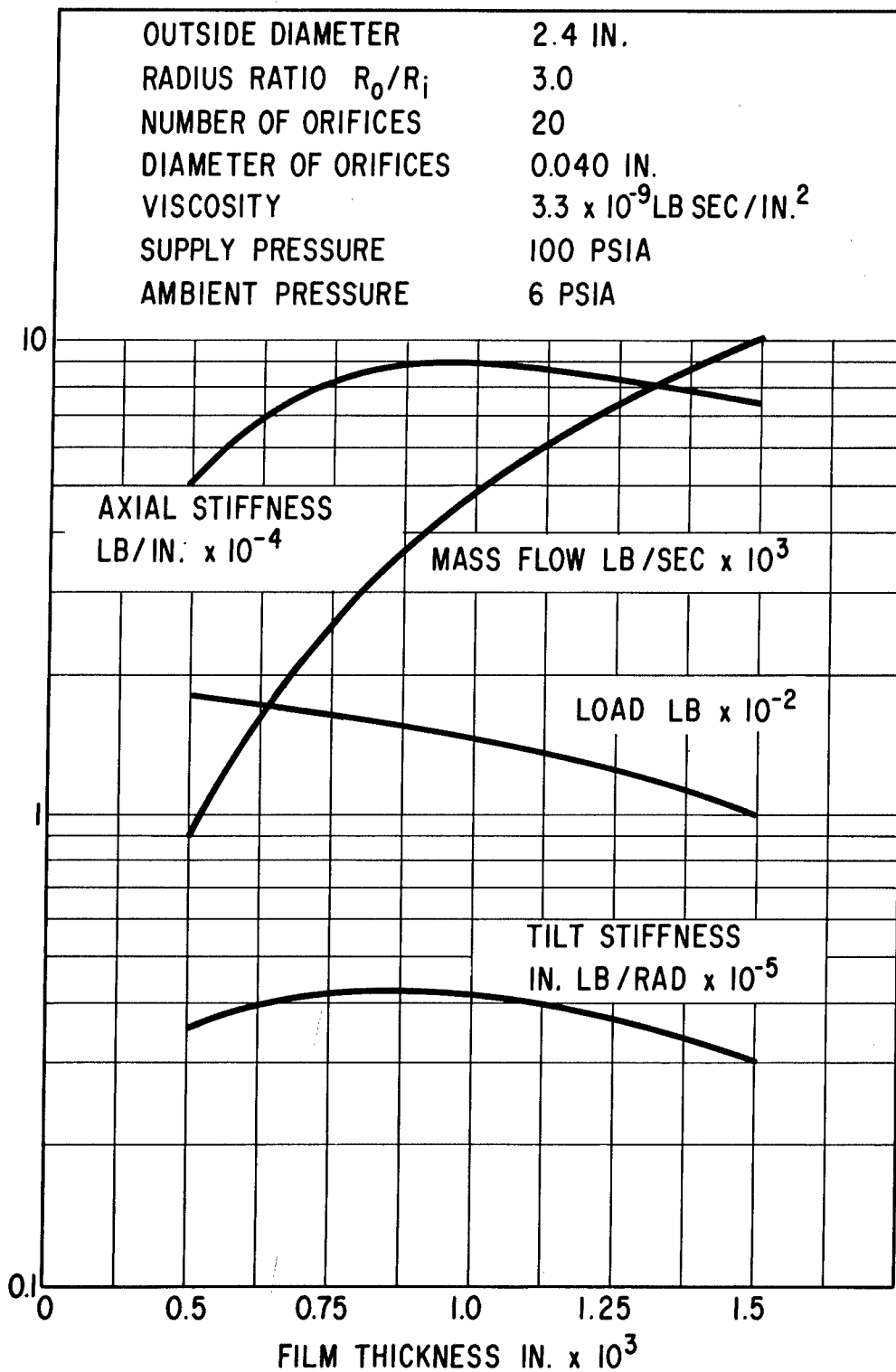


Fig. C-6 - Calculated Performance Of The Initial Design Of The Forward Hydrostatic Thrust Bearing With 20 Orifices

Rotor Dynamics of the Initial Bearing System Design

The critical speeds for the initial design of the turbocompressor rotor-bearing system are plotted in Figure C-7 as a function of bearing stiffness. Superimposed on this plot are the calculated stiffnesses of the No. 1 and No. 2 journal bearings as a function of speed. The intersections of the critical speed and bearing stiffness curves identify the speeds at which rotor resonances could be expected to occur in the presence of sufficient rotor unbalance. The two lowest critical speeds are essentially rigid-body resonances of the rotor due to the stiffness of the gas film and the pivot-support flexures. It is seen from Figure C-7 that the two "rigid-body" resonances should occur at approximately 8,700 and 14,000 rpm, which are sufficiently low to be of little concern to turbocompressor operation. The third critical speed, which is slightly above 90,000 rpm, is the first free-free bent shaft critical of the rotor and is virtually unaffected by bearing stiffness. Although a slight influence of this critical speed would be expected at the 50,000 and 60,000 rpm design and overspeed conditions, it is sufficiently above these speeds to be considered a minimal development problem and well within the state-of-the-art of present balancing techniques.

The calculated bearing loads due to 0.002 ounce-inches of unbalance in the turbine plane (the rotor being otherwise perfectly balanced) are plotted in Figure C-8 as a function of speed. The value of 0.002 ounce-inches of unbalance was assumed to occur over a period of 10,000 hours due to unsymmetrical mass shift in the turbine. It is seen from Figure C-8 that the unbalance will cause the No. 2 journal to experience resonant amplitudes at the lowest rigid-body critical, while the No. 1 journal will resonate at the second rigid-body critical. In other words, the nodal point for the second critical speed is located at the No. 2 bearing. This result was confirmed by the calculated mode shapes for the rotor at the two rigid-body critical speeds.

It should be pointed out that the stiffness and damping data for the two bearings which was used to calculate the dynamic bearing loads of Figure C-8 are, rigorously speaking, valid only at 50,000 rpm. Hence, the absolute values of bearing forces

in the vicinity of the rigid-body criticals may be appreciably in error. However, over the range of 30,000 to 60,000 rpm, it is seen that the 0.002 ounce-inches of unbalance adds approximately 1.0 pound of rotating load to the steady-state loading of the No. 1 journal, and approximately 1.7 pounds of rotating load to the No. 2 journal. The plots of maximum safe bearing load capacity, shown in Figures C-9 and C-10, indicate that this additional amount of load due to unbalance should not be a problem. The criterion used to define 'safe bearing load capacity' is that $\epsilon_b \cos\psi$ for the bearing should not exceed a value of 0.4 at 50,000 rpm. This criterion assures that the film thickness at the pivot location of the loaded pads for the No. 1 and No. 2 bearings will never be less than 0.22 and 0.32 mils, respectively, over a speed range from 30,000 to 60,000 rpm. Based on practical experience, these film thicknesses are judged to be safe for continuous long-term operation of the bearings.

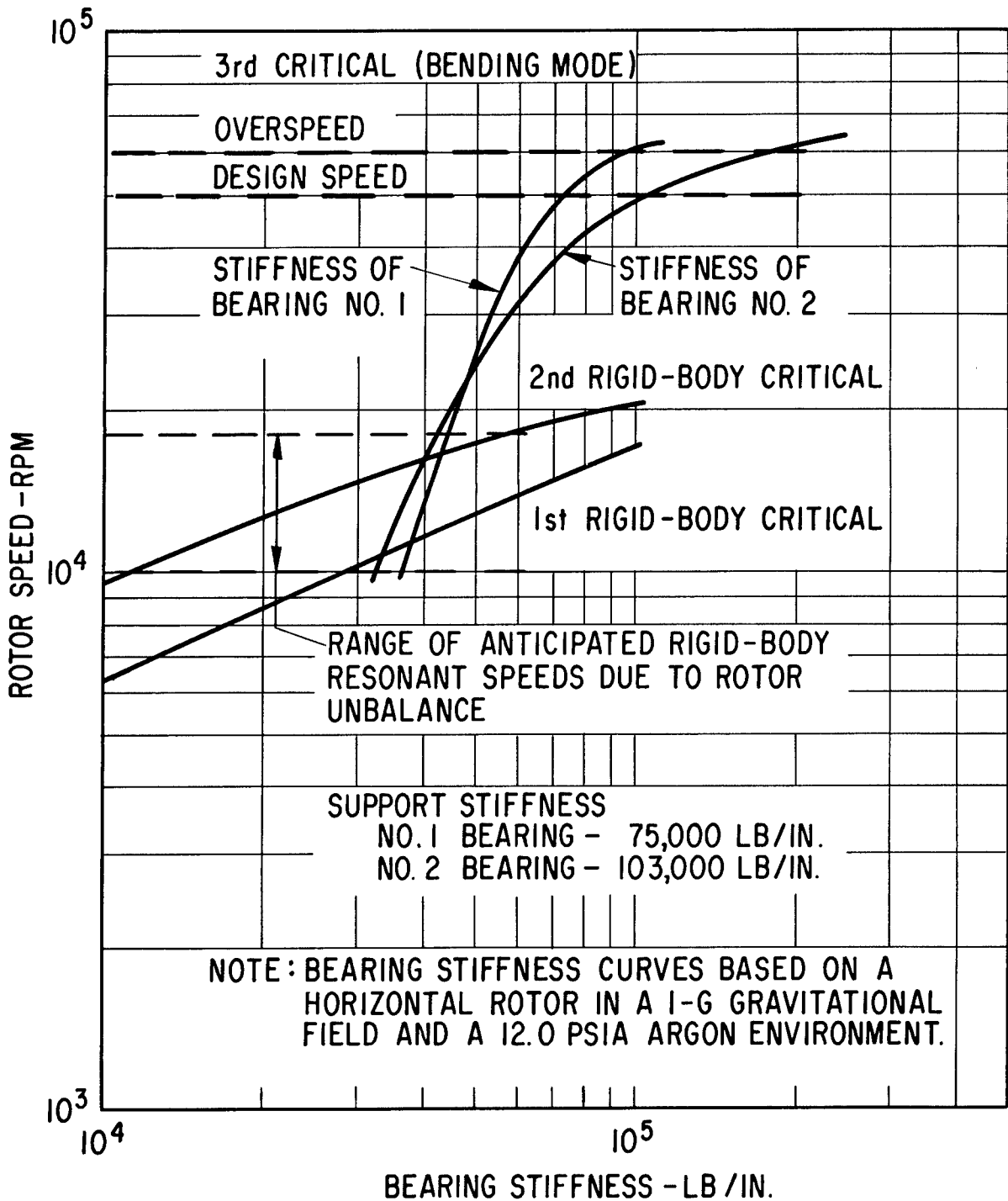


Fig. C-7 - Calculated Critical Speeds And Bearing Stiffness For The Initial Bearing System Design (Bearing stiffness data based on horizontal rotor orientation relative to a 1-g gravitational field and a 12.0 psia argon environment)

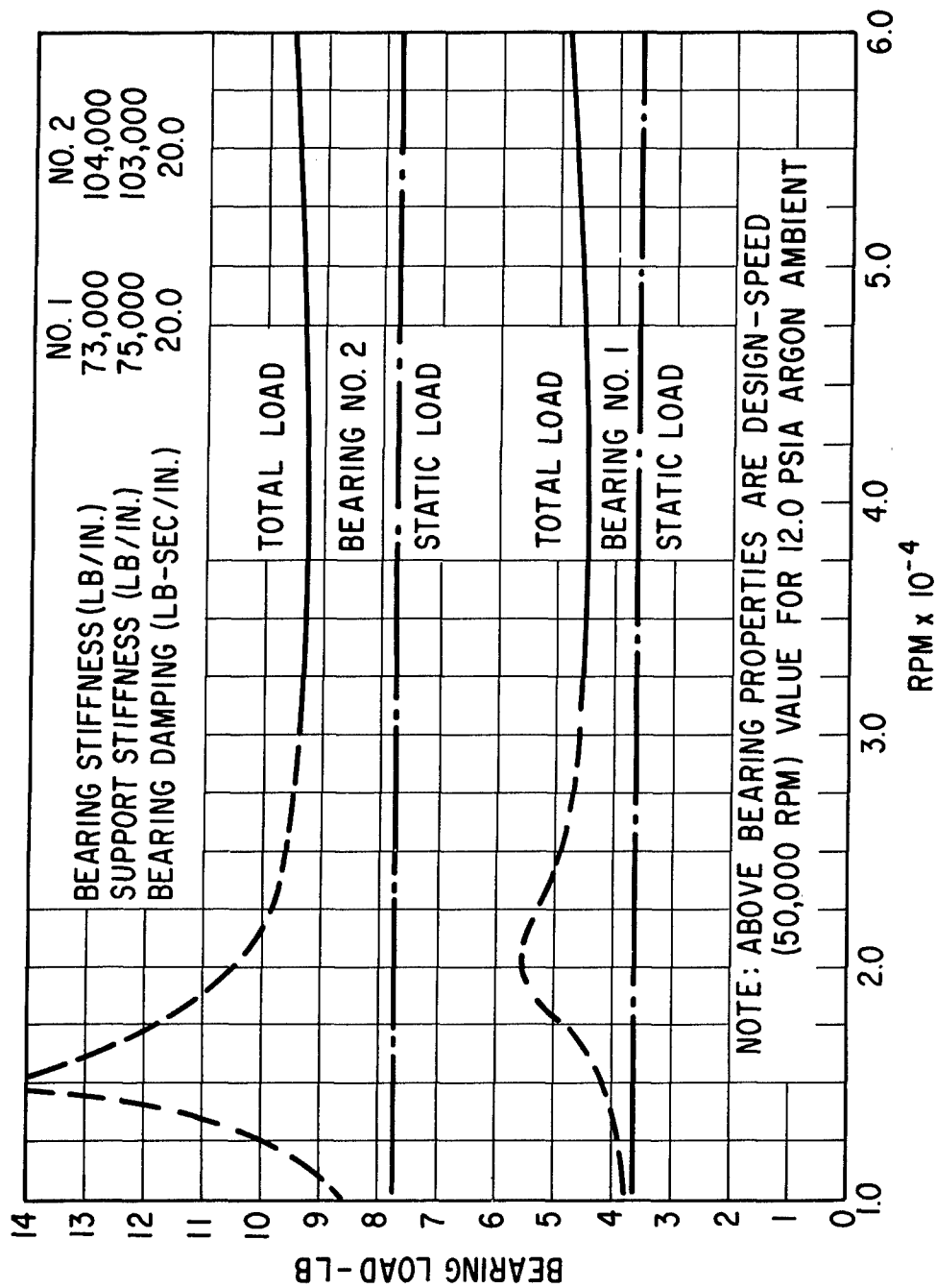


Fig. C-8 - Calculated Maximum Bearing Loads For The Initial Bearing Design Due To 0.002 Ounce-Inches Unbalance In The Turbine Plane

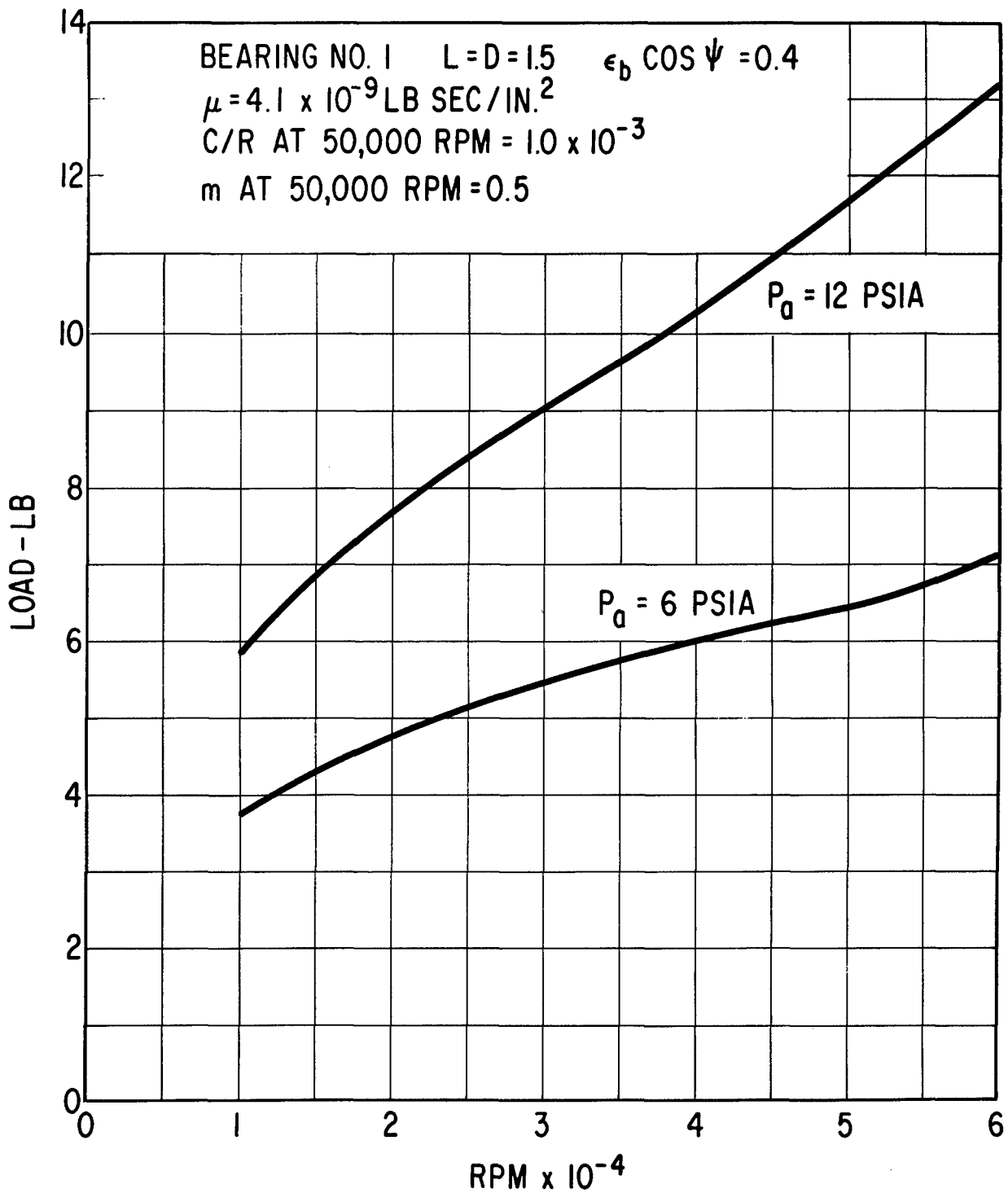


Fig. C-9 - Maximum Recommended Load Capacity Vs. Speed For Continuous-Duty Operation Of The Initial Design Of The No. 1 Journal Bearing

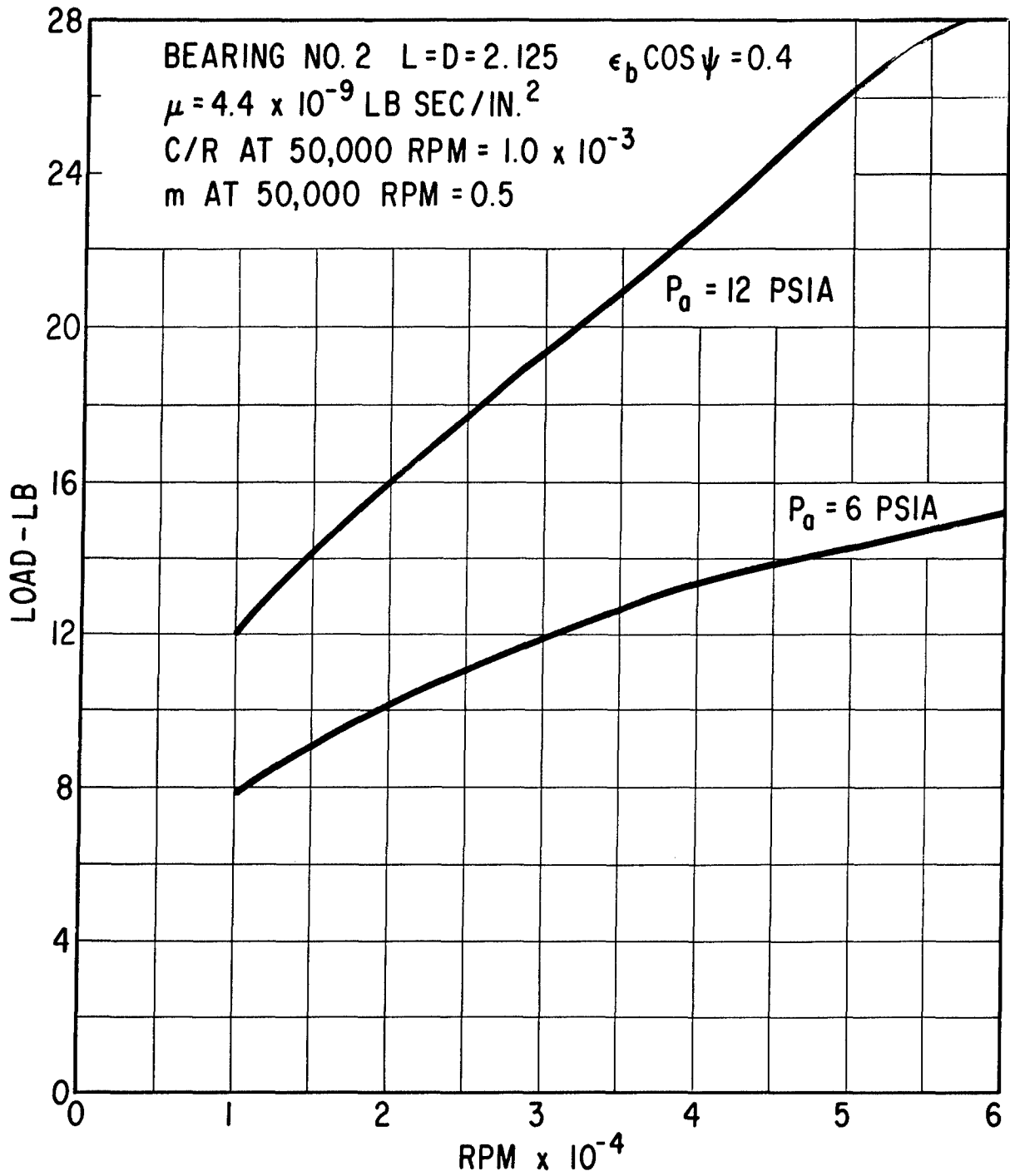


Fig. C-10 - Maximum Recommended Load Capacity Vs. Speed For Continuous-Duty Operation Of The Initial Design Of The No. 2 Journal Bearing .

Heat Transfer Design for Initial Bearing System

The design of a satisfactory cooling technique for the turbocompressor bearing system was a difficult task and one that illustrates the importance of careful consideration of all the various interrelated aspects of turbomachinery design. The problem was defined as one of maintaining safe gas-bearing clearances while removing bearing friction losses with

1. a minimum of temperature rise in the bearing regions;
2. a minimum of thermal distortion of the bearing parts;
3. a minimum of system power loss for auxiliary bearing coolant flows (in the form of either turbocompressor bleed-gas flows, or externally circulated liquid flows).

Maximum allowable bearing region temperature was fixed at 400 F by the insulation of the lead wire for the bearing system capacitance probes (the bearing materials themselves had been successfully tested for short periods of time at temperatures up to 500 F as described in Appendix F).

Three different approaches to cooling the bearings were considered.

1. Transfer of friction losses by conduction to a naturally occurring heat sink within the turbocompressor (i.e., compressor discharge gas).
2. Transfer of losses by conduction and convection to a flow of argon passing through the journal bearing regions.
3. Transfer of losses by convection and/or conduction to a flow of secondary liquid coolant fluid.

All of these techniques were examined for the turbocompressor application. Since the No. 2 (turbine) bearing is in the most severe thermal environment, and since this bearing has the highest heat generation rate, the heat transfer investigation for this bearing is discussed in detail below. Similar consideration and investigations were, of course, also required for the No. 1 journal bearing and for the thrust bearings. However, only the final heat transfer design for these bearings will be presented here.

The No. 2 bearing mount is located on the compressor discharge duct and hence assumes a temperature very close to compressor discharge gas temperature, which is about 350 F. The rotor section between the bearing and the turbine is reduced in cross-section to limit heat conduction from the turbine to the bearing region. Since gas pressure at the exit of the turbine nozzle is lower than compressor exit pressure, some argon will tend to flow through the bearing compartment from the compressor to the turbine. This leakage flow is controlled by labyrinth seals and is utilized to cool the rotor section between the bearing and the turbine to further aid in thermal isolation of the turbine.

In an effort to find a simple low-penalty heat rejection system, the possibility of removing bearing friction losses via the gas leaking from the compressor to the turbine, in combination with heat transfer from the bearing through the rotor and into the compressor discharge gas, was examined. The resulting maximum bearing temperature was between 800 and 900 F — obviously unsatisfactory. In order to improve rotor heat conduction, silver was added to the bore of the rotor. Similarly, to improve the gas cooling, the labyrinth seal clearances were enlarged to permit a larger leakage flow. This configuration resulted in a reasonably uniform temperature distribution, but the maximum temperature of the bearing was 670 F and the design was still considered unsatisfactory.

Additional cooling was clearly required. Since liquid coolant was to be used for alternator cooling elsewhere in the power plant, the use of this coolant was next considered for cooling the No. 2 bearing. A stationary cooling jacket was designed to encase the bearing and the rotor in the immediate area of the bearing. Since the bearing pads and the rotor must be free to move, a clearance of 0.01 inches was provided between the jacket and the bearings. The clearance space would, of course, contain bearing ambient gas (i.e., argon at compressor discharge pressure). However, it was found that this clearance space represented an excessive thermal barrier and the resulting bearing temperature of 615 F did not meet the design criterion. Addition of silver to the bore of the rotor to further improve rotor heat conduction further decreased the bearing temperature to 470 F, but this still did not satisfy the design criterion. In addition to the silver heat shunt, the use of a stationary cooling plug projecting inside the bearing was investigated.

Because of machining and assembly tolerances, and thermal expansions during transient operation of the turbocompressor, a gap of 0.025 inches was required between the plug and the shaft. This gap likewise represented an excessive thermal barrier and the combination of liquid-cooled jacket on the outside of the bearing and liquid-cooled plug on the inside of the journal still did not provide a satisfactory bearing temperature.

In order to use liquid coolant effectively, it became apparent that the liquid should be introduced as close to the source of heat generation as possible. Therefore, internal liquid cooling of the journal bearing pivoted-pads was examined. The net result was excellent. With liquid flowing through the pads at about 310 F, the bearing operated at 350 F. This approach was very satisfactory except for one factor. In a pivoted-pad bearing, the pads must be free to move. Restraint of the pads can lead to unstable operation of the rotor system. The basic bearing system design philosophy for the turbocompressor was to employ established practice as much as possible. Since liquid-cooled pads had not been demonstrated experimentally, and since the liquid lines would introduce pad restraints, the liquid-cooled pad concept was rejected for the journal bearings.

As demonstrated by the results of the liquid cooling studies, the coolant should be introduced as close to the heat source as possible. A gas-cooling system was therefore next examined in which argon would be introduced into heat exchangers located inside the rotating journals. The cooling flow path is shown in Figures C-11 and C-12 for this arrangement. A flow of argon is taken from compressor discharge and passed through an external heat exchanger to cool the gas to approximately 100 F. The cooled argon is then fed into the thrust bearing compartment and from there flows down the center of the rotor, passing through heat exchangers located in the bores of the No. 1 and No. 2 journal bearings. From the No. 2 heat exchanger the argon is discharged into the No. 2 bearing compartment. Since the argon cooling flow is derived from compressor discharge, the pressure in the No. 2 bearing compartment is determined by the coolant flow and is higher than the downstream pressure of all seals communicating with the No. 2 bearing compartment. Argon flow into the bearing compartment is thus balanced by four flows out of the compartment as follows:

1. Labyrinth leakage to the inlet of the compressor diffuser
2. Labyrinth leakage to the high-pressure side of the turbine disc
3. Labyrinth leakage to the low-pressure side of the turbine disc, and
4. intentional bleed-flow from the No. 2 bearing compartment to the No. 1 bearing compartment to warm the No. 1 bearing housing in order to maintain proper bearing clearances.

The argon cooling gas is thus used for three purposes in this heat transfer concept; (1) to cool the journal bearing regions, (2) to provide labyrinth seal leakage flows, and (3) to provide gas at the highest possible pressure to both the No. 1 and No. 2 self-acting journal bearings.

A photograph of the No. 1 and No. 2 journal bearing heat exchangers is shown in Figures C-13 and C-14, respectively. Figure C-15 shows the boundary conditions for the heat transfer model of the No. 2 journal bearing region and the isotherms as determined by computer solution of the heat transfer model. It is seen that the surface temperature of the rotating journal will vary from approximately 345 to 370 F while the temperature of the pivoted-pads will vary from 380 to approximately 400 F. This cooling technique thus provides a fairly uniform temperature distribution in the No. 2 bearing and provides bearing operating temperatures within the design objectives. Since this type of bearing cooling had been successfully applied to previous gas-bearing applications, and was a solution to the present turbocompressor cooling requirements, this concept was selected as the basis for the initial journal bearing cooling system design.

As mentioned above, and illustrated by Figures C-11 and C-13, the No. 1 journal bearing is also gas-cooled via a heat exchanger located at the ID of the journal. However, all attempts to gas cool the forward (hydrodynamic) thrust bearing were found to be unsatisfactory in that excessively high thrust bearing temperatures resulted and/or significant temperature gradients existed which would produce excessive thermal distortion of the thrust plate. Consequently, the concept of a liquid-cooled thrust stator was adopted wherein the coolant (Versilube, glycol, or similar fluids) is circulated through annular passages within the aluminum

thrust plate. Figure C-16 shows the calculated performance of the thrust bearing liquid cooling system as a function of coolant flow rate. It is seen that a flow rate between 100 and 200 lb./hr. at an inlet temperature of 150 F will result in reasonable thrust bearing temperatures and temperature gradients, as well as low coolant pressure-drop values.

The heat transfer model for the No. 1 journal bearing and the liquid-cooled thrust bearing is shown in Figure C-17. The design philosophy for this model was to achieve an essentially isothermal area. This was accomplished by thermally isolating the journal and thrust bearing support housing from the relatively cool (76 F) casing which forms part of the compressor gas inlet duct, and to which the bearing housing is physically attached. The calculated isotherms for the heat transfer model are shown in Figure C-18. It is seen that the surface temperature of the No. 1 journal varies from approximately 199 to 213 F, while the pad temperature varies from 228 to 233 F. The thrust runner temperature ranges from 208 to 218 F. Hence, the compact and highly integrated assembly of the No. 1 journal bearing and the thrust bearing is closely matched in temperature level, and temperature gradients within any given component are quite small.

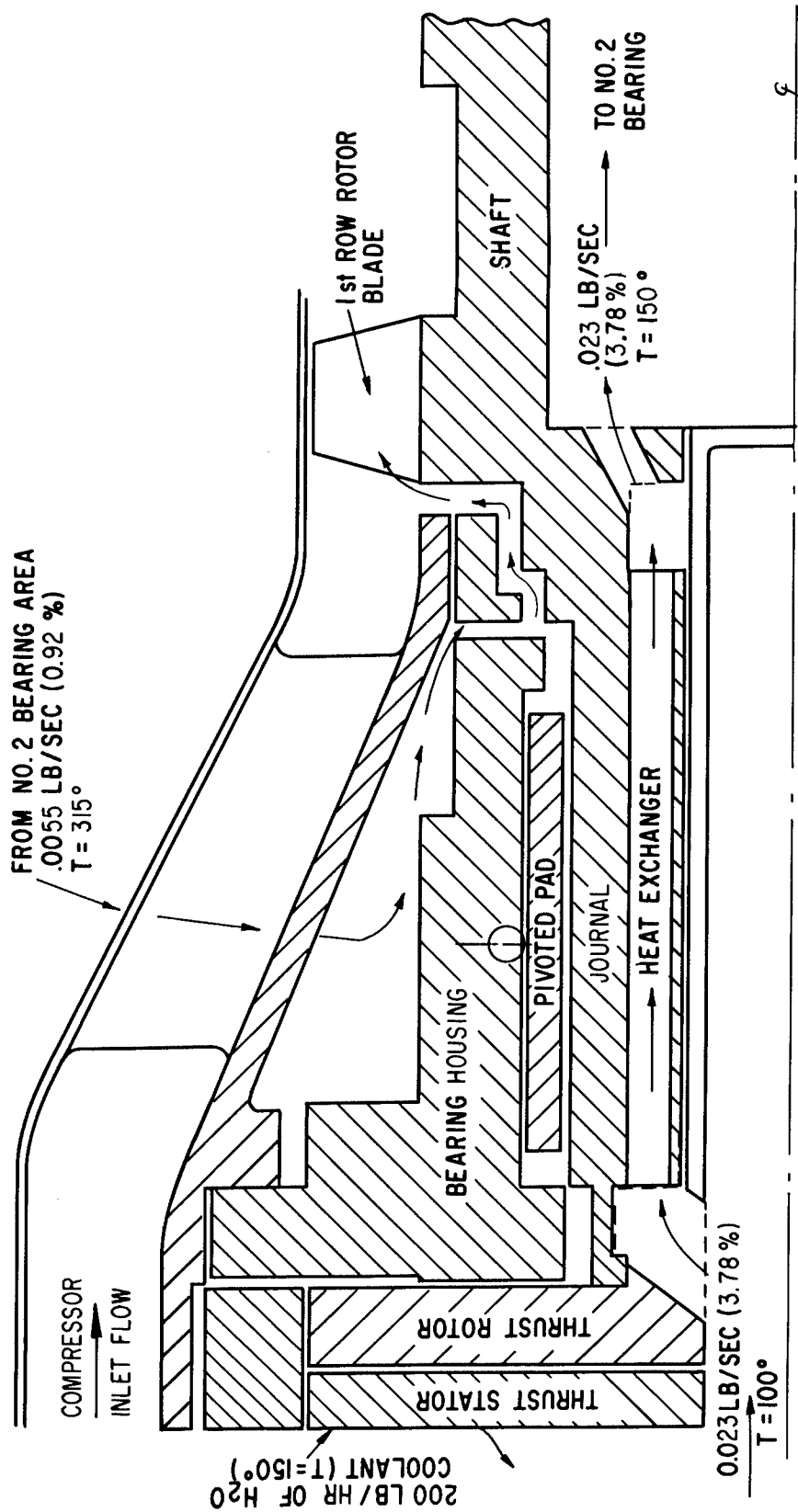


Fig. C-11 - Argon Cooling Gas Flow Diagram For The Initial Design Of The No. 1 Journal Bearing And Thrust Bearing

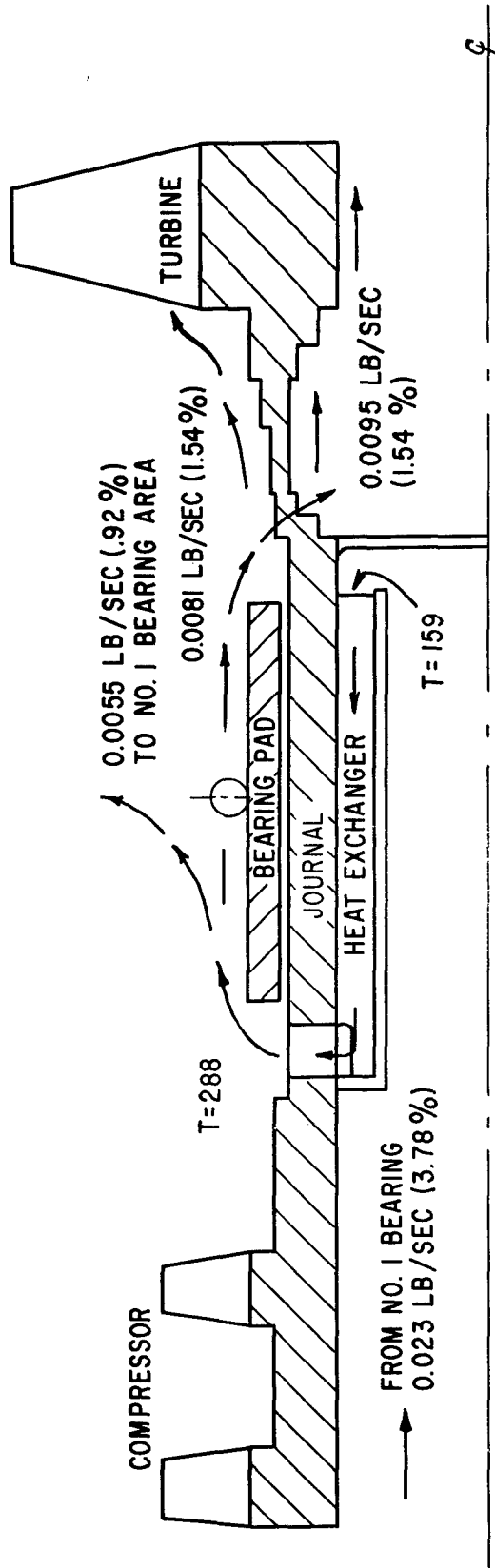


Fig. C-12 - Argon Cooling Gas Flow Diagram For The Initial Design Of The No. 2 Journal Bearing

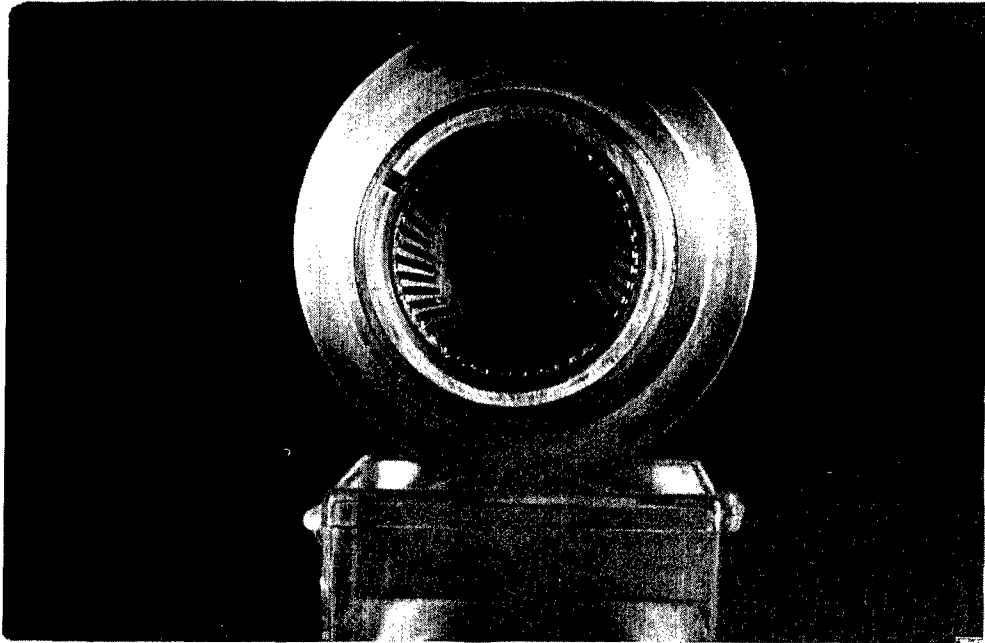


Fig. C-13 - Heat Exchanger For No. 1 Journal After Brazing Into Rotor

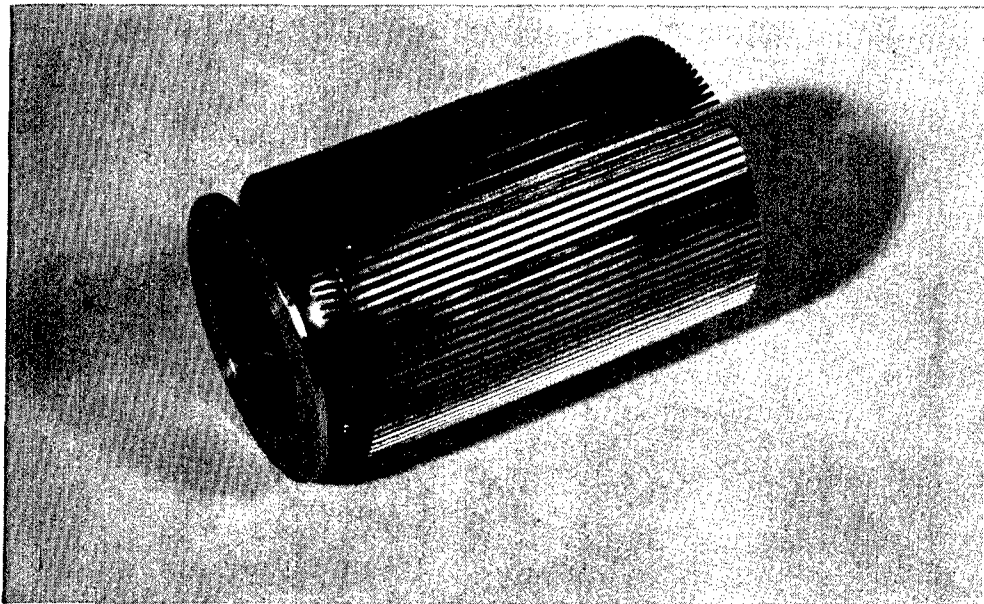
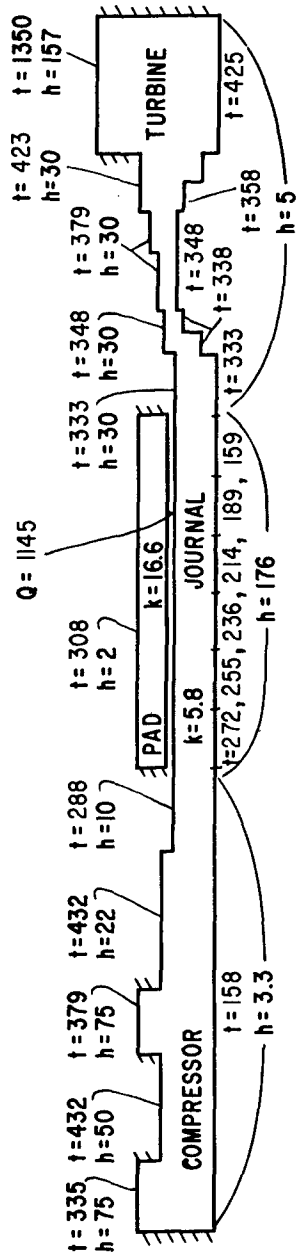
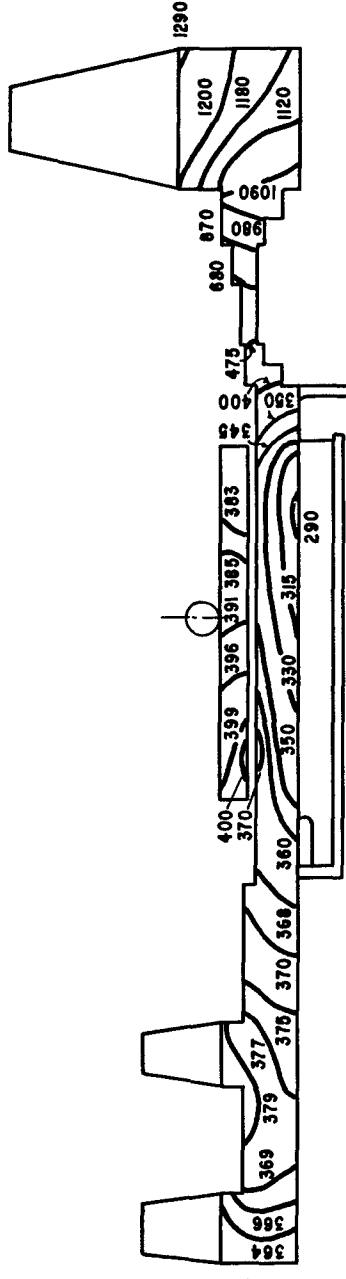


Fig. C-14 - Heat Exchanger For No. 2 Journal Prior To Brazing Into Rotor

$$h = \frac{\text{BTU}}{\text{hr ft}^2 \text{ of}}, \quad k = \frac{\text{BTU}}{\text{hr ft}^2 \text{ of/ft}}, \quad Q = \frac{\text{BTU}}{\text{hr}}, \quad k = 0.0144 \text{ FOR ARGON IN CLEARANCE GAP.}$$



BOUNDARY CONDITIONS FOR MODEL



ISOTHERMS FOR NO. 2 JOURNAL BEARING AREA

Fig. C-15 - Thermal Boundary Conditions And Calculated Isotherms For The Initial Design Of The No. 2 Journal Bearing

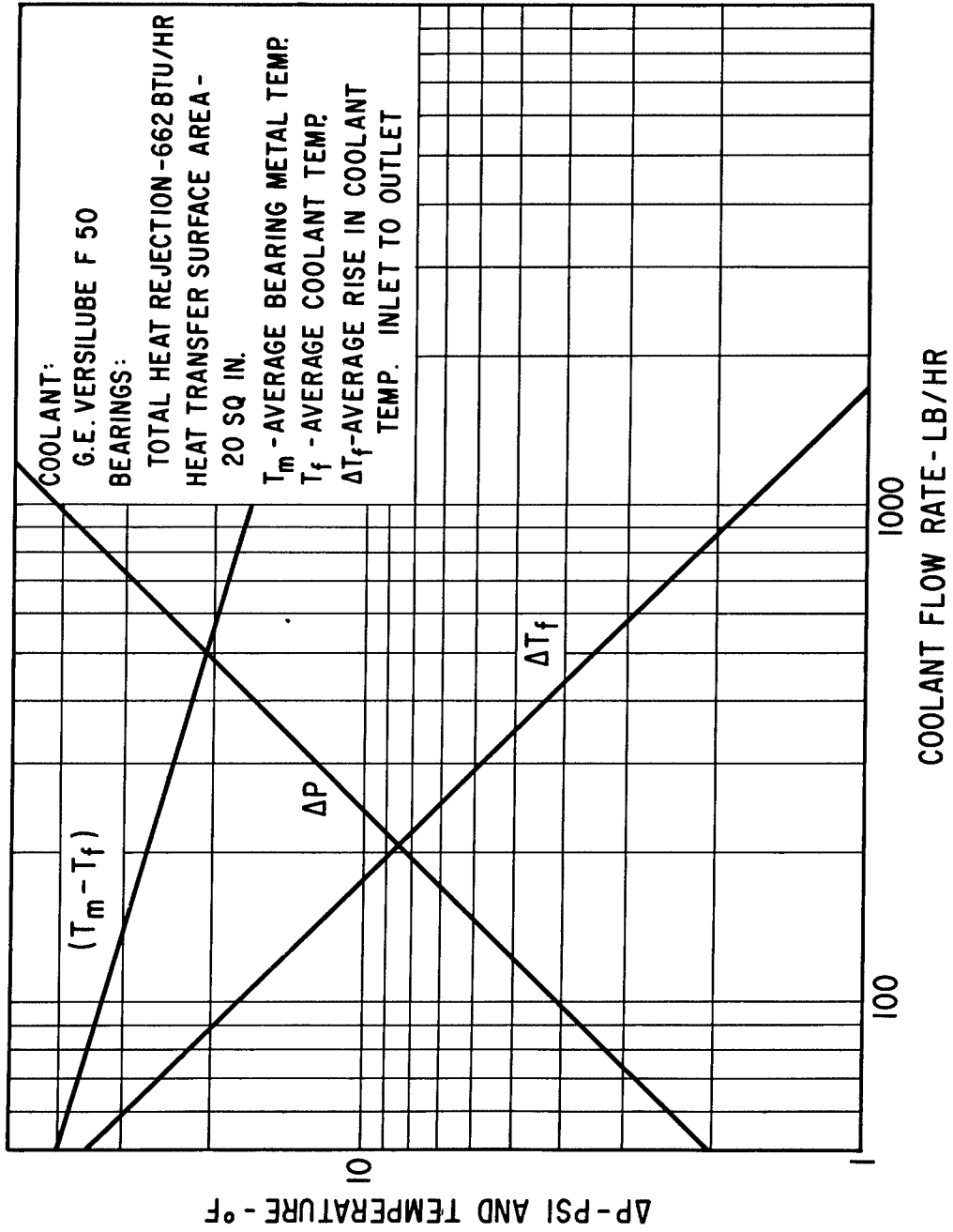


Fig. C-16 - Calculated Performance Of Thrust Bearing Cooling System

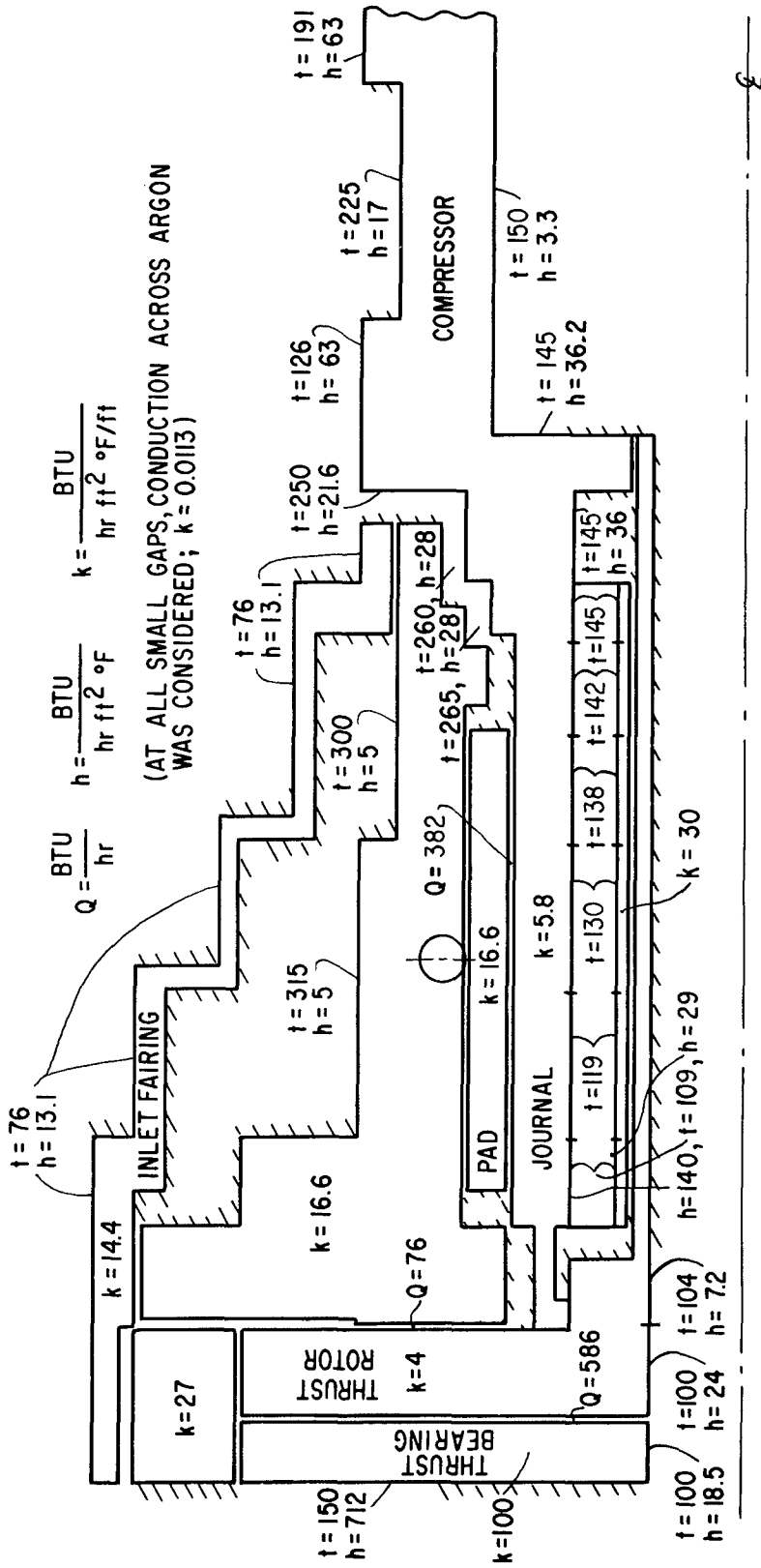


Fig. C-17 - Thermal Boundary Conditions For The Initial Design Of The No. 1 Journal Bearing And Thrust Bearing

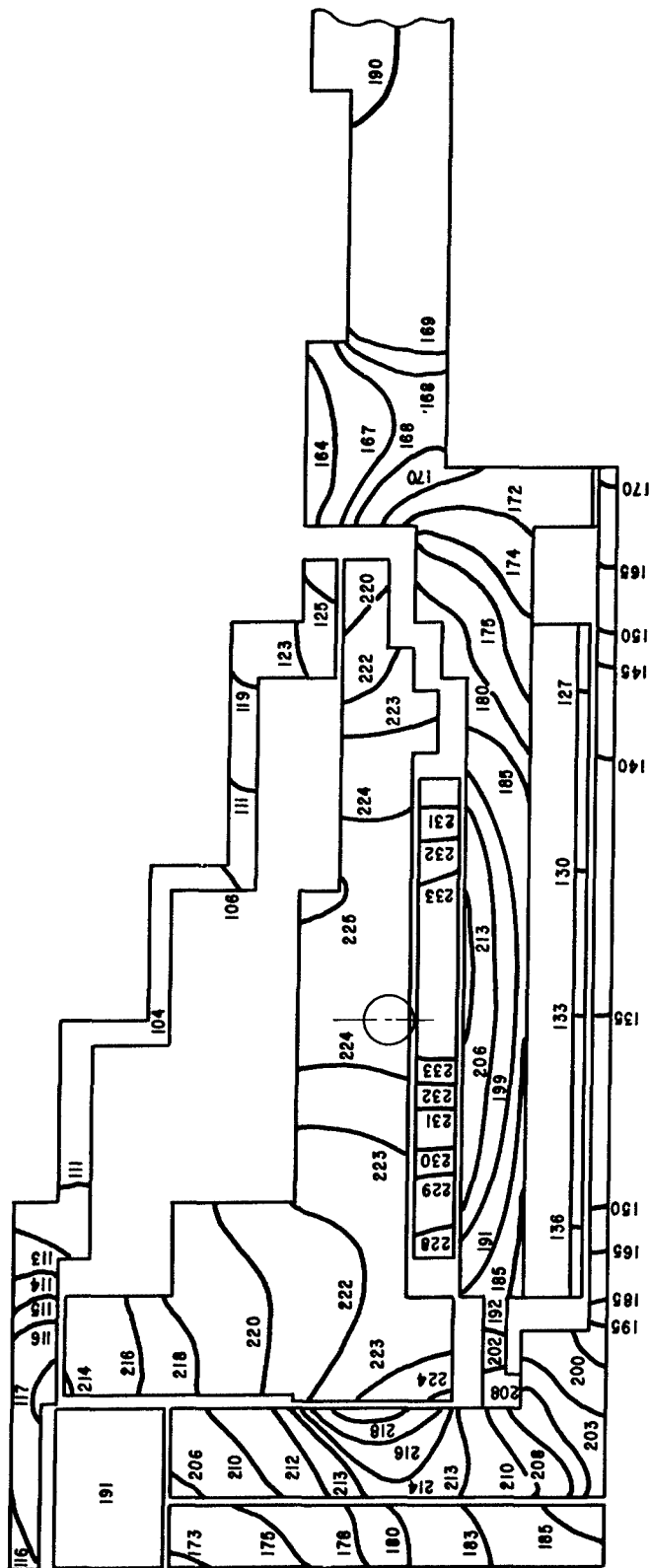


Fig. C-18 - Calculated Isotherms For The Initial Design Of The
No. 1 Journal Bearing And Thrust Bearing

Test Evaluation of Initial Bearing System Design

Subsequent to fabrication of parts for the initial bearing system design, but prior to assembly of these parts into the rotor-bearing system simulator, the following preliminary data was obtained.

1. The stiffness of each of the four flexures for the No. 1 and No. 2 journal bearings was determined from load versus deflection measurements. Figures C-19 and C-20 are plots of the load-deflection data for the flexures.
2. The forward thrust bearing stator was assembled to the aluminum thrust flexure and the flatness of the stator surface rechecked. Whereas the stator surface had been flat to within 0.1 mils prior to assembly of the flexure, it was found that the interference fit of the flexure caused a 0.25 mil concave distortion of the stator surface. However, since this distortion would be opposite to the distortion which would occur due to thrust loads and due to axial heat transfer of friction losses through the thrust plate, no attempt was made to reduce or otherwise change this assembly distortion.
3. The forward hydrostatic thrust bearing was calibrated. Figure C-21 shows a plot of load capacity versus film thickness for different hydrostatic supply pressures. It was noted during this calibration that the bearing developed a pneumatic instability at simultaneous conditions of low load (less than 25 pounds) and low supply pressure (less than 30 psi).
4. The weight of the complete rotating assembly was found by measurement to be 10.5 lbs. The c.g. of the complete stator assembly was likewise found by measurement to be 8.531 \pm 0.031 inches from the forward most face of the thrust runner. The corresponding calculated weight and c.g. location of the rotor assembly (based on analysis of MTI detail drawings for the rotor assembly) was 10.6 lbs. and 8.75 inches respectively.
5. Based upon the above rotor weight and c.g. data, the actual loads on the No. 1 and No. 2 journal bearings for a horizontal orientation of the

rotor were calculated to be 3.25 and 7.25 pounds respectively. These loads are slightly less than the 3.63 and 7.72 pound values used during design of the bearing system. The explanation for the smaller actual loads is that a detailed design change was made to the rotor design, for mechanical reasons, subsequent to completion of the design analyses. Since this change was small, and in the direction of lighter bearing loads, it was not necessary to correct the design calculations for the final load condition.

The bearing system was then assembled into the simulator and several bearing system set-ups were made to establish correct labyrinth clearances, correct positioning of the capacitance probes, etc., as well as to resolve the usual set-up bugs which normally accompany the first assembly of a new machine. In actual fact, the simulator and bearing system assembly and set-up procedure was accomplished with minimum of difficulties considering (1) the complexity of the design, (2) the precision of set-up required, and (3) the large amount of instrumentation and auxiliary gas and coolant lines which had to be installed in a very limited amount of space, particularly in the forward end of the machine.

The journal bearings were set up with the following zero-speed room temperature diametral bearing clearances:

1. No. 1 bearing - 0.9 to 1.0 mils
2. No. 2 bearing - 1.9 to 2.0 mils.

The reverse thrust bearing was set up square to the runner to within 0.1 mils TIR. The forward thrust bearing was then set up to allow 5.0 mils total axial clearance between the thrust runner and thrust stators. No attempt was made initially to obtain close parallelism between the forward thrust stator and the thrust runner, since the initial start-up tests were to be run against the reverse thrust bearing only.

A succession of start-up tests was performed between July 17 and July 23, 1965. During these tests the simulator was vertical with the turbine-end down (i.e., the

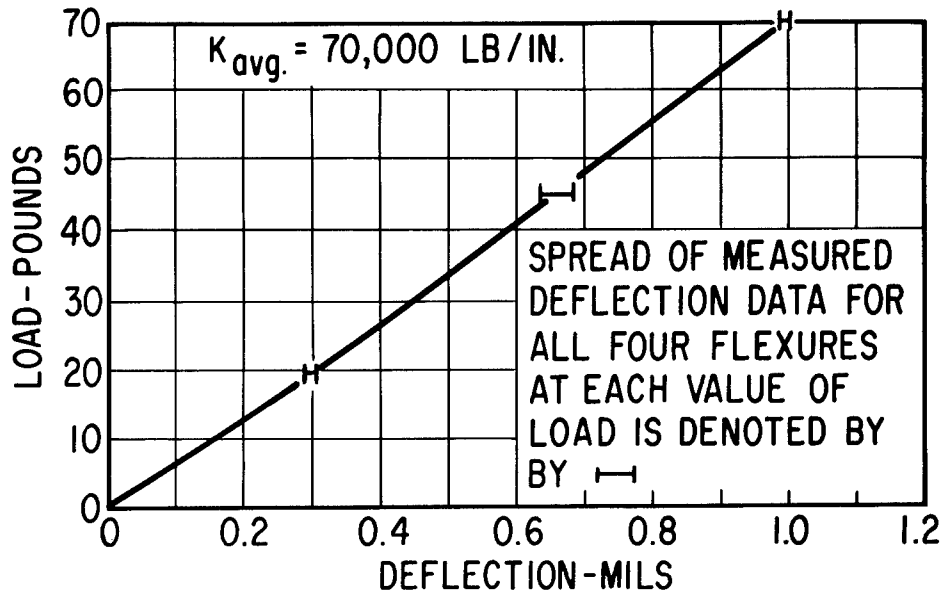


Fig. C-19 - Measured Load Versus Deflection Plot For The Initial Design Of The Pivot-Support Flexures For No. 2 Journal Bearing

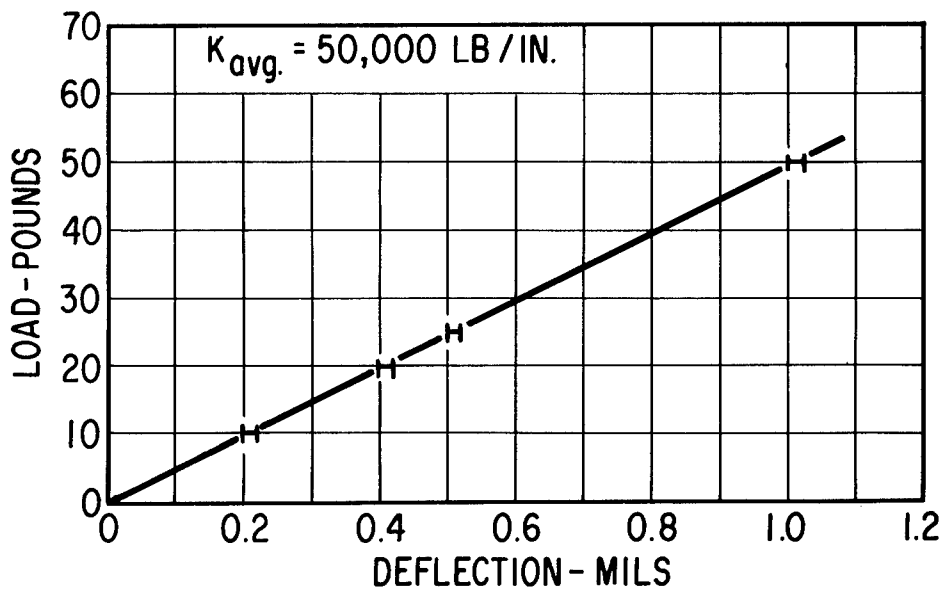


Fig. C-20 - Measured Load Versus Deflection Plot For The Initial Design Of The Pivot-Support Flexures For No. 1 Journal Bearing

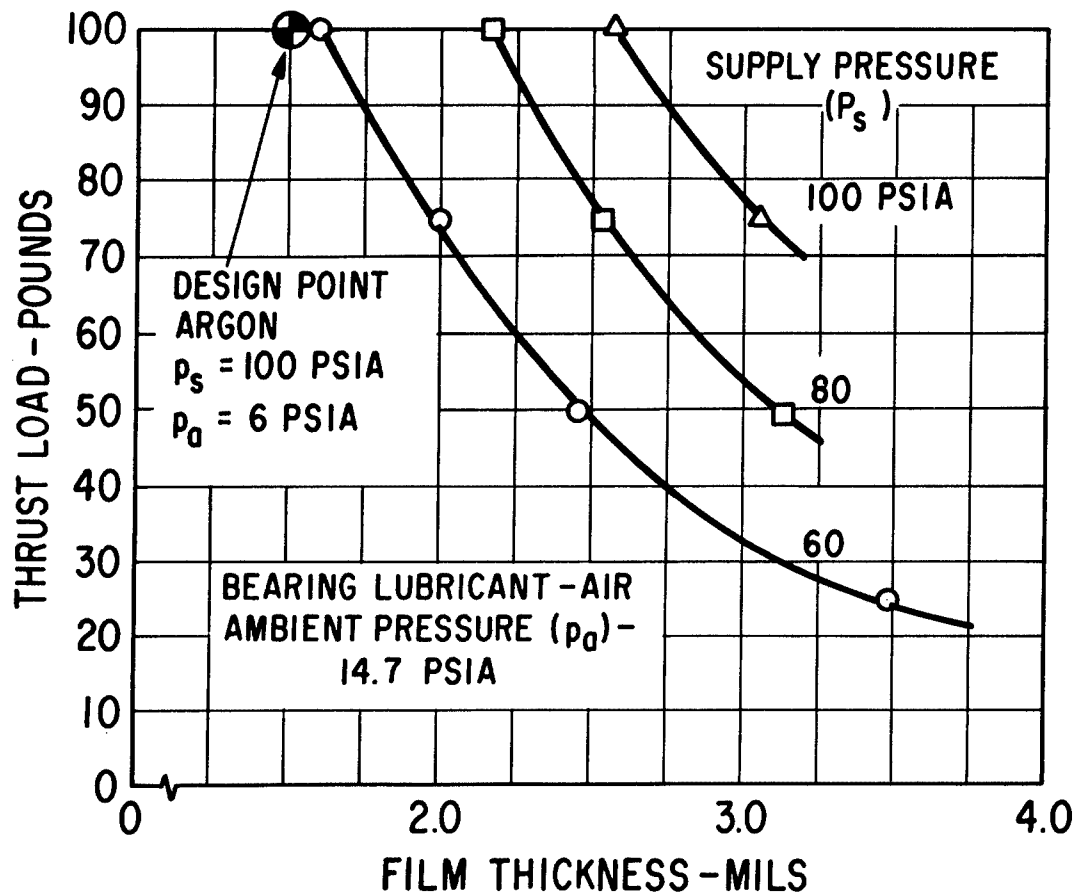


Fig. C-21 - Measured Load Versus Film Thickness For The Initial Design (20 Orifices) Of The Forward Hydrostatic Thrust Bearing

rotor weight was supported by the reverse hydrostatic thrust bearing). Speeds up to 35,800 rpm were obtained without difficulty and without any in-place balancing of the rotor on the gas bearings (the rotor assembly had been preliminarily balanced, of course, on the MTI balancing machine). During these preliminary runs, capacitance probe and thermocouple instrumentation was checked out, as was also operation of the No. 2 bearing bulkhead heater and the cooling-gas system for the journal bearings. Also during these tests, a small resonance of the forward thrust stator was detected between 28,000 and 30,000 rpm (this resonance is discussed in Section II of this report).

The first attempt at in-place balancing on the gas bearings was made on July 27. The drive turbine and thrust runner balance planes were used. Three trial balance runs were made at 25,000 rpm. The data from these runs was then used as input for a two-plane digital computer balancing program. The program output indicated that the major correction should be made in the turbine plane. This correction was accordingly made.

On July 29 an attempt was made to obtain the 50,000 rpm design speed with the rotor vertical, turbine down, and rotor weight supported on the reverse thrust bearing. A speed of 47,230 rpm was obtained, at which point maximum opening of the air control valve for the drive turbine was reached. It was suspected that pressure drops in the line between the control valve and the turbine were preventing attainment of full manifold pressure at the turbine nozzles. The test was accordingly terminated and larger air supply lines and fittings were installed.

On July 30 a speed of 50,250 rpm was obtained. Representative bearing temperatures during this run were

No. 1 bearing pads - 148 F
No. 1 bearing housing - 139 F
No. 2 bearing pads - 225 F
No. 2 bearing housing - 222 F.

During the week of August 2, exploratory testing was continued with the following results.

1. The 50,000 rpm design speed was obtained with both horizontal and vertical orientation of the rotor. Hydrodynamic lift-off of the journal bearings in the horizontal position was accomplished with no difficulty. About 65 psig turbine nozzle pressure was required to "break" the rotor away, but once "breakaway" occurred, the rotor accelerated very rapidly (so much so, that it was not possible to determine actual lift-off speed from the instrumentation). Touchdown speed of the rotor during shut-down was quite accurately measured due to the long coast-down time. Touch-down occurred consistently at about 1,400 to 1,500 rpm.
2. The forward thrust stator was next aligned parallel to the thrust runner within 0.1 mils TIR. Completely hydrodynamic operation of the spiral-grooved self-acting thrust bearing was then achieved at design speed in both the horizontal and vertical positions of the simulator. Preliminary load versus film thickness calibrations were made at thrust loads up to 33 lbs. at 50,000 rpm (maximum design point thrust load being 24 pounds). Testing was accomplished at ambient pressures from 14.7 to 10.0 psia. Performance of the self-acting spiral-grooved thrust bearing was excellent during these tests.
3. One definite problem area was identified — namely, pneumatic instability of the forward externally-pressurized thrust bearing over a specific range of supply pressures and thrust loads. Figure C-22 shows a map of the stable and unstable regions of thrust bearing performance as a function of supply pressure and thrust load.

Comparison of Figures C- 6 and C-21 show that the measured load capacity of the forward hydrostatic thrust bearing was 2 to 2.5 times greater than the calculated load capacity (for a given supply pressure and film thickness). This discrepancy is due to a conservative assumption used for the calculated curve — namely, the OD of the hydrostatic bearing was assumed to be the same as the root diameter of the spiral grooves for the hydrodynamic bearing. The higher values of measured load capacity indicate that

hydrostatic pressurization did exist across the spiral-grooved section of the bearing. In other words, the spiral grooves were not deep enough to completely vent the hydrostatic bearing at the root diameter of the grooves, as was assumed in the design calculations. Accordingly, the spiral grooves probably acted as appreciable volumes within the pressurized clearance space of the hydrostatic bearing. Such volumes are known to normally be the cause of pneumatic instability.

The pneumatic instability phenomenon in the forward hydrostatic thrust bearing was the only problem of any significance uncovered by the exploratory simulator tests. Since it was deemed impractical and undesirable to restrict thrust bearing operation to the stable region shown in Figure C-22, modification of the bearing was clearly indicated as being required in an effort to eliminate the instability problem. On the assumption that the spiral grooves were not deep enough to act as effective vents for the hydrostatic bearing, it was hypothesized that the desired venting effect could, perhaps, be obtained by reducing the amount of flow passing through the grooves. Such a flow reduction could be achieved by either reducing the number of orifices in the hydrostatic bearing or by reducing the diameter of the existing orifices. From a practical standpoint it was considerably simpler to do the former.

Accordingly, the forward hydrostatic thrust bearing was set up on the "bench" and the pneumatic instability characteristics duplicated by using the actual simulator rotor to provide correct mass properties. A step-by-step reduction in the number of orifices in the hydrostatic bearing was then investigated as a possible means for eliminating the instability. By reducing the number of orifices from the original twenty down to five, it was possible to eliminate the instability, at least on the "bench".

The hydrostatic bearing was recalibrated for the five orifice condition. Figure C-23 shows a comparison of the load versus film thickness calibration of the original twenty orifice bearing and the modified five orifice bearing for a 100 psia supply pressure. It is seen that while the load capacity of the five orifice bearing was considerably reduced relative to the original configuration, the film thickness at the 100 pound design load was still in excess of

1.0 mils. This was considered to be a quite adequate film thickness, and the modified bearing was therefore accepted as far as static load carrying capability was concerned.

The simulator was reassembled with the five orifice forward thrust bearing. Operation over the full range of hydrostatic supply pressure (0 to 100 psia) and at thrust loads from zero to 100 pounds was checked at speeds up to 50,000 rpm (design speed). During these tests ambient pressures as low as 6 psia were obtained inside the simulator casing. Operation up to 60,000 rpm was also checked at 14.7 psia ambient pressure and essentially zero thrust load. No pneumatic instability was detected during these tests.

During the first half of October 1965, evaluation testing of the rotor-bearing system was continued. Testing of the hydrodynamic thrust and journal bearings was extended from 50,000 to the 60,000 rpm overspeed condition. Tests with 0.0033 ounce-inches of unbalance in the turbine plane were also performed up to 60,000 rpm. Finally, acceleration tests from zero speed were attempted. By quickly opening the drive turbine control valve, acceleration to 50,000 rpm was achieved in 48 seconds. This test was repeated two times with approximately the same acceleration time. Operation of the rotor-bearing system throughout the above series of tests was quite satisfactory.

Measurements of load versus film thickness for the hydrodynamic thrust and journal bearings, as a function of speed and ambient pressure, were also made. The thrust bearing data is shown in Figures IV-4 and IV-5 of Section IV of this report. Average film thickness data at the pivot location of the loaded journal bearing pads is shown in Figures C-24 and C-25, together with the corresponding bearing temperatures.

Figures C-26 and C-27 are oscilloscope photographs of the bearing orbits for the No. 1 and No. 2 journal bearing at 50,000 and 60,000 rpm, with and without unbalance in the turbine plane. (The fuzziness of the No. 1 journal bearing orbits is due to the fact that only half of the detection area of the X and Y displacement

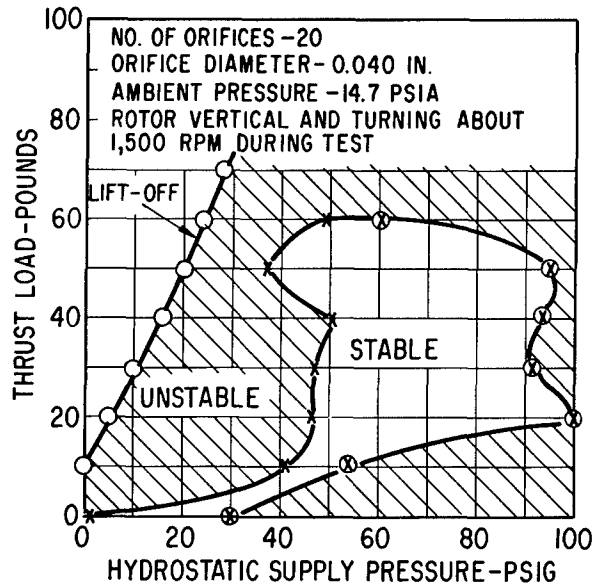


Fig. C-22 - Measured Stability Map For The Initial Design (20 Orifices) Of The Forward Hydrostatic Thrust Bearing

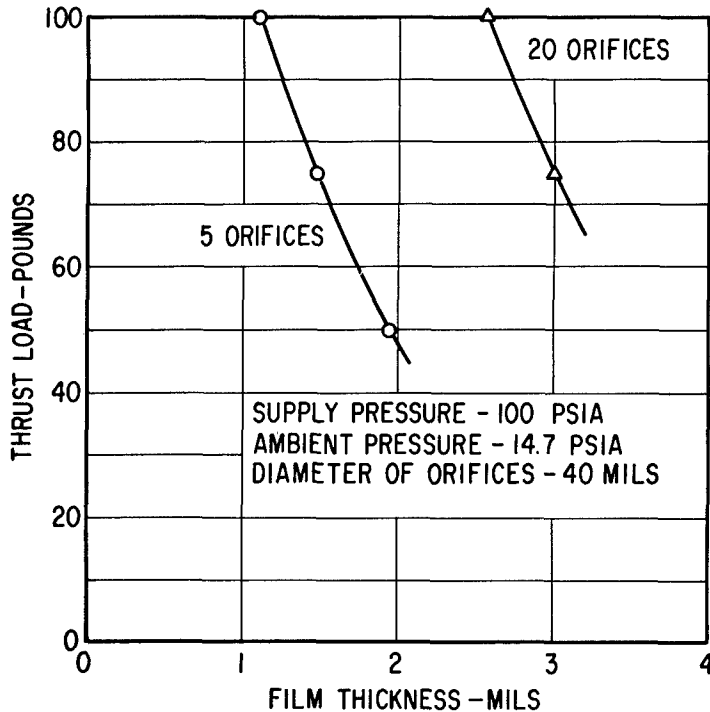


Fig. C-23 - Comparison Of Measured Load Versus Film Thickness Data For The Forward Hydrostatic Thrust Bearing Before And After Reduction Of The Number Of Feed Orifices

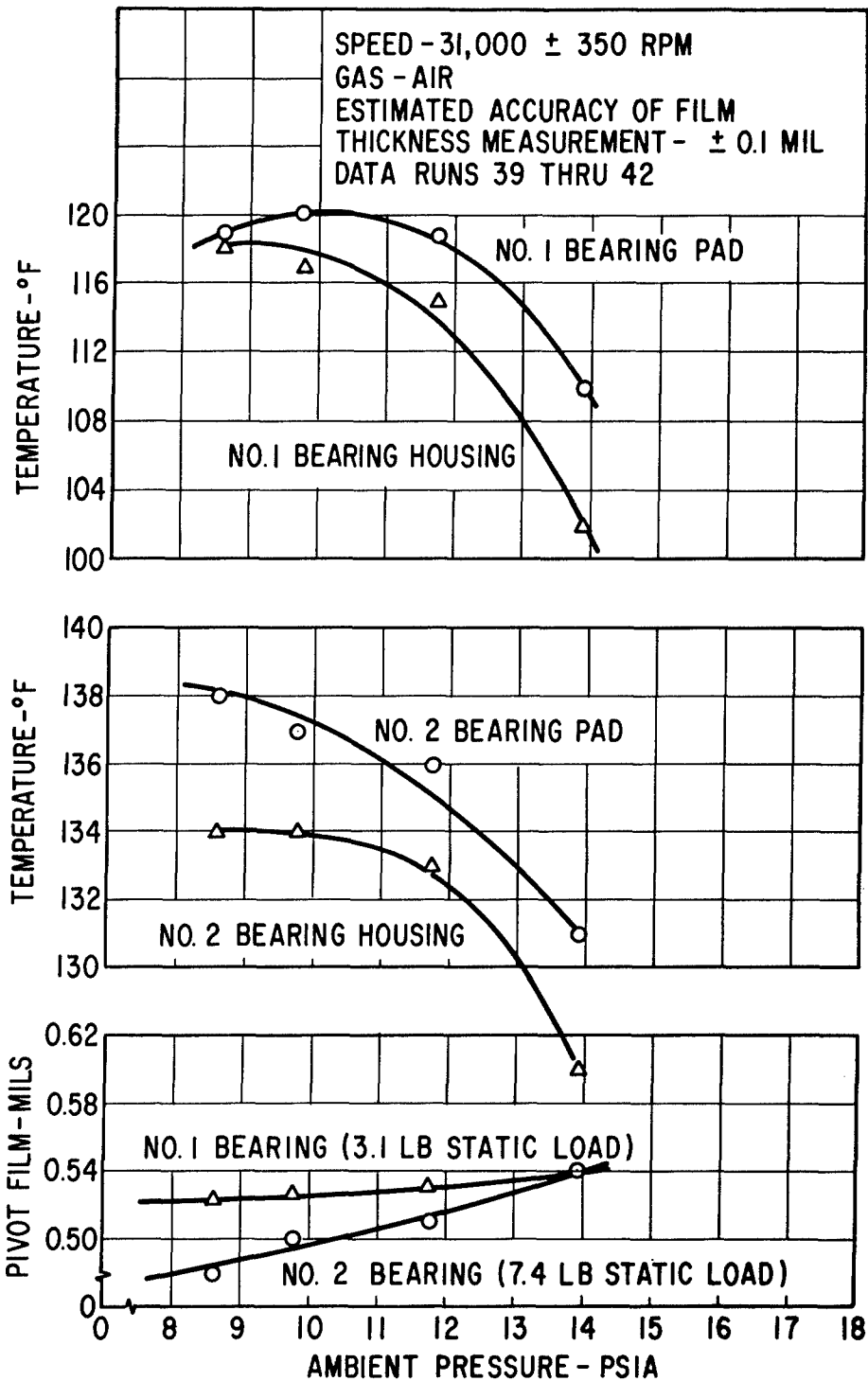


Fig. C-24 - Measured Average Pivot Film Thickness For The Loaded Pads, And Corresponding Temperatures, At 31,000 RPM Versus Ambient Pressure (Initial journal bearing designs)

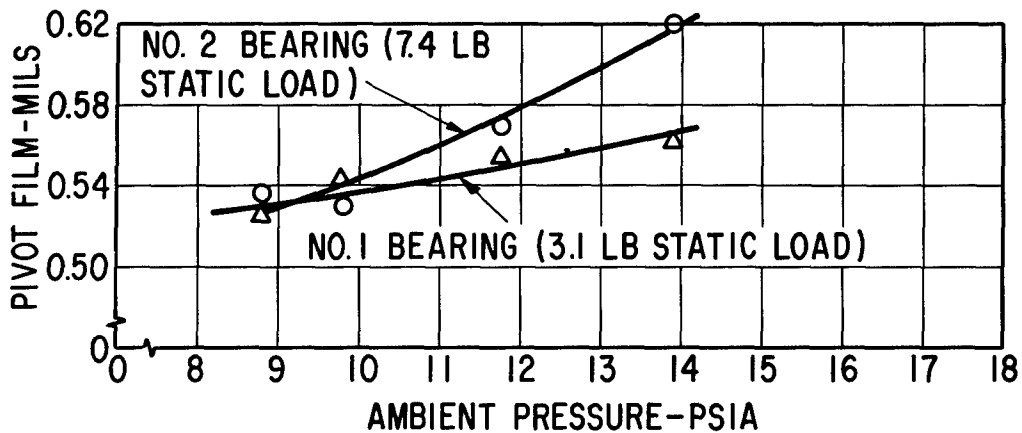
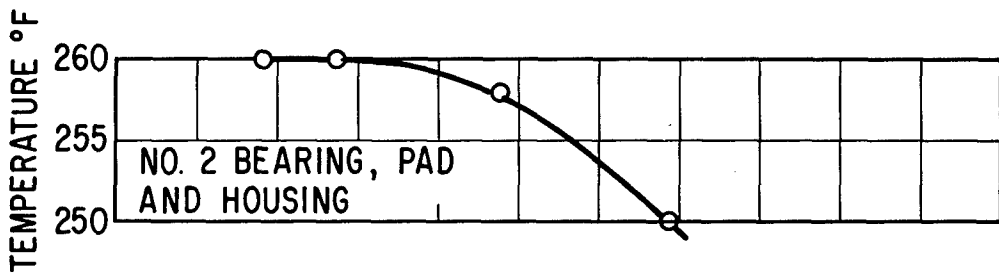
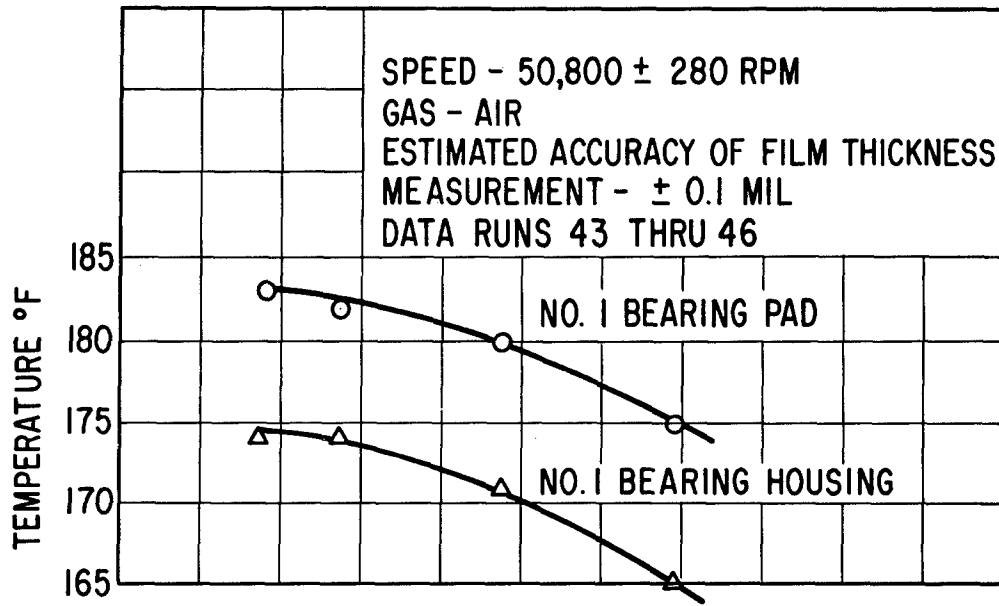
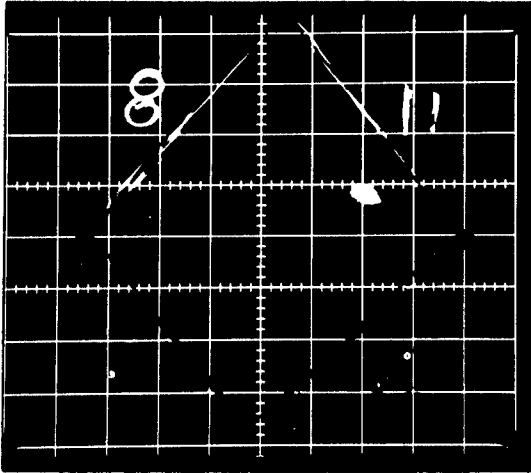


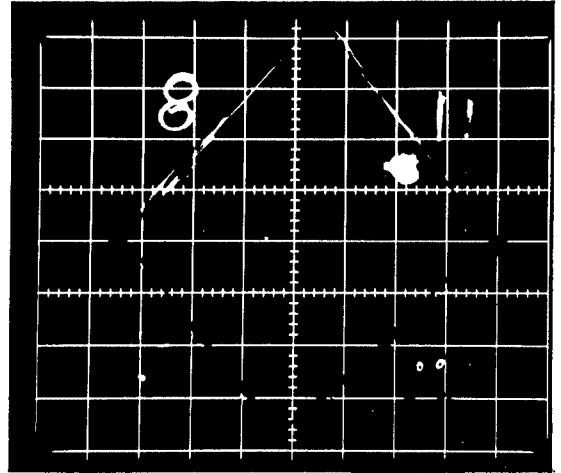
Fig. C-25 - Measured Average Pivot Film Thickness For The Loaded Pads, And Corresponding Temperatures, At 50,800 RPM Versus Ambient Pressure (Initial journal bearing designs)

RESIDUAL UNBALANCE

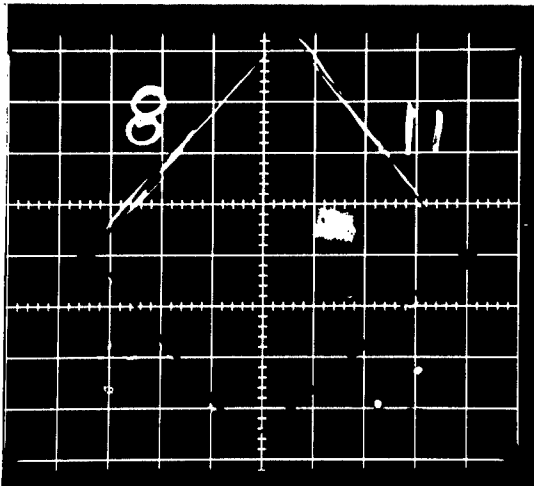


50,700 RPM (RUN 119)

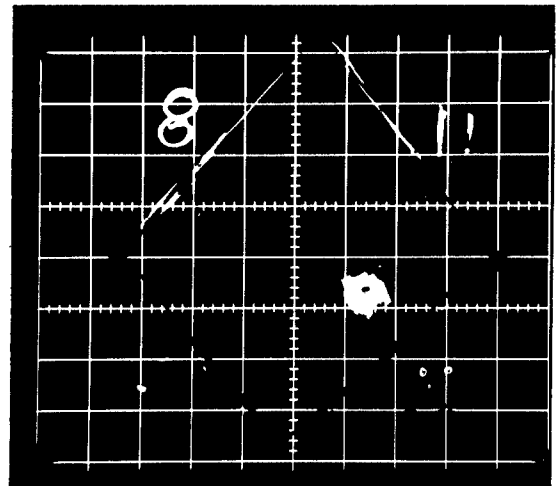
RESIDUAL UNBALANCE PLUS
0.0024 OZ.-IN. UNBALANCE
IN TURBINE PLANE



50,400 RPM (RUN 99)



60,300 RPM (RUN 122)



61,000 RPM (RUN 102)

X and Y Oscilloscope Calibration

0.2 Mils per Major Grid Division

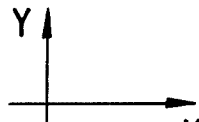
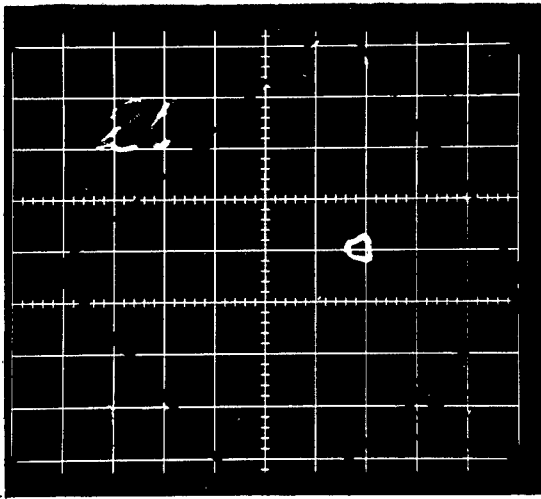
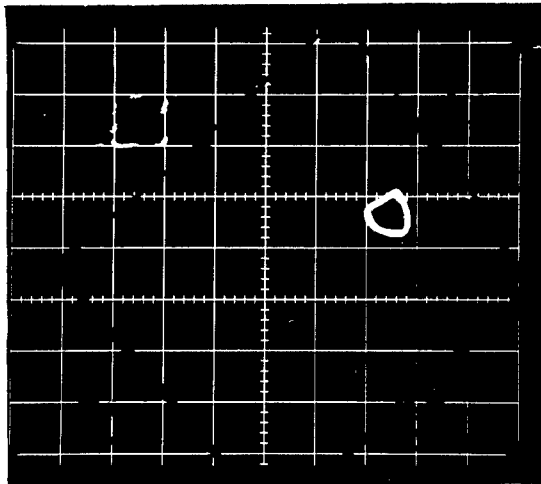


Fig. C-26 - Oscilloscope Photographs Of The No. 1 Journal Orbit As A Function Of Speed And Rotor Unbalance (Initial bearing system design)

RESIDUAL UNBALANCE

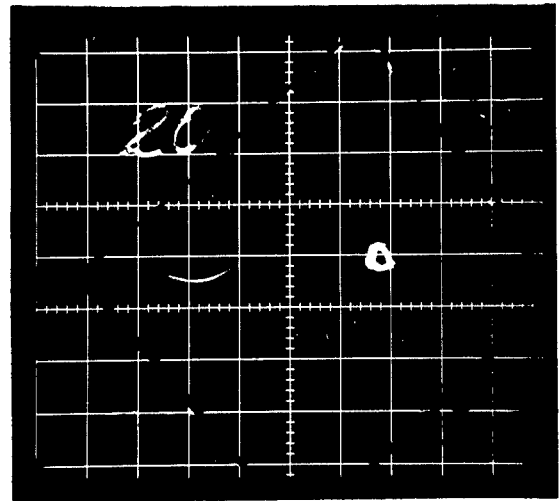


50,700 RPM (RUN 119)

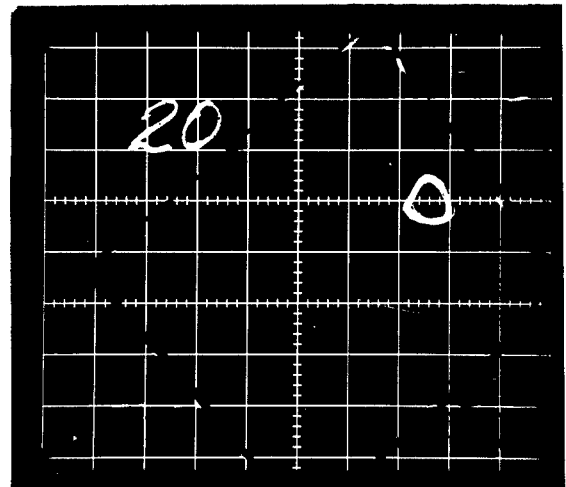


60,300 RPM (RUN 122)

RESIDUAL UNBALANCE PLUS
0.0024 OZ.-IN. UNBALANCE
IN TURBINE PLANE



50,400 RPM (RUN 99)



61,000 RPM (RUN 100)

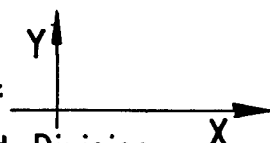
X and Y Oscilloscope Calibration : 
0.2 Mils per Major Grid Division

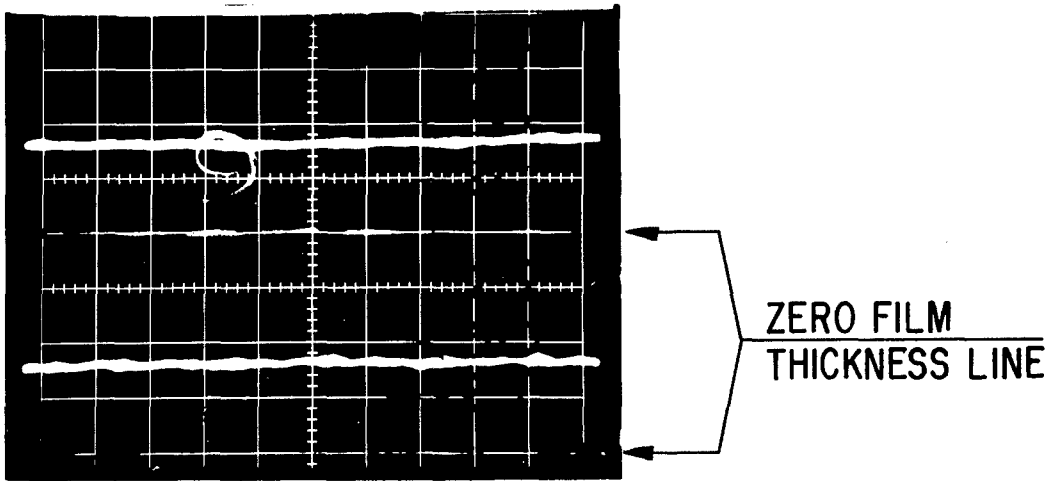
Fig. C-27 - Oscilloscope Photographs Of The No. 2 Journal Orbit As A Function Of Speed And Rotor Unbalance (Initial bearing system design)

capacitance probes was actually exposed to the journal surface. The other half of the probe faces were exposed to an irregular chrome oxide radius which caused a high-frequency low-amplitude noise signal to be superimposed on the primary signal.) It is seen that there is no detectable effect of unbalance on the No. 2 bearing orbit. A very slight increase in the No. 1 orbit was, however, observed. This effect of unbalance on the No. 1 bearing is also seen on the pad-to-shaft capacitance probe signal shown in the oscilloscope photographs of Figure C-28.

It is also seen from Figures C-26 and C-27 that, regardless of the condition of rotor unbalance, the orbit diameter for both the No. 1 and No. 2 journal bearings almost doubles from 50,000 to 60,000 rpm. This is due to the influence of the third critical speed resonance mode which is the fundamental free-free (i.e., rotor bending) mode. In actual fact, the residual unbalance orbits could have been considerably reduced from those shown in Figures C-26 and C-27 by utilizing a three-plane balancing technique rather than the simpler two-plane technique which was actually used.

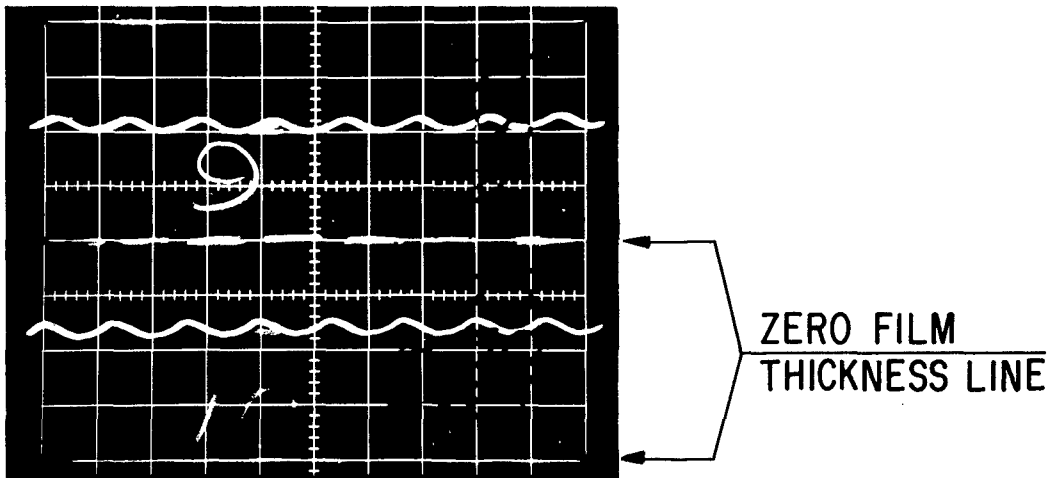
Acceptance testing of the turbocompressor rotor-dynamic simulator, with the initial bearing system design installed, was accomplished on October 19 and 20, 1965, in accordance with Pratt & Whitney Aircraft Specification 6355-A (this specification is enclosed in Appendix B of this report). All conditions of this specification were successfully met. Total simulator running time to complete the acceptance tests exceeded nine hours. During the simulator acceptance test, two runs were made using argon as the bearing lubricant and cooling gas. During the first run, the argon cooling flow rate was 0.014 lb./sec. down the bore of the rotor. For the second run this flow was reduced to 0.007 lb./sec. The simulator speed was maintained at 50,200 rpm during both runs. Completely self-acting bearing operation with approximately 15 pounds thrust load was also maintained. During the first run, maximum pad temperature in the No. 2 bearing reached 287 F. During the second run at reduced argon coolant flow rate, maximum temperature of the No. 2 pads reached 322 F.

RESIDUAL UNBALANCE



50,600 RPM (RUN 109)

RESIDUAL UNBALANCE PLUS 0.0024 OZ-IN. UNBALANCE IN TURBINE PLANE



49,500 RPM (RUN 90)

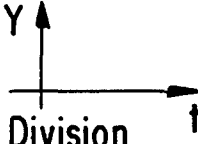
Y Axis Oscilloscope Calibration : 
0.25 Mils per Major Grid Division

Fig. C-28 - Oscilloscope Photographs Showing Effect Of Rotor Unbalance At 50,000 RPM On Two Of The No. 1 Journal Bearing Pad-To-Shaft Film Thickness Traces (Initial bearing system design)

APPENDIX D

DESIGN AND TEST OF SECOND BEARING SYSTEM

As mentioned in the Introduction to this report, three variations of the basic bearing system for the turbocompressor were designed and tested. The final design is documented in Section II. The initial design is documented in Appendix C. This appendix documents the bearing and rotor-dynamics design and test data for the second bearing system modification.

The second modification affected only the journal bearings and was concerned with (1) increasing bearing operating clearances to decrease bearing friction losses, and (2) decreasing stiffness of the pivot-support flexures for the two "upper" or "unloaded" pads in each journal bearing to obtain improved ability to accommodate temperature changes and temperature gradients (both steady-state and transient) without exceeding safe bearing clearances.

The basic design parameters of the second journal bearing design were the same as those given for the final journal bearing design in Table C-1 (see Appendix C), except for the mass properties of each individual pad of the No. 2 bearing, and the bearing preload ratio (m) for the No. 2 bearing. A comparison of the difference in mass properties of the No. 2 pads is given in Table D-1 below. The design value of preload ratio for the second design was maintained at 0.5, the same as the initial design.

Table D-1 - Mass Properties of a Single No. 2 Bearing Pad (all No. 2 pads being identical)

	Initial & Final Designs	Second Design
Pad Mass, lb.	0.14	0.21
Pad Inertia in Roll Direction, in.-lb.-sec. ²	0.000124	0.000252
Pad Inertia in Pitch Direction, in.-lb.-sec. ²	0.000084	0.000098

Reduction of Bearing Friction Losses

For a given size of bearing and set of operating conditions, bearing friction loss can be reduced by designing the bearing to operate at larger clearances. An increase in bearing clearance can be achieved by either one or a combination of the following two methods.

1. Decrease pad preload ratio (m) while maintaining the same pad clearance ratio (C_p/R). This can be physically achieved merely by moving the initial-design pads away from the rotor.
2. Increase pad clearance ratio while maintaining approximately the same preload ratio. This would require that the pads be reground to a curvature of larger radius.

It was elected to achieve reduced friction loss by increasing the pad clearance ratio. Reference to Figure D-1 (friction loss versus diametral clearance) reveals the reason for this choice. Note that curves are shown for C_p/R equal to 0.003 and C_p/R equal to 0.001. Movement along either of these curves by changing diametral clearance is analogous to changing the preload ratio at constant C_p/R . The larger C_p/R yields a slightly lower friction loss at any given diametral clearance. The determining factor, however, is that the pads with the lower C_p/R become completely unloaded at a clearance which would still produce significant losses.

Since the hydrodynamic lift-off speed increases and the bearing stiffness decreases as diametral clearance is increased, it was desirable that the increase in clearance (or C_p/R) be kept to a minimum. It was found that friction loss for the No. 2 bearing (with m equal 0.5) decreased for increasing values of C_p/R up to about 0.003, beyond which no further significant decrease in friction loss could be gained. The value of C_p/R equal to 0.003 was therefore chosen for the No. 2 bearing. As a consequence of the increased bearing diametral clearance, the pad film stiffness decreased, which reduced the resonant frequencies of the pads in the pitch and roll modes. Operation at the turbocompressor design point conditions

at 50,000 rpm would have produced a pad resonant frequency in the roll mode for the No. 2 bearing very nearly identical to the rotor speed. Additional mass was therefore added to each end of the No. 2 bearing pads to increase the pad moment of inertia in the roll direction and thus reduce this resonant frequency below the design-speed rotational frequency. As seen from Table D-1, addition of mass in this manner did not appreciably change the pad moment of inertia in the pitch direction. This was the desired result since the pitch resonant frequency, based on the original pitch inertia, was still significantly above rotational frequency of the turbocompressor, even with the softer, high-clearance bearings.

Although the No. 1 bearing contributed only 25 percent of the total journal bearing losses in the initial design, the possible reduction in friction losses therein was nonetheless significant. However, the No. 1 bearing envelope would not permit the addition of weights to the pads for the purpose of controlling the roll resonant frequency. The C_p/R of the No. 1 bearing was therefore increased from 0.001 to only 0.0018 as limited by the approach of the pad roll resonant frequency to the design speed rotational frequency.

The ratios of roll and pitch resonant frequencies of the pads to rotational speed are plotted in Figures D-2 through D-5 for the No. 1 and No. 2 journal bearings. From Figure D-2 it is seen that the roll frequency ratio at 50,000 rpm and 12.0 psia ambient pressure for the unloaded pads of the No. 1 bearing is about 1.4, while the roll frequency ratio for the loaded pads is about 1.7. The pitch frequency ratios are greater than 3.0 for both the upper and lower pads. From Figure D-3, however, it is seen that the roll frequency ratio of the No. 1 unloaded pads at 6 psia and 50,000 rpm approaches unity. This indicated that resonance of the unloaded pads in the roll direction might occur in the vicinity of 50,000 rpm if sufficient excitation in the roll direction were present. Since operation at 6.0 psia was not a primary design requirement, it was decided to accept the possibility of a roll resonance condition at low ambient pressures and to determine, by test, whether this was really a significant operational problem.

From Figures D-4 and D-5 it is seen that the roll frequency ratio for the No. 2 unloaded bearing pads is always below 0.65 over a speed range of 20,000 to 60,000 rpm, and a pressure range from 6.0 to 12.0 psia. The pitch frequency ratio of the loaded pads, however, is greater than 1.0 at speeds below 30,000 rpm, equal to 1.0 at 30,000 rpm, and approaches a value of 0.7 at 50,000 rpm. This indicated that a resonance of the No. 2 loaded pads might occur in the vicinity of 30,000 rpm. Again, since this condition had not arisen in previous machinery experience, it was decided to determine the implications of this condition, together with the fact that the roll frequency ratios would be less than 1.0 at design speed, by actual test.

Change in Pivot Support Flexure Stiffnesses

At the same time that the second journal bearing designs were formulated, design of the pivot-support flexures for both the No. 1 and No. 2 bearings was also modified. The reduced film stiffness of the higher clearance bearings made it almost mandatory that the flexure stiffnesses be reduced. If this were not done, the effects of rotor centrifugal growth and shaft-to-housing temperature differences would be absorbed primarily by changes in the bearing clearance, rather than by flexure deflection.

The acceptability of a preferred horizontal orientation of the rotor while operating in a 1-g acceleration field allowed the use of a non-isotropic flexure system. The original "stiff" flexures were retained for the lower pads of both bearings (as determined with the rotor in the horizontal position) to support rotor weight during horizontal operation. A decreased stiffness was achieved for the upper pad flexures by reducing the cross-section of the flexure beams. This change was effected for both the No. 1 and No. 2 bearings. The design values of upper flexure stiffness selected for the modified designs were 10,000 lb./in. for both bearings.

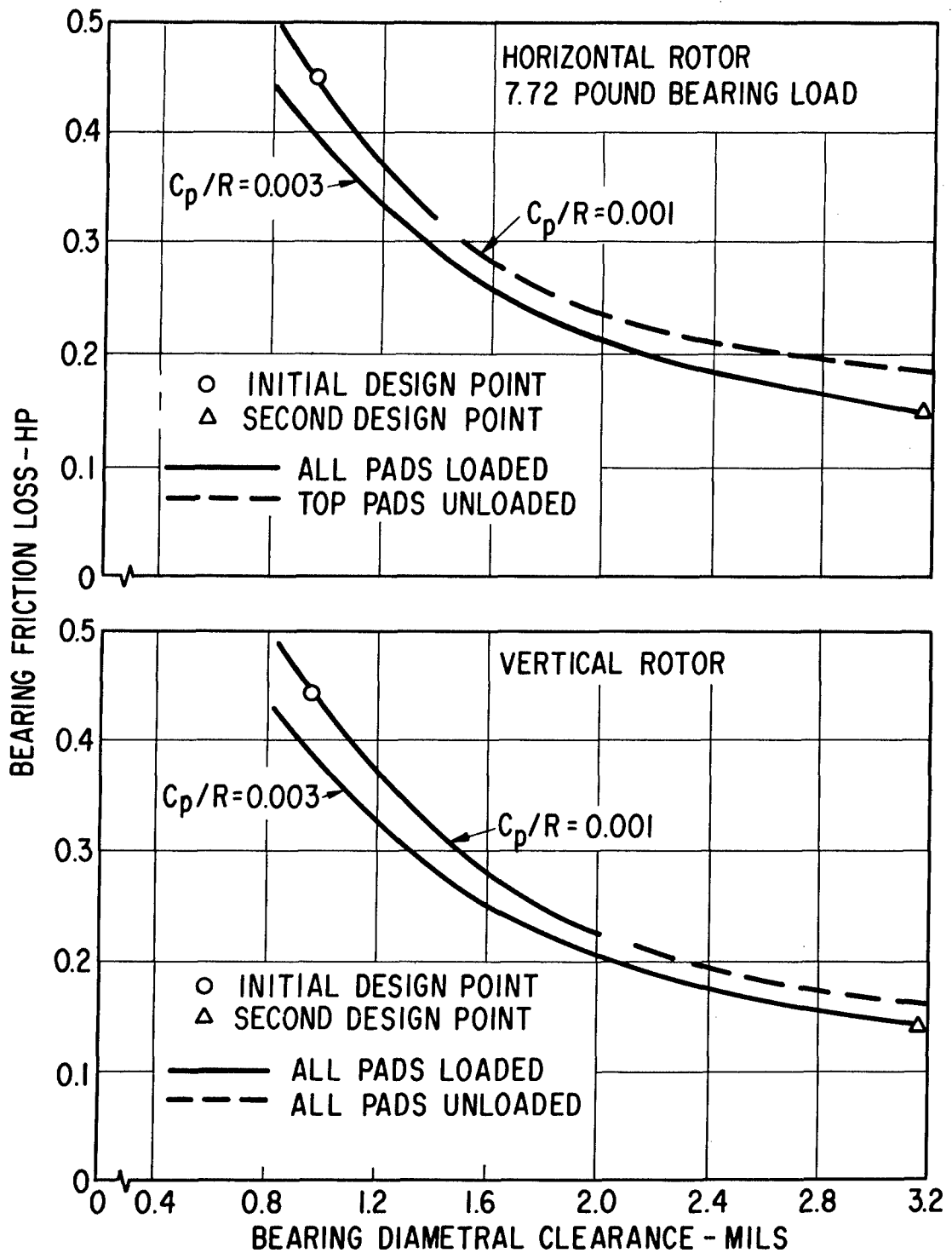


Fig. D-1 - Friction Loss Versus Bearing Diametral Clearance (Preload) For The No. 2 Journal Bearing As A Function of Pad Clearance Ratio (C_p/R)

Calculated Journal Bearing Performance

Figures D-2 through D-5 show the calculated performance of the second No. 1 and No. 2 journal bearing designs as a function of speed for ambient pressures of 12.0 and 6.0 psia. At 12.0 psia ambient pressure and 50,000 rpm design speed, it is seen that the total friction loss for the journal bearings is approximately 172 watts. This can be compared to the total friction loss for the initial design of the bearings of 440 watts. Hence, the second journal bearing designs represented a potential 61 percent reduction in journal bearing friction loss relative to the initial journal bearing designs.

Table D-2 shows the calculated extremes of temperature variation which can be accommodated by the second journal bearing system based on arbitrary minimum and maximum film thickness criterion. It is seen that for horizontal operation in a 1-g field, the No. 2 bearing housing temperature can vary from 262 degrees below design-point temperature to 82 degrees above design point without exceeding the limiting film thickness criterion. The No. 1 bearing housing can vary from 116 degrees below design-point temperature to 50 degrees above design point. In the vertical shaft position (or equivalently, at a zero-g condition) the range of temperature excursion for the No. 2 bearing housing (for the same film thickness criteria) is 331 degrees below design-point temperature to 181 degrees above design point.

TABLE D-2 CALCULATED TEMPERATURE EXTREMES PERMITTED FOR SECOND BEARING
SYSTEM DESIGN

Rotor Horizontal In A 1-G Gravitational Field

	<u>No. 1 Bearing</u>	<u>No. 2 Bearing</u>
Flexure Stiffness, lb./in.		
Upper	10,000	10,000
Lower	50,000	70,000
Maximum Film Thickness Criterion	$\epsilon_p \cos\phi = 0.2$	$\epsilon_p \cos\phi = 0.1$
Minimum Film Thickness Criterion	$\epsilon_p \cos\phi = 0.8$	$\epsilon_p \cos\phi = 0.9$
Design-point temperature differentials, °F		
$T_s - T_o$	98	120
$T_s - T_p$	-19	-3
$T_h - T_s$	46	150
Maximum $T_h - T_s$ for maximum film thickness criterion, °F	96	232
Maximum pivot film thickness for $(T_h - T_s)_{\max.}$, mils	1.1	2.86
Minimum $T_h - T_s$ for min. film thickness criterion, °F	-70	-112
Minimum pivot film thickness for $(T_h - T_s)_{\min.}$, mils	0.27	0.32

No. 2 Journal Bearing At Zero-G Conditions

Maximum $T_h - T_s$ for max. film thickness criterion, °F	331	331
Minimum $T_h - T_s$ for minimum film thickness criterion, °F	181	-181

Temperature Designations

- T_o - Journal reference temperature (taken as 70 F throughout this report)
- T_s - Journal temperature
- T_h - Bearing housing temperature
- T_p - Pad temperature

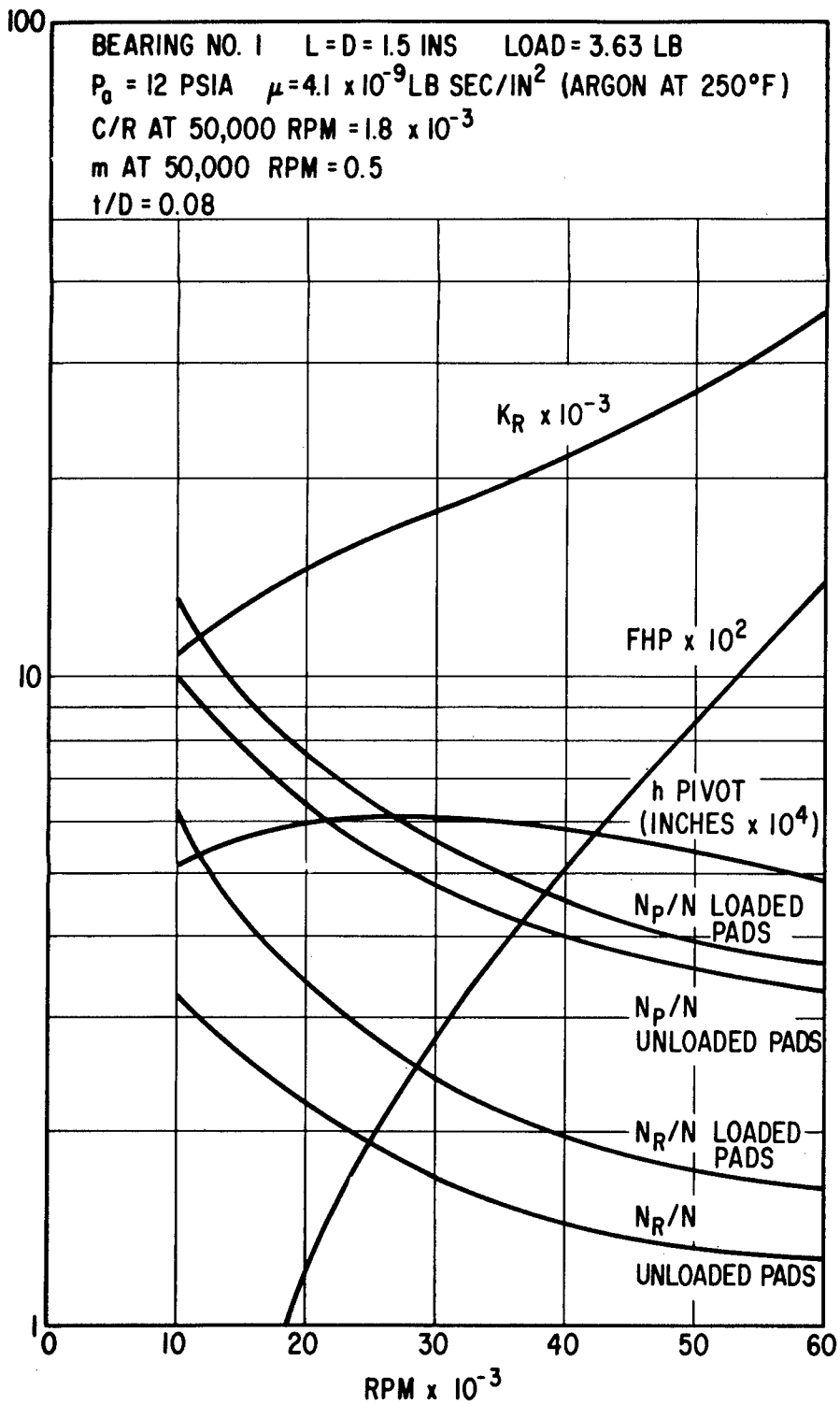


Fig. D-2 - Calculated Performance In A 12.0 PSIA Argon Environment For The Second Design Of The No. 1 Journal Bearing (Rotor horizontal relative to a 1-g gravitational field)

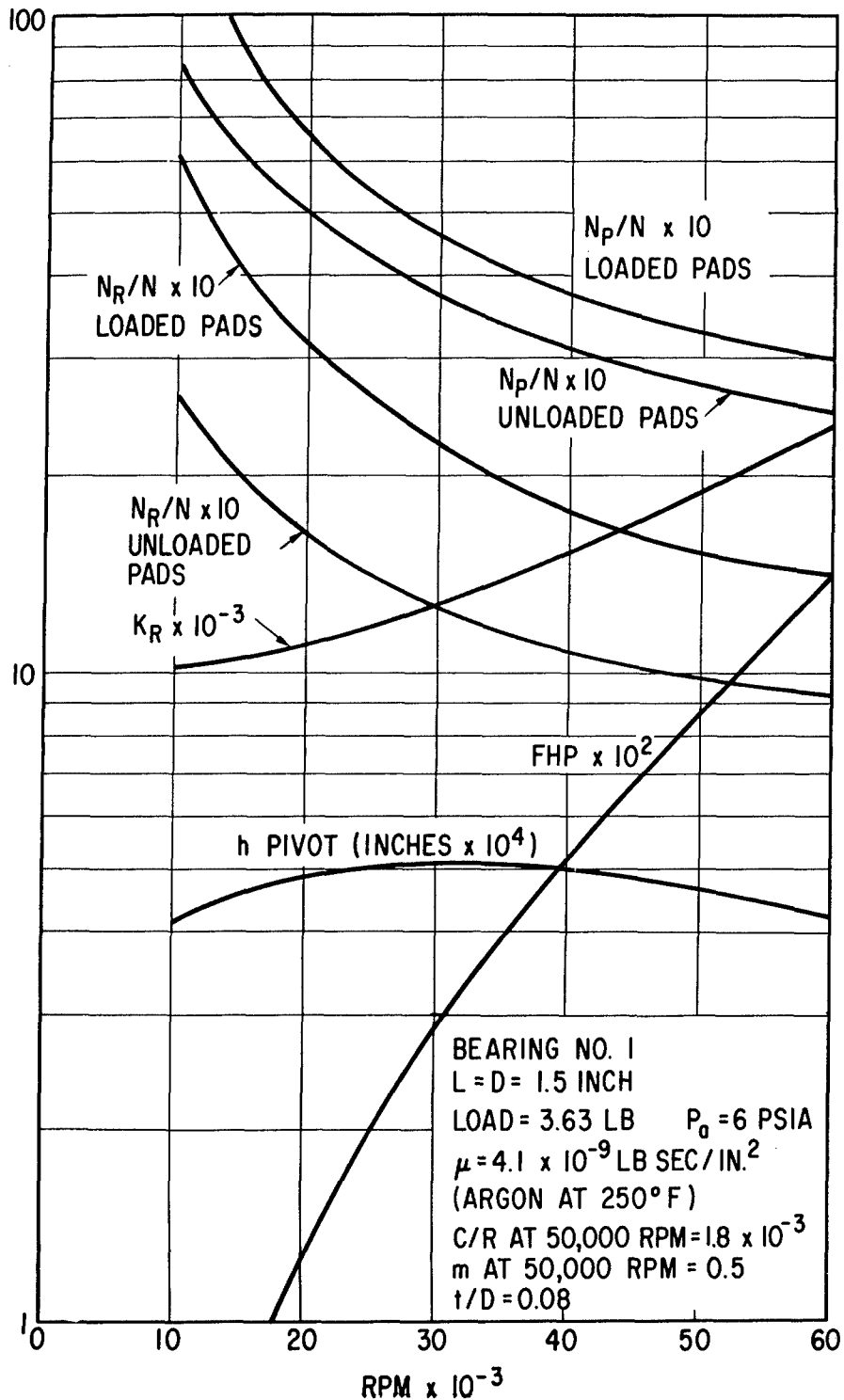


Fig. D-3 - Calculated Performance In A 6.0 PSIA Argon Environment For The Second Design Of The No. 1 Journal Bearing (Rotor horizontal relative to a 1-g gravitational field)

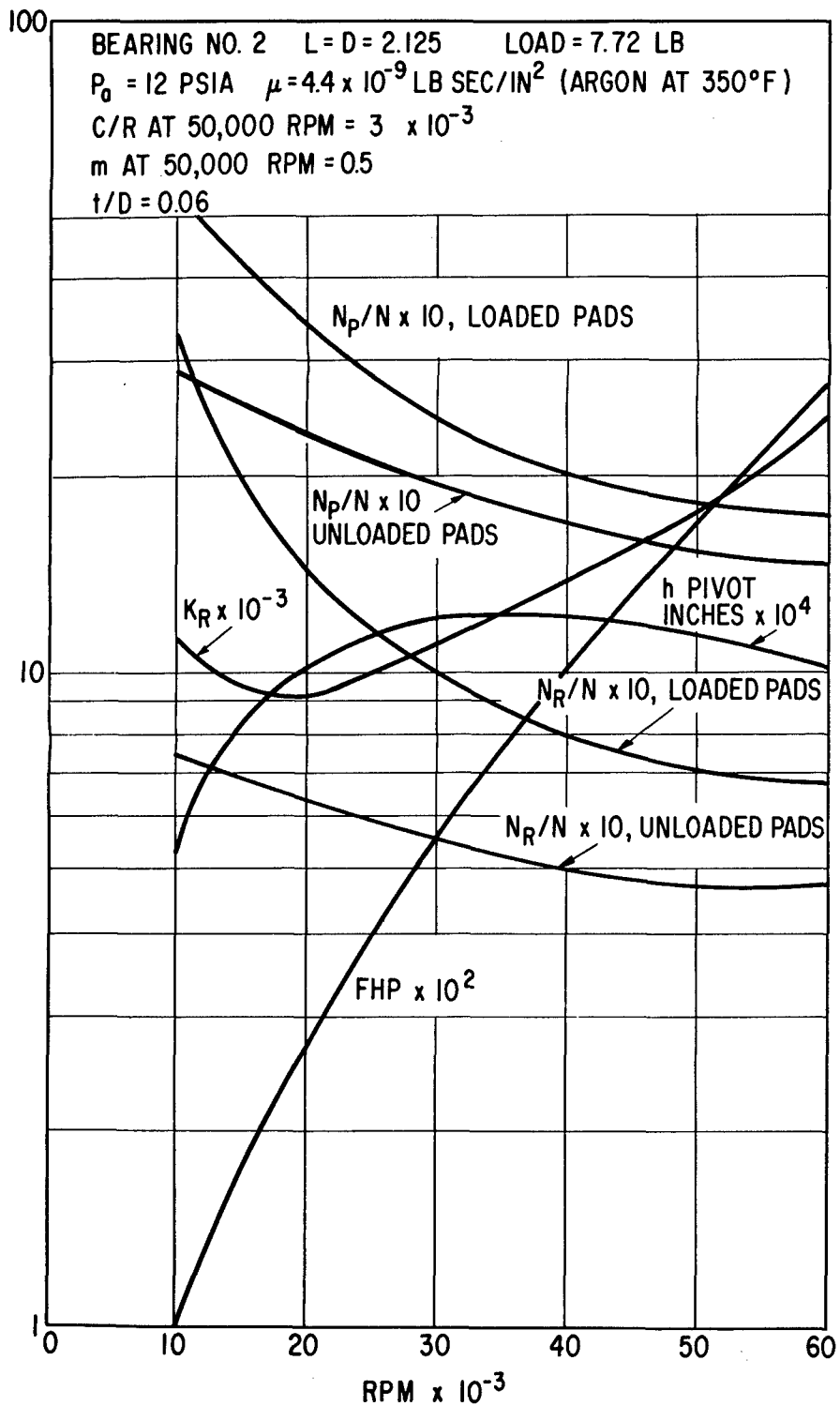


Fig. D-4 - Calculated Performance In A 12.0 PSIA Argon Environment For The Second Design Of The No. 2 Journal Bearing (Rotor horizontal relative to a 1-g gravitational field)

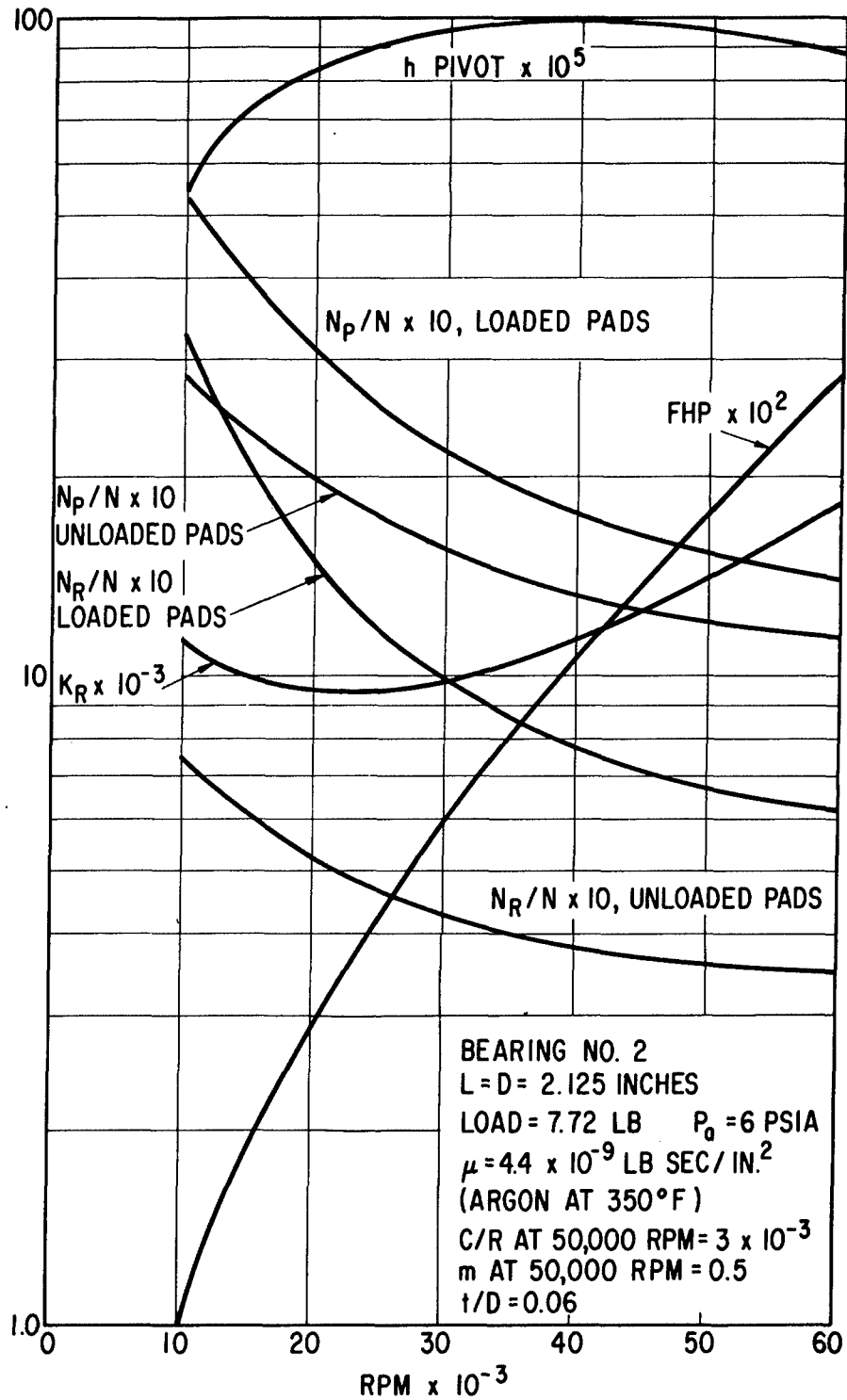


Fig. D-5 - Calculated Performance In A 6.0 PSIA Argon Environment For The Second Design Of The No. 2 Journal Bearing (Rotor horizontal relative to a 1-g gravitational field)

Rotor-Bearing System Dynamics

The critical speed map for the second journal bearing design is shown in Figure D-6 (for explanation of this map refer to the discussion of rotor-bearing system dynamics presented in Appendix C and Section II). Relative to the initial journal bearing design (Figure C-7), it is seen that the two rigid-body critical speeds are considerably lower for the second bearing system design. This is primarily a result of the reduced stiffness of the gas film (due to the larger operating clearance), although the reduced stiffness of the upper pivot-support flexures also has a small influence. The third critical speed (i.e., the free-free bending critical) was not affected by the modification to the journal bearing system.

A plot of combined dynamic and steady-state bearing forces versus speed for 0.002 ounce-inches of unbalance in the turbine plane is shown in Figure D-7 (again, discussion pertaining to this type of plot is presented in Appendix C and Section II). It is seen that the once-per-rev rotating force component due to the unbalance is significantly reduced relative to the initial bearing design (Figure C-7). This again is due primarily to the reduced gas-film stiffnesses of the second journal bearing designs.

Maximum recommended bearing loads as a function of speed and ambient pressure for the two journal bearings are plotted in Figures D-8 and D-9. It is seen that the bearings can "safely" support the combined rotating unbalance and steady-state 1-g horizontal loads at speeds above 20,000 rpm, and at ambient pressures above 6.0 psia for the No. 1 bearing, and above 10.0 psia for the No. 2 bearing. The maximum load criterion used in calculating the plots of Figures D-8 and D-9 was $\epsilon_b \cos\phi$ equal to 0.4. This criterion is based upon engineering judgement and field experience with previously developed gas-bearing machinery, and results in minimum "safe" film thicknesses for continuous normal operation of 0.40 and 0.95 mils for the No. 1 and No. 2 bearings, respectively. However, it is seen from Figures D-2 through D-5 that the bearings should actually be able to carry the maximum anticipated loads down to very low rotor speeds before the gas films would actually be ruptured.

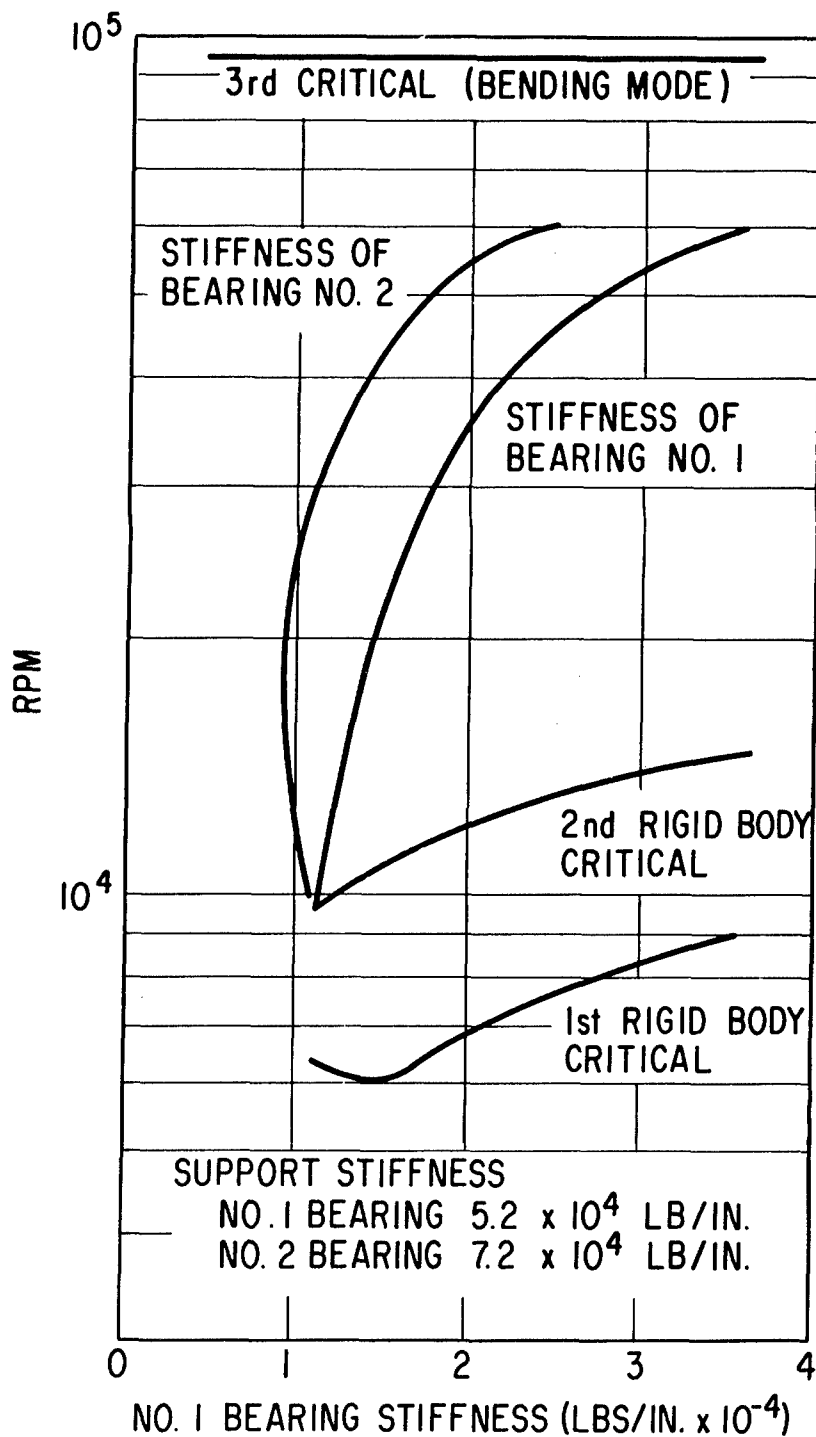


Fig. D-6 - Calculated Critical Speeds And Bearing Stiffnesses For The Second Bearing System Design (Bearing stiffness data is based on horizontal rotor orientation relative to a 1-g gravitational field and a 12.0 psia argon environment)

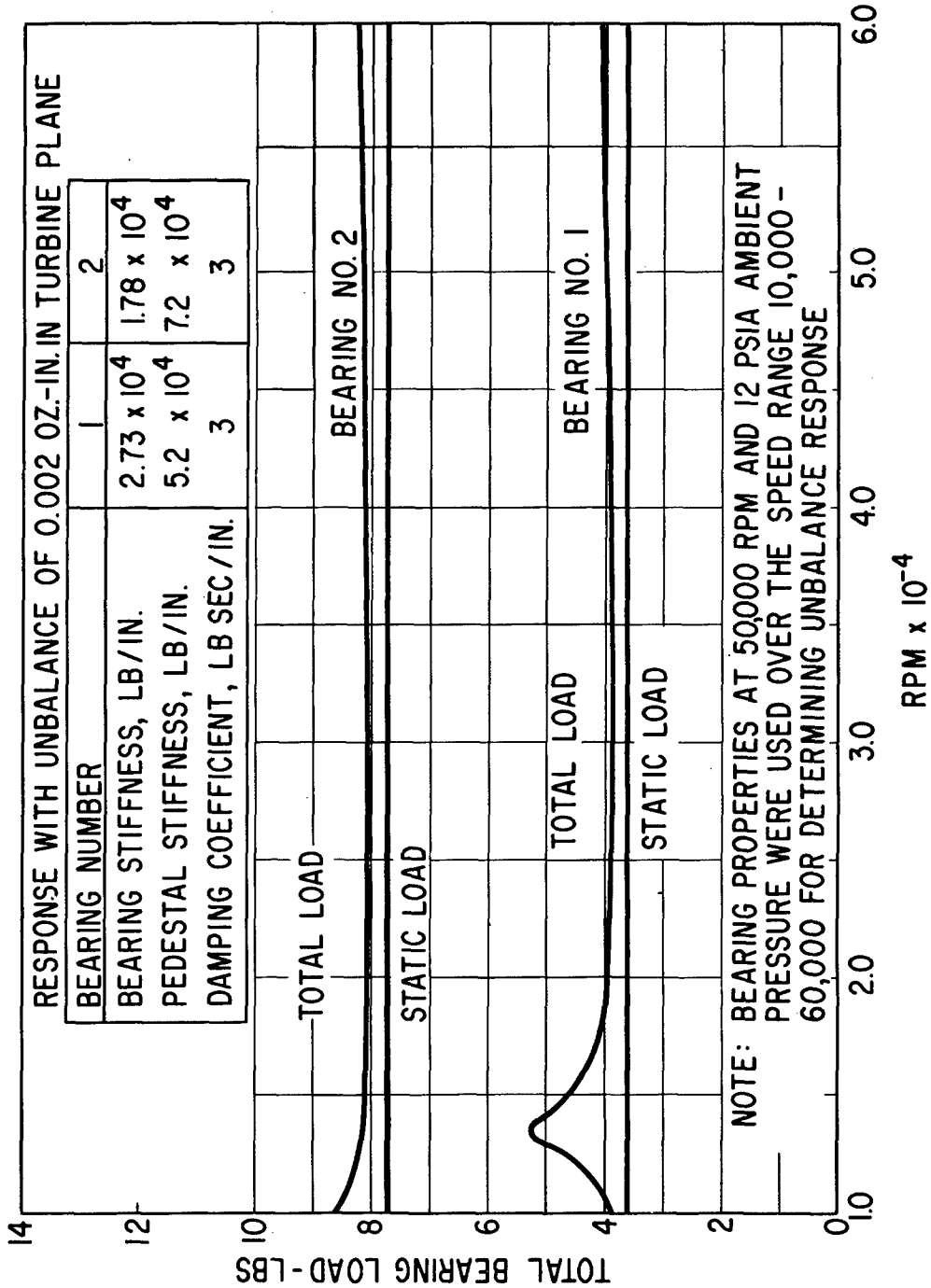


Fig. D-7 - Calculated Maximum Bearing Loads For The Second Bearing System Design Due To 0.002 Ounce-Inches Unbalance In The Turbine Plane

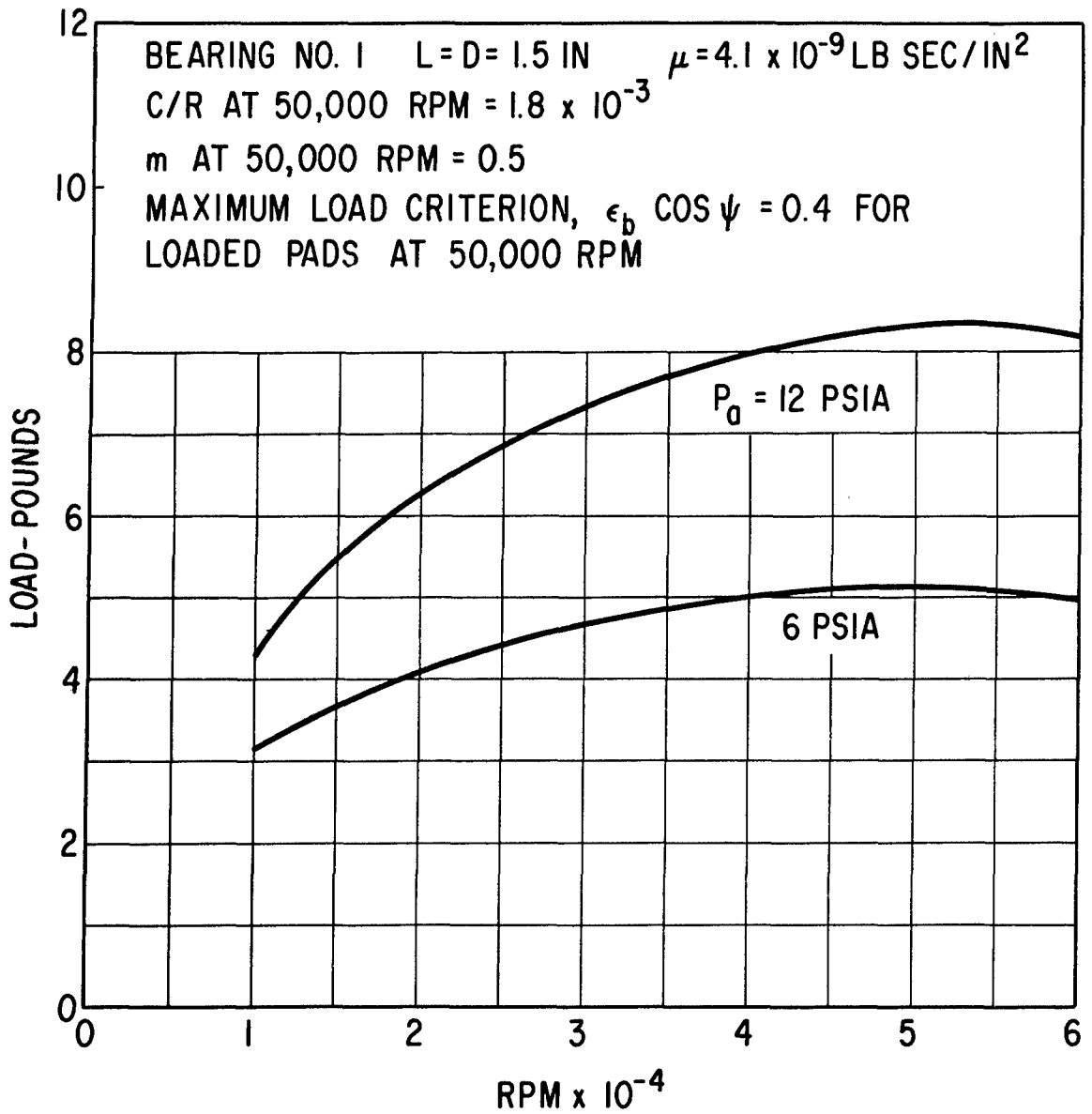


Fig. D-8 - Maximum Recommended Load Capacity Versus Speed For Continuous-Duty Operation Of The Second Design Of The No. 1 Journal Bearing

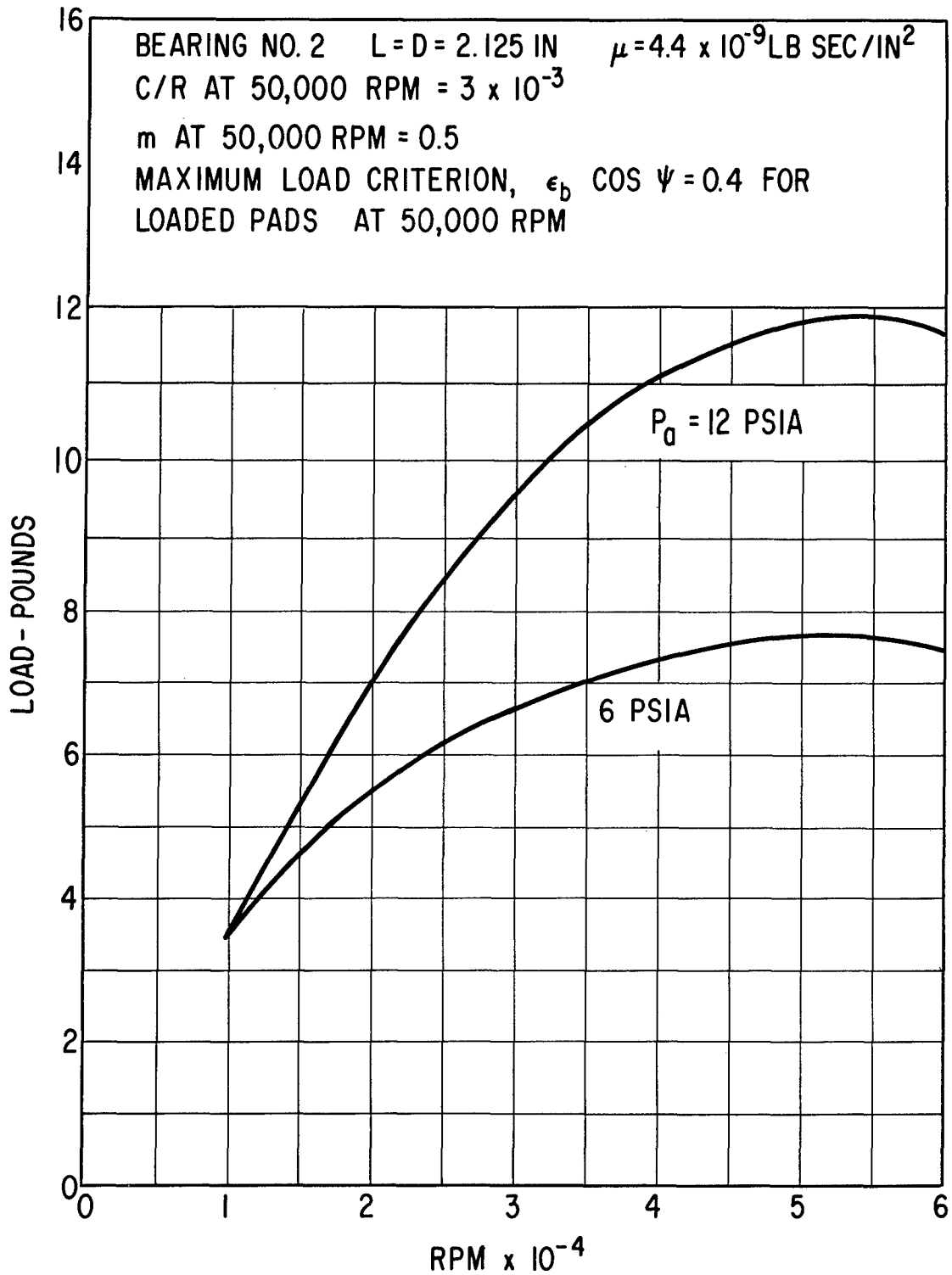


Fig. D-9 - Maximum Recommended Load Capacity Versus Speed For Continuous-Duty Operation of the Second Design Of The No. 2 Journal Bearing

Bearing Cooling Design

The journal and thrust bearing cooling mechanisms used for the second journal bearing design are identical to those used for the initial design. The background studies which led to the cooling techniques adopted are discussed in Appendix C. The flow paths and flow rates for the argon cooling gas are defined in Figures C-11 and C-12. The thermal boundary conditions used for the thermal analysis of the second bearing system design are defined in Figures D-10 and D-12. The calculated isotherms for the two bearing regions are shown in Figures D-11 and D-12. It is seen from Figures D-11 and D-12 that the operating temperatures of the No. 1 and No. 2 journals are considerably lower than those calculated for the initial journal bearing design (see Figures C-15 and C-18).

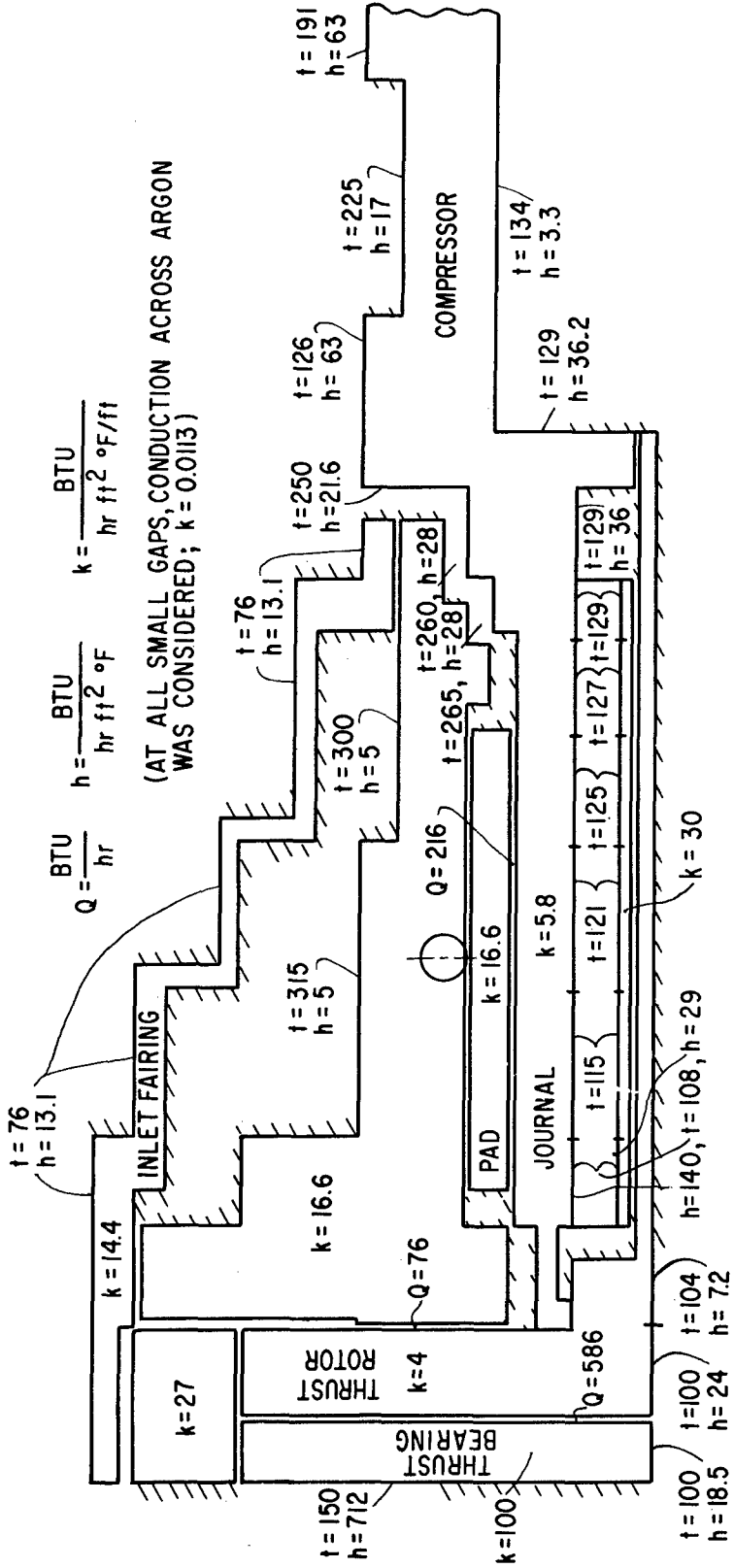


Fig. D-10 - Internal Boundary Conditions For The Second Design Of The No. 1 Journal Bearing And Thrust Bearing

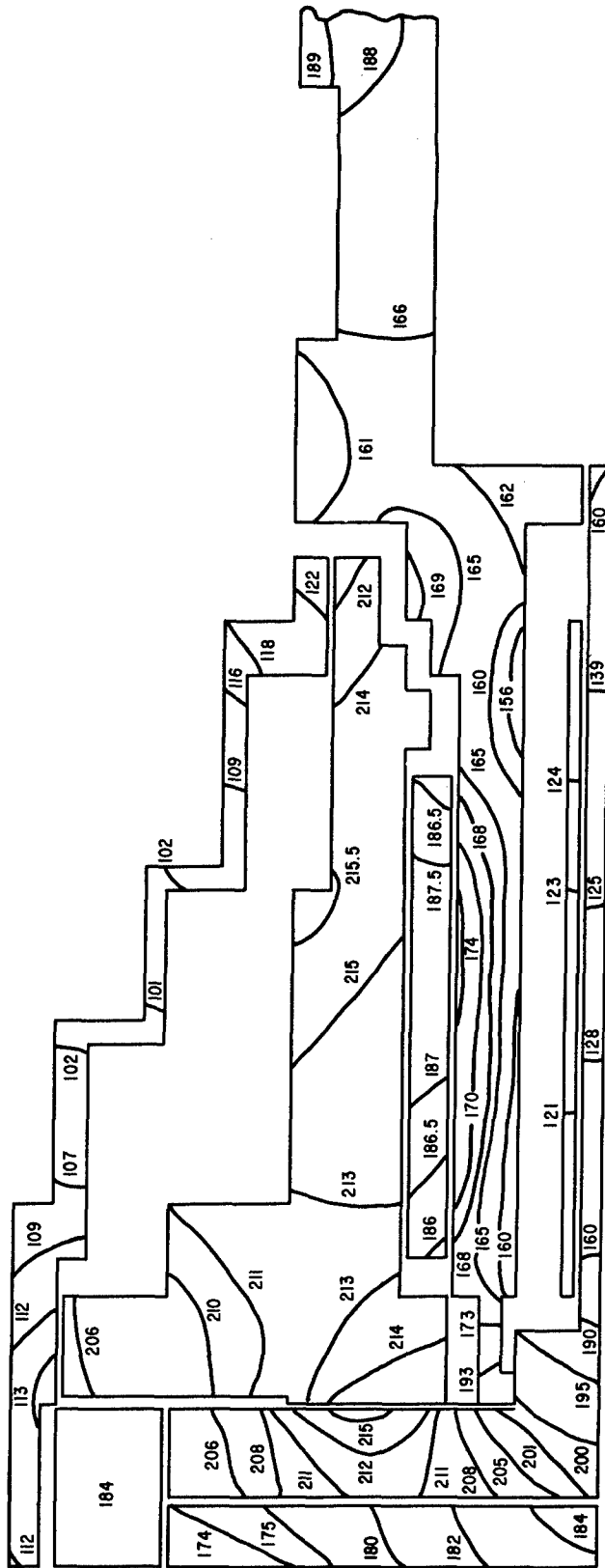
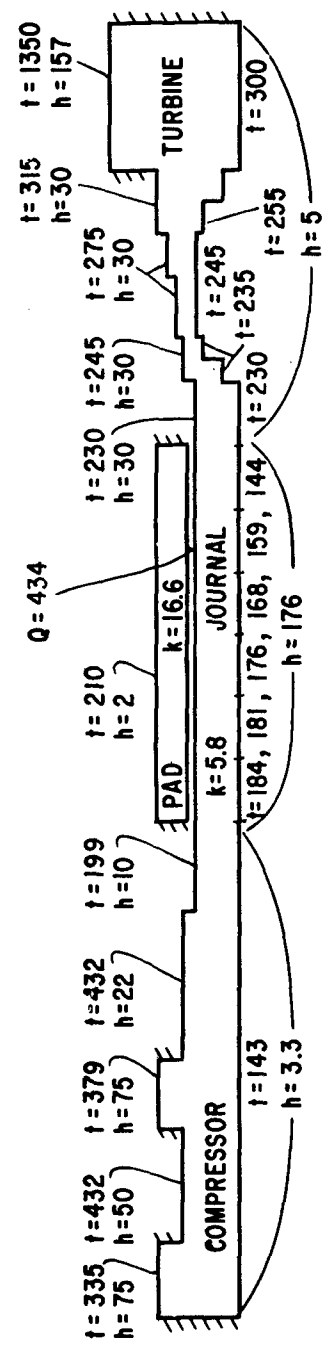
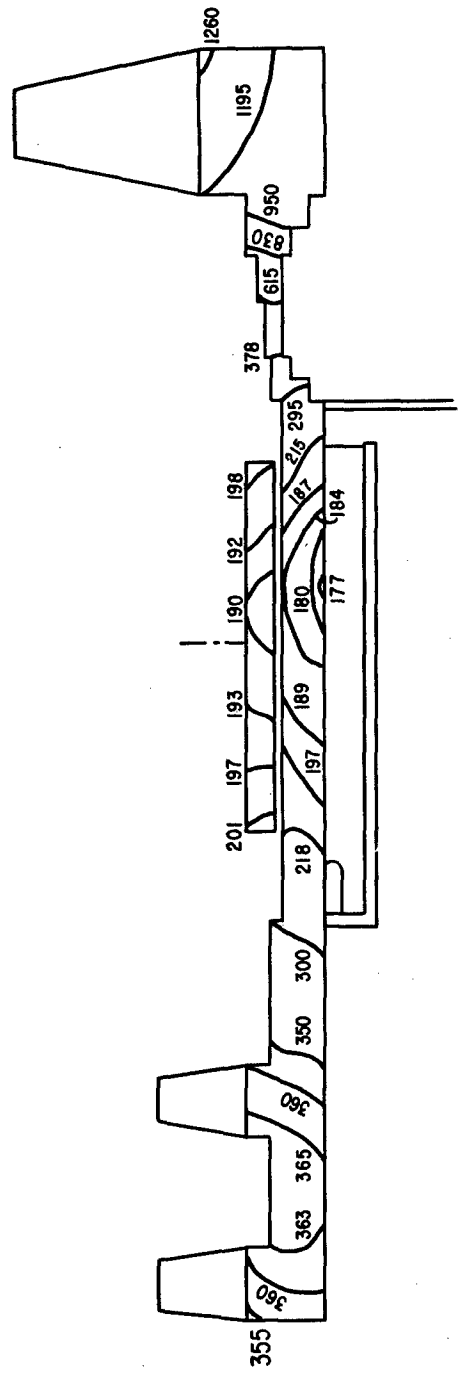


Fig. D-11 - Calculated Isotherms For The Second Design Of The No. 1 Journal Bearing And Thrust Bearing

$$h = \frac{\text{BTU}}{\text{hr ft}^2 \text{ of } \theta}, \quad k = \frac{\text{BTU}}{\text{hr ft}^2 \text{ of } \theta / \text{ft}}, \quad Q = \frac{\text{BTU}}{\text{hr}}, \quad k = 0.0144 \text{ FOR ARGON IN CLEARANCE GAP.}$$



BOUNDARY CONDITIONS FOR MODEL



ISOTHERMS FOR NO. 2 JOURNAL BEARING AREA

Fig. D-12 - Thermal Boundary Conditions And Calculated Isotherms For The Second Design Of The No. 2 Journal Bearing

Test Evaluation of Second Bearing System Design

Subsequent to fabrication of the modified parts for the second bearing system design, but prior to assembly of these parts into the simulator, the stiffness of each of the new upper flexures for the No. 1 and No. 2 journal bearings was determined from load versus deflection measurements. Figure D-13 is a plot of the load-deflection data for the four new flexures. Whereas the design value of stiffness for the new flexures was 10,000 lb./in., it is seen from Figure D-13 that the measured average stiffness of the flexures was 9,800 lb./in. for the No. 1 bearing and 8,400 lb./in. for the No. 2 bearing. The explanation for this discrepancy is the same as discussed in Appendix C (page C-7). Figure D-14 is a photograph of the new upper flexures.

Photographs of one of the pads for the No. 2 bearing are shown in Figure D-15. The basic design of the pad is the same as was used for the initial No. 2 pad design, except that the radius of the pad is slightly larger in accordance with the larger C_p/R ratio. The technique used to obtain the higher moment of inertia in the roll direction (as noted in Table D-1) was simply to epoxy additional weights to the ends of the pad as shown in Figure D-15.

The journal bearings were set up with the following zero-speed room temperature diametral bearing clearances:

1. No. 1 bearing - 1.1 to 1.2 mils
2. No. 2 bearing - 1.6 to 1.7 mils.

The thrust bearings were set up the same as described in Appendix C. Throughout the tests of the second journal bearing design, the modified five orifice configuration of the forward hydrostatic thrust bearing was used.

Test evaluation of the second journal bearing system was started on December 30, 1965. Acceptance testing of the bearing system in accordance with P&WA specification 6355-A was accomplished on January 13 and 14, 1966. The bearing system

was successfully operated at all of the required conditions of the P&WA acceptance test. However, it was not possible to operate the No. 2 bearing at the total design-point clearance. The calculated diametral clearance for the No. 2 bearing running in argon at design point conditions was 3.17 mils for the second bearing configuration. The maximum diametral clearance obtained during the test program was 2.1 mils at 50,000 rpm during operation in air at 14.7 psia. At this clearance condition, the rotor developed a low-frequency low-amplitude whirl motion. The whirl frequency was approximately 7,500 rpm. Attempts to further increase the bearing clearance resulted in increased size of the low-frequency whirl orbit. Attempts were also made to attain design-point clearances at 40,000 and 30,000 rpm. Again, however, the low-frequency whirl condition was encountered at total diametral clearances of 2.5 and 2.7 mils, respectively. In each case the whirl frequency was approximately 7,500 rpm.

This sequence of tests marks the first observance by MTI of a whirl condition in a pivoted-pad gas-bearing system. It also marks the first time that MTI has tested a pivoted-pad bearing designed to operate at a large clearance condition. (The design-point diametral clearance of the initial No. 2 journal bearing design was 0.88 mils, as contrasted to the 3.17 mil design point clearance of the second design. During acceptance testing of the initial design, the 0.88 mil design-point clearance was achieved, and even exceeded, without evidence of any whirl condition.) Since the pads were far from being unloaded at the onset of whirl, no immediate explanation was available for the cause of the whirl condition. Furthermore, since the rotor-bearing system simulator was to be used by P&WA, it was decided not to risk damaging the machine by attempting to operate more deeply into the whirl region until a well defined program for investigating the whirl phenomenon could be worked out. Accordingly, testing was temporarily terminated at the conclusion of the acceptance tests.

One of the primary objectives of the second bearing system design was to achieve significant reduction in bearing friction loss. For the No. 2 bearing alone, the second design represented a calculated 66 percent reduction in friction loss relative to the initial design. This total reduction was not, of course, achieved, due to the whirl phenomenon mentioned above. However, whirl-free operation of the No. 2 bearing was achieved at a 1.65 mil average diametral clearance with the

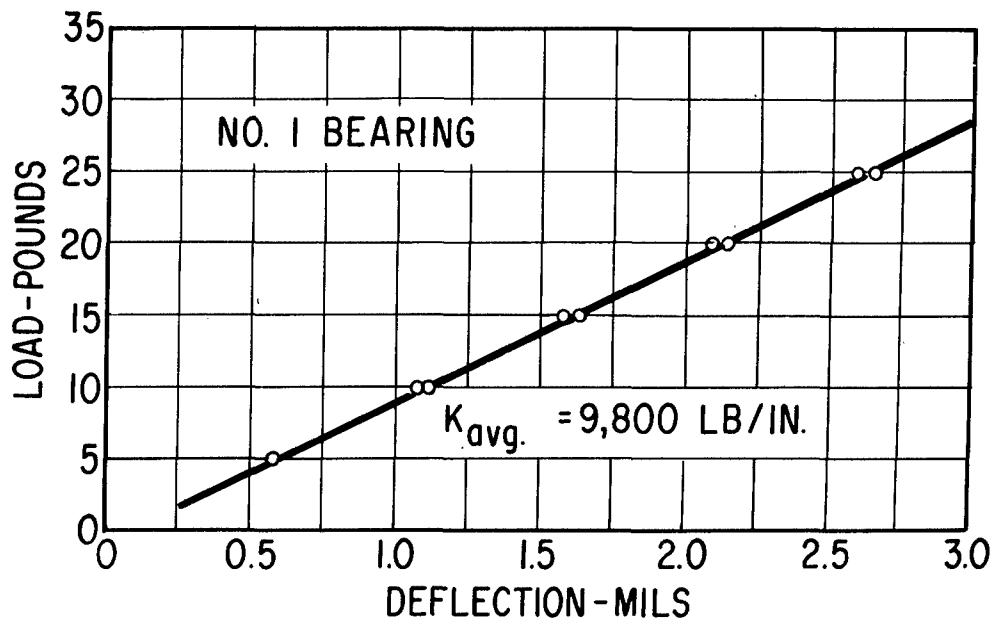
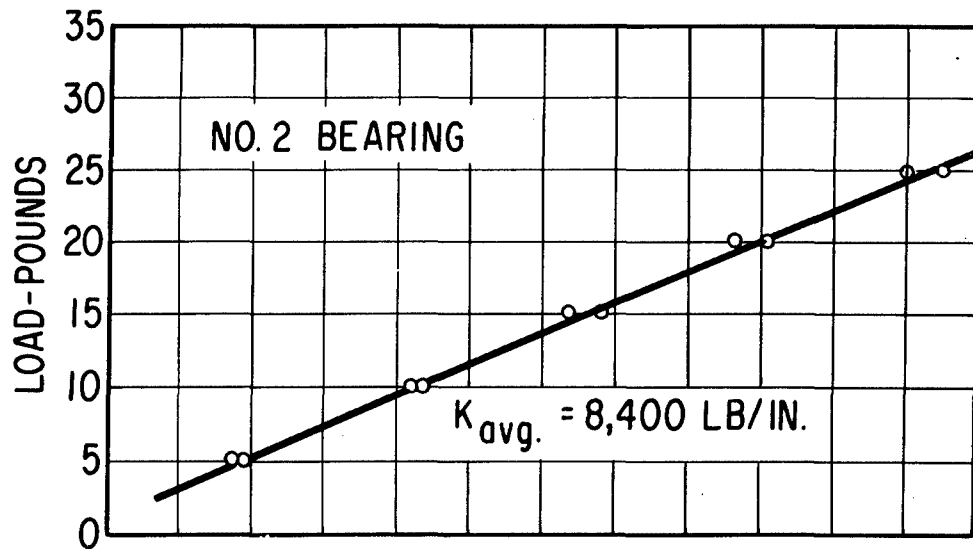


Fig. D-13 - Measured Load Versus Deflection Plot For The Revised Upper Pivot-Support Flexures For The Second Design Of No. 1 and No. 2 Journal Bearings

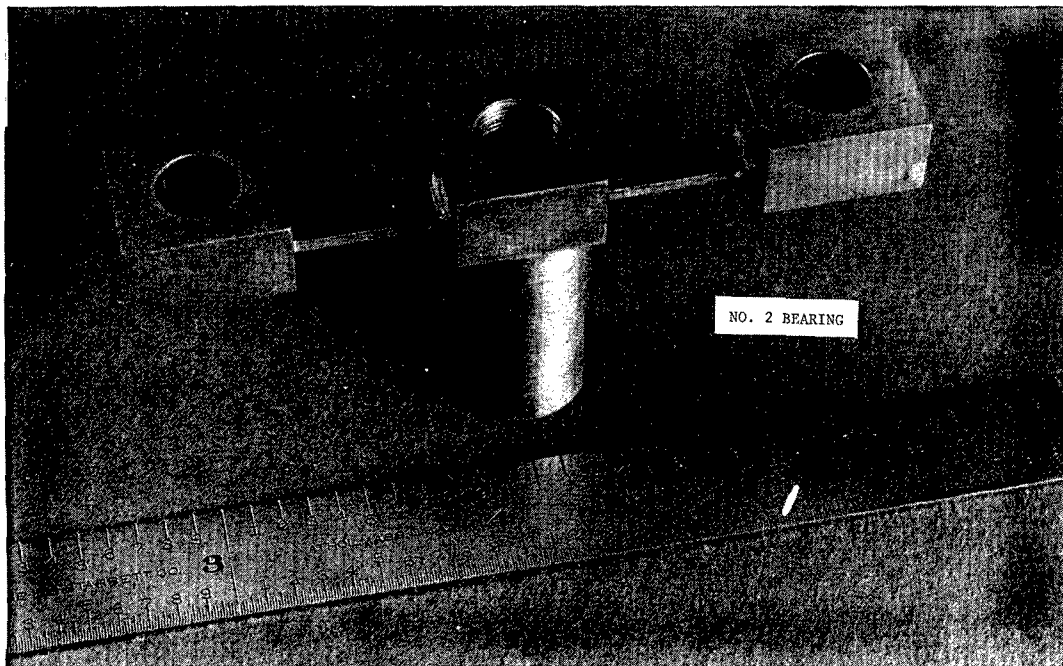
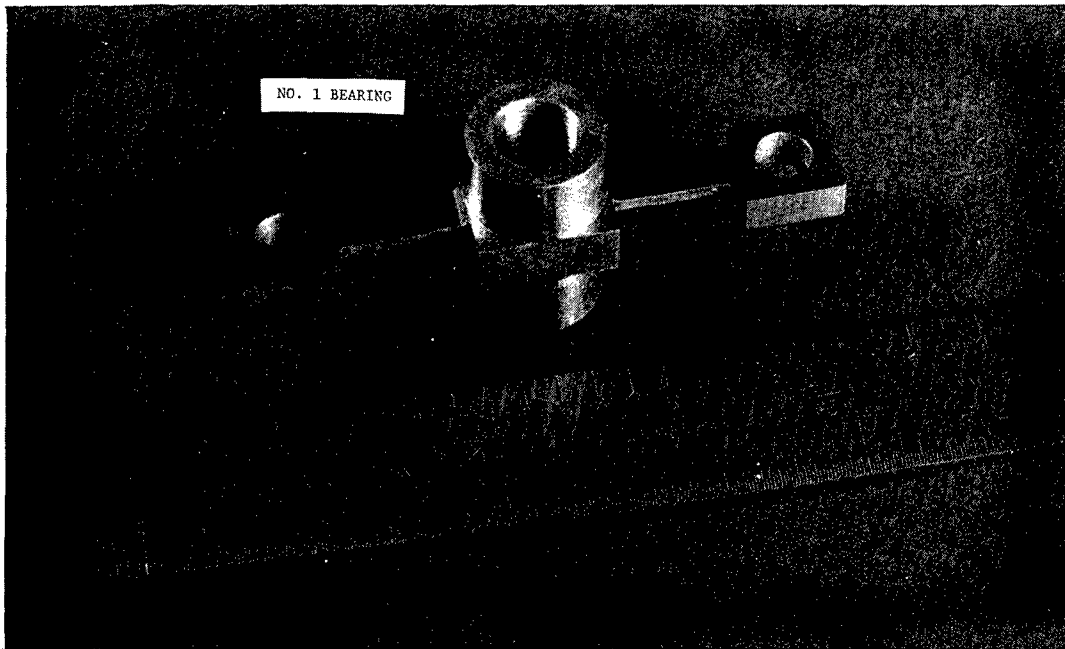


Fig. D-14 - View Of Revised Upper Pivot-Support Flexures For The Second Design Of The No. 1 and No. 2 Journal Bearings

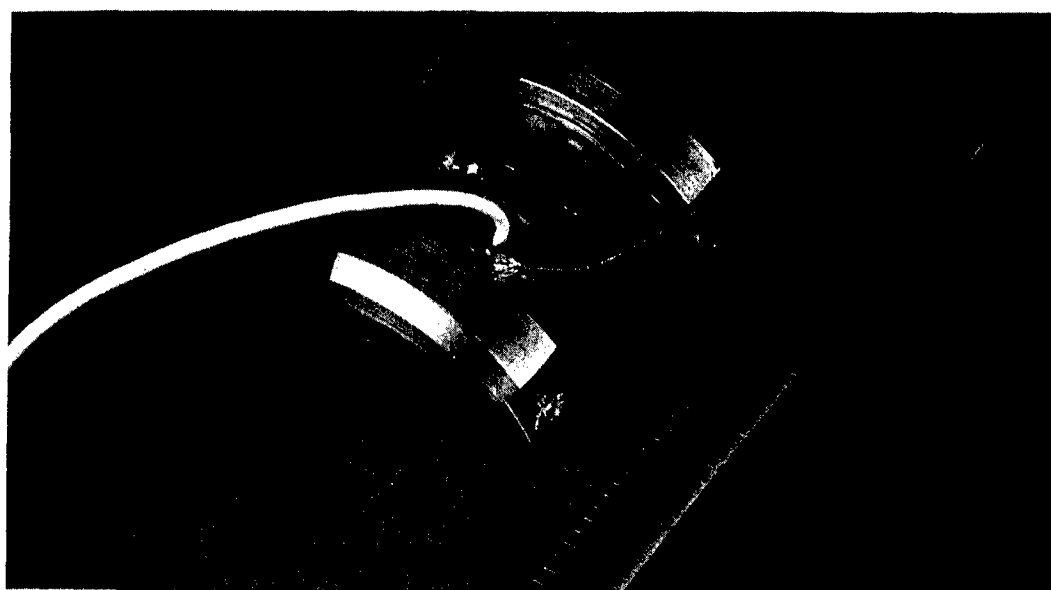
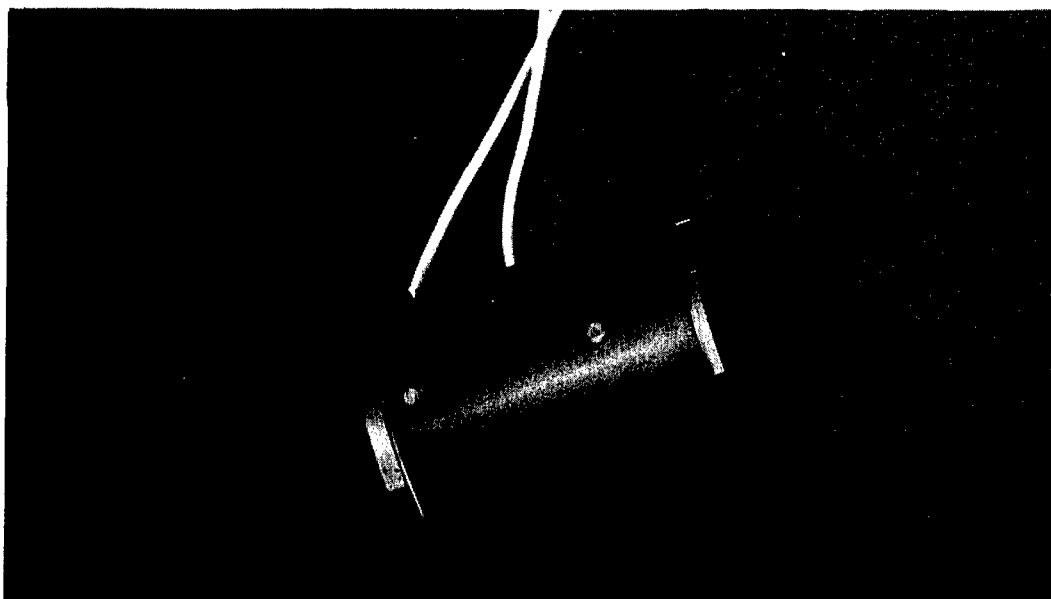


Fig. D-15 - Views Of One Pad For The Second No. 2 Journal Bearing Design Showing Weights Added To Increase Pad Inertia In Roll Direction

rotor-bearing system running at 50,000 rpm in a horizontal position in an argon environment at 12.0 psia ambient pressure. The calculated friction loss at this clearance is 179 watts, as compared to 336 watts for the initial No. 2 bearing design. Hence, a significant 48.2 percent reduction in friction loss was, in fact, obtained with the second No. 2 bearing design.

At no time during the test program was any whirl observed in the No. 1 journal bearing. The design-point diametral clearance (in argon at 12.0 psia) was 1.35 mils. During the acceptance tests, the average clearance obtained during the brief argon test run was 1.25 mils.

Figures D-16 and D-17 show plots of calculated and measured pivot film thickness for the No. 1 and No. 2 bearings, respectively. The calculated and measured results pertain to test runs 243 and 244 of the acceptance tests. It is seen that there is quite close agreement between the calculated and measured data.

Based on the test results for the second bearing system design, MTI made the following recommendations:

1. that the second design for the No. 1 journal bearing be adopted for the turbocompressor;
2. that the pivot flexure designs for both the No. 1 and No. 2 journal bearings be adopted;
3. that a C_p/R ratio of 0.003 be adopted for the No. 2 journal bearing;
4. that additional tests be conducted to determine a specific design-point diametral clearance for the No. 2 journal bearing which would minimize friction losses and, at the same time, assure whirl-free operation throughout the entire spectrum of anticipated operating conditions.

The whirl phenomenon is more completely described in Section IV of this report. The results of a test program to accomplish the objectives of recommendation four above are also documented.

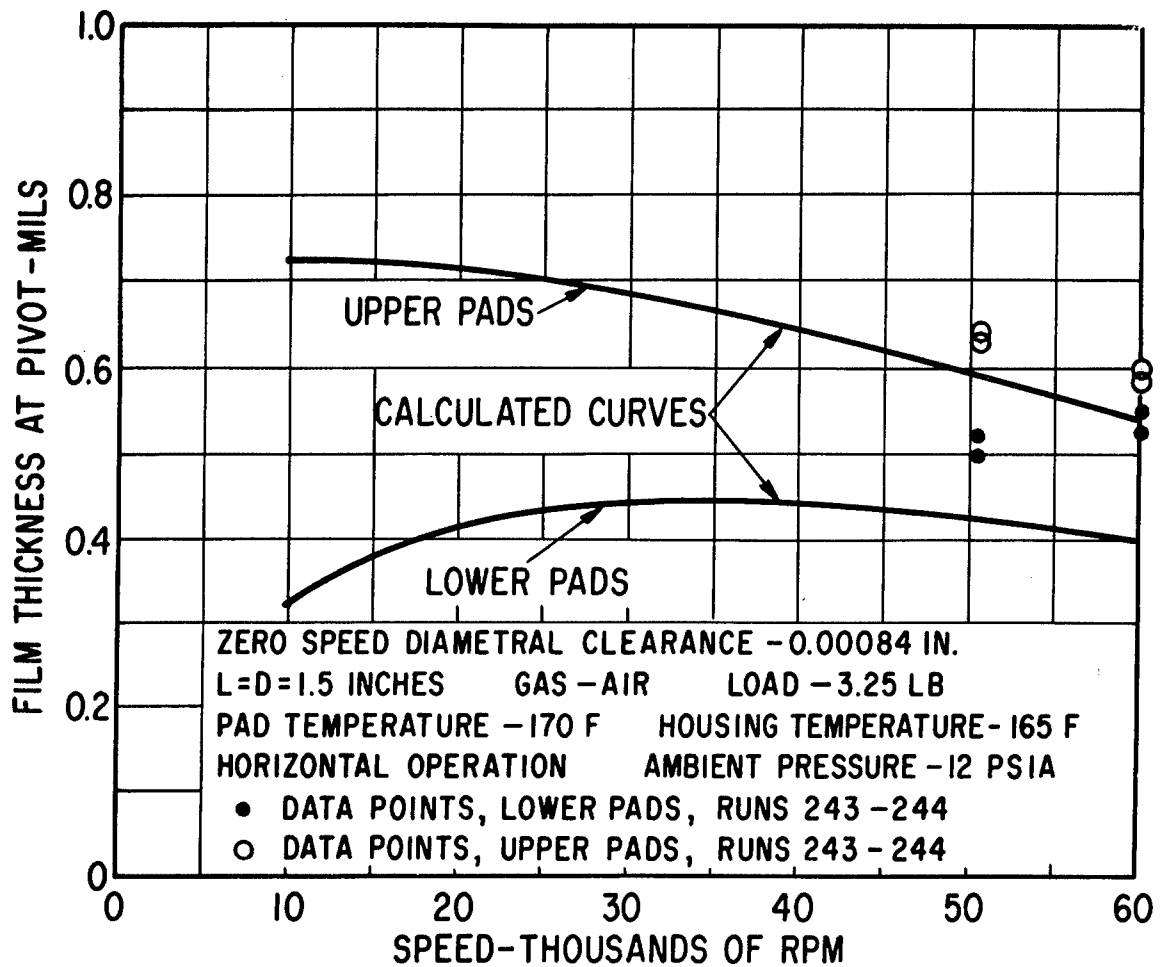


Fig. D-16 - Comparison Of Measured And Calculated Pad Pivot Film Thickness For The Second No. 1 Journal Bearing Design Operating In Air At 12.0 PSIA With The Rotor Horizontal

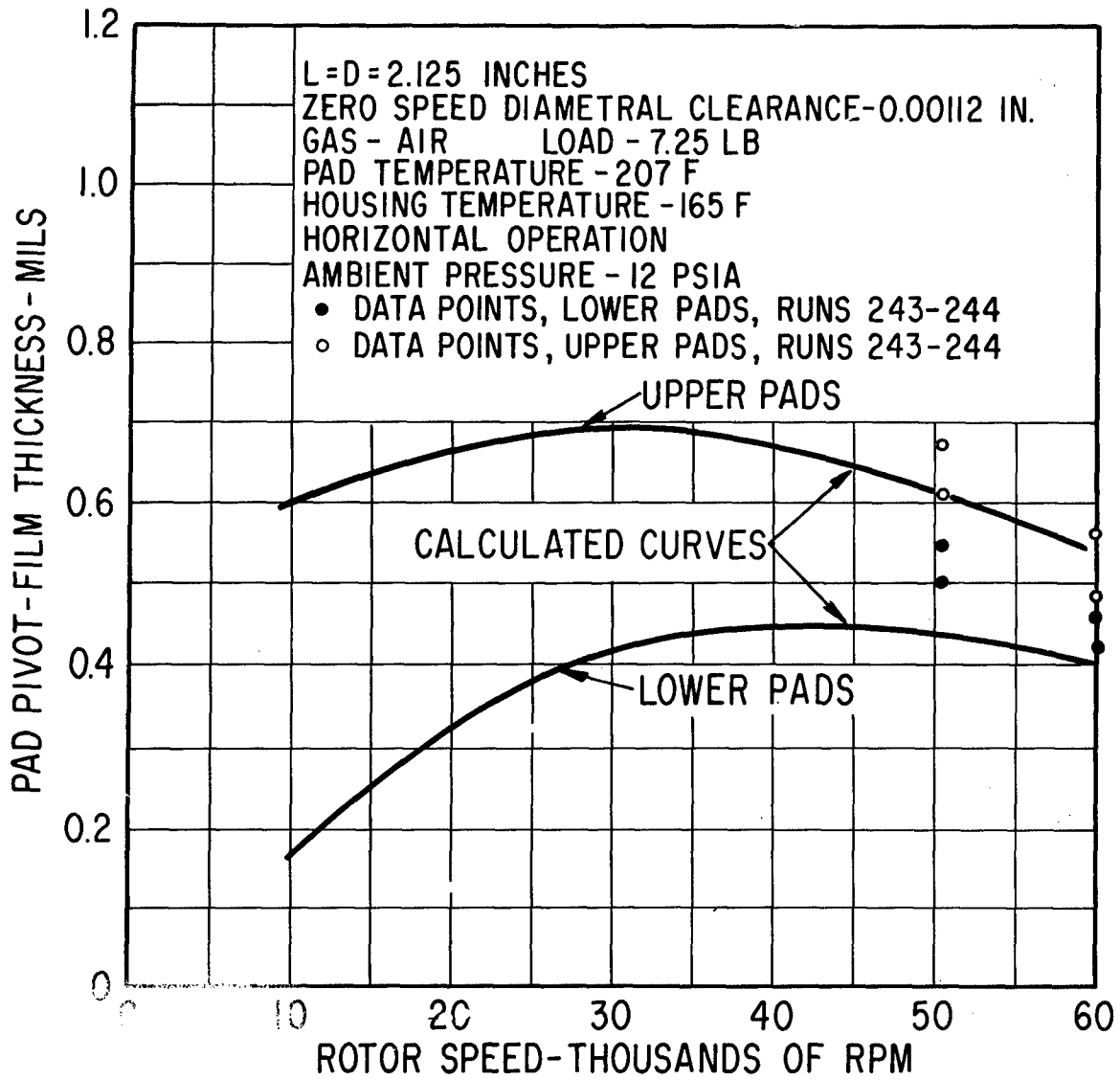


Fig. D-17 - Comparison Of Measured And Calculated Pad Pivot Film Thickness
 For The Second No. 2 Journal Bearing Design Operating In Air
 At 12.0 PSIA With The Rotor Horizontal

APPENDIX E

FINAL REPORT - FIRST BEARING MATERIALS EVALUATION

INTRODUCTION

This report describes the results of the work on Item 3 of the Pratt and Whitney Aircraft subcontract to MTI under prime contract NAS 3-4179. This work item reads as follows:

"Item 3 Conduct an evaluation, including analysis and bench tests, of four bearing materials to determine the combination of materials which is most promising for application in the turbine-compressor gas bearings. Material specifications of the optimum materials selected shall be provided to Pratt and Whitney Aircraft".

The advantages of gas-lubricated bearing systems for space power plants are well-known. However, little emphasis has been placed on the hardware aspects of the problem, in particular, the need for preventing surface damage between moving surfaces. Since the viscosity of any gas is extremely low, the generated film thickness will be small. Therefore, effective bearing performance requires that very fine clearances be maintained between the bearings and the shaft.

As long as the bearing materials maintain dimensional integrity, and the shaft is supported on a film of gas, the life of the bearing system will be extremely long. However, when the bearing surfaces contact the shaft, as they will during starts and stops or during vibration or shock loads at high speeds, any surface damage or wear may destroy the dimensional accuracy of the surfaces. Even a small amount of loose wear debris could cause serious abrasion damage.

The design of the bearing system can also have considerable influence on the ability of the bearing to tolerate high-speed rubs or wear debris. For example, a plain journal bearing is very susceptible to abrasion damage and jamming by loose debris. On the other hand, tilting-pad bearings can often accommodate loose particles and can tolerate some misalignment. The interrupted surfaces of the tilting-pad bearing system will also permit debris to escape. Nevertheless, there is still a problem in choosing suitable materials which will be resistant to surface damage, regardless of the type of bearing used.

The selection of gas bearing materials with adequate sliding compatibility is difficult, largely because little effort has been devoted to this problem. There is a wealth of information available on the sliding behavior of materials; however, the exacting requirements of gas bearings, and the lack of any extensive practical experience, makes it almost impossible to choose one particular combination with any degree of assurance.

For this reason, an experimental study was made for the evaluation of four promising bearing material combinations for the turbine-compressor package. To make the tests as meaningful as possible, the material combinations were tested by using a hydrodynamic, tilting-pad bearing as the test specimen. Both start-stop and high-speed contact tests were made in an argon environment at 350 F. In all cases, the pad-to-shaft clearances were identical.

SUMMARY OF RESULTS

Tests were run for the evaluation of the sliding behavior of four material combinations which appeared to be promising coatings for the bearings and shaft surfaces in the turbine-compressor package. The choice of these materials was based on previous MTI experience.

To simulate the actual application as closely as possible, the test specimens were evaluated as hydrodynamic bearings in an argon environment at 350 F. Both the start-stop and high-speed sliding performance was determined.

Start-Stop Evaluations

In these tests, each combination was run for one thousand start-stop cycles at a stress of 4.0 psi.* The only exception was the DU material which was evaluated under a stress of 2.4 psi. The results of these tests were as follows:

1. Two combinations of flame-sprayed coatings were very effective. These combinations were:
 - a. Tungsten Carbide vs. Aluminum Oxide
 - b. Chrome Oxide vs. Chrome Oxide

Except for some polishing in the contact areas, no surface damage was observed and the total wear was practically negligible for both combinations.

2. The Electrofilm 4396 coating mated against hardened 416 stainless was satisfactory although it should be anticipated that wear and loose debris will be produced by the sliding action.
3. As far as start-stop behavior is concerned, the DU gave relatively poor results. The DU pad would not lift when a stress of 4.0 psi was applied and it was necessary to decrease the stress to 2.4 psi in order to run the tests. Some light transfer of bronze was observed on the shaft after the test.

High-Speed Evaluations

The high-speed rub tests were made at 60,000 rpm and consisted of a series of shock loads of gradually increasing magnitude which caused the bearing to contact

*See page 11 for definition of stress.

the shaft for a fraction of a second during each impact. The results were as follows:

1. The tungsten carbide-aluminum oxide was damaged and intermittent contact through the gas film was detected during the latter stages of the test.
2. The Electrofilm 4396 coating, running against hardened 416 stainless, was worn through in some areas at the end of the test, and metal-to-metal contact was taking place.
3. Both the chrome oxide mated against itself and the DU sliding against sprayed molybdenum were still effective at the end of the test. The DU generally appeared to be in better condition.

CONCLUSIONS

Of the four material combinations evaluated in this work, the chrome oxide is the most promising. The DU, mated against sprayed molybdenum, was more effective than the chrome oxide under high speed rub conditions. However, experience has shown that the high speed compatibility of this material is its only attribute. Some of the characteristics of DU, as compared with chrome oxide, are summarized below.

	DU	Chrome Oxide
Temperature Resistance	Limited to less than 500 F by softening of surface layer	900 F or higher
Availability	One source. Limited sizes, only in strip form	Several suppliers. Can be applied to any open surface by plasma coating
Techniques of Application	Requires development effort	Straightforward
Ease and Accuracy of Finishing	Passable with proper techniques	Excellent
Start-stop Behavior	Appears to have higher lift-off speed for given load. May transfer.	Low lift-off speed. Very low wear, no surface damage
High-Speed Compatibility	Low wear. Bearing polished by high-speed sliding contacts.	Wears by smooth abrasion

THE SELECTION OF PROMISING COMBINATIONS

General Background

There is very little information in the literature regarding materials for gas bearings. References 1-4 appear to be the only papers which make any contribution to the subject. Because of the practical importance of the problem, MTI has devoted considerable effort to the selection and evaluation of materials for this type of application. The general approach, and the results obtained, are summed up briefly in the following paragraphs.

There are certain general requirements which must be satisfied in any hydrodynamic gas-bearing application. These include:

1. Dimensional stability of the bearing and shaft materials.
 - a. Intrinsic stability of the materials themselves to long-term stress relaxation, centrifugal forces at high speed, metallurgical changes or similar effects.
 - b. Resistance of the material to permanent deformation under load at the maximum temperature of usage.
2. Corrosion resistance of the bearing and shaft materials.
3. Sliding compatibility of the materials, both under start-stop conditions and during a high-speed rub.
4. Ease of fabrication to desired finish and dimensions.

Past experience in the design and fabrication of gas-bearing machinery has shown that a step-by-step approach is preferable for reconciling all of these material requirements, especially if the equipment has to operate over a wide temperature range. For example, if one attempts to select a given shaft and bearing combination to achieve adequate strength and stability, required coefficients of thermal expansion, satisfactory corrosion resistance and suitable compatibility, all in one package, the problems are almost insurmountable. The most logical breakdown is to choose base materials for their bulk properties, such as: strength, density, dimensional stability, etc. The same material can be used for both the bearings

and the shaft. Having established the identity of the base material, the surface problems such as corrosion and sliding compatibility can then be solved by the use of coatings or surface modifications.

As far as the coatings themselves are concerned, the following general criteria have been found to be useful in choosing compatible sliding combinations:

<u>Criteria</u>	<u>Typical Examples</u>
1. Hard, wear-resistant coatings on both shaft and bearings.	Oxides, carbides, hard facings such as Stellites and nitride coatings
2. Soft phase materials (mated against hard, lapped shaft).	Sprayed bronze or nickel-copper-indium on bearings vs. hard shaft.
3. Self-lubricating materials (mated against hard, lapped shaft).	DU or carbon-graphite film stock vs. hard shaft.
4. Solid lubricant films (mated against hard, lapped shaft).	Resin or ceramic bonded films of MoS_2 , graphite, PbO , etc. vs. hard shaft.

Previous MTI Evaluations

Using the criteria listed above, several material combinations were selected and evaluated in start-stop tests at room temperature, using a dry air environment. The results of those tests showed that four bearing combinations were promising enough to warrant further investigation. These included:

1. Flame-sprayed tungsten carbide pad (Linde LW-5) vs. flame-sprayed Al_2O_3 shaft (Linde LA-2).
2. Flame-sprayed chrome oxide pad (Linde LC-4) vs. flame-sprayed chrome oxide shaft.
3. Electrofilm 4396 coating on pad vs. hardened steel shaft.
4. DU strip stock bonded to steel backing vs. hardened steel shaft.

There are other material combinations which would be equally good, but these four are the best that have been found to date by staff members of MTI. All of these combinations appeared to be suitable for use in an inert environment such as argon.

Based on the background and test experience described above, it was recommended that these four combinations be evaluated for their sliding compability under test conditions which simulated the operating conditions in this turbine-compressor package. These conditions were as follows:

1. Environment - argon
2. Bearing temperature - 350 F
3. Bearing type - tilting pad
4. Shaft diameter - 1.5 inches
5. Speed range of interest - 0-60,000 rpm

Since hydrodynamic bearings will be used in this application, the evaluations were proposed to include:

1. Multiple start-stop tests to evaluate low-speed sliding behavior.
2. Short duration, high-speed rubs at 60,000 rpm to simulate the effect of vibration or shock on bearing material compatibility.

TEST EQUIPMENT

Test Rig

The test rig which was used for this work was built with MTI funds as a test device to evaluate gas bearing materials for a variety of applications. Essentially, the equipment consisted of a test shaft, 1-1/2 inches in diameter by 8 inches long, supported on each end by externally-pressurized, gas-supported journal bearings. A single, hydrodynamic, tilting-pad test bearing was deadweight loaded against the center portion of this shaft. With the exception of the pivot materials and the load arm, all parts of the rig, including the test bearings and the test shafts, were made of 416 stainless steel. To simplify the design, axial motions of the test shaft were restrained by hemispherically-tipped rods of filled Teflon which were carefully aligned to contact the centers of both ends of the shaft. These were used only in the high-speed tests. In the start-stop tests, the shaft was coupled directly to a motor and no thrust capability was required.

The test equipment used in this work is shown schematically in Figure 1. Figure 2 is a photograph of the rig with the low-speed drive attached to the shaft. Figure 3 is another view of the rig which also shows the pad assembly, a low-speed shaft and a high-speed shaft. Figure 4 is an overall view of the test area and instrumentation for the high-speed evaluations.

The construction of the tilting-pad test bearing is shown schematically in Fig. 5. A hardened steel bushing, cut in half in the axial direction, was cemented to the back of the pad at the desired pivot point. A hardened steel ball, brazed on the end of a vertical loading arm, was seated in this bushing. The clearance between the ball and the bushing was generous enough to permit the bushing to roll freely against the contact surface of the ball. To restrict lateral motions of the pad, a machined washer was cemented to the bushing. This kept the ball centered in the pivot.*

*Appendix B of this report is a brief discussion of pivot design problems and operating experience.

Drives

Two different types of drives were used in this work. For the low-speed, start-stop tests, the shaft was coupled directly to a 3450 rpm electric motor by means of a quill shaft and a flexible coupling.

In the high-speed tests, slots were milled in one end of the test shaft. These slots acted as a turbine which was driven by means of compressed gas supplied from a cylinder.

Instrumentation

To monitor the performance of the tilting-pad test bearing, two capacitance probes were mounted on the pad — one on each side of the pivot point. The signals from these probes were fed through two Wayne-Kerr proximity meters into an oscilloscope. Running film thickness and wear were measured with this system. In Fig. 6, a photograph of typical oscilloscope traces is shown. The upper "zero line" is set at the beginning of the test, while the bearing is stationary on the shaft. The two lower signal traces show that the pad is running on an average film thickness of approximately 200 microinches and that the pad is tilted about 60 microinches off horizontal. When the bearing or shaft becomes worn, the probe signals on the stationary bearing will be displaced above the "zero line" at zero speed. This is a very accurate means of measuring the total wear in a bearing system.

In the high-speed tests, the motions of the test shaft were monitored by means of two sets of capacitance probes which sensed the radial position of the shaft in the x and y directions. These probes were mounted just inboard of each of the two hydrostatic support bearings.

To measure speed in the high-speed tests, a signal from a single probe was compared with a signal supplied from a variable frequency oscillator. When a one-to-one correspondence was achieved between the probe signal and the oscillator signal, the rotor speed in cycles-per-second could be read directly from the oscillator tuning dial.

Temperature Control and Gas Supply

The test rig was heated by means of two banks of quartz, infrared heater tubes — one bank on each side of the rig. Two powerstats were used to control the voltage to the quartz heaters. The test temperature was measured with a thermocouple which penetrated through the housing wall and sensed the temperature in the housing cavity at a distance of 1/8 inch from the surface of the test shaft.

Since it was planned that the hydrostatic support bearings would be supplied with argon as the jacking gas, this also took care of the problem of blanketing the bearing cavity with argon. Stainless steel tubing, coiled inside a high temperature furnace, was used to preheat the argon gas which was being supplied from a cylinder to the support bearings.

In the high-speed tests, temperatures at several locations were monitored. Besides the housing thermocouple, a thermocouple was inserted in the tilting-pad test bearing and another measured the temperature in the nozzle box through which the driving gas was supplied. Thermocouples were also used to monitor the temperatures of the jacking gas supply to the hydrostatic bearings and the turbine drive gas supply. The turbine drive gas supply temperature proved to be the most difficult control problem because of the high gas flow rates which were required during the test. Two high-temperature furnaces and a heating tape were needed to preheat the gas to the required temperature.

Definition of Stress

The bearing stress was based on the projected area of the journal ($L \times D$). The width of the test bearing was 1.25 inches and the diameter of the shaft was 1.5 inches. Thus, the projected area was 1.875 square inches and the load, divided by this area, was the average stress in pounds per square inch. The true stresses are actually much higher since contact does not take place over the entire bearing area.

TEST PROCEDURE

Start-Stop Tests

For the low-speed, start-stop tests, a deadweight load was applied to the test bearing and the test rig was heated to 350 F by a low flow of preheated argon being supplied to the housing. When the test temperature had been stabilized, the probe signals were zeroed and the test was started. A program timer was used to turn on the motor, run the test for five seconds at speed, then shut off the motor and allow the shaft to coast to a dead stop. This sequence was repeated until one thousand starts and stops had been accumulated. Observations were made at periodic intervals to see if the running film thickness had changed and to determine if the probe signals on the stationary bearing indicated wear. At the end of the test, the bearing and shaft were examined and photographed.

High-Speed Rub Tests

In these tests, a deadweight load was applied to the test bearing to produce a stress of 2.5 psi. The test rig was heated to the desired temperature and both the bearing support and turbine gas supplies were brought up to a reasonably stable temperature using a by-pass valving system. Then the support bearings were lifted with the preheated argon gas and the shaft was brought up to 60,000 rpm, using preheated argon gas to drive the turbine.

As soon as the speed had been stabilized, a series of shock loads were imposed on the test pad by means of a hinged arm which weighed one pound. This arm was dropped fifty times in rapid succession on the top of the vertical load rod from a pre-set height of one inch. At each impact, the tilting-pad probe signals indicated that the pad had actually contacted the shaft. If the pad was still operating satisfactorily after this series of impacts, weight was added to the hinged arm to increase the load to three pounds and the arm was dropped on the load rod twenty times, again from a height of one inch. The test was then disassembled, the pad was photographed and the pad and shaft were examined.

In the cases where the pad was still in good condition, the test was continued. A load of five pounds was dropped ten times from a height of one inch and a load of seven pounds was dropped ten times, also from a height of one inch. The test was then disassembled and both the pad and the shaft were examined and photographed.

TEST RESULTS

Start-Stop Evaluations

Problems were encountered almost immediately with the hydrostatic support bearings in the test rig. A preliminary evaluation was run using a tungsten carbide coated pad against an Al_2O_3 coated shaft with a stress of 2 psi. During this test, the shaft seized on one of the support bearings after 738 starts and stops. The reason for this failure was not clear, but was probably due to thermal gradients in the housing and misalignment of the drive motor. Since the test schedule was very tight, and since the hydrostatic gas bearings were not required for these low-speed tests, they were replaced with rolling contact bearings. This permitted the start-stop evaluations to continue while changes were made in the furnace and auxiliary equipment.

Some inch-series ball bearings were obtained and cleaned to remove the grease. A very small quantity of a high-temperature, diester-base grease was then added to provide some lubrication. Using these bearings, it was found that one series of a thousand starts and stops at 350 F could be completed before replacement of the bearings was necessary. To blanket the system with argon, preheated gas was supplied to the housing cavity through stainless tubing.

The tungsten carbide- Al_2O_3 test at 2 psi was completed by running the last 262 starts and stops on the ball bearing supported shaft. The contact areas on the shaft and bearing were extremely faint and less than 20 microinches of wear was detected.

During this, and subsequent tests, on the ball bearing supported shaft, careful examinations were made to see if grease was migrating along the shaft into the test area. In no case was any indication of grease contamination observed on the test specimens. The argon blanketing gas kept oil vapors out of the cavity.

The results of the start-stop tests at 350 F were as follows:

1. Tungsten Carbide Coated Pad vs. Al_2O_3 Coated Shaft

Using a stress of 4.0 psi (based on the projected area), one thousand start-stop cycles were accumulated on this combination without any problems. In these tests, a program timer turned the motor on for five

seconds, then turned the motor off and allowed the test to coast down to a full stop. This cycle was repeated until the desired number of starts and stops had been achieved.

A consistent running film thickness of about 100 microinches was obtained throughout the test. The total wear on the bearing pad and the shaft was about 25 microinches at the end of the test. The accuracy of the instrumentation is approximately ± 20 microinches.

The results of this test compare favorably with the data obtained in the test run prior to this contract at room temperature in dry air. In that test, six hundred start-stop cycles at 5.0 psi gave 20 microinches total wear. Most of the wear on this combination appeared to be the result of polishing away microscopic peaks rather than the gross removal of material.

In Figure 7, photographs of the test pad and shaft surfaces are shown. A photograph of the test pad and a new pad is given in the upper right-hand frame of Figure 7, indicating the high finish on the carbide surfaces. The upper left-hand frame of Figure 7 was obtained by reflecting a light from a sheet of white paper to the surfaces. This highlighted the contact area. The other two photographs in Figure 7 show the contact area on the Al_2O_3 shaft. The mottled splotches which are visible on the Al_2O_3 coating appear to be some form of contamination. When the shaft was first sprayed, these discolorations were not visible, but they developed as soon as the coating was ground to finish dimensions. Since they did not appear to be detrimental, as far as surface finish, adherence or sliding behavior is concerned, no significance is attached to these discolorations. No transfer or surface damage was observed on either the pad or the shaft surfaces. The contact areas were smooth and polished and the materials appeared to be in excellent condition.

During this series, some measurements were made to determine the speed at which the bearing pad touched down on the shaft during the coastdown. For these measurements, a signal from one of the probes on the tilting-pad bearing was compared with a signal supplied from a variable frequency oscillator. When a one-to-one correspondence was achieved between the probe signal and the oscillator signal, the rotor speed in cycles-per-second could be read directly from the oscillator tuning dial. It was not possible to get an absolute value by this technique because of the low touchdown speed, but the values could be placed in the range of 390 to 420 rpm. This result is in reasonable accordance with analytical predictions.

2. Chrome Oxide Coated Pad vs. Chrome Oxide Coated Shaft

This combination also ran effectively for one thousand starts and stops at 4.0 psi. The running film thickness was reasonably consistent at 100 to 120 microinches. During most of the test, very slightly negative wear values, on the order of minus 25 microinches, were observed. This may have been due to a minute amount of wear debris trapped under the pad. At the end of the test, the pad was removed, the pad and shaft were wiped off with lens tissue, and the test was re-assembled. No measurable wear or buildup could be detected then. However, no loose debris was observed on the lens tissue.

In previous tests at room temperature in dry air, chrome oxide against itself had given 25 microinches of wear after 660 start-stop cycles at 5.0 psi.

Photographs of the test pad and shaft are shown as Fig. 8. The contact areas on the pad and shaft surfaces were highly polished with no visible surface damage.

3. Electrofilm 4396 Coated Pad vs. Hardened (40 R_C) 416 Shaft

With a stress of 4.0 psi, this combination gave about 50 microinches of wear in one thousand starts and stops. The running film thickness varied periodically between 100 and 150 microinches. In the latter stages of the test, a slightly negative wear rate was observed. This was on the order of minus 2⁵ microinches. When the pad and shaft were wiped off with lens tissue, some very fine, black wear debris was obtained and, when the test was re-assembled, the "negative wear" reading was no longer observed.

In the room temperature tests with a dry air environment, an Electrofilmed pad running against a nitrided shaft had given 65 microinches of wear in 410 starts and stops at 2.3 psi. However, a direct comparison of these results is not justifiable since the technique for lapping these pads has been improved since then.

Photographs of the test pad and shaft are shown as Figure 9. Examination of the pad showed that most of the contact had occurred on the sides although some evidence of light contact was visible in the center. This indicated that the pad was slightly "dished". The shaft surface indicated that the pad was contacting across the complete width of the pad. At first glance, the shaft appeared to have a series of fine scratches in the direction of rotation. However, these scratches did not appear to have any significant depth and were probably more of a series of discolorations than surface damage marks.

4. DU Pad vs. Sprayed Molybdenum Coated Shaft

Several attempts were made to run DU pads at the standard 4.0 psi stress level, but the pads would not lift completely even after they had been run-in at extremely high stress levels. This was similar to the experience obtained in room temperature tests in air. In those tests, electrical continuity was used to determine lift-off. A 40 milliamp current was passed through the bearing and shaft. Although continuity measurements indicated that the pad had partially separated, the meter still indicated 2 to 10 milliamps, apparently because of intermittent contacts through the film. Only at very light loads was complete separation achieved. In spite of this contact, very little damage was observed on either the pad or the shaft — even after numerous starts and stops. It was this freedom from damage that made the DU so attractive as a bearing material.

The performance of the DU pad was then evaluated at several stress levels. The pad lifted easily at 2 psi but would not separate at 3 psi.

The test load was finally selected to give a stress of 2.4 psi, and the thousand start-stop cycles were run off. The running film thickness was about 140 microinches. About 30 microinches of wear was measured in this test. At the end of the test, the load was increased to 3.3 psi to see if run-in had improved the ability of the pad to lift. It had not. No comparison with the old room temperature test results is possible because the technique of preparing the surfaces has been changed completely.

Photographs of the pad and shaft surfaces are shown in Fig. 10. Some transfer of bronze was visible on the molybdenum surface of the shaft and the contact area had numerous, very fine scratches in the direction of sliding. However, as was the case with the Electrofilm test, these scratches did not appear to have any significant depth. The pad surface showed very definite contact smears in the load zone but no serious damage was observed.

High-Speed, Shock Load Test Results

While the start-stop tests were being completed, a new furnace was set up with longer quartz heaters to get a more uniform heat distribution. A stainless steel cover was also built to enclose the test rig and several changes were made in the instrumentation to monitor temperatures in critical areas.

A preliminary high-speed test was run at room temperature with a chrome oxide-coated shaft. The purpose of this test was to check out the performance of the tilting-pad test bearing. The pad was unloaded except for the weight of the pad itself and the weight of the vertical load arm on which the pad was pivoted. This totaled 0.4 pound (about 0.2 psi stress). At approximately 45,000 rpm, the pad began to flutter. This type of instability had been anticipated, but the speed at which it should occur was an unknown factor. The driving gas was shut off and the shaft was allowed to coast down. At about 30,000 rpm, the pad again became stable. In practice, geometrical preloading of the bearing pads is used to assure that they are not unloaded and thus subject to flutter at high speed.

In the next test, sufficient deadweight was used to apply a stress of 2.5 psi to the bearing. This stress was chosen because it is reasonably close to the value which would normally be used on a bearing of this type. With this load, the pad remained stable at all speeds up to and including 60,000 rpm. For the rest of the high-speed tests, every pad was run with a deadweight load sufficient to apply a stress of 2.5 psi to the pad.

The results of the high-speed tests are described in the following paragraphs.

1. Tungsten Carbide Coated Pad vs. Al_2O_3 Coated Shaft

The test pad temperature was approximately 340 F when the speed was stabilized at 60,000 rpm. Fifty shock tests were made by dropping the one pound weight from a height of one inch and twenty more shock tests by dropping three pounds from one inch. A record of these impacts was made by putting one of the tilting-pad probe signals into a Visicorder. Figure 11 is a photograph of a portion of a typical record showing the impact of one pound dropped from a height of one inch. The chart speed was 50 inches per second and the time in contact was about .035 second. In general, the actual time in contact between the bearing and the shaft during each shock test varied from .03 to .05 second regardless of the weight applied.

After these initial shock tests, the tilting-pad test bearing was removed, cooled and photographed. The shaft surface was examined without removing it from the rig. In Fig. 12a, a photograph of the tungsten carbide pad is shown. The pad showed abrasion damage in the load zone but the bearing still ran effectively. The shaft had some smooth transfer streaks on the surface and it appeared to be in good condition.

The test was reassembled with the same bearing pad, temperatures were stabilized and a second test, consisting of ten drops of five pounds from one inch and ten drops of seven pounds from one inch, was run. This time, sharp spikes were observed on the oscilloscope trace of the tilting-pad probe. These spikes persisted even when the turbine drive gas was shut off and the shaft was coasting down. The spikes indicate that isolated contacts were taking place through the gas film, apparently because the surface of either the pad or the shaft was rougher than the thickness of the film. This constituted a failure. In Fig. 12b and 12c, photographs of the pad and shaft surfaces are shown. The Al_2O_3 coated shaft was completely covered with transferred material from the pad. This transfer was very smooth and polished. The carbide pad had a fairly large contact area consisting primarily of sharp abrasion scratches. In Fig. 13, photomicrographs of sections of the shaft and pad are shown at a magnification of 30x.

2. Chrome Oxide Coated Pad vs. Chrome Oxide Coated Shaft

The fifty shock tests of one pound and twenty more of three pounds were made with no significant change in bearing performance. The test pad was then photographed (Fig. 14a). Both the test bearing and the shaft appeared to be polished in the contact areas and showed no evidence of surface damage.

Ten more shock tests of five pounds and ten of seven pounds were then run. At this point, the bearing was still operating effectively. The pad and shaft were photographed and examined. There was a definite increase in the contact area on the pad. However, both the pad and the shaft surfaces appeared to be fairly smooth and polished. Photographs of these surfaces are shown in Figs. 14b and 14c.

Photomicrographs of portions of the contact areas on the pad and on the shaft are shown in Fig. 15. Definite abrasive wear is visible, but the amount and type of damage is much less severe than was the case with the carbide sliding against Al_2O_3 .

3. Electrofilm 4396 on Pad vs. Hardened 416SS Shaft

Figure 16a shows a photograph of the Electrofilmed pad after subjection to fifty drops of one pound and twenty drops of three pounds. The pad was still in fairly good condition but the coating was obviously worn down to a very thin film. The shaft had numerous streaks of an extremely smooth, black coating which appeared to be transferred Electrofilm.

Ten drops of five pounds and ten of seven pounds were then made on these specimens. At the end of this test, the probe signals indicated very unstable operation and intermittent contact. Figures 16b and 16c are photographs of the test pad and the shaft. Although some film still remained on the test pad, there were definite signs that the film had broken through in certain areas and metal-to-metal contact was taking place. The shaft was almost completely covered with transferred Electrofilm. In Fig. 17, photomicrographs of the contact areas on these specimens are shown.

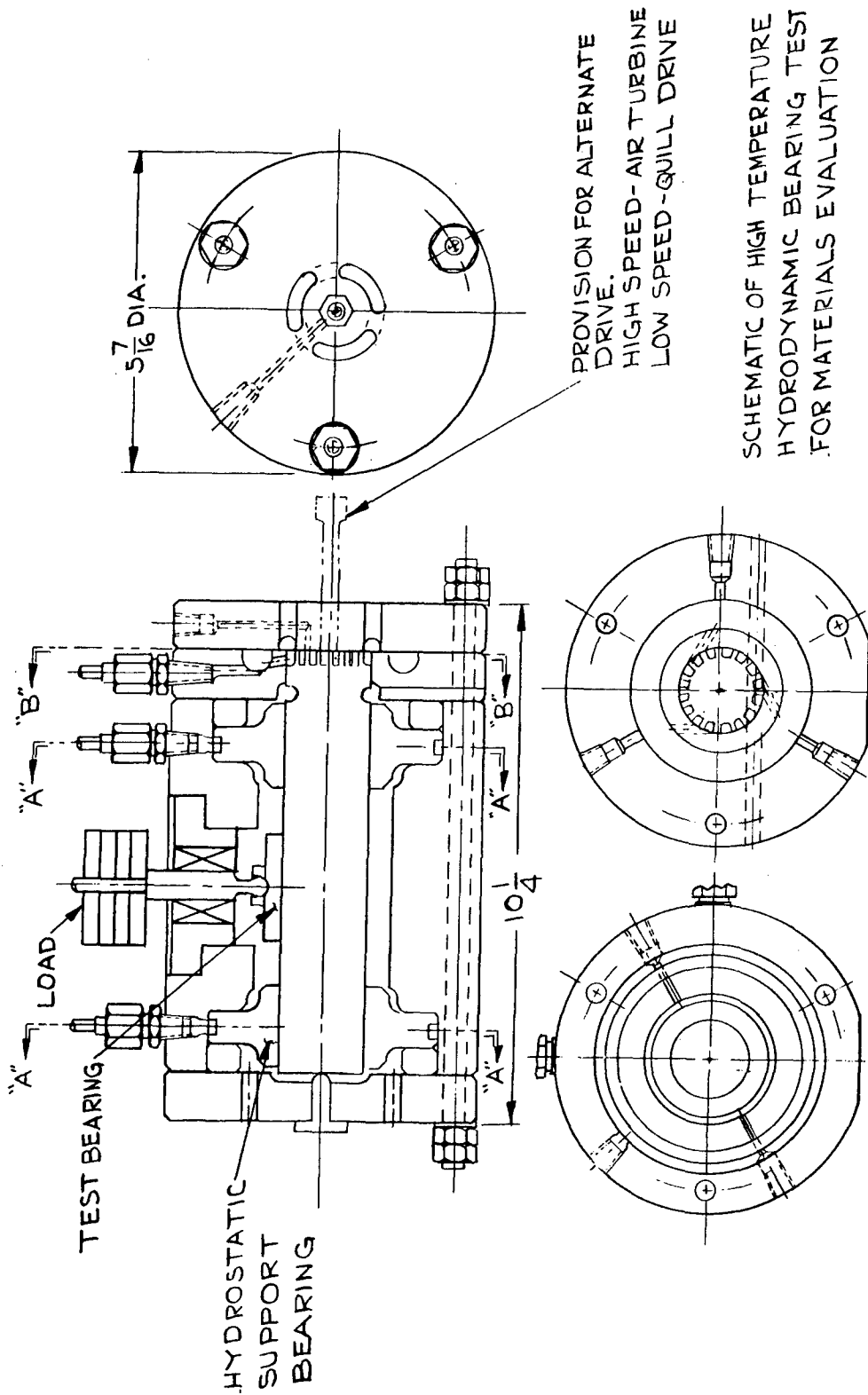
4. DU vs. Sprayed Molybdenum Shaft

As had been anticipated, the DU gave very favorable results in these high-speed tests. Figure 18a shows the pad after the fifty drops of one pound and twenty drops of three pounds. Both the shaft and pad surfaces were smooth and polished.

After 10 drops of five pounds and 10 drops of seven pounds, the pad and shaft were both photographed and examined. Figures 18b and 18c show the gross appearance of the surfaces. The DU pad was "polishing up" very well. Except for a few faint scratches on the shaft, no damage was observed on the molybdenum coating. Photomicrographs of portions of the contact areas are shown in Fig. 19.

REFERENCES

1. Macks, E. F., "Gas Lubrication of Radial and Thrust Bearings at High Temperature, High Speeds and Low Lubricant Flow Rates". WADD TR61-83. Feb. 1961.
2. Drescher, H., "Special Features of Self-Acting Air Bearings and Their Effects on Practical Application". First International Symposium Gas Lubricated Bearings, Edited by Dudley D. Fuller, October 26-28, 1959. ACR-49 ONR.
3. Adams, C. R., "Step Gas Bearings". SAE Journal, pp. 29-31. June 1960.
4. Murray, S. F. and M. B. Peterson, "The Selection and Evaluation of Materials and Lubricant Films for Gas-Lubricated Gyro Bearings". MTI 64TR1, June 6, 1964. Prepared for Director, SP-24 under Contract NOBS-88615(FBM).



SK-A-1740

Figure 1

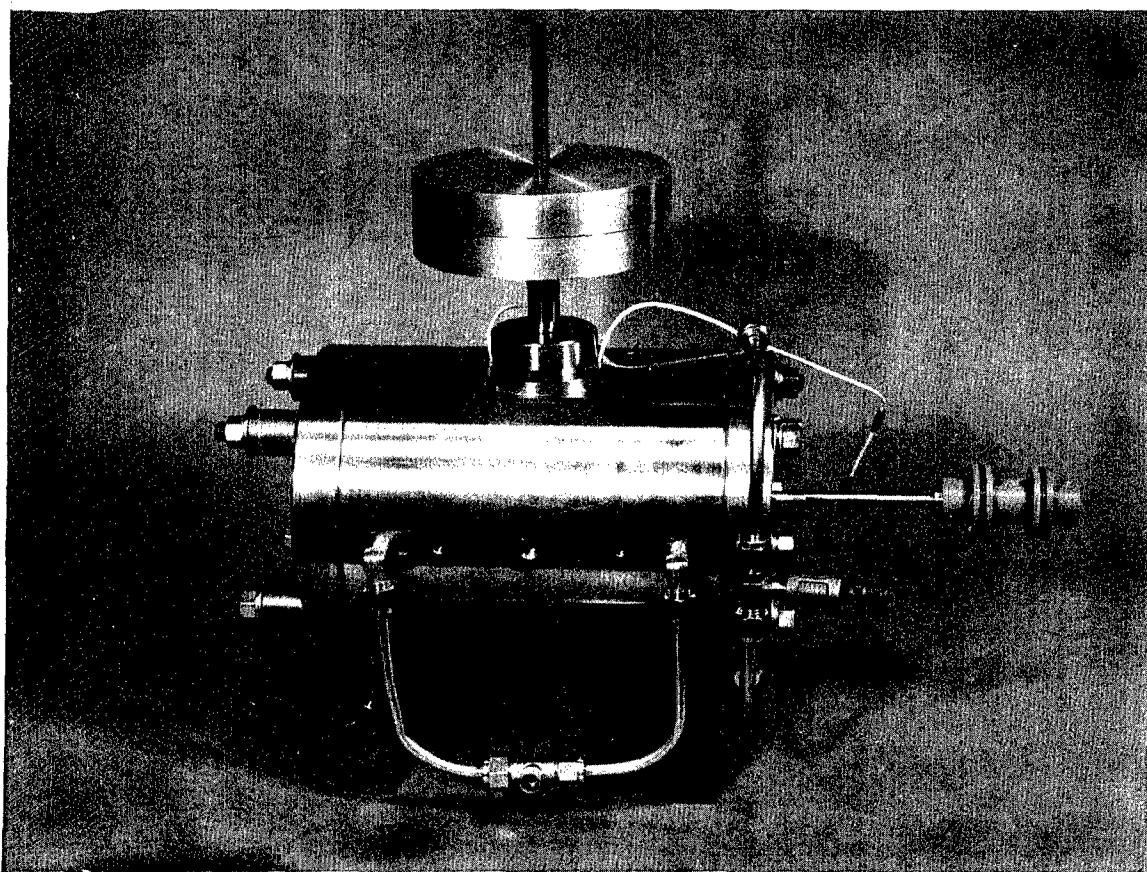


Fig. 2 Hydrodynamic Bearing Materials Test Rig
Showing Drive for Start-Stop Evaluations

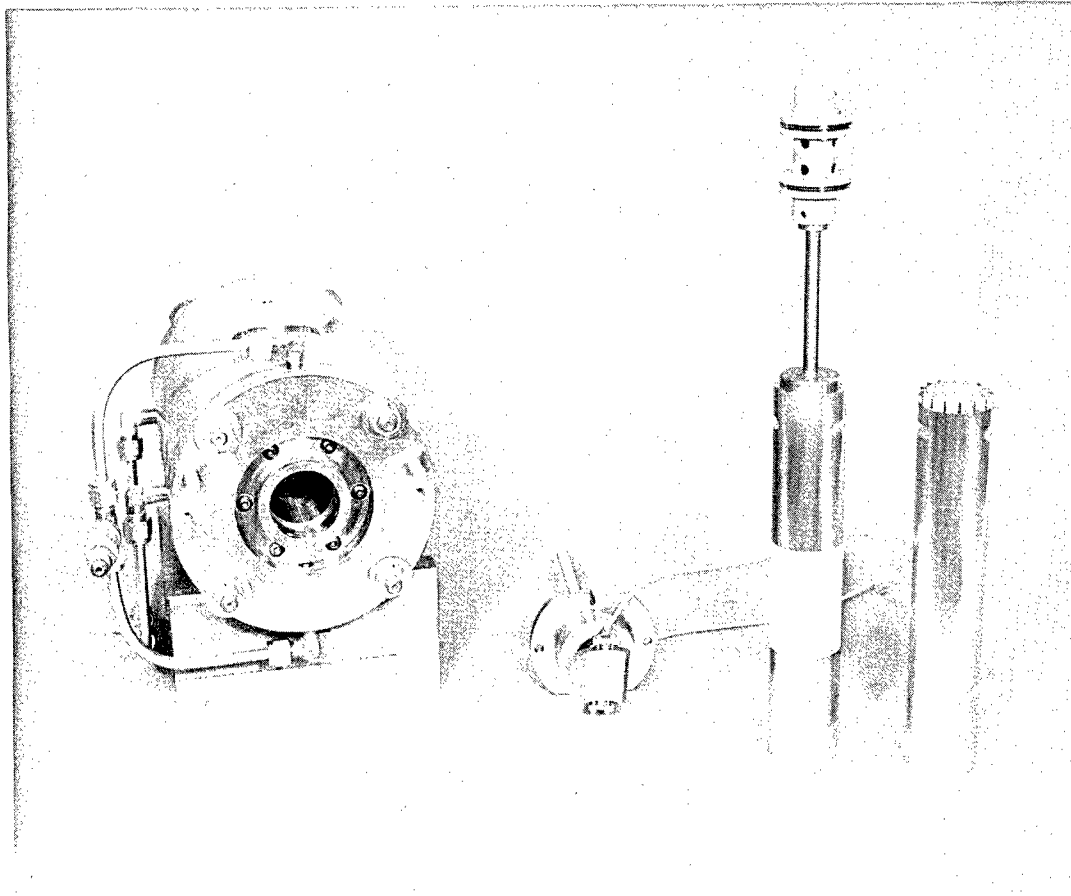


Fig. 3 - Disassembled View of Test Rig Showing Test Shafts and Tilting-Pad Bearing



Fig. 4 - Overall View of Test Area Showing Instrumentation
for High Speed Tests

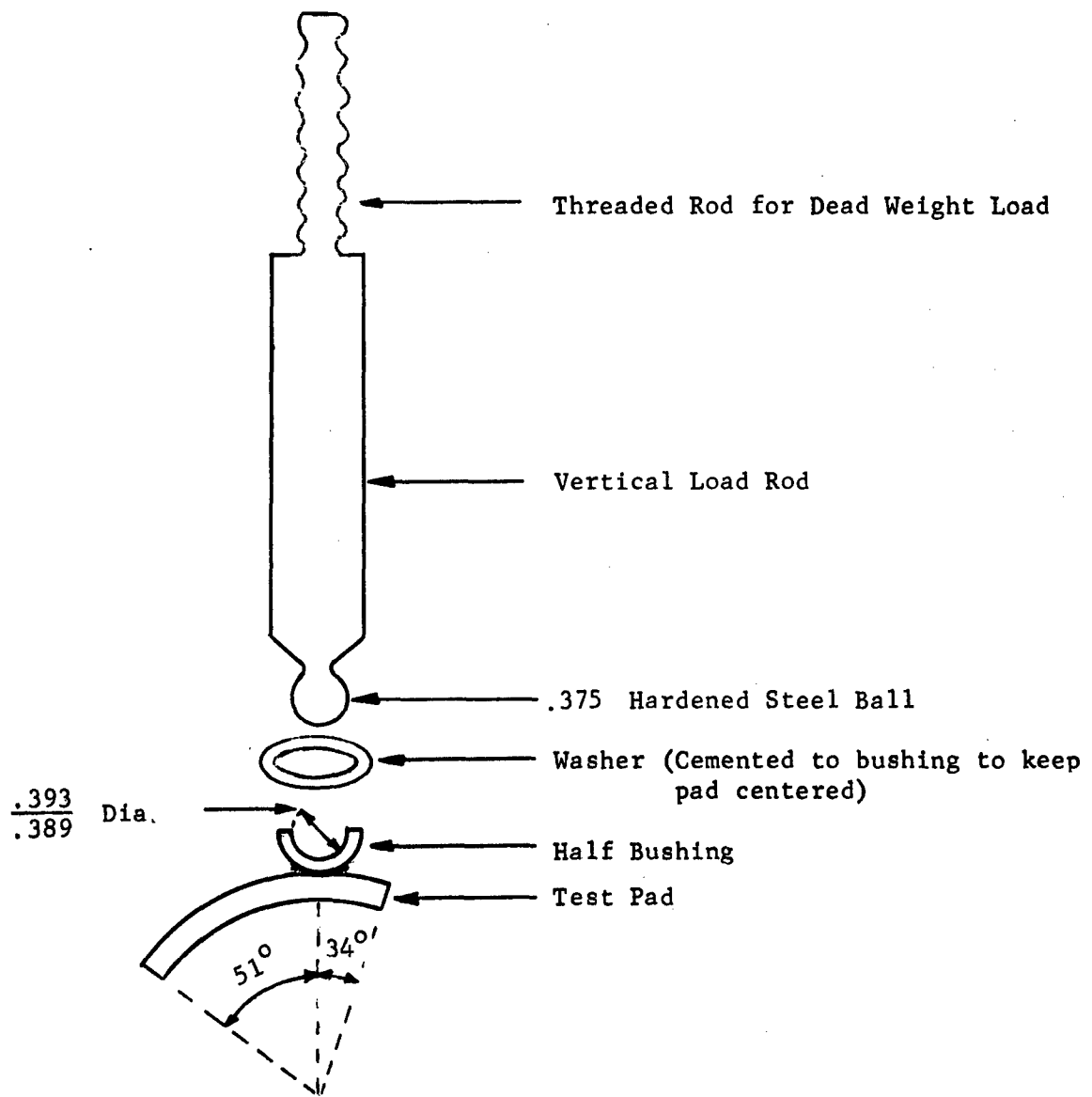


Fig. 5 Exploded View of Pad and Pivot Design

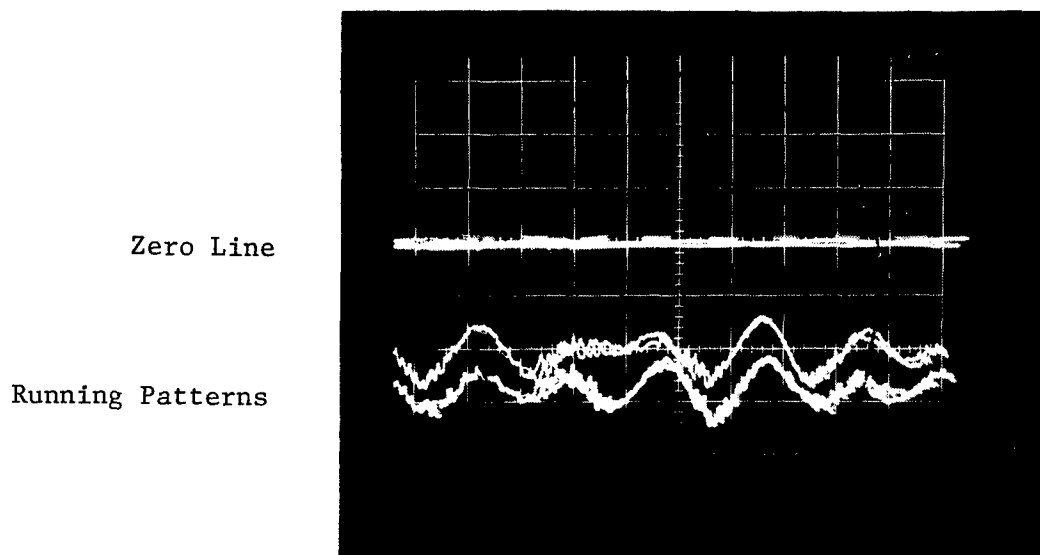
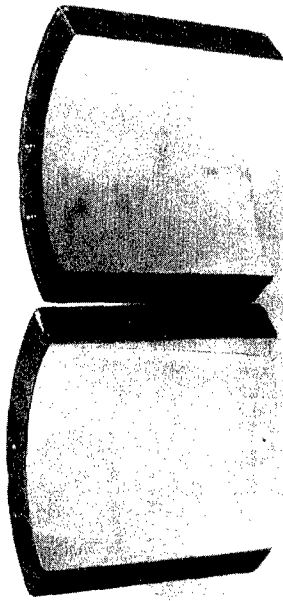


Fig. 6 Oscilloscope Patterns From Two Capacitance Probes Mounted on Each Side of a Tilting Pad Shoe in Line with the Pivot Point

Scale One Large Division = 80 Microinches



Used

New

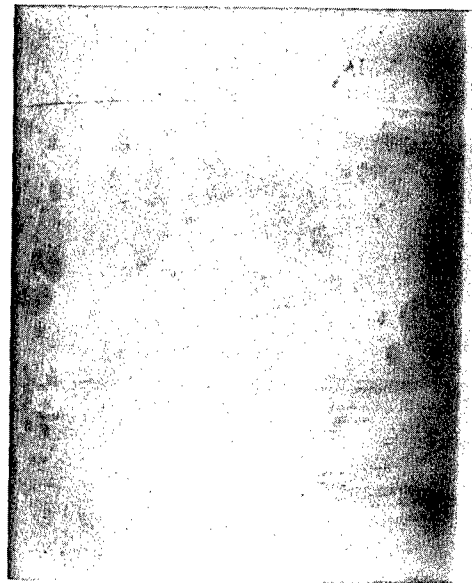


New and Used Pads, White Paper Reflected Off Surface for Contrast.

Same Pads Without Using Reflection for Contrast.

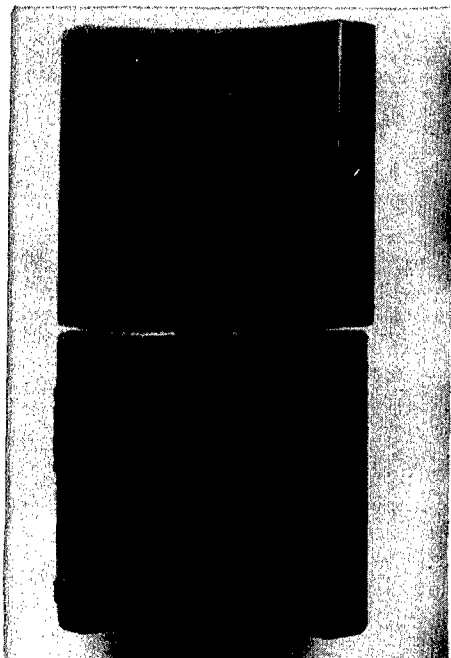


Al_2O_3 Shaft
mag. 1.25x

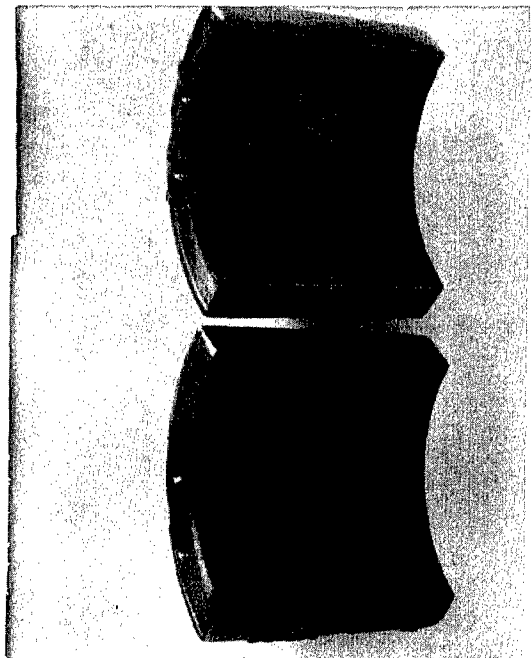


Al_2O_3 Shaft
mag. 2.5x

Fig. 7 Pad and Shaft Specimens from Start-Stop Tests.
Flame-Sprayed Tungsten Carbide Pad vs. Flame-Sprayed Al_2O_3 Shaft.
1000 Starts and Stops at 4 psi.

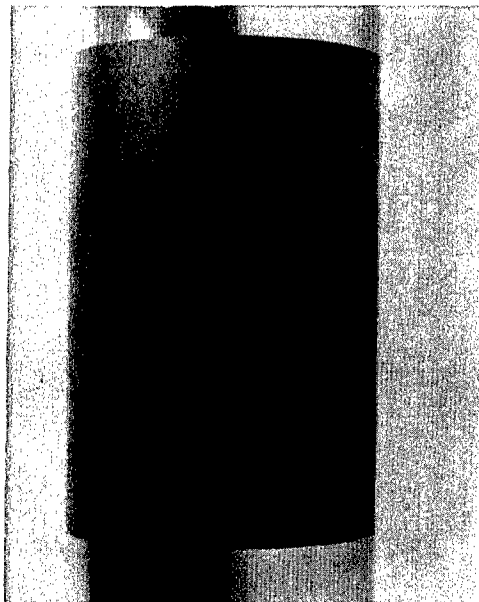


Used

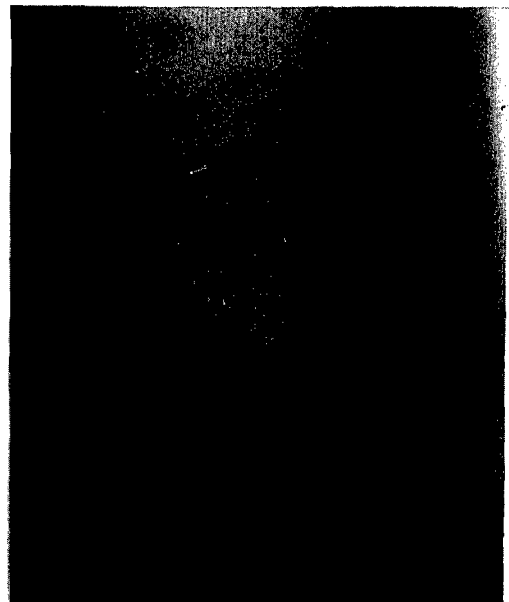


New

Pad Surfaces from Different Angles



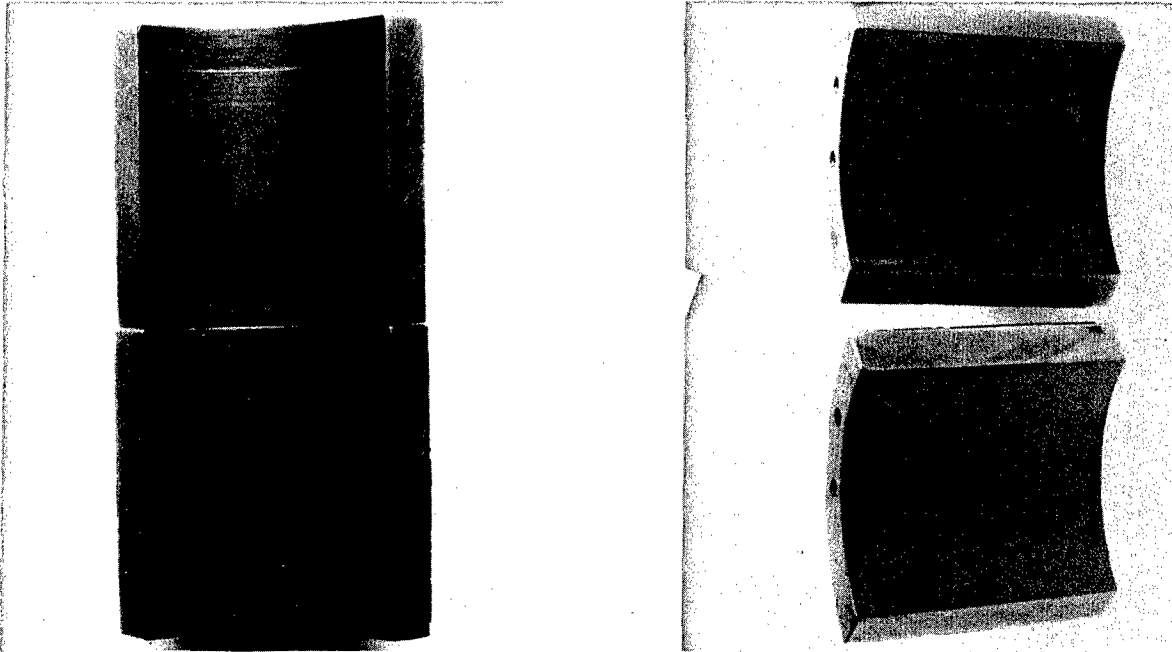
Mag. 1.25x



Mag. 2.5x

Fig. 8 Contact Surfaces on Tilting Pad Bearing and Shaft After Start-Stop Tests. Flame-Sprayed Chrome Oxide Pad and Shaft.

1000 Starts and Stops at 4 psi.



Pad Surfaces from Different Angles

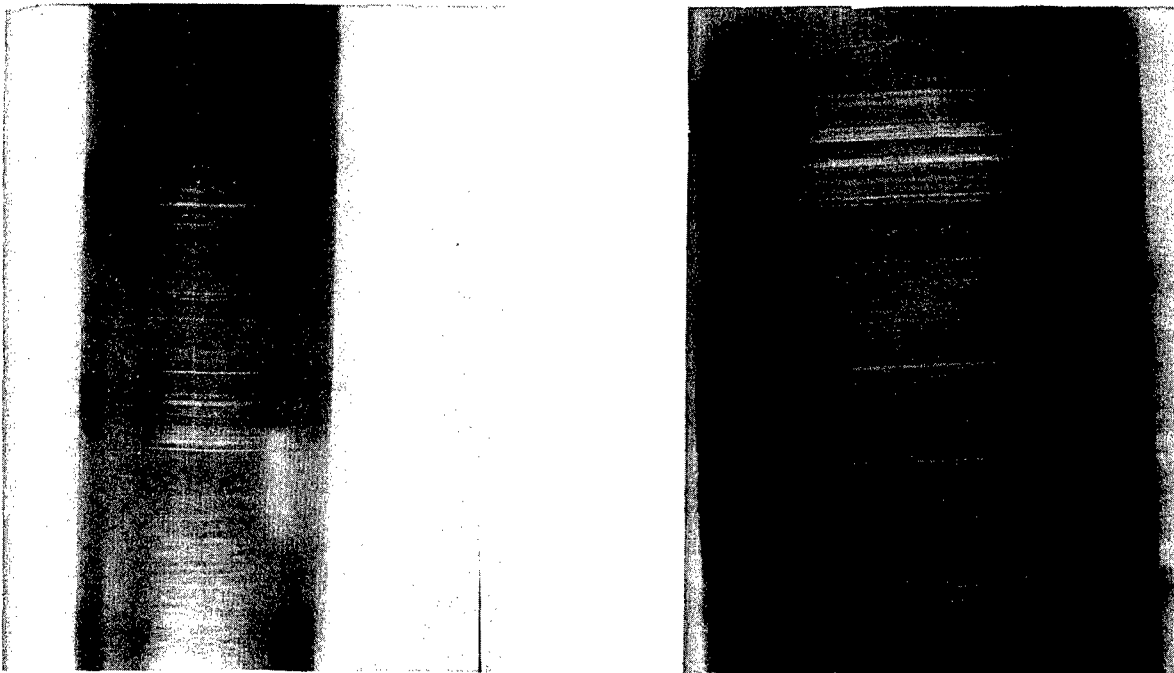
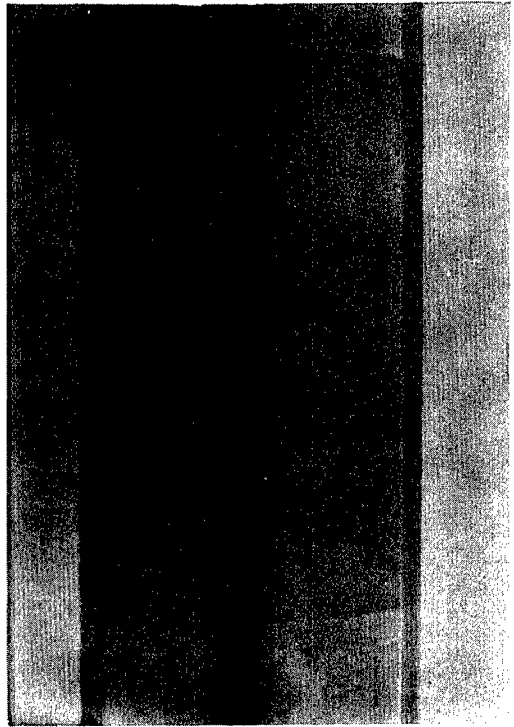
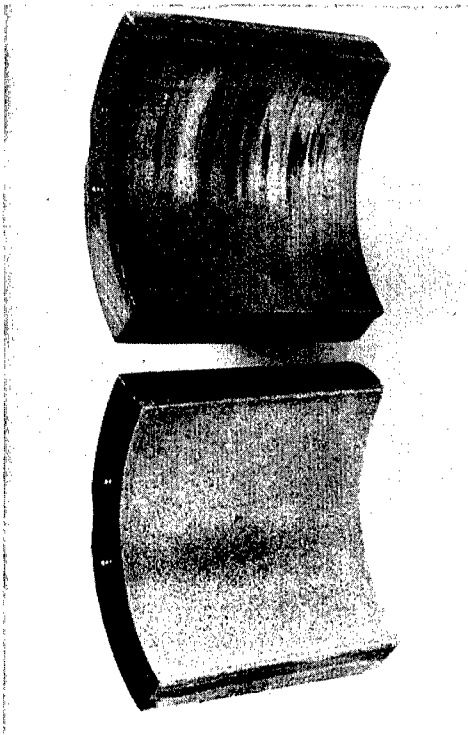
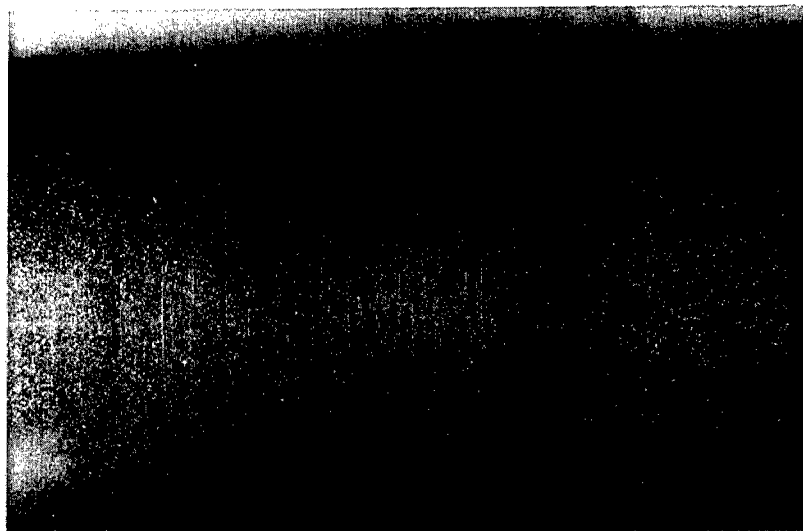


Fig. 9 Contact Surfaces on Tilting Pad Bearing and Shaft After Start-Stop Tests. Electrofilm 4396 Coated Pad vs. Hardened 416 Shaft.
1000 Starts and Stops at 4 psi.



Mag. 1.25x



Mag. 2.5x

Fig. 10 Contact Surfaces on Tilting Pad Bearing and Shaft After Start-Stop Tests. DU Pad vs. Sprayed Molybdenum Coated Shaft.
1000 Starts and Stops at 2.4 psi.

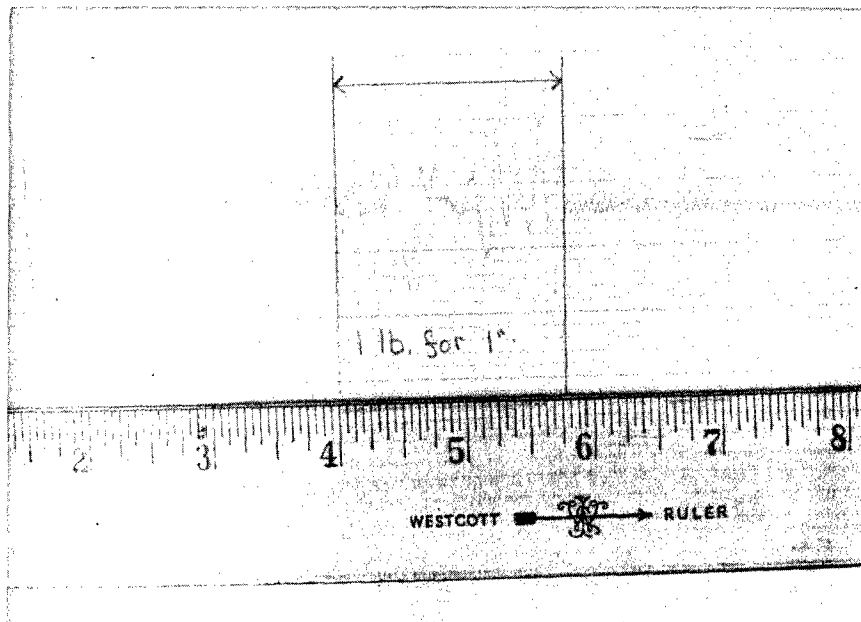
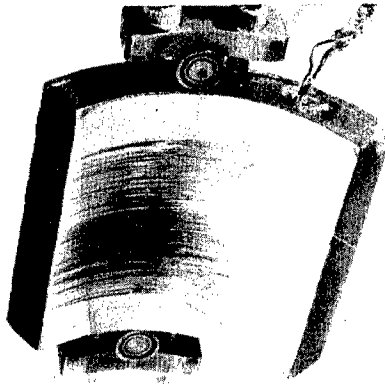
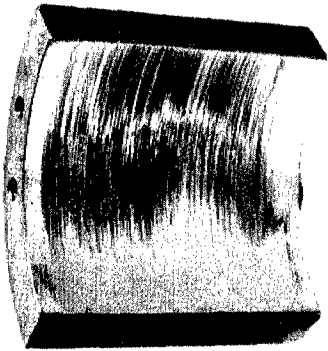


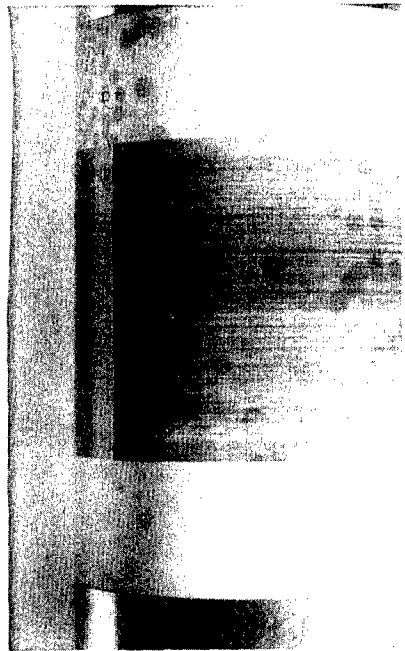
Fig. 11 Portion of Visicorder Trace Showing Impact Caused by Dropping One Pound Weight from One Inch Height. Chart Speed - 50 in/second.



(a)

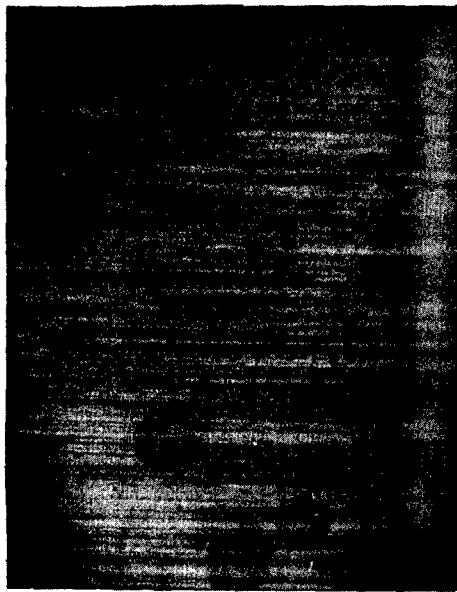


(b)



(c)

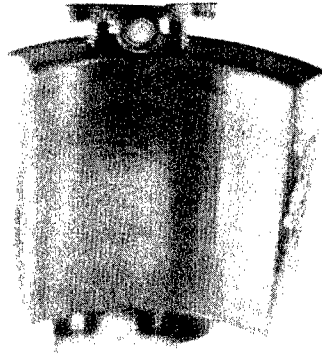
Fig. 12 Contact Surfaces on Tilting Pad Bearing
and Shaft After High Speed Rubs
Flame-Sprayed Tungsten Carbide Pad vs.
Flame-Sprayed Al_2O_3 Shaft



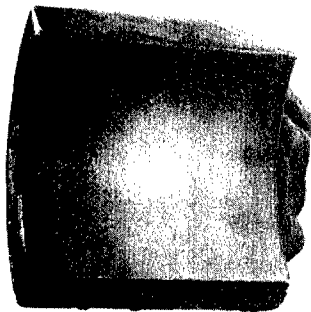
Al₂O₃ Coated Shaft

Tungsten Carbide Coated Pad

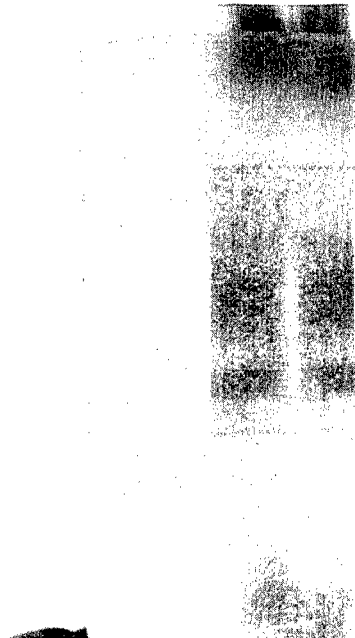
Fig. 13 Photomicrographs of Portions of Contact Areas on Pad and Shaft Surfaces After High Speed Rub Tests. Magnification x 30.



(a)

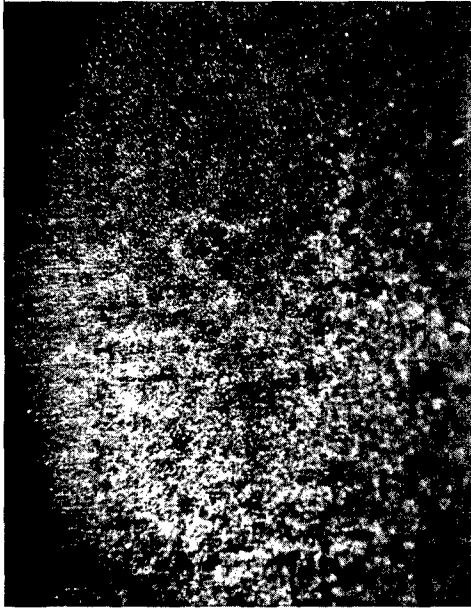


(b)



(c)

Fig. 14 Contact Surfaces on Tilting-Pad Bearing
and Shaft After High Speed Rubs
Flame-Sprayed Chrome Oxide Pad vs.
Flame-Sprayed Chrome Oxide Shaft

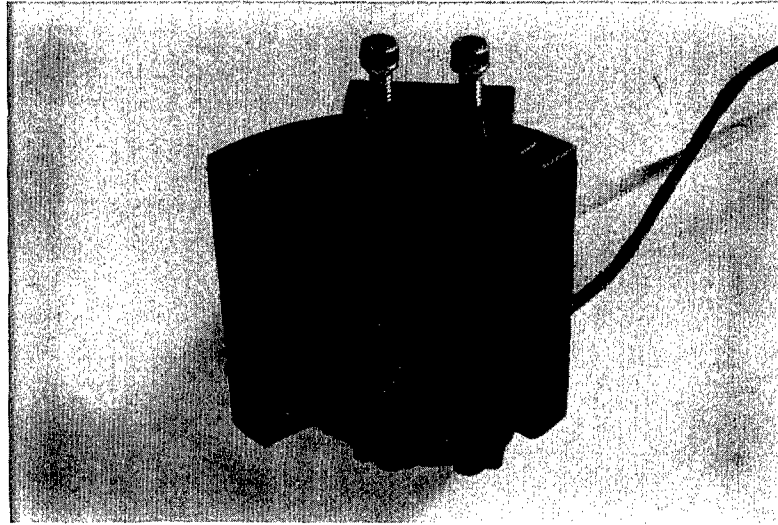


Chrome Oxide Coated Shaft

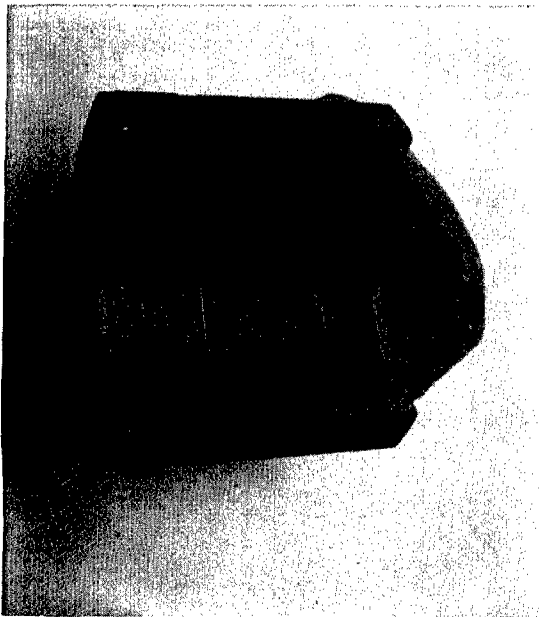


Chrome Oxide Coated Pad

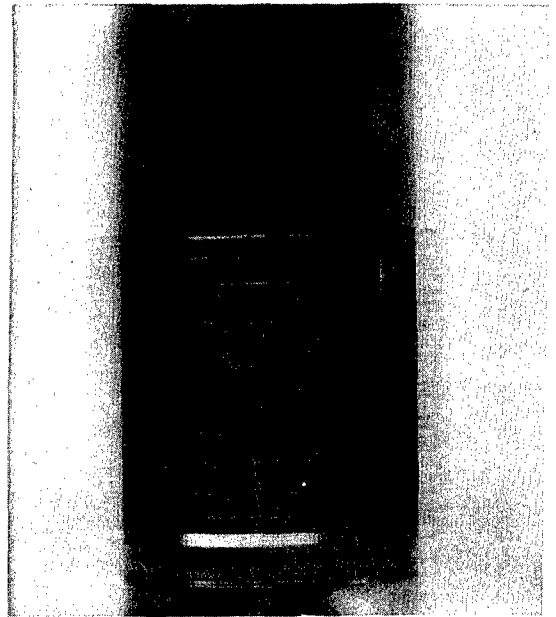
Fig. 15 Photomicrographs of Portions of Contact Areas on Pad and Shaft Surfaces After High Speed Rub Tests. Magnification x 30.



(a)

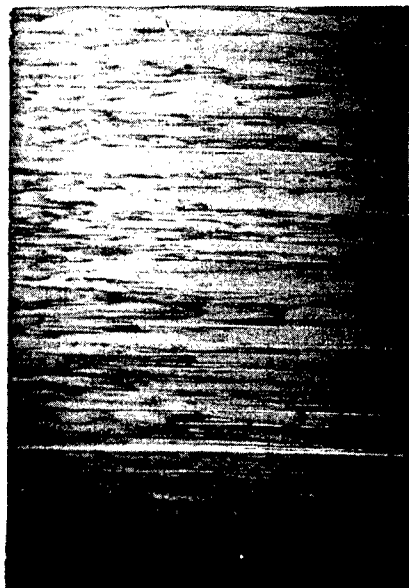


(b)

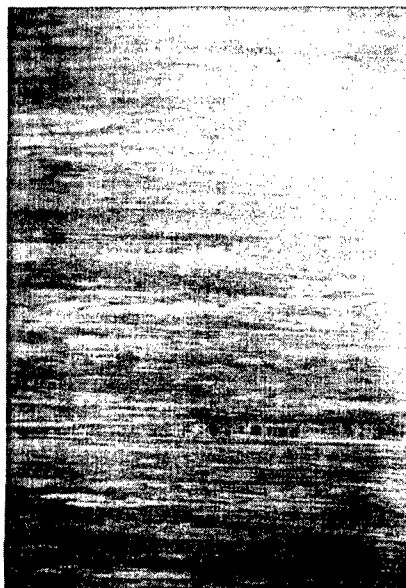


(c)

Fig. 16 Contact Surfaces on Tilting Pad Bearing and Shaft After High Speed Rubs. Electrofilm 4396 Coating on Pad vs. Hardened 416 Shaft.



416 Stainless Shaft Surface



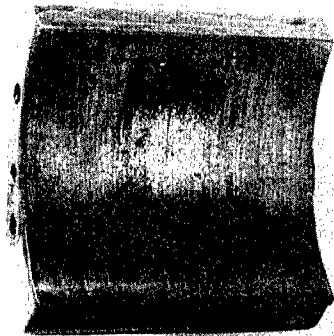
Electrofilmed Pad Surface

Fig. 17 Photomicrographs of Portions of Contact Areas on Pad and Shaft Surfaces After High Speed Rub Tests.

Magnification x 30.



(a)

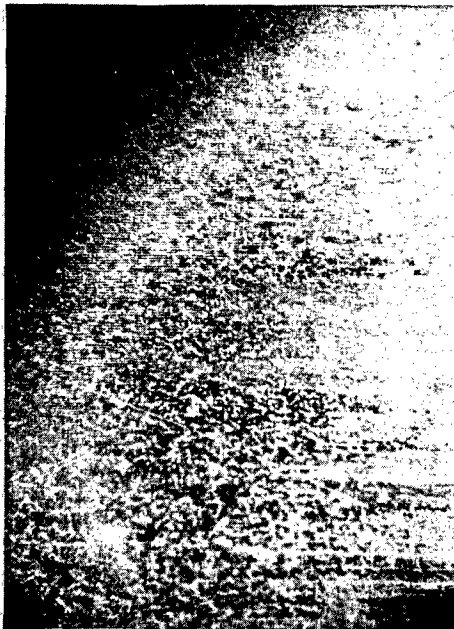


(b)

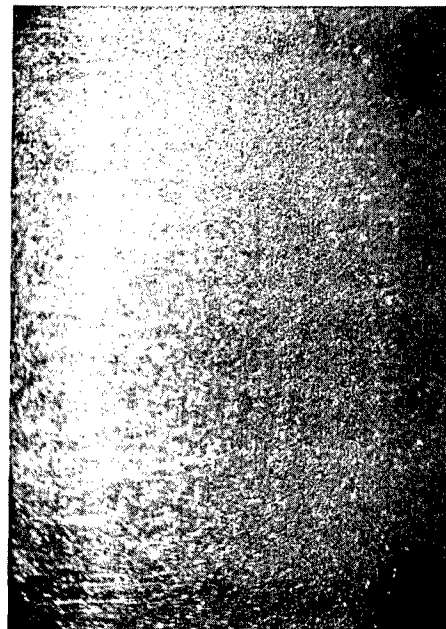


(c)

Fig. 18 - Contact Surfaces on Tilting-Pad Bearing and Shaft After High Speed Rubs. DU vs. Molybdenum Coated Shaft.



DU Pad



Molybdenum Coated Shaft

Fig. 19 Photomicrographs of Portions of Contact Areas on Pad and Shaft Surfaces After High Speed Rub Tests.
Magnification x 30.

APPENDIX A - Preparation of Test Specimens

The base material for all of the test specimens was 416 stainless steel — heat-treated and tempered to give a hardness of 23-26 Rc. The hardened 416 stainless test shafts were 40 Rc.

The test pads were made by machining round stock to form a plain sleeve, 1.900 inch O.D., 1.49 inch I.D. and 1.25 inch long. This sleeve was then cut axially to form four equal segments. Using a standard fixture, slots were milled along the back of the pads at the desired pivot point. The four pads were then "epoxied" into the bore of a steel housing and the inside diameter of the pads was turned to the desired dimensions for coating.

For the flame-sprayed coatings, the pads were turned .003 inch undersize on the radius. The housing, with the four pads cemented in place, was then flame-sprayed. The tungsten carbide coating was done by the Linde Company (Linde LW-5) and the chrome oxide was done by the Avco Corporation. Normally, it is customary to spray on a coating .007 inch thick and finish back to a .003 inch thickness. However, since this configuration required spraying from an angle to cover the inside bore, the instructions called for sufficient material to provide a coating .003 inch thick after finishing.

After flame-spraying, the inside diameter of the four pads (still cemented in the housing) was ground and lapped to $1.5006 \pm .0001$ inches with a surface finish of 1-2 rms. Then the housing and pads were heated to 400 F to soften the epoxy cement and the four pads were pressed out of the steel housing. The edges of the pads were stoned to remove any sharp corners, holes were drilled and tapped for the probe holders and thermocouple, and the hardened steel half-bushing was cemented in place on the back of the pad as shown in Fig. 5.

The pads which were to be Electrofilmed were turned in the steel housing to a diameter of 1.5007 inches, then they were removed from the housing and hand-lapped against a dummy, cast iron shaft. The pads were then coated individually with Electrofilm 4396 using the standard recommended procedure of sandblasting, phosphating and coating. The pads then were hand-lapped to a smooth finish against a

cast iron shaft, using naphtha as the lubricant for the lap. This technique removes any excess solid film lubricant and produces a smooth, well-bonded film with no loose particles.

To bond DU to the steel pads, .040 inch DU stock was formed to pads which had been previously machined .038 inch undersize. Using pressure, in a 400 F oven, the DU was cemented to the steel pads with Eccobond 104, a high-temperature epoxy. After curing, the pads were cemented in the standard steel housing and the I.D. was turned to 1.5005 inches. The pads were then pushed out of the housing and were hand-lapped against cast iron to good conformity and surface finish.

It should be noted that MTI recently has had considerable difficulty in getting consistently good epoxy bonds between the DU sheet stock and the steel backing. The choice of DU as a test material was made before these problems were experienced. Until a satisfactory technique is available for bonding the DU with good assurance of reproducibility, the use of this material in the turbine-compressor package is not recommended.

Three sets of shafts were coated and one set was hardened 416 stainless. The shafts which were to be hardened were rough machined to 1.52 inches in diameter and were heat-treated by the following procedure:

1. Oil quench from 1800 F
2. Temper at 900 F — Final measured hardness 40 Rc.

The shafts were then finished to $1.4991 \pm .0001$ inches, straight and concentric within .000050 inch T.I.R., with a surface roughness of less than 4 rms.

The shafts which were to be coated were rough machined and a 2.3 inches long relief in the center of the shaft was turned to 1.493 inches. The shafts were then coated in the relieved section with .007 inch of the following materials:

1. Al_2O_3 Linde LA-2
2. Chrome oxide - Avco
3. Molybdenum - Avco

Then the entire length of the shaft was ground and lapped to $1.4991 \pm .0001$ inches straight and concentric within .000050 inch T.I.R. with a surface finish better than 4 rms. This left a coating about .003 inch thick in the center of each of the shafts.

The high-speed shafts were balanced at MII.

APPENDIX B - Pivot Design and Materials

The major problem in the pivot appears to be one of design although suitable materials must also be selected. The tracking capability of the bearing is affected by pivot radius and it is also affected if moments due to pivot friction are not negligibly small compared to moments due to hydrodynamic pressures. The amplitudes of oscillation will also affect long-term pivot performance. These will be functions of the dynamic loading and the rotor geometry.

Assuming that the pivot must undergo some adjustment with each revolution of the shaft, it is apparent that the pivot will be subjected to high-frequency, small-amplitude motions which could result in surface damage. Improperly designed pivots, where the motions have a large component of sliding, will exhibit serious damage very rapidly. It is very important to design the pivots so that the motions are as close to pure rolling as possible. Since some degree of slip will always take place, the materials combination used in the pivots is also an important aspect.

The stress level in the pivots must be kept sufficiently low to prevent brinelling, fatigue or material fracture — particularly if a brittle material, such as tungsten carbide, is used. The stress level can be reduced, for example, by using a ball vs. socket design instead of a ball vs. flat design. Care must be exercised, however, to assure that the percentage of sliding motion is not increased. Even with relatively low contact stress, sliding motion will cause considerably more surface damage than will rolling motion. The mathematical expression for calculating pivot stresses, deflections and compliance are available, adapted from similar analyses for rolling element bearings.

To sum up, long-term satisfactory operation of the pivots will depend on:

1. Configuration and degree of sliding motion
2. Materials combination
3. Stress level
4. Amplitudes of oscillation.
5. Frequency
6. Temperature.

At the present time, MTI is using a ball-sleeve pivot design. For temperatures below 350 F, 52100 steel hardened to 59-62 Rc has been used for both the ball and the sleeve material. Up to 600 F, M-1 or M-10 tool steel was selected for its dimensional stability and hot hardness. Above 600 F, cemented tungsten carbide is preferred. The carbide oxidizes rapidly in air above 900 F, but would be suitable for higher temperatures in argon. For better run-in and surface conditioning, a resin bonded MoS₂ film is generally applied to the surface of the sleeve.

Practical gas-bearing machines employing steel pivots of the type described above have been built by MTI and have accumulated more than 5000 hours of running time with no significant change in bearing performance.

In spite of these successes, there is still much to be learned about these tilting-pad bearing pivots. The design is empirical and the effects of variables such as stress, temperature, shaft speed and shaft balance are not clearly understood.

APPENDIX F

FINAL REPORT - SECOND BEARING MATERIALS EVALUATION

INTRODUCTION

This report describes the results of additional evaluations of bearing materials at 500 F for the argon-lubricated bearings in the NASA Turbine-Compressor. The work was done as a subcontract to Pratt and Whitney Aircraft under prime contract NAS3-4179. Previous work, which was done at 350 F, is described in Ref. 1*.

There is a possibility that it will be necessary to operate the turbine-compressor bearings at a higher temperature than was originally planned. In addition, future space power plant applications will certainly involve higher bearing temperatures. Therefore, additional tests have been made to evaluate chrome oxide-coated bearings at 500 F, in argon. At the request of NASA, tests were also run with a combination of a hardened M-50 tool steel pad bearing against a flame plated, cobalt bonded tungsten carbide coated shaft.

These tests were done at MTI using a gas-lubricated bearing test rig which was specifically designed for materials evaluations under realistic test conditions. Both start-stop and high speed contact tests were made.

*Reference 1 - "Evaluation of Bearing Material Combinations for the NASA Turbine-Compressor." S. F. Murray, MTI-64TR56, September 30, 1964.

SUMMARY OF RESULTS

Tests have been run to evaluate the sliding behavior of two material combinations for the turbine-compressor package. One of these material combinations, a chrome oxide-coated pad bearing mated against a chrome oxide-coated shaft had been evaluated previously at lower temperatures. The evaluation of the second combination, a hardened M-50 tool steel pad versus a tungsten carbide coated shaft, was requested by NASA.

To simulate the actual application as closely as possible, these materials were evaluated as hydrodynamic gas-lubricated bearings in an argon environment at 500 F. Both the start-stop and high-speed sliding performance was determined.

Start-Stop Evaluations

In these tests, each combination was run for one thousand start-stop cycles at a stress of 4.0 psi*. The results were as follows:

1. The chrome oxide coated combination showed negligible wear. The contact areas were smooth and polished. Comparison of these 500 F test results with previous data obtained at 350 F indicates that temperature has no effect on the sliding effectiveness of this combination in this temperature range.
2. The M-50 pad sliding against a tungsten carbide coated shaft appeared to be operating effectively for about the first 375 start-stop cycles but performance deteriorated rapidly beyond this point. Surface damage, rather than wear, was the dominant mode of failure.

High Speed Evaluations

The high speed rub tests were made at 60,000 rpm and consisted of a series of shock loads of gradually increasing magnitude which caused the bearing to con-

*See page 7 for definition of stress.

tact the shaft for a fraction of a second during each impact. The results were as follows:

1. Chrome oxide mated against itself was still operating effectively after fifty shock tests of one pound dropped from a height of one inch; twenty shock tests of three pounds dropped from a height of one inch, and ten drops of five pounds and ten drops of seven pounds, both dropped from a height of one inch. The chrome oxide appeared to be as good in the 500 F tests as it was in the previous tests at 350 F.
2. The M-50 pad sliding against the tungsten carbide coated shaft showed considerable abrasion after fifty shock tests of one pound dropped from a height of one inch and twenty drops of three pounds, also from a height of one inch. After ten more shock tests of five pounds dropped from a height of one inch, the pad was not able to operate hydrodynamically. Heavy transfer and metal flow was observed on the test specimens after the test.

CONCLUSIONS

Of all the material combinations which have been evaluated at MTI, self-mated chrome oxide coatings are still the most promising for both start-stop and high speed sliding compatibility. This conclusion is based on a substantial amount of test data in both air and argon atmospheres. The coating has been proven to be effective in the temperature range from 70 F to 500 F at sliding velocities up to 23,400 feet per minute.

The combination of a hardened M-50 tool steel pad and a tungsten carbide-coated shaft showed no promise either for start-stop or for high speed sliding compatibility.

A chrome oxide-coated disk, which had been used for another investigation, was subjected to several impacts with a ball peen hammer. It was found that the sharp edges were very susceptible to damage but the flat surface could be brinelled without cracking the coating.

Consideration of the types of surface damage which take place during high speed rubs has indicated that the ideal coating for a bearing material should have the following characteristics:

1. The coating should be a self-bonded, non-metallic material with good friction and wear behavior.
2. The coating should wear in the form of fine debris rather than large crystal agglomerates.
3. The coating should have good integrity and good adhesion to the substrate but high density does not appear to be an essential attribute.

TEST EQUIPMENT

Test Rig

The test rig which was used for this work, was built with MTI funds as a test device to evaluate gas bearing materials for a variety of applications. Essentially, the equipment consisted of a test shaft, 1-1/2 inches in diameter by eight inches long, supported on each end by externally-pressurized, gas-supported journal bearings. A single, hydrodynamic, tilting-pad test bearing was dead-weight loaded against the center portion of this shaft. With the exception of the pivot materials and the load arm, all parts of the rig, including the test bearings and the test shafts, were made of 416 stainless steel. To simplify the design, axial motions of the test shaft were restrained by hemispherically-tipped rods of high temperature carbon-graphite which were carefully aligned to contact the centers of both ends of the shaft. These were used only in the 60,000 rpm tests. In the start-stop tests, the shaft was coupled directly to a motor and no thrust capability was required.

The test equipment used in this work is shown schematically in Fig. 1. Fig. 2 is a photograph of the rig with the low-speed drive attached to the shaft. Fig. 3 is another view of the rig which also shows the pad assembly, a low-speed shaft and a high-speed shaft. Fig. 4 is an overall view of the test area and instrumentation for the high-speed evaluations.

The construction of the tilting-pad test bearing is shown schematically in Fig. 5. A hardened steel bushing, cut in half in the axial direction, was spot welded to the back of the pad at the desired pivot point. A hardened steel ball, brazed on the end of a vertical loading arm, was seated in this bushing. The clearance between the ball and the bushing was generous enough to permit the bushing to roll freely against the contact surface of the ball. To restrict lateral motions of the pad, a machined washer was cemented to the bushing. This kept the ball centered in the pivot.

Drives

Two different types of drives were used in this work. For the low-speed, start-stop tests, the shaft was coupled directly to a 3450 rpm electric motor by means of a quill shaft and a flexible coupling.

In the high-speed tests, slots were milled in one end of the test shaft. These slots acted as a turbine which was driven by means of compressed gas supplied from a cylinder.

Instrumentation

To monitor the performance of the tilting-pad test bearing, two capacitance probes were mounted on the pad - one on each side of the pivot point. The signals from these probes were fed through two Wayne-Kerr proximity meters into an oscilloscope. Running film thickness and wear were measured with this system. In Fig. 6, a photograph of typical oscilloscope traces is shown. The upper "zero line" is set at the beginning of the test, while the bearing is stationary on the shaft. The two lower signal traces show that the pad is running on an average film thickness of approximately 200 microinches and that the pad is tilted about 60 microinches off horizontal. When the bearing or shaft becomes worn, the probe signals on the stationary bearing will be displaced above the "zero line" at zero speed. This is a very accurate means of measuring the total wear in a bearing system.

In the high-speed tests, the motions of the test shaft were monitored by means of two sets of capacitance probes which sensed the radial position of the shaft in the x and y directions. These probes were mounted just inboard of each of the two hydrostatic support bearings.

To measure speed in the high-speed tests, a signal from a single probe was compared with a signal supplied from a variable frequency oscillator. When a one-to-one correspondence was achieved between the probe signal and the oscillator signal, the rotor speed in cycles-per-second could be read directly from the oscillator tuning dial.

Temperature Control and Gas Supply

The test rig was heated by means of two banks of quartz, infrared heater tubes — one bank on each side of the rig. Two powerstats were used to control the voltage to the quartz heaters. The test temperature was measured with a thermocouple which penetrated through the housing wall and sensed the temperature in the housing cavity at a distance of 1/8 inch from the surface of the test shaft.

Since it was planned that the hydrostatic support bearings would be supplied with argon as the jacking gas, this also took care of the problem of blanketing the bearing cavity with argon. Stainless steel tubing, coiled inside a high temperature furnace, was used to preheat the argon gas which was being supplied from a cylinder to the support bearings.

In the high-speed tests, temperatures at several locations were monitored. Besides the housing thermocouple, a thermocouple measured the temperature in the nozzle box through which the driving gas was supplied. Thermocouples were also used to monitor the temperatures of the jacking gas supply to the hydrostatic bearings and the turbine drive gas supply. The turbine drive gas supply temperature proved to be the most difficult control problem because of the high gas flow rates which were required during the test. A specially designed 15 KW gas preheater had to be built to preheat the argon driving gas to 500 F.

Definition of Stress

The bearing stress was based on the projected area of the journal ($L \times D$). The width of the test bearing was 1.25 inches and the diameter of the shaft was 1.5 inches. Thus, the projected area was 1.875 square inches and the load, divided by this area, was the average stress in pounds per square inch. The true stresses are actually much higher since contact does not take place over the entire bearing area.

TEST PROCEDURE

Start-Stop Tests

For the low-speed, start-stop tests, a deadweight load was applied to the test bearing and the test rig was heated to 500 F. A low flow of preheated argon was supplied to the housing during this time. When the test temperature had been stabilized, the probe signals were zeroed and the test was started. A program timer was used to turn on the motor, run the test for five seconds at speed, then shut off the motor and allow the shaft to coast to a dead stop. This sequence was repeated until one thousand starts and stops had been accumulated. Observations were made at periodic intervals to see if the running film thickness had changed and to determine if the probe signals on the stationary bearing indicated wear. At the end of the test, the bearing and shaft were examined and photographed.

High-Speed Rub Tests

In these tests, a deadweight load was applied to the test bearing to produce a stress of 2.5 psi. The test rig was heated to the desired temperature and both the bearing support and turbine gas supplies were brought up to a reasonably stable temperature using a by-pass valving system. Then the support bearings were lifted with the preheated argon gas and the shaft was brought up to 60,000 rpm, using preheated argon gas to drive the turbine.

As soon as the speed had been stabilized, a series of shock loads were imposed on the test pad by means of a hinged arm which weighed one pound. This arm was dropped fifty times in rapid succession on the top of the vertical load rod from a pre-set height of one inch. At each impact, the tilting-pad probe signals indicated that the pad had actually contacted the shaft. If the pad was still operating satisfactorily after this series of impacts, weight was added to the hinged arm to increase the load to three pounds and the arm was dropped on the load rod twenty times, again from a height of one inch. The test was then disassembled, the pad was photographed and the pad and shaft were examined.

In the cases where the pad was still in good condition, the test was continued. A load of five pounds was dropped ten times from a height of one inch and a load of seven pounds was dropped ten times, also from a height of one inch. The test was then disassembled and both the pad and the shaft were examined and photographed.

The following table summarizes this sequence of high speed shock loads:

<u>Number of Drops</u>	<u>Load</u>	<u>Drop Height</u>	
50	1 pound	one inch	Proceed if performance satisfactory
20	3 pounds	one inch	Disassemble and examine
10	5 pounds	one inch	Proceed if performance satisfactory
10	7 pounds	one inch	Disassemble and examine

TEST RESULTS

The general test conditions for this work were as follows:

1. Environment - argon
2. Bearing temperature - 500 F
3. Bearing type - tilting pad
4. Shaft diameter - 1.5 inches
5. Speed range of interest - 0 to 60,000 rpm

The evaluations included:

1. Multiple start-stop tests to evaluate low-speed sliding behavior
2. Short duration, high speed rubs at 60,000 rpm to simulate the effect of vibration or shock on bearing material compatibility.

Start-Stop Evaluations

As was the case in the 350 F tests, problems were encountered with the hydrostatic support bearings in the test rig. It is now evident that the flexible coupling, used to connect the shaft to the drive motor, cannot compensate for thermal distortions. The test rig has been run effectively at room temperature with this motor drive. After three support bearing failures, the hydrostatic gas bearings were replaced with rolling contact bearings. These bearings were cleaned with solvents to remove any grease or oil and a film of MoS₂ powder was burnished on the balls and races to provide lubrication. This technique permitted one series of a thousand starts and stops at 500 F before the bearings had to be replaced. In every case, retainer breakage was noted but the balls and races were smooth and highly polished.

To blanket the system with argon, preheated gas was supplied to the housing cavity through stainless steel tubing.

The results of the start-stop tests at 500 F in argon were as follows:

1. Chrome Oxide Coated Pad Versus Chrome Oxide Coated Shaft

Using a stress of 4.0 psi (based on the projected area), one thousand start-stop cycles were accumulated on this combination without any problems. In these tests, a program timer turned the motor on for five seconds, then turned the motor off and allowed the shaft to coast down to a full stop. This cycle was repeated until the desired number of starts and stops had been achieved. Measurements of temperature on the tilting pad bearing showed that the actual pad temperature was about 540 F during these tests.

A consistent running film thickness of about 64 microinches was obtained throughout the test at the maximum motor speed of 3450 rpm. Photographs of the test pad and shaft are shown as Fig. 7. The wear areas on the pad indicated that the pad surface had a very slight "dish." The shaft surface was well polished and showed no surface damage.

In the previous tests at 350 F (Ref. 1)^{*}, slightly negative wear values, on the order of 25 microinches, had been measured on the chrome oxide. This was apparently due to a small amount of wear debris which was trapped under the pad. When those specimens had been wiped off with lens tissue and reassembled, no measurable wear or buildup could be detected.

2. Hardened M-50 Tool Steel Pad Versus Flame Plated Tungsten Carbide-Coated Shaft

Under a stress of 4.0 psi, this combination appeared to be operating effectively for the first 375 starts and stops. The average running film thickness was about 125 microinches. During the next 200 starts and stops, it was noted that the stationary probe signals gradually showed positive wear on one side of the pad and negative wear on the other. These readings indicated that the pad was being cocked in a tilted position when the shaft

^{*}"Evaluation of Bearing Material Combinations for the NASA Turbine-Compressor. S.F. Murray, MTI-64TR56, September 30, 1964.

was not rotating. This could have been caused by debris being trapped under one side of the pad or it could have been the result of surface damage on one side of the bearing or shaft. After approximately 600 starts and stops, the readings on both running film thickness and stationary wear were so distorted that the data was very questionable. At the end of 1000 starts and stops, the pad was apparently still lifting and the running film thickness appeared to be about 85 micro-inches.

Photographs of the M-50 pad and the carbide shaft, which were taken after this test, are shown in Fig. 8. The pad was badly scored in one area. The shaft showed corresponding damage which appeared to be due to transfer of metal from the M-50 pad to the carbide surface and subsequent gouging by this transferred material. This type of surface damage was apparently the cause of the unusual probe signals. When the pad was resting on the shaft, the damaged area, which was predominantly on one side of the pad, indicated a positive displacement from the zero line while the probe on the other side indicated a negative displacement.

High Speed, Shock Load Test Results

In all of these high speed tests, the tilting pad test bearing had a deadweight preload sufficient to apply a stress of 2.5 psi. This preload had been found to be necessary in the 350 F tests in order to prevent pad flutter at high speeds.

The results of these tests were as follows:

1. Chrome Oxide Coated Pad Versus Chrome Oxide Coated Shaft

In these tests, the test pad bearing temperature was approximately 490 to 510 F at 60,000 rpm. Fifty shock tests were made by dropping a one pound weight on the test bearing from a height of one inch and twenty more shock tests by dropping three pounds from one inch. The probes mounted on each side of the tilting pad bearing indicated that contact was made through the film during each shock test. Previous measurements had shown that the

actual time in contact varied from .03 to .05 seconds, regardless of the weight applied. The steady-state film thickness of this bearing at 60,000 rpm was about 1000 microinches.

After this initial series of shock loads, the tilting-pad test bearing was removed, cooled and photographed. The shaft surface was examined without removing it from the test rig. Fig. 9 is a photograph of the chrome oxide-coated pad after this first series of high speed rubs. The contact areas were smooth and polished. As was the case with the start-stop tests, the wear areas indicated that the pad was very slightly "dished" so that contact was concentrated on two areas to each side of the center of the pad. The shaft was well polished and smooth.

The test was then reassembled with the same test bearing, temperatures were stabilized and a second high speed test was run. This test consisted of ten drops of a five-pound weight from a height of one inch and ten drops of seven pounds from a one inch height. At this point, the steady-state running film thickness averaged about 880 microinches and the probes showed that the pad was tilted about 100 microinches off of horizontal. The bearing still appeared to be operating effectively when the test was shut down.

During the coastdown, some measurements were made to determine the touchdown speed. For these measurements, a signal from one of the probes on the tilting-pad bearing was compared with a signal supplied from a variable frequency oscillator. When a one-to-one correspondence was achieved, the rotor speed in cycles-per-second could be read directly from the oscillator tuning dial. The touchdown speed was approximately 400 rpm, which agrees very closely with previous measurements taken on this test rig.

Photographs of the test bearing pad and the shaft are shown in Fig. 10. The contacting areas were smooth and polished and very little wear had taken place.

In Fig. 11, photomicrographs of the pad and shaft surfaces were shown. Under the microscope, the surfaces show definite abrasive wear but no destructive damage.

2. Hardened M-50 Steel Pad Versus Carbide Coated Shaft

This combination was subjected to the standard fifty shock tests by dropping a one pound weight from a height of one inch and twenty shock tests by dropping a three pound weight from the same distance. The steady-state running film thickness on this test bearing was about 750 microinches at the beginning of the test and about 350 microinches after this first series of shock loads.

The bearing and shaft were both removed from the test rig, cooled, and photographed. Figure 12 shows the overall appearance of the test pad and shaft surfaces. The steel had transferred to the shaft surface and the pad showed considerable abrasion damage. In Fig. 13, photomicrographs of the contact areas are shown. Discrete "pullouts" were visible on the pad and heavy transfer can be seen on the shaft surface.

The test rig was then reassembled with the same specimens and the second series of shock tests were started after the rig and gas supply temperatures had been stabilized. Ten shock loads were applied to the bearing by dropping a five pound weight from a height of one inch. The probe signals at this point indicated that the pad was rubbing in continuous contact with the shaft so the test was shut down without running the seven pound shock load tests. Normally, the shaft coasts down gradually to a standstill but, in this test, the shaft stopped almost instantaneously when the turbine drive gas was shut off.

Fig. 14 shows the overall appearance of the test pad and shaft after this test had been concluded. The pad surface was severely "worked" and showed considerable plastic flow. The shaft was almost completely covered with transferred metal.

In Fig. 15, photomicrographs of these contact surfaces are shown.

The most apt description of the appearance of this bearing combination which comes to mind is to say the bearing was "creamed."

IMPACT RESISTANCE OF CHROME OXIDE COATINGS

To demonstrate the fact that thin coatings of chrome oxide would not shatter when impacted, a simple test was made. A machinist ball peen hammer with a one pound head was dropped against a coated flat disk from a height of about two inches. The disk was aluminum with a .003 inch coating of chrome oxide. When the disk was struck on the edge, a small amount of the coating flaked off. However, when the disk was impacted on the flat surface, the surface brinelled but the coating did not crack. Fig. 16 is a photograph of the surface damage which was observed. The results of this test, coupled with other experience, indicates that the edges are the most susceptible areas to damage. Generous radii can help this condition but the edges will always be a problem.

This test was not a part of the scope of this program and was not intended to provide engineering data, but rather, to illustrate the fact that the coating has the ability to tolerate some mishandling.

FURTHER CONSIDERATIONS OF CRITERIA FOR THE SELECTION OF GAS BEARING MATERIAL COMBINATIONS

In Ref. 1,* the following general criteria were suggested for use in selecting compatible sliding material combinations for gas-lubricated bearings.

<u>Criteria</u>	<u>Typical Examples</u>
1. Hard, wear-resistant coatings on both shaft and bearings.	Oxides, carbides, hard facings such as Stellites and nitride coatings.
2. Soft phase materials (mated against hard, lapped shaft).	Sprayed bronze or nickel-copper-indium on bearings versus hard shaft.
3. Self-lubricating materials (mated against hard, lapped shaft).	DU or carbon-graphite film stock versus hard shaft.
4. Solid lubricant films (mated against hard, lapped shaft).	Resin or ceramic bonded films of MoS ₂ , graphite, PbO, etc. versus hard shaft.

Using these criteria, representative material combinations were selected and evaluated. A self-mated ceramic coating, chrome oxide, proved to be the most satisfactory. This material falls under the criterion of a hard, wear-resistant coating.

The observations which were made during the work reported in Ref. 1, and also in the work reported here, permit certain hypotheses to be made in defining the characteristics of a suitable hard coating. These are discussed briefly in the following paragraphs.

(a) The Effect of Metallic Constituents

Based on the experience which MTI has accumulated to date, the problem of finding material combinations which can survive a large number of low speed

*"Evaluation of Bearing Material Combinations for the NASA Turbine-Compressor."
S. F. Murray, MTI-64TR56, September 30, 1964.

sliding cycles during starts and stops is not particularly difficult and at least three combinations are known to be satisfactory. On the other hand, satisfactory resistance to surface damage during high speed rubs is a much more difficult problem. Test experience indicates that the problem is caused by material transfer and subsequent welding or scoring. Fig. 17 shows the types of damage which were sustained by three different tilting-pad bearings in other tests. These pads were all subjected to at least seventy impacts against a 1.5 inch diameter shaft rotating at 60,000 rpm. The hardened M-50 tool steel pad, which was sliding on a cobalt-bonded tungsten carbide coating, shows heavy welding and plastic flow on the pad surface. The nickel-bonded tungsten carbide coated pad, mated against an Al_2O_3 coated shaft, has sharp abrasion scratches which are the result of transfer of the nickel binder metal to the Al_2O_3 shaft and subsequent scoring of the carbide pad. The third pad is a chrome oxide coated pad that was mated against a chrome oxide coated shaft. The only surface change with this material was a small amount of fine abrasive wear which resulted in a polished contact area.

Since the bearing is sliding against the shaft at a velocity of 390 feet per second during each impact, it is not surprising that substantial heat generation and metal transfer could occur, even in a fraction of a second.

Of these three bearing materials, only the chrome oxide showed real promise. This material is a non-metallic, self-bonded oxide coating. These results indicate that self-bonded, non-metallic coatings have a much greater chance of surviving a high speed rub than metal-bonded or metallic surfaces since the presence of metals can lead to transfer between surfaces.

(b) The Effect of the Type of Wear Debris

The surface appearance of the Cr_2O_3 coating before and after the test also suggests that the polishing effect is the result of the fact that a small amount of very fine wear debris is formed. This debris appears to polish rather than to score the contacting surfaces. This suggests that a good coating should wear in the form of very fine debris rather than by the fracture of large agglomerates of crystals which could score the coating.

(c) The Effect of Coating Density

The density of the surface coating may also have a significant effect on the results. Fig. 18 shows the surfaces of two chrome oxide coating tilting-pad bearings. Both of these bearings were subjected to the same number of high speed rubs. One bearing is a somewhat porous, plasma-sprayed chrome oxide. The surface was polished smoothly by the sliding contact. The second bearing was coated with chrome oxide by a detonation process. This results in a denser, better-bonded coating. However, the contact area shows definite abrasion scratches. This indicates that a somewhat porous coating is preferable to a high density material because wear debris which cannot escape from the contact area will be trapped in the pores.

To summarize, it appears that the ideal coating for high speed sliding compatibility should have the following characteristics:

1. The coating should be a self-bonded, non-metallic material with good friction and wear behavior.
2. The coating should wear in the form of fine debris rather than larger crystal agglomerates.
3. The coating should have good integrity and good adhesion, but high density does not appear to be an essential attribute.

Further work is required to demonstrate the general applicability of these hypotheses to the problem of material selection.

APPENDIX A - PREPARATION OF TEST SPECIMENS

The base material for all of the test specimens, with the exception of the M-50 steel pads, was 416 stainless steel - heat-treated and tempered to give a hardness of 23-26 R_c. The M-50 steel pads were hardened to 60-62 R_c.

All test pads were made by machining round stock to form plain sleeves, 1.900 inch O.D., 1.49 inch I.D. and 1.25 inch long. Each sleeve was then cut axially to form four equal segments. Using a standard fixture, slots were milled along the back of the pads at the desired pivot point.

The test pads which were to be coated with chrome oxide were then "epoxied" into the bore of a steel nest and the inside diameter of the pads was turned .003 inches undersize on the radius. The pads were then removed from the nest and coated with .006 to .007 inches of chrome oxide. This coating was plasma sprayed by the Avco Corporation. Then the pads were cemented back in the steel nest and were ground and lapped to a $1.5006 \pm .0001$ inch bore with a surface finish of 5 rms. The four pads were pressed out of the steel housing. The edges of the pads were stoned to remove any sharp corners, holes were drilled and tapped for the probe holders and thermocouple, and the hardened steel half-bushing was spot welded in place on the back of the pad as shown in Fig. 5.

The M-50 pads were turned .010 inches oversize on the radius, probe and thermocouple holes were drilled, and the pads were then heat treated by the following procedure:

1. Stand parts on side in wire mesh baskets and separate to give one inch free space between parts during heating and quenching.
2. Preheat at 1650 F holding five to ten minutes at temperature (metal temperature).
3. Transfer to controlled atmosphere furnace at 2200 ± 10 F. Allow to equalize and hold two minutes at temperature.

4. Quench in oil until vibrations cease (about 1050 F), then remove and air cool to about 90 F.
5. Temper immediately at 1060 F, hold three hours at temperature and air cool.

The measured hardness of these pads was 59 to 61 Rockwell C after this heat treatment.

The pads were cemented back in the steel nest and were ground and lapped to a $1.5006 \pm .0001$ inch bore and a surface finish of 4 rms. Then the pads were removed from the nest and assembled.

Two sets of shafts were coated for these tests. The shafts were rough machined and a 2.3 inches long relief in the center of the shaft was turned to a diameter of 1.493 inches. The shafts were then coated in the relieved section with .006 - .007 inches of the following materials:

1. Chrome oxide - Avco
2. Tungsten carbide LW-1N40 (15-17 percent Co binder) - Linde

Then the entire length of the shaft was ground and lapped to $1.4991 \pm .0001$ inches straight and concentric within .000050 inch T.I.R. with a surface finish better than 4 rms. This left a coating about .003 inch thick in the center of each of the shafts.

The high-speed shafts were balanced at MTI.

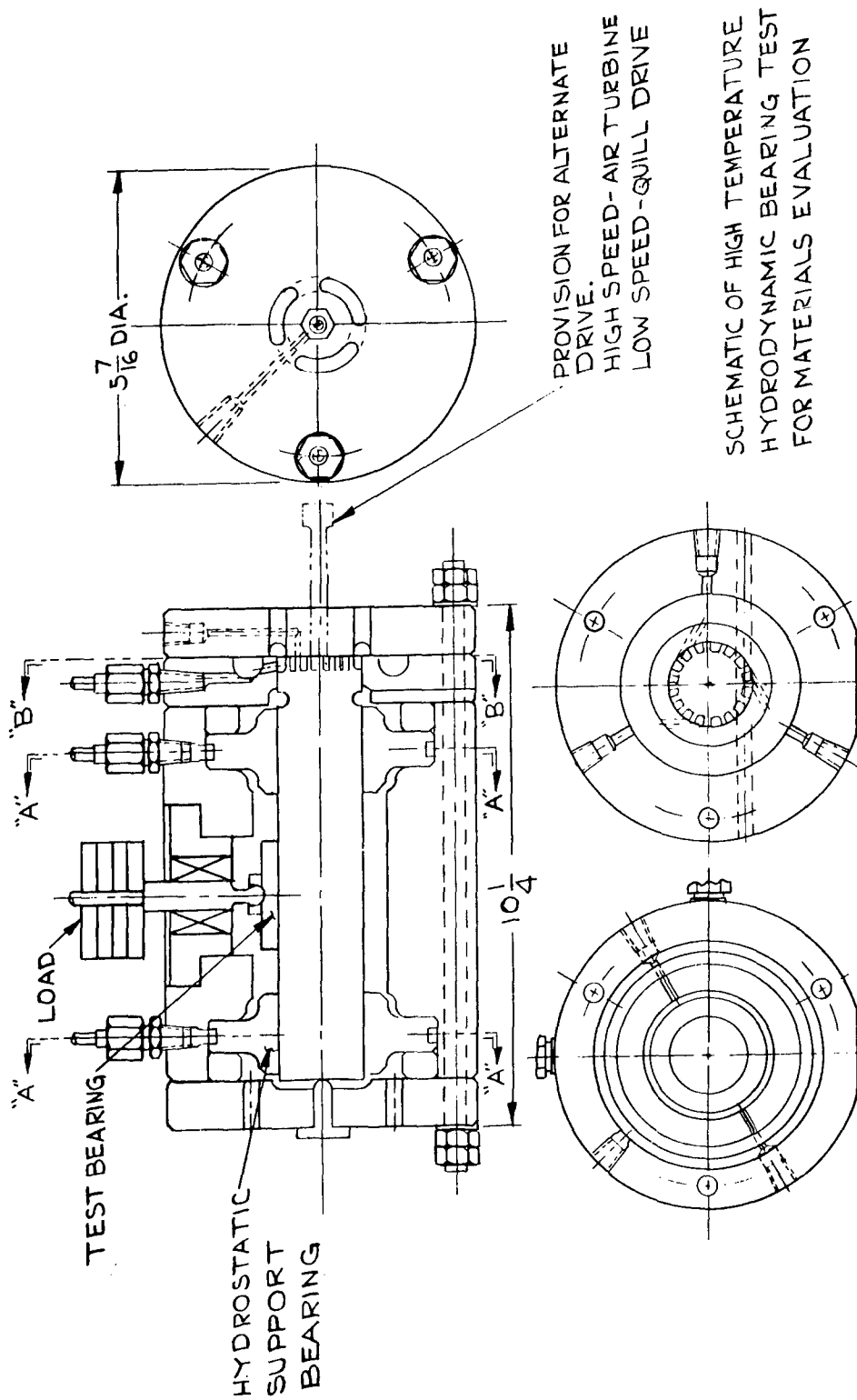


Figure 1

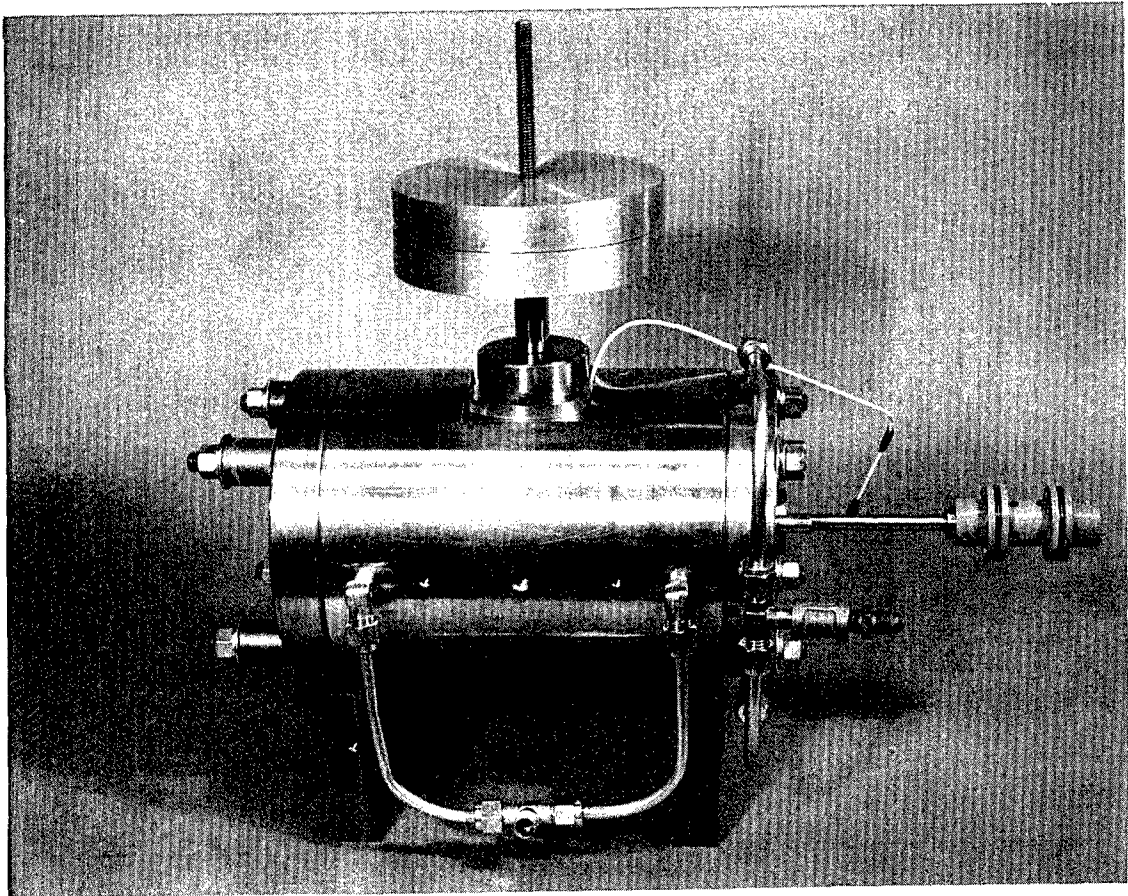


Fig. 2 - Hydrodynamic Bearing Materials Test Rig
Showing Drive for Start-Stop Evaluations

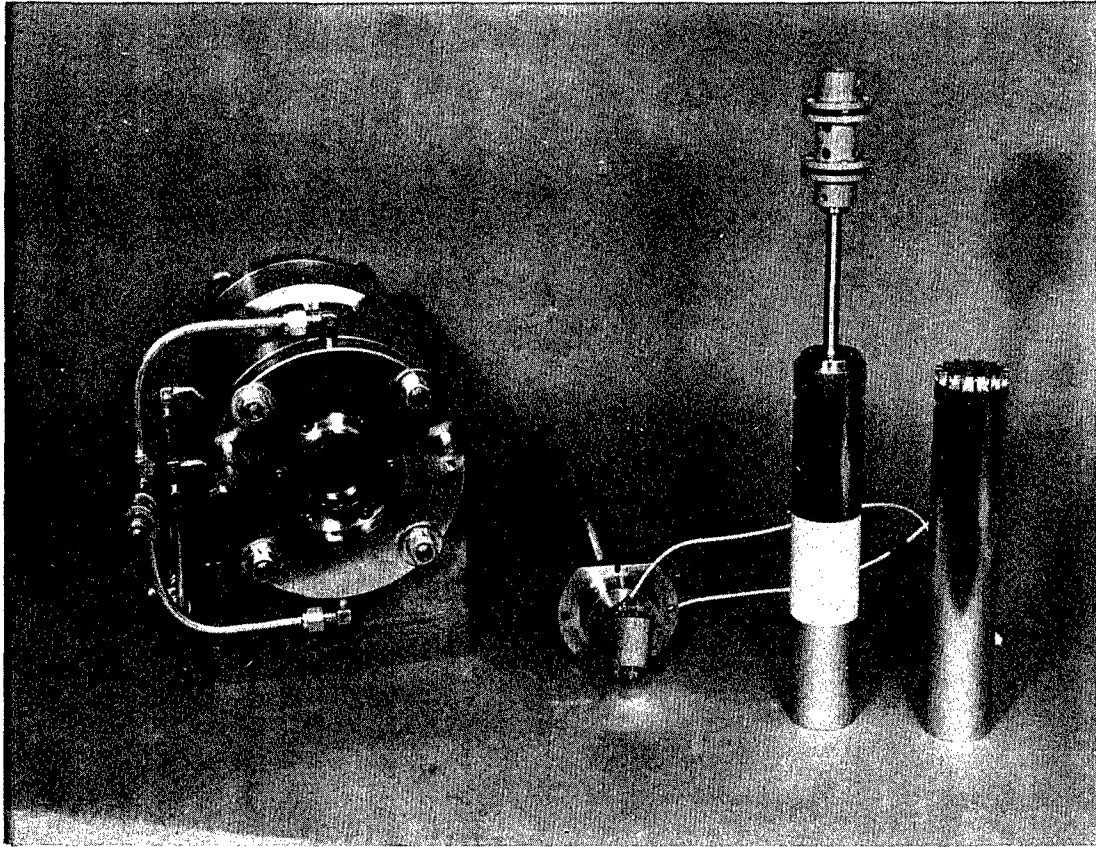


Fig. 3 Disassembled View of Test Rig Showing Test Shafts and Tilting-Pad Bearing

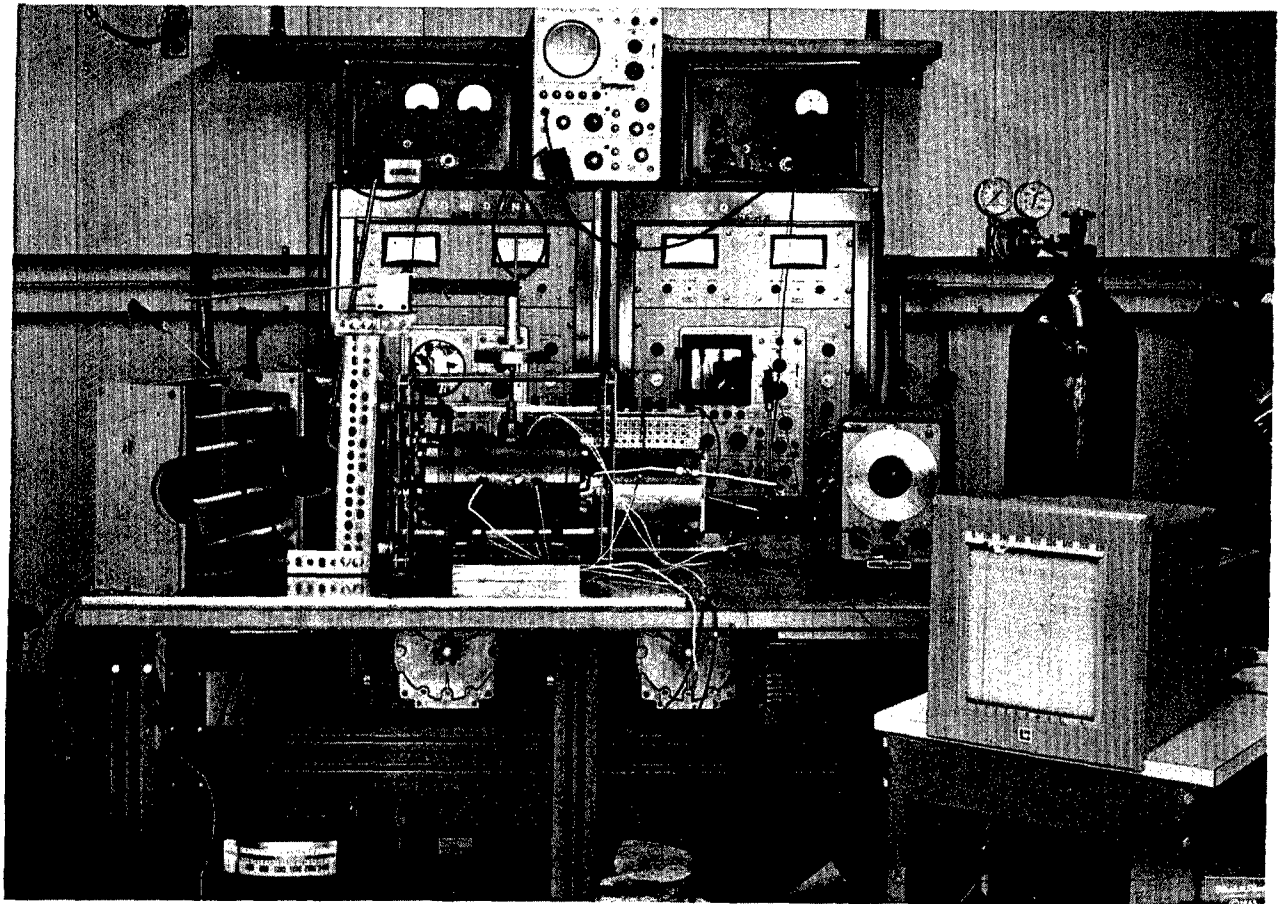


Fig. 4 - Overall View of Test Equipment

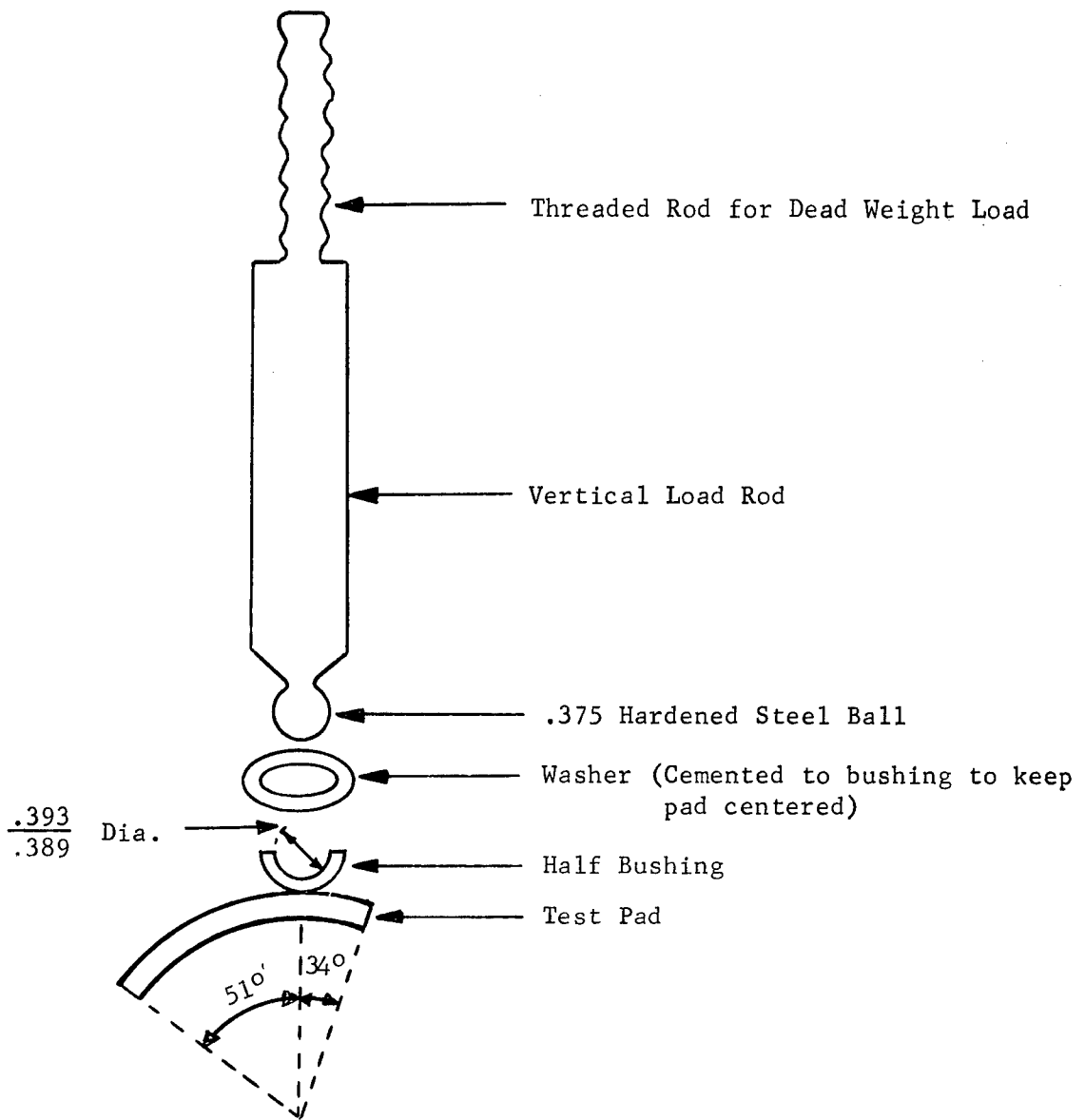


Fig. 5 Exploded View of Pad and Pivot Design

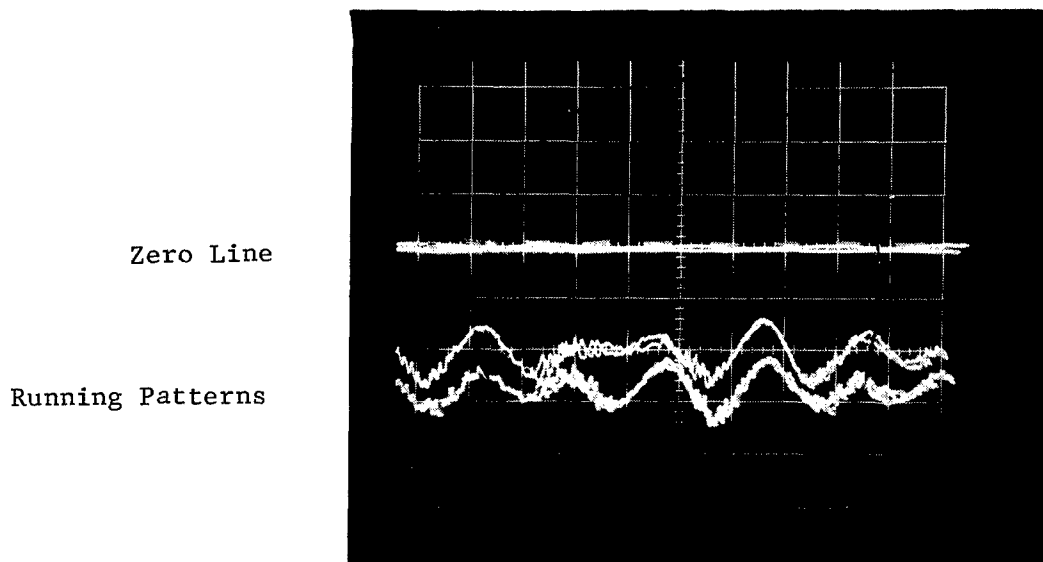
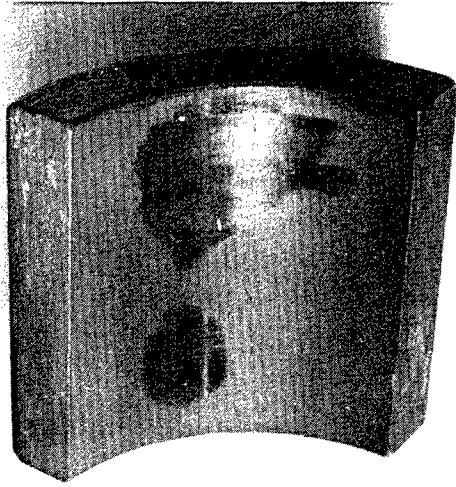
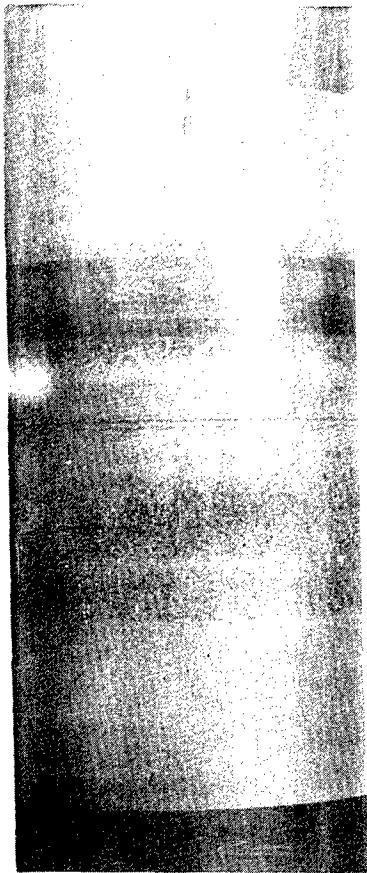


Fig. 6 Oscilloscope Patterns from Two Capacitance Probes Mounted on Each Side of a Tilting-Pad Shoe in Line with the Pivot Point

Scale: One Large Division - 80 Microinches

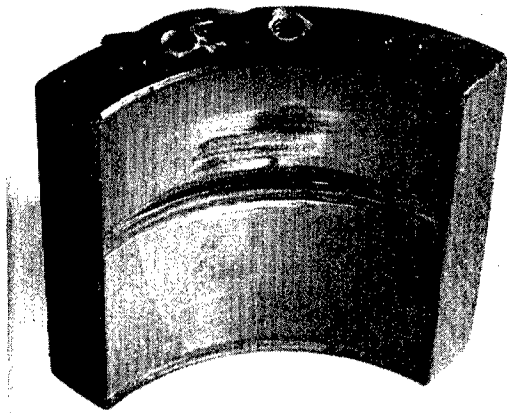


Chrome Oxide
Coated Pad



Chrome Oxide
Coated Shaft

Fig. 7 Pad and Shaft Specimens from Start-Stop Tests
Chrome Oxide Coated Pad Versus Chrome Oxide Coated Shaft
1000 Starts and Stops at 4.0 PSI



M-50 Pad



Carbide Coated Shaft

Fig. 8 Pad and Shaft Specimens from Start-Stop Tests
Hardened M-50 Tool Steel Pad Versus Flame Plated
LW-1 N 40 Tungsten Carbide Coated Shaft
1000 Starts and Stops at 4.0 PSI

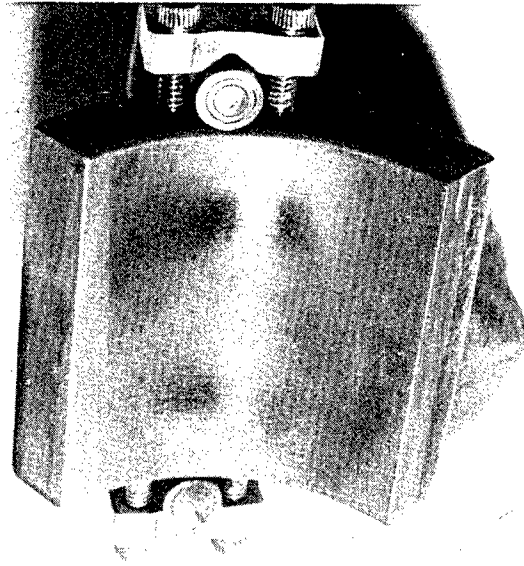


Fig. 9 - Contact Surface on Tilting Pad Bearing After First Series of High Speed Rubs

Chrome Oxide Coated Pad Versus Chrome Oxide Coated Shaft

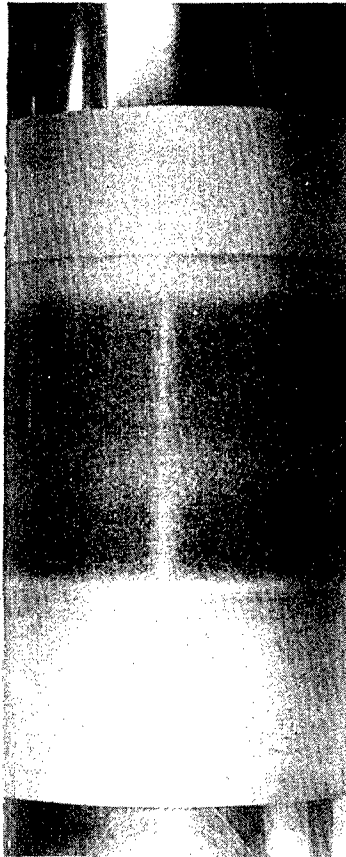
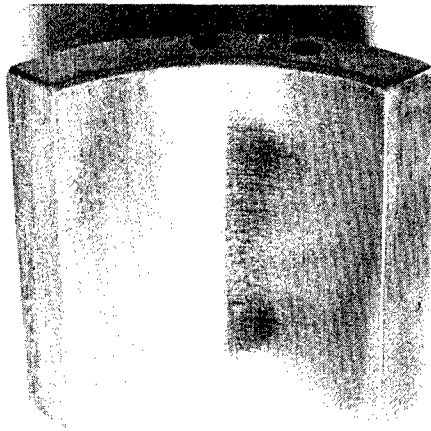
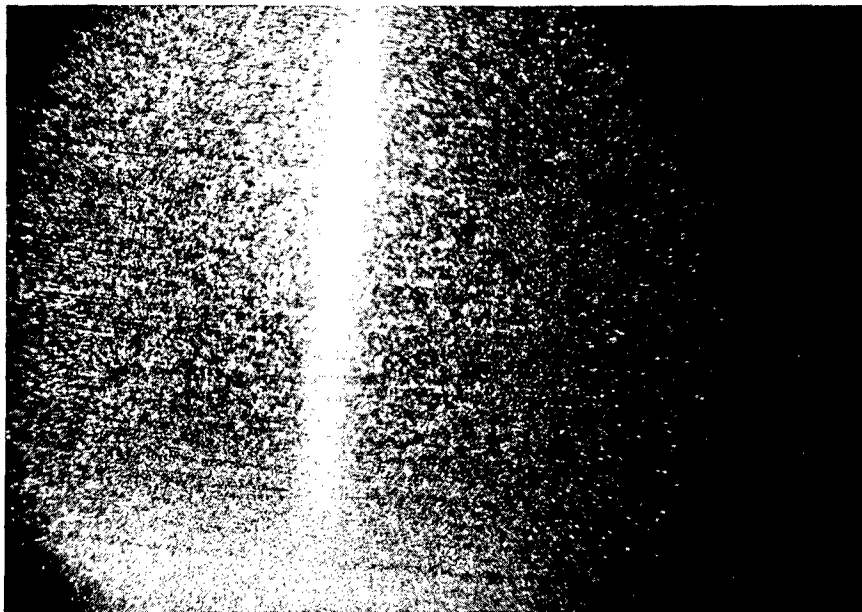


Fig. 10 Contact Surfaces on Tilting Pad Bearing and Shaft After
Second Series of High Speed Rubs
Chrome Oxide Coated Pad Versus Chrome Oxide Coated Shaft



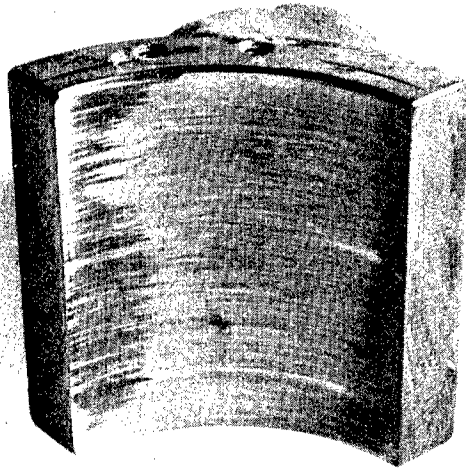
Pad Surface



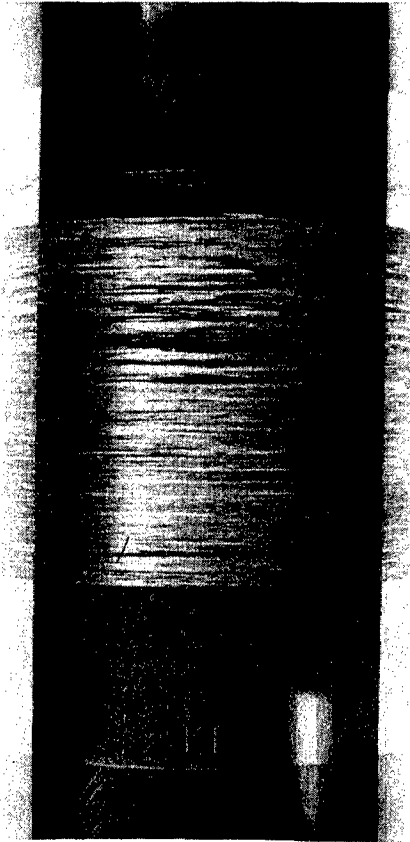
Shaft Surface

Fig. 11 Photomicrographs of Contact Surfaces on Tilting Pad Bearing and Shaft After Second Series of High Speed Rubs Chrome Oxide Coated Pad Versus Chrome Oxide Coated Shaft

Magnification 30x

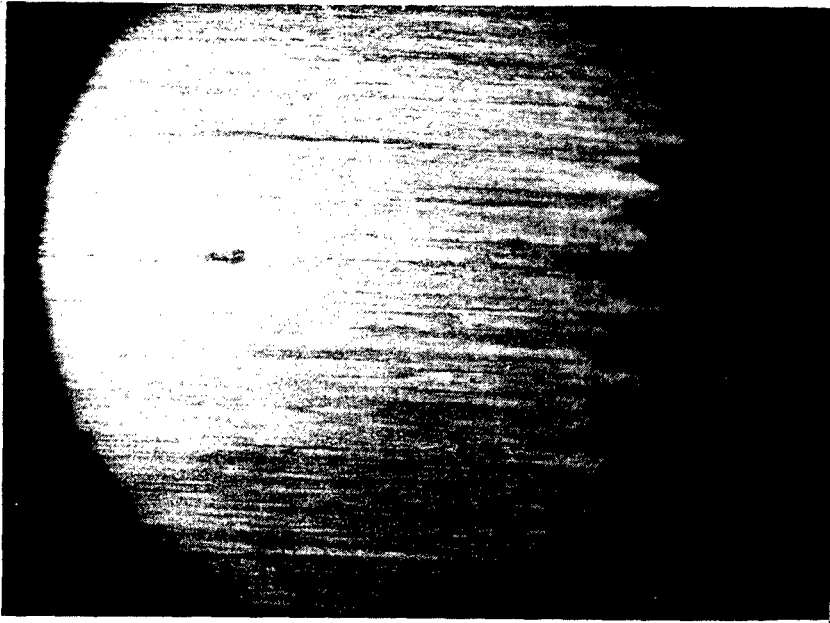


M-50 Pad

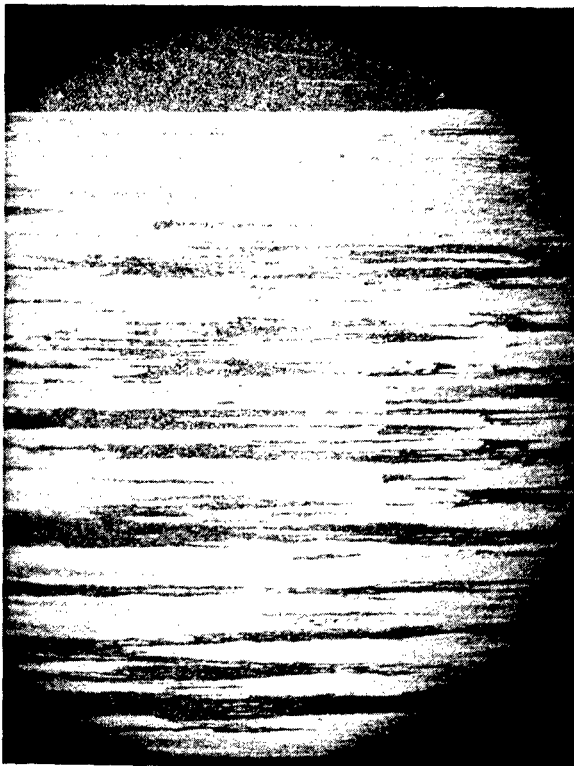


Carbide Coated Shaft

Fig. 12 Contact Surfaces on Tilting Pad Bearing and Shaft
After First Series of High Speed Rubs
Hardened M-50 Tool Steel Pad Versus LW-1 N-40
Tungsten Carbide Coated Shaft

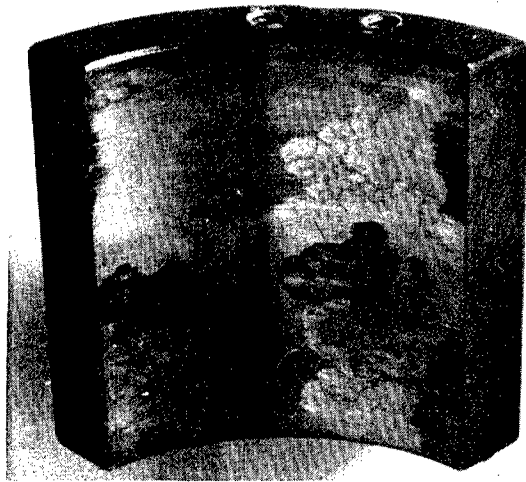


M-50 Pad Surface

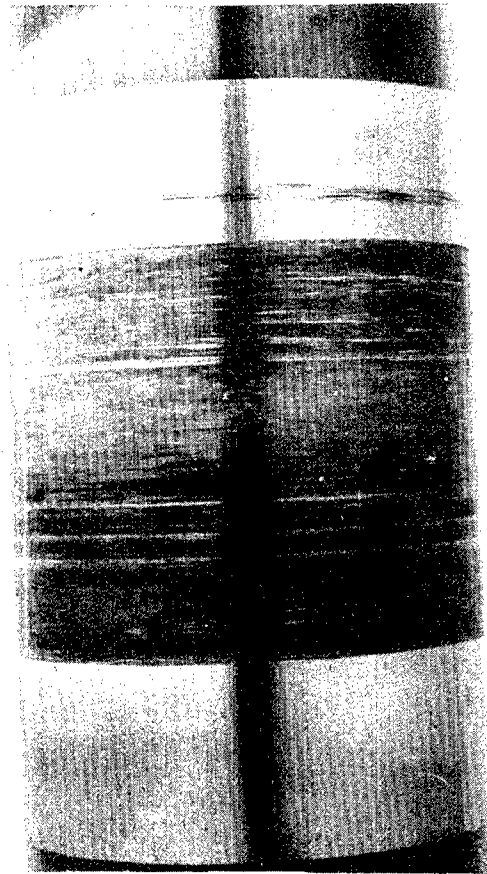


Carbide Coated
Shaft Surface

Fig. 13 Photomicrographs of Contact Surfaces on Tilting Pad
Bearing and Shaft After First Series of High Speed Rubs
Hardened M-50 Tool Steel Pad Versus LW-1 N-40 Tungsten
Carbide Coated Shaft
Magnification 30x

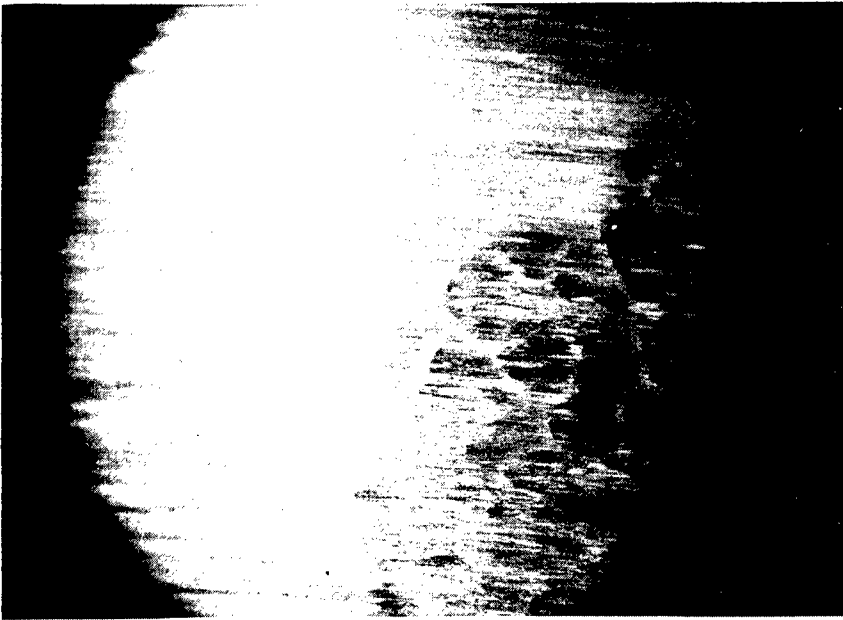


M-50 Pad

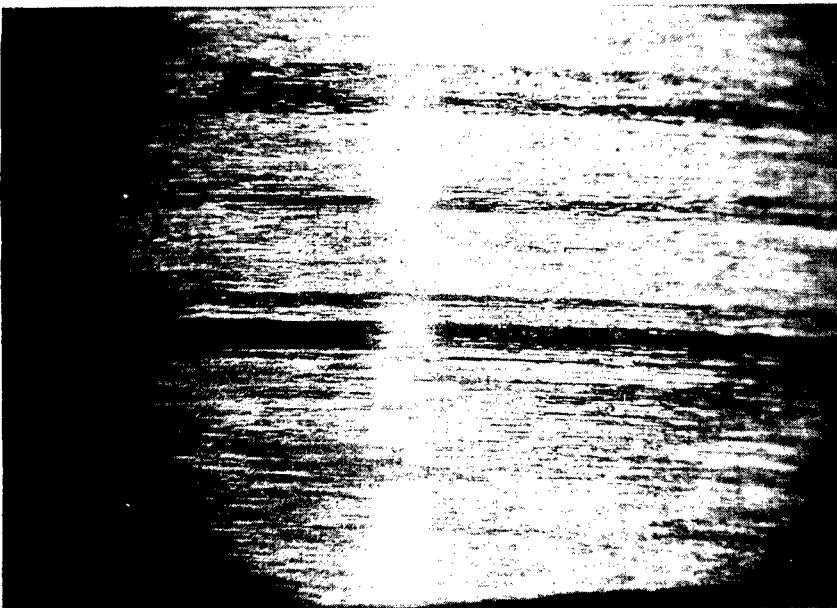


Carbide Coated Shaft

Fig. 14 Contact Surfaces on Tilting Pad Bearing and Shaft
After Second Series of High Speed Rubs
Hardened M-50 Tool Steel Pad Versus LW-1 N-40
Tungsten Carbide Coated Shaft



M-50 Pad Surface



Carbide Coated
Shaft Surface

Fig. 15 Photomicrographs of Contact Surfaces on Tilting Pad Bearing and Shaft After Second Series of High Speed Rubs
Hardened M-50 Tool Steel Pad Versus LW-1 N-40 Tungsten Carbide Coated Shaft

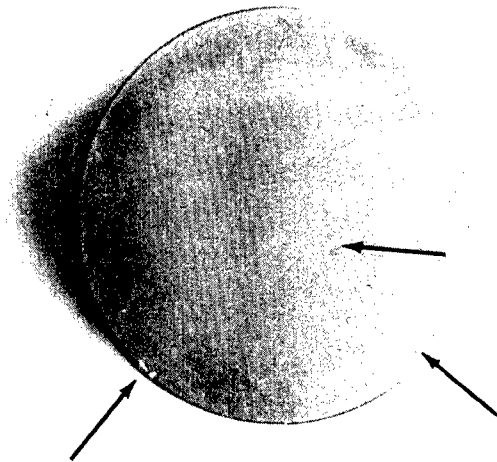
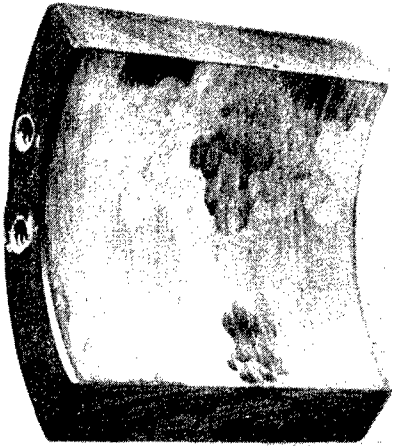


Fig. 16 Impact Damage to Chrome Oxide Coated Disk Caused by Dropping Ball Peen Hammer on Surface at Various Points - Deliberately

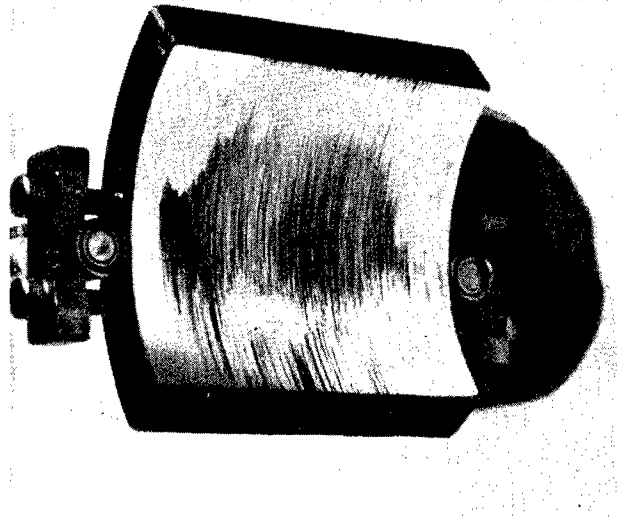
Weight of Hammer 620 grams

Drop Height 2 inches

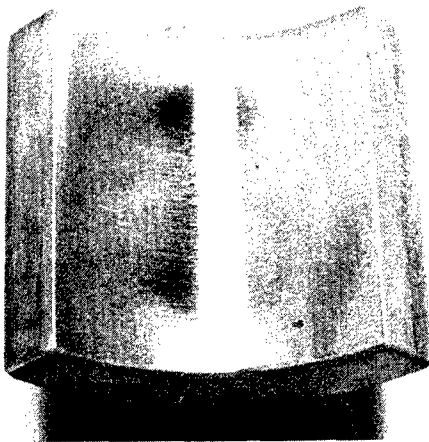
Coating flaked off at edge but is still intact on flat surface area



Hardened M-50 Tool Steel. Run
Versus Carbide Coated Shaft



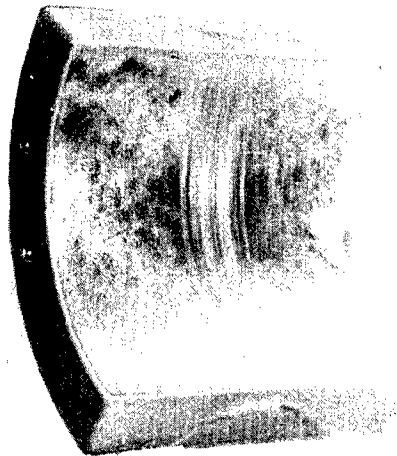
Flame-Plated Tungsten Carbide.
Run Versus Al_2O_3 Coated Shaft



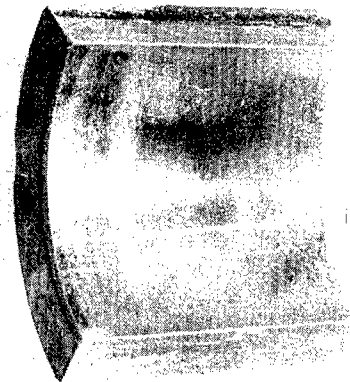
Plasma Coated Chrome Oxide. Run
Versus Chrome Oxide Coated Shaft

Fig. 17 - Photomicrographs of Portions of Contact Areas on Pad and
Shaft Surfaces After High Speed Rub Tests.

Magnification x 30.



Pad Detonation-Coated With Chrome
Oxide Versus Same Coating on Shaft



Pad Plasma-Coated With Chrome
Oxide Versus Same Coating on Shaft

Fig. 18 Surface Appearance of Chrome Oxide Coated Pads With
Different Density Coatings.

Both Pads Subjected to One Hundred High Speed Rubs
at 48,000 RPM in Air

APPENDIX G

TEST PROCEDURE FOR WHIRL THRESHOLD TESTS

The simulator rotor had been balanced during a previous series of tests. Balancing had been done in the simulator gas-lubricated bearings using an IRD vibration analyzer coupled to the output of one of the capacitance probes at each end of the rotor. The balancing planes used during this process were located in the thrust runner and in the turbine wheel. Balancing was started at speeds of 20,000 and 25,000 rpm; final balancing was performed at 40,000 rpm. The balancing process was carried to the limit of the instrumentation sensitivity. This was the condition of rotor balance during the tests reported herein, except where specifically stated otherwise.

The pad pivot supports had been set-up prior to this test series to provide a diametral clearance in No. 2 bearing of 0.0011 inch at 70 F at zero rpm. This initial set-up clearance had been calculated to result in the design preload value of 0.5 at 50,000 rpm with the journal and the housing at the calculated temperatures for the second bearing system design of 190 F and 340 F respectively (see Appendix D). This calculation took into account the flexure stiffness, centrifugal growth, and thermal expansion effects. The No. 1 bearing set-up diametral clearance was 0.0008 inch, based on a similar calculation.

All threshold tests were performed with the following auxiliary conditions:

- main thrust bearing supply pressure - 40 psig
- main thrust bearing film thickness - 0.0032 to 0.0042 inch
- reverse thrust bearing supply pressure - 30 psig
- reverse thrust bearing film thickness - 0.0017 to 0.0025 inch
- thrust bearing cooling water flow - None
- No. 1 bearing heating gas flow - None
- bearing ambient pressure - 14.7 psia

The shaft cooling gas flow and the bearing heater voltage were varied during each run to control the No. 2 bearing diametral clearance. The diametral clearance in No. 1 bearing was not specifically controlled, and varied between a maximum of 0.0015 and a minimum of 0.0008 inch.

Determination of Threshold Clearance vs RPM at 14.7 psia in Air with Residual Unbalance

The test was started with the rotor axis in a horizontal orientation. A rotor speed of 20,000 \pm 100 rpm was established and data was recorded after temperatures had stabilized with zero shaft cooling gas and zero bulkhead heater voltage. The resulting running condition in No. 2 bearing was as follows:

diametral clearance (PF 21 + PF 23) - 0.00110 inches
diametral clearance (PF 20 + PF 22) - 0.00117 inches
diametral clearance, average - 0.00113 inches
bulkhead temperature - 82 F
average pad temperature - 96 F
rotor behavior - stable.

The bulkhead heater was then turned on to raise the bulkhead temperature and increase the bearing clearance, while the speed was maintained constant. The rotor speed tended to increase slightly as the clearance increased, presumably due to decreased friction losses. This was compensated for by decreasing the turbine drive pressure. The rate of increase of the bearing clearance was slow; after 45 minutes the following operating condition was reached:

diametral clearance (PF 21 + PF 23) > 0.00274* inches
diametral clearance (PF 20 + PF 22) > 0.00275* inches
diametral clearance, average > 0.00274 inches
average bulkhead temperature - 198 F
average pad temperature - 137 F
rotor behavior - stable.

*clearance at unloaded pads exceeded max. CRO indication of 0.002 inch.

No instability was observed and the test run was discontinued, as the behavior and clearance of the unloaded pads could no longer be monitored.

The bulkhead heater was then turned off and the simulator was allowed to cool while

operating at about 20,000 rpm. When the No. 2 bearing diametral clearance had decreased to approximately its initial value, the rotor speed was increased to 30,000 rpm. When temperatures had stabilized, the following running condition was recorded (zero cooling gas flow and bulkhead heater voltage):

diametral clearance (PF 21 + PF 23) - 0.00139 inches
 diametral clearance (PF 20 + PF 22) - 0.00133 inches
 diametral clearance, average - 0.00136 inches
 average bulkhead temperature - 124 F
 average pad temperature - 98 F
 rotor behavior - stable.

Shaft cooling gas and the bulkhead heater were then turned on and the bearing clearance was slowly increased. The threshold of the whirl phenomenon, as described in the previous section, was noted at the following conditions (which were maintained while data was recorded):

diametral clearance (PF 21 + PF 23) - 0.00259 inches
 diametral clearance (PF 20 + PF 22) - 0.00278 inches
 diametral clearance, average - 0.00268 inches
 average bulkhead temperature - 195 F
 average pad temperature - 139 F

The response of the lower or loaded pads to the whirl was more pronounced than that of the upper pads. The clearance was further increased slowly, during which time the whirl orbit became more permanent and then started to increase in diameter. This process was terminated at the following recorded conditions, since the clearance at the unloaded pads had reached the limit of the CRO scale:

diametral clearance (PF 21 + PF 23) - 0.00285 inches
 (PF 22 + PF 20) - 0.00310 inches
 average - 0.00297 inches
 average bulkhead temperature - 218 F
 average pad temperature - 144 F

Operation at the above condition was not considered hazardous in any respect.

After recording data at the conditions cited above, the rotor was decelerated and allowed to cool, after which the rotor speed was increased to 40,000 rpm. A stable condition was recorded as for previous runs (data presented in Table G-1) and the clearance was again slowly increased. The conditions at the threshold of whirl are noted in Table G-1. The clearance was increased beyond the threshold point (average diametral clearance of 0.00217 inch) to a maximum average value of 0.00240 inches. At this condition, the whirl orbit reached a diameter of 0.0004 inches on occasion and bore some resemblance to unstable orbits of other bearings which had been known to diverge. The clearance was decreased and the rotor decelerated.

The same sequence of operations was performed for speeds of 50,000 and 60,000 rpm. The drive turbine was switched from shop air to high-pressure nitrogen supply for the 60,000 rpm test runs. The recorded clearance and temperature data are presented in Table G-1. The threshold data are discussed in a later section.

After test runs were made at reduced bearing ambient pressure (discussed in the following subsection), the simulator housing was rotated to align the rotor axis vertically, turbine end down. In this orientation the terms "loaded" and "unloaded" pads lose significance, as all pads are subject only to preload and rotating unbalance forces. These forces act equally on all pads.

The test procedure described for horizontal test runs was employed for the vertical runs. The whirl phenomenon was encountered at 20,000 rpm during the vertical rotor tests. The average diametral clearance at the threshold was 2.47 mils. (Note that an average diametral clearance of 2.74 mils was reached without encountering whirl at 20,000 rpm in the horizontal orientation.) Test runs were made to determine threshold conditions at speeds of 30,000, 40,000, 50,000 and 60,000 rpm. The recorded clearance and temperature data are presented in Table G-1.

Tests at Reduced Ambient Pressure

Test runs were made in air, with residual unbalance, in both horizontal and vertical orientations, while maintaining an ambient pressure of 10 inches mercury vacuum

(approximately 10 psia) in the chamber surrounding the No. 2 bearing. This pressure was arrived at from the observation that the threshold clearance tended to decrease as the ambient pressure was reduced. A whirl-free operating clearance established on the basis of test performance at 10 psia would therefore offer some margin of safety at the turbocompressor design ambient pressure of 12 psia. During these tests the desired running condition was arrived at by the following sequence:

1. at bearing ambient pressure of 14.7 psia, accelerate to the first test speed.
2. at constant speed, reduce bearing ambient pressure slowly to the desired value; thrust loading chamber pressures must be continually adjusted during this process as relatively small changes in the bearing ambient pressure produce significant changes in thrust load.
3. adjust shaft cooling gas flow and bulkhead heater to achieve desired effect on No. 2 bearing clearance.
4. acceleration to successive test speeds was performed at the reduced ambient pressure.

Test runs were made at the rotor speeds previously cited in both horizontal and vertical orientations. The test procedure was identical to that described previously.

Tests in Argon

The effect on the whirl threshold of changing the lubricant gas from air to argon was determined by re-running the 10 psia, vertical rotor test series, using argon for all gas flows except the turbine supply. This condition was chosen because it was apparently the most severe from the standpoint of causing whirl at a relatively low clearance, and because it most nearly duplicated the design conditions for the turbocompressor. Since the effects of changing the rotor orientation and the ambient pressure should be the same for either gas, only the one test series was performed in argon. The test procedure followed during this test was identical to that described for the previous tests. Several minutes of

operation with argon flow were allowed before any data were recorded to flush air from the interior of the simulator. The recorded clearance and temperature data are presented in Table G-1. It was noted that increasing the clearance beyond the threshold value resulted in less severe accentuation of the whirl phenomenon in argon than in air.

The variation of the whirl threshold clearance with speed at all of the several test conditions is presented in Section IV of this report.

Test With Added Unbalance

An unbalance weight of 70 milligrams was added to the turbine wheel at a radius of 1.375 inches (resulting unbalance of 0.0034 ounce-inch). With this condition of unbalance, a test run was made to determine the whirl threshold clearance at the following conditions:

rotor orientation - vertical
ambient pressure - 14.7 psia
lubricant gas - air
rotor speed - 40,000 rpm.

The average diametral clearance at the condition chosen as the threshold of whirl was 1.68 mils, as compared with 1.77 mils for the same conditions with residual unbalance. The change in the No. 2 bearing orbit during stable operation at 60,000 rpm in air at 10 psia with the rotor vertical, due to the added unbalance, is shown in Figure 18. This negligible change in the orbit during stable operation indicated that the bearing was practically unaffected by the added unbalance. In view of this, the above check point of threshold diametral clearance was considered adequate to define the effect of unbalance.

Tests of No. 1 Bearing

No evidence of whirl in the No. 1 bearing had been seen throughout the tests of No. 2 bearing. Additional tests were made with the specific purpose of determining whirl threshold clearances for the No. 1 bearing.

The gas supply system was modified slightly in an effort to achieve larger clearances in the No. 1 bearing. The heater originally installed in the shaft cooling gas line was disconnected from that line, and the reverse thrust bearing hydrostatic supply gas was routed through this heater. The reverse thrust bearing gas is supplied through passages in the No. 1 bearing housing. It was consequently anticipated that increasing this gas temperature would heat the bearing housing.

The test runs were made at the following conditions:

- rotor orientation - vertical
- ambient pressure - 10 psia
- lubricant gas - air
- rotor speeds - 40,000 rpm
50,000 rpm
60,000 rpm

These conditions were chosen as being most conducive to whirl. The No. 1 bearing-housing heating gas was supplied at the maximum temperature which could be achieved (125 F). The reverse thrust bearing gas was heated to approximately 175 F. However, the gas flow rate to the reverse thrust bearing was apparently so low that no appreciable heating of the housing was achieved. The shaft cooling gas flow was increased beyond the range of the flowmeter to keep the journal as cool as possible. The recorded conditions at the maximum attainable bearing clearances are as follows:

No. 1 Bearing

<u>RPM</u>	<u>Average diametral clearance</u>	<u>Pad temperature</u>	<u>Housing Temperature</u>	<u>Rotor behavior</u>
40,000	0.00136"	114 F	125 F	stable
50,000	0.00132"	124 F	131 F	stable
60,000	0.00130"	136 F	143 F	stable

The whirl phenomenon was not evident in the No. 1 bearing at the above conditions.

TABLE G-1
Summary of Test Results

Low-Frequency Whirl Threshold Tests of Turbocompressor No. 2 Low-Loss Journal Bearing

Rotor Orientation	Lubricant Gas	Ambient Pressure PSIA	Rotor Speed RPMx10 ⁻³	Diametral Clearance, mils			Average Temperature		Stability *
				PF21+PF23	PF22+PF20	Avg.	Pads, °F	Housing, °F	
HOR.	AIR	14.7	20	1.24	1.21	1.22	96	82	
			20	>2.74	>2.75	>2.75	136	198	
			30.7	1.39	1.33	1.36	124	98	
			30.1	2.59	2.78	2.68	139	194	x
			40.2	1.30	1.34	1.32	138	113	
			40.9	2.14	2.20	2.17	158	187	x
			49.7	1.06	1.05	1.05	167	110	
			50.1	1.84	1.90	1.87	195	205	x
			59.4	1.00	1.00	1.00	197	135	
			59.7	1.39	1.43	1.41	226	197	x
		10.0	20.4	1.37	1.46	1.41	114	113	
			20.5	2.95	3.12	3.03	108	188	
			30.3	1.36	1.35	1.35	98	83	
			30.4	2.34	2.48	2.41	108	155	x
			40.5	1.24	1.28	1.26	129	104	
			40.9	2.16	1.96	2.06	133	146	x
			50.0	1.06	1.15	1.10	157	116	
			50.0	1.62	1.80	1.71	161	175	x
			59.6	1.18	1.29	1.23	198	172	
			60.0	1.38	1.41	1.39	203	196	x
VERT.	AIR	14.7	19.8	1.41	1.47	1.44	90	87	
			20.2	2.45	2.49	2.47	99	144	x
			30.2	1.65	1.62	1.63	102	105	
			30.3	2.20	2.16	2.18	114	143	x
			40.0	1.45	1.43	1.44	127	107	
			40.2	1.76	1.78	1.77	132	126	x
			49.4	1.24	1.20	1.22	164	119	
			49.4	1.69	1.65	1.67	180	166	x
			59.8	1.00	0.89	0.94	202	134	
			58.9	1.18	1.10	1.14	225	174	x
		10.0	20.0	1.61	1.56	1.58	100	101	
			20.0	2.12	2.14	2.13	100	126	x
			30.0	1.55	1.50	1.52	105	100	
			30.2	1.87	1.82	1.84	107	114	x
			40.0	1.31	1.24	1.27	128	107	
			39.5	1.55	1.49	1.52	137	122	x
			49.9	1.20	1.15	1.17	157	119	x
			60.3	0.82	0.68	0.70	207	133	
			59.5	0.93	0.79	0.86	215	143	x
			20.1	1.47	1.48	1.47	88	76	
VERT.	ARGON	10.0	19.8	2.39	2.35	2.37	98	131	x
			29.8	1.45	1.37	1.41	113	94	
			30.3	2.08	2.03	2.05	132	144	x
			39.8	1.15	1.09	1.12	157	103	
			40.1	1.68	1.60	1.64	172	153	x
			49.6	1.13	0.98	1.05	214	148	
			49.9	1.40	1.32	1.36	227	185	x
			59.8	0.79	0.73	0.76	286	177	
			60.0	1.20	1.08	1.14	300	231	x

* An "x" in the stability column denotes the threshold condition; a blank denotes the initial stable condition.